Expressions of Mantle Dynamics in Landscapes and Sedimentary Basins

Fergus McNab

A dissertation submitted for the degree of
Doctor of Philosophy
at the University of Cambridge

Magdalene College
September 27, 2019

Declaration

This dissertation is the result of my own work and includes nothing which is the outcome of work done in collaboration except as declared in the text. It is not substantially the same as any that I have submitted, or, is being concurrently submitted for a degree or diploma or other qualification at the University of Cambridge or any other University or similar institution except as declared in the Preface and specified in the text. I further state that no substantial part of my dissertation has already been submitted, or, is being concurrently submitted for any such degree, diploma or other qualification at the University of Cambridge or any other University or similar institution except as declared in the text. It does not exceed the prescribed word limit for the relevant Degree Committee. Work presented in Chapter 3 was conducted in close collaboration with P. W. Ball.

Fergus M^{c}Nab
September 27, 2019

Expressions of Mantle Dynamics in Landscapes and Sedimentary Basins

Fergus M^{c}Nab

The majority of Earth's surface topography is controlled by variations in crustal and lithospheric thicknesses and densities that are principally generated at plate boundaries. Nevertheless, it is recognised that some fraction of topography is maintained by convective circulation of the Earth's interior. Geodynamic simulations typically predict that this dynamic component of surface topography varies on wavelengths of $\sim$ 10,000 km with amplitudes of up to $\sim \pm$ 2 km. However, recent compilations of oceanic residual depth measurements reveal topographic anomalies on much shorter wavelengths of $\sim$ 1,000 km. Limited observational constraints exist regarding the spatial and temporal evolution of this dynamic topography on the continents. In this dissertation, I explore two ways in which such constraints might be obtained from fluvial landscapes and from sedimentary basins. I first investigate the growth of the Anatolian Plateaux. Elevated Miocene marine sedimentary deposits distributed across Anatolia indicate that significant uplift has occurred during Neogene and Quaternary times. However, the precise timing and spatial pattern of uplift are not well constrained. Fluvial drainage networks appear to contain quantitative information about the spatial and temporal evolution of continental topography. Such information is extracted from Anatolian drainage networks using an inverse modelling approach. Separately, estimates of asthenospheric temperature were obtained by modelling geochemical compositions of mafic volcanic rocks. Results suggest that elevated topography is supported by anomalously hot asthenosphere and by a thinned lithospheric plate. Regional uplift and magmatism appear to have propagated from east to west since $\sim$ 20 Ma. Consistent patterns linking uplift, magmatism and asthenospheric temperature imply that convective processes have had an important influence on the spatial and temporal evolution of the Anatolian Plateaux. Secondly, I focus on the Surprise Canyon Formation, a Carboniferous deposit that is exposed in the Grand Canyon of western North America. This formation, which contains terrestrial flora, consists of isolated channels incised into the underlying marine Redwall Limestone. These channels are overlain by the marine Supai Group. This stratigraphic relationship requires an episode of transient base-level fall. The chronology and evolution of the Surprise Canyon Formation is reviewed and revised, in order to compile a regional database of subsidence histories. Emplacement and subsequent cooling of warm asthenospheric material can explain significant stratigraphic relationships. Thirdly, I explore the structure and evolution of the intracratonic Congo sedimentary basin. This enigmatic basin's protracted stratigraphic record, which includes periods of rapid sedimentary acculation separated by long unconformities, remains poorly understood. Seismic reflection profiles acquired during the 1970s are re-analysed in order to improve the stratigraphic architecture. Subsidence histories for four wells are calculated and modelled. I show that these histories are consistent with basin initiation during a Neoproterozoic-Cambrian phase of rifiting followed by a long phase of thermal relaxation, a consequence of the basin's location on thick cratonic lithosphere. This post-rift phase is punctuated by periods of uplift and denudation that can be explained by emplacement and cooling of warm asthenospheric material at the base of the plate. I conclude that quantitative information about the dynamics of the Earth's mantle can be obtained by careful analysis of landscapes and the stratigraphic record.

Publications arising from this dissertation

Chapters 2 and 3 are based on:

M^{c}Nab, F., Ball, P. W., Hoggard, M. J. & White, N. J., 2018. Neogene uplift and magmatism of Anatolia: Insights from drainage analysis and basaltic geochemistry, *Geochemistry, Geophysics, Geosystems*, **19**, 175–213.

M^{c}Nab, F., Ball, P. W., Hoggard, M. J. & White, N. J., 2019. Reply to "Geochemical characteristics of Anatolian basalts: Comment on 'Neogene uplift and magmatism of Anatolia: Insights from drainage analysis and basaltic geochemistry' by McNab et al.", *Geochemistry, Geophysics, Geosystems*, **20**, 542–544.

Cooper (re. coffee):

Boy that hits the spot.

Twin Peaks, Episode 6
H. Peyton, D. Lynch, M. Frost
1989

Acknowledgements

First and foremost I must thank my supervisor, Nicky White, for the opportunity to work at Bullard and for his guidance throughout my time here. It was a privilege in many ways to share an office with Mark Hoggard for my first two years, and his continued input and support have been invaluable. It was also a pleasure to collaborate with Paddy Ball, whom I can't seem to shake off. Along with Mark and Nicky, Andy Jackson and Conor O'Malley provided able assistance on a 'light' field trip to the Grand Canyon in December 2016. Thanks also to Verónica Rodríguez Tribaldos for sharing her advice and data from the Parnaíba basin. I would also like to thank Lorcan Kennan and Karin Warners for organising funding from Shell and for their continued interest in my work.

I will fondly remember the unique working environment of the DRUM Building, where work and relaxation are seamlessly merged. For all the coffee breaks, ping pong games, tichu rounds and, most recently, overs of cricket, thanks go to Jacky Austermann, Ben Conway-Jones, Laurence Cowton, Alex Dickinson, Hannah Galbraith-Olive, Kathy Gunn, Megan Holdt, Marthe Klöcking, Fred Richards, Patrícia Santana, Charlie Schoonman, Leonardo de Siqueira, Simon Stephenson, and, of course, Conor, Mark, Paddy and Verónica. I suspect that, wherever I end up next, my working days will not be the same, and that makes me sad. Elsewhere at Bullard I would like to thank Ian Frame, Dave Lyness and Gill Turner for keeping us running in their respective ways, Joyce Howard for my daily brew, and Clare Donaldson for all the *fun*.

Away from work the other defining feature of my time in Cambridge has been the hockey club. Thank you to all the Deals, in particular Matt Cockerill, Monty Fynn, TJ Jackson, Kieran Gilmore and Johnny Staunton Sykes, for making four years of pumping Oxford and sinking pints so enjoyable. Never forget.

I also hugely appreciate the continued friendship and support of numerous people outside Cambridge including David Lee Astley, Kiran Barhey, Corinne Stuart, George Woodward from Univ; Jonny Attwood, Ronak Patel, Henry Taylor and James Taylor from OUHC; Gavin Hogg, Adam MacNeil, Graham Proctor, and Hugh Simons from Edinburgh; and many others. Catching up with you all—a little too infrequently—over the last four years has always been a welcome escape.

Most importantly, I would like to thank my family. My mum, Lilian, sister, Shona, and everyone in Ayr have been a constant source of support and encouragement. I always look forward to our time together, whether at home, on longer-than-planned walks in the Scottish hills, or 'bouncing' in Mauchline. Ann Laube has been a thoughtful and generous companion throughout the last four years. Sharing this time, and many delicious meals, with her has been a joy and I couldn't have made it this far without her. Finally, I would like to thank my dad, Hamish, for introducing me to science, research, and the natural world, and to whom this dissertation is dedicated.

Fergus

September 2019

Contents

List of Figures

List of Tables

Chapter 1

Introduction

The majority of surface topography on Earth is controlled by variations in crustal and lithospheric thicknesses and densities (e.g. Airy, 1855; Pratt, 1855). Similarly, the majority of surface uplift and subsidence is a result of changes in these thicknesses and densities that are generated at plate boundaries. Nevertheless, it has been recognised for several decades that some fraction of topography is maintained by convective circulation of the Earth's interior (e.g. Pekeris, 1935; Morgan, 1965; McKenzie, 1977). Pekeris (1935) demostrated that upwelling and downwelling currents impose normal stresses upon the base of the lithosphere that act to uplift and depress the surface, respectively. Subsequently, many authors have attempted to calculate global patterns of this dynamic component of surface topography, and its evolution through time, based on mantle density structures inferred from seismic tomography or subduction zone histories (e.g. Hager *et al.*, 1985; Ricard *et al.*, 1993; Steinberger, 2007; Conrad & Husson, 2009; Flament *et al.*, 2013). These geodynamic simulations typically predict that dynamic topography varies on wavelengths of $\sim 10^4$ km with amplitudes of up to $\sim \pm$ 2 km and evolves over timescales of hundreds of millions of years. It has also been recognised that changes in the thickness of the lithosphere, Earth's thermal boundary layer, particularly thinning by thermal erosion or the loss of destabalised lithospheric blocks, can generate surface deflections away from plate boundaries (e.g. Bird, 1979; Yuen & Fleitout, 1985; Flament *et al.*, 2013; Göğüş & Ueda, 2018).

Despite significant numerical modelling efforts, there have been relatively few attempts to evaluate surface expressions of these mantle dynamic processes using geological observations. An exception has been the study of oceanic residual depth anomalies (e.g. Menard, 1973; Cochran & Talwani, 1977; Cazenave *et al.*, 1986, 1988; Hoggard *et al.*, 2016, 2017). After correcting for sediment and crustal thickness variations and subsidence associated with plate cooling, these compilations reveal topographic anomalies of $\sim \pm 1$ km on wavelengths of $\sim$ 1,000 km (i.e. an order of magnitude shorter than that predicted by most numerical simulations). For example, residual depth anomalies from around the African continent are shown in Figure 1.1a. Positive and negative residual topographic undulations can be identified along the east and west African margins. These undulations coincide with long wavelength free-air gravity anomalies with amplitudes of $\sim \pm 50$ mGal, consistent with convective support (Figures 1.1a and 1.1b; M^{c}Kenzie, 2010). It has been suggested that a relatively short wavelength planform of dynamic support is principally generated by thermal anomalies in an asthenospheric channel immediately beneath the plate (Phipps Morgan *et al.*, 1995; Hoggard *et al.*, 2016, 2017). Constraining the temporal evolution of this convective planform remains a challenge.

Unlike the oceanic realm, the crustal and lithospheric structure of the continents is complex, so that residual topography cannot easily be determined and relatively few observational constraints on dynamic topography have been available (Flament *et al.*, 2013). However, it has recently been noted that convectively driven vertical motions should have recognisable expressions in the landscape (Braun, 2010; Roberts & White, 2010; Allen, 2011). Indeed, African fluvial networks radially drain topographic swells associated with positive long wavelength free-air gravity anomalies and, in some case, intraplate magmatism (e.g. Hoggar, South Africa, Tibesti; Figures 1.1a and 1.1b; Burke, 1996; Paul *et al.*, 2014). Note that swells which intersect the coastline correlate with positive residual depth anomalies offshore (e.g. Angola, Figures 1.1a and 1.1b; Al-Hajri *et al.*, 2009). It is thought that the shape of a river's longitudinal profile (i.e. elevation as a function of distance along a river) reflects the interplay between uplift and erosion (e.g. Whipple, 2009). Furthermore, it has been shown that suites of longitudinal river profiles can be inverted to obtain regional uplift histories (Pritchard *et al.*, 2009; Roberts & White, 2010; Fox *et al.*, 2014; Goren *et al.*, 2014; Rudge *et al.*, 2015). Thus, analysis of the landscape and its evolution may provide constraints on the spatial and temporal evolution of convective topographic support.

Another way that convective processes may be expressed at the surface is in stratigraphic records

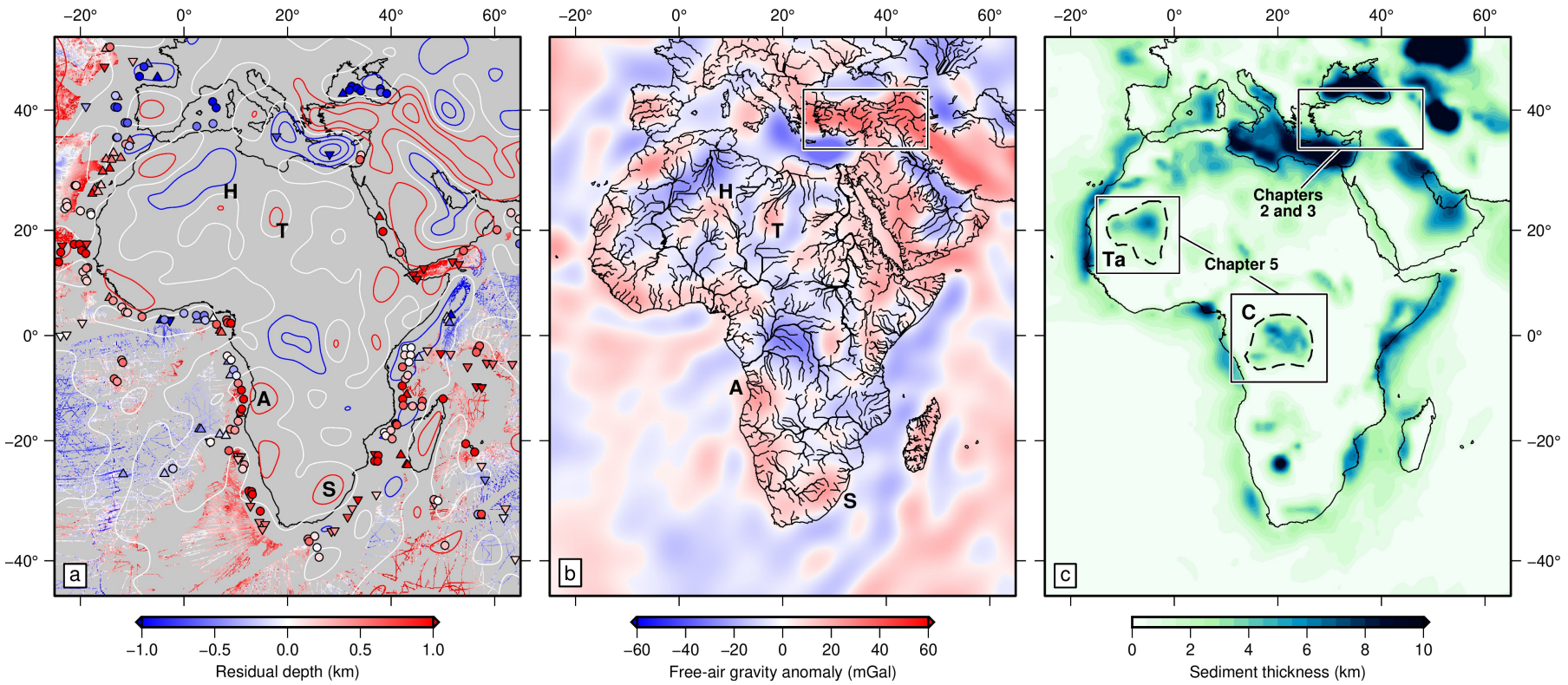

Figure 1.1: Residual topography, gravity, drainage and sedimentary basins of Africa.
(a) Oceanic residual depth anomalies surrounding the African continent. Coloured circles and upward/downward-pointing triangles = accurate estimates and lower/upper bounds of observed oceanic residual depths (Hoggard *et al.*, 2017); criss-crossing network = residual depth estimates based on ship-track bathymetry in regions of thin sediment and normal oceanic crust (Smith & Sandwell, 1997); red/white/blue contours = positive/zero/negative GGM03C non-hydrostatic low-pass filtered anomalies plotted every 25 mGal (Tapley *et al.*, 2007). A = Angolan, H = Hoggar, S = South African, T = Tibesti swells. (b) GGM03C non-hydrostatic low-pass filtered anomalies (Tapley *et al.*, 2007). Black lines = drainage networks from global compilation of O'Malley (2019). Study region for Chapters 2 and 3 shown. (c) Sediment thicknesses from Laske & Masters (1997). Study regions for Chapters 2, 3 and 5 shown. C = Congo, Ta = Taoudeni basins.

of sedimentary basins (e.g. White & Lovell, 1997; Jones *et al.*, 2001; Peterson *et al.*, 2010). These basins generally represent regions of gradual long-term subsidence and sedimentation driven by, for example, thermal relaxation following a period of lithospheric stretching (e.g. McKenzie, 1978b). However, it has been suggested that this background subsidence may be punctuated by shorter-term convectively-driven vertical motions, giving rise to periods of uplift and erosion or enhanced subsidence (e.g. Jones *et al.*, 2001; Rodríguez Tribaldos & White, 2018; van Wijk *et al.*, 2018). Transient uplift events associated with the Icelandic plume are thought to have generated landscapes now buried in the Faroe-Shetland Basin and North Sea (Hartley *et al.*, 2011; Stucky de Quay *et al.*, 2017). It has also been suggested that cratonic basins, such as Congo and Taoudeni of Africa, are surface manifestations of long-lived convective downwellings (Figure 1.1c; e.g. Hartley & Allen, 1994). These basins contain prominent erosional unconformities which have also been interpreted as evidence for instances of transient convective uplift (Rodríguez Tribaldos & White, 2018).

The aim of this dissertation is to explore ways by which spatial and temporal patterns of dynamic processes operating within the Earth's mantle can be constrained by analysis of their surface expressions on the continents. First, I investigate the evolution of the Anatolian Plateaux (Figures 1.1b and 1.1c). This youthful landscape is analysed and results compared to information obtained from the geochemistry of magmatic rocks and earthquake tomography. Secondly, a Carboniferous transient landscape exposed in the Grand Canyon, North America, is examined. Thirdly, I focus on the formation and development of the Congo Basin (Figure 1.1c). Similarities between this cratonic basin and two others, Parnaíba and Taoudeni, are then discussed.

1.1 Dissertation Structure

Chapter 2: Uplift and Landscape Evolution of Anatolia. Geological evidence for Neogene and Quaternary uplift of Anatolia is compiled and reviewed. A regional inventory of longitudinal river profiles is extracted and modelled using an inverse approach. This inverse model is calibrated using independent uplift and incision rate observations. Results are compared to other independent uplift constraints and implications are discussed.

Chapter 3: Magmatism and Mantle Dynamics of Anatolia. Relationships between topography, crustal thickness and gravity are assessed using a compilation of receiver function analyses and admittance analysis. An extensive database of Neogene-Quaternary

geochemical analyses of mafic volcanic rocks is compiled. This database is used to investigate melt-generating processes and to estimate depths and temperatures of melting. Results are compared to estimates from earthquake tomography. Potential mechanisms driving Neogene and Quaternary uplift and magmatism in Anatolia are discussed.

Chapter 4: A Buried Transient Landscape. Stratigraphic information relating to the Carboniferous Surprise Canyon Formation and surrounding units is presented. The chronology of events is reviewed and regional setting discussed. A regional database of water-loaded subsidence curves is developed and compared with predictions of flexural and thermal models. Causes and consequences of the development of this transient landscape are discussed.

Chapter 5: Origin and Evolution of Congo Basin. Newly digitised seismic reflection profiles from the Congo basin are re-interpreted to characterise basin architecture. Geochemical and seismologic constraints on the thickness and composition of the lithosphere are assembled. Subsidence histories are calculated and modelled. The basin is compared to Parnaíba and Taoudeni basins. Mechanisms controlling the origins and evolution of these intracratonic basins are discussed.

Chapter 6: Conclusions and Further Work.

Chapter 2

Neogene-Quaternary Uplift and Landscape Evolution of Anatolia

The origin of Anatolian topography is the subject of considerable debate (e.g. Şengör *et al.*, 2003; Göğüş & Psyklywec, 2008; Bartol & Govers, 2014; Schildgen *et al.*, 2014). This landscape is dominated by the low relief Central and East Anatolian Plateaux, which have elevations of 1–2 km (Figure 2.1, Table 2.1). A patchy distribution of marine sedimentary rocks indicates that large portions of Eastern and Central Anatolia were below mean sea level until Middle and Late Miocene times, respectively (Figure 2.2; Poisson *et al.*, 1996; Hüsing *et al.*, 2009; Cosentino *et al.*, 2012; Schildgen *et al.*, 2012a,b; Cipollari *et al.*, 2012, 2013; Bartol & Govers, 2014; Schildgen *et al.*, 2014). Nevertheless, the spatial and temporal evolution of this topographic signature and the nature of the processes that drive regional uplift are not well understood.

Anatolia has undoubtedly undergone a complex tectonic history. During the Cenozoic era, gradual closure of the Neotethys Ocean was accommodated by subduction of oceanic lithosphere and by accretion of different crustal fragments, culminating in the collision of Arabia with Eurasia between Late Eocene and Early Miocene times along the Bitlis Suture Zone (Figure 2.3a; e.g. Şengör & Yilmaz, 1981; Şengör *et al.*, 2008; Jolivet & Brun, 2010; van Hinsbergen *et al.*, 2010; Ballato *et al.*, 2011; McQuarrie & van Hinsbergen, 2013; Schildgen *et al.*, 2014).

Table 2.1: Marine sedimentary rocks of Anatolia.

Basin	Location	Marine Microfossil Fauna	Epoch (Stage)	Age (Ma)	Elevation (km)	Ref.
Mut-Ermenek	Sarıkavak	PF: *Globigerinoides tenellus*. C: *Calcidiscus macintyrei*; *Geophyocapsa caribbeanica* and *G. oceanica* (medium *G.*).	Pleistocene (Calabrian)	1.73–1.66	0.6–0.65	a, b
	Hacıahmetli	C: *Calcidiscus leptoporus*, small *Geophyocapsa*.	Pleistocene (Calabrian)	1.66–1.62	1.2	a, b
	Başyala	PF: *Orbulina suturalis* and *O. universa*; *Cataspidrax parvalus*; *Globigerinoides trilobus*, *G. quadrilobatus* and *G. extremus*. C: *Helicosphaera stalis* Theodorisis and *H. walbersdorfensis* T.; *Umbilicospaera jafari*	Miocene (Tortonian)	8.35–7.81	1.9	c, d
	Olukpınar	C: *Calcidiscus floridanus*; *Reticulofenestra pseudoumbicilus*; *Helicosphaera walbersdorfensis* and *H. carteri*; *Coccolithus pelagicus*.	Miocene (Serravallian)	13–12.5	1.65	d
Köprü	Sarıalan	PF: *Heterostegina* spp.; *Globigerinoides extremus*; *Sphaeroidinellopsis* spp.; *Orbulina universa*; *Globorotalia menardi*; *Siphonia reticulata*. BF: *Elphidium* spp.; *Lobatula lobatula*	Miocene (Tortonian)	7.17–6.7	1.5	e
Aksu	Gebiz	PF: *Globigerinoides trilobus*, *G. extremus*, *G. sacculifer* and *G. conglobatus*; *Globoturborotalia nepenthes*; *Globoratalia margaritae margaritae*, *G. m. evoluta* and *G. primitiva*. C: *Amaurolithus delicatus*; *Cyclococcolithus macintyrei*; *Discoaster brouweri*, *D. pentradiatus* and *D. surculus*; *Triquetrorhabdus rugosus*.	Pliocene (Zanclean)	5.3–3.6	0.45	f
Adana	Avadan	PF: *Sphaeroidinellopsis seminulia* and *S. disjuncta*; *Orbulina universa*; *Globigerinoides* spp. BF: *Lenticula* spp.; *Cibicides* spp. C: *Reticulofenstral zanclea* and *R. pseudoumbicilus*; *Helicosphaera carteri* and *H. intermedia*.	Pliocene (Zanclean)	5.3–5.2	0.35–0.65*	g
	Borehole T-191	PF: *Neogloboquadrina dutertrei* and *N. pachyderma*. BF: *Ammonia* spp.; *Elphidium* spp.	Pleistocene (Gelasian–Calabrian)	2.6–0.8	0.03–0.23*	g
Sivas	Central-Eastern Sivas	BF: *Miogypsinoides*; *Miogypsina*; *Nephrolepidina*. PF: *Globigerinoides trilobus*.	Miocene (Aquitian–Burgidalian)	23.0–16.0	1.5	h, i
Muş	Eastern Muş	PF: *Paragloborotalia pseudokugleri*, *P. siakensis*; *Globigerinoides primordius*.	Oligocene (Chattian)	25.9–23.0	1.5	j
Elazığ	Gevla	PF: *Paragloborotalia opima nana*; *Globigerina ciperoensis* and *G. angulisuturalis*; *Globigerinoides primordius*.	Oligocene (Chattian)	27.5–23.0	1.1	j
Kahramanmaraş	'Road', Avcılar	PF: *Globoratalia partimlabiata*; *Paragloborotalia siakensis*; *Globigerinoides subquadratus*. C: *Cyclicargolithus abisectus*; *Spenolithus heteromorphus*.	Miocene (Serravallian–Tortian)	12.8–9.9	0.8	j
Devrakani	—	BF: *Nummulites*; *Discocyclina*.	(Early) Miocene	23–16	1.1	k

* Total uplift including estimated water depths during deposition.
PF = planktic foraminifera, BF = benthic foraminifera, C = calcareous nannoplankton.
[a] Yıldız *et al.* (2003).
[b] Schildgen *et al.* (2012a).
[c] Cosentino *et al.* (2012). Age consistent with ostracod assemblages and paleomagnetic analyses.
[d] Cipollari *et al.* (2013). Echinoid, coral, bryzoa, sponge spicule bioclasts. Bioturbation (*Thalassinoides* and *Chondrites*).
[e] Schildgen *et al.* (2012b). Patch coral reefs, sponge spicules, bryozoa, pebbles with *Lithofaga* borings. Age consistent with U-Pb zircon dating of reworked ash.
[f] Poisson *et al.* (2011). Patch coral reefs, stromatolites. Age consistent with Ostracod assemblages.
[g] Cipollari *et al.* (2012). Ages consistent with Ostracod assemblages.
[h] Poisson *et al.* (1996). Patch and larger coral reefs. Sand bodies with gutter casts, hummocky cross stratification, 3D ripples; interpreted as storm deposits.
[i] Çiner *et al.* (2002).
[j] Hüsing *et al.* (2009). Echinoderms, corals, sponges. Fining-upward sand bodies with flute casts, displaced nummulites and gastropods; interpreted as turbiditic.
[k] Tunoğlu (1991, 1994).

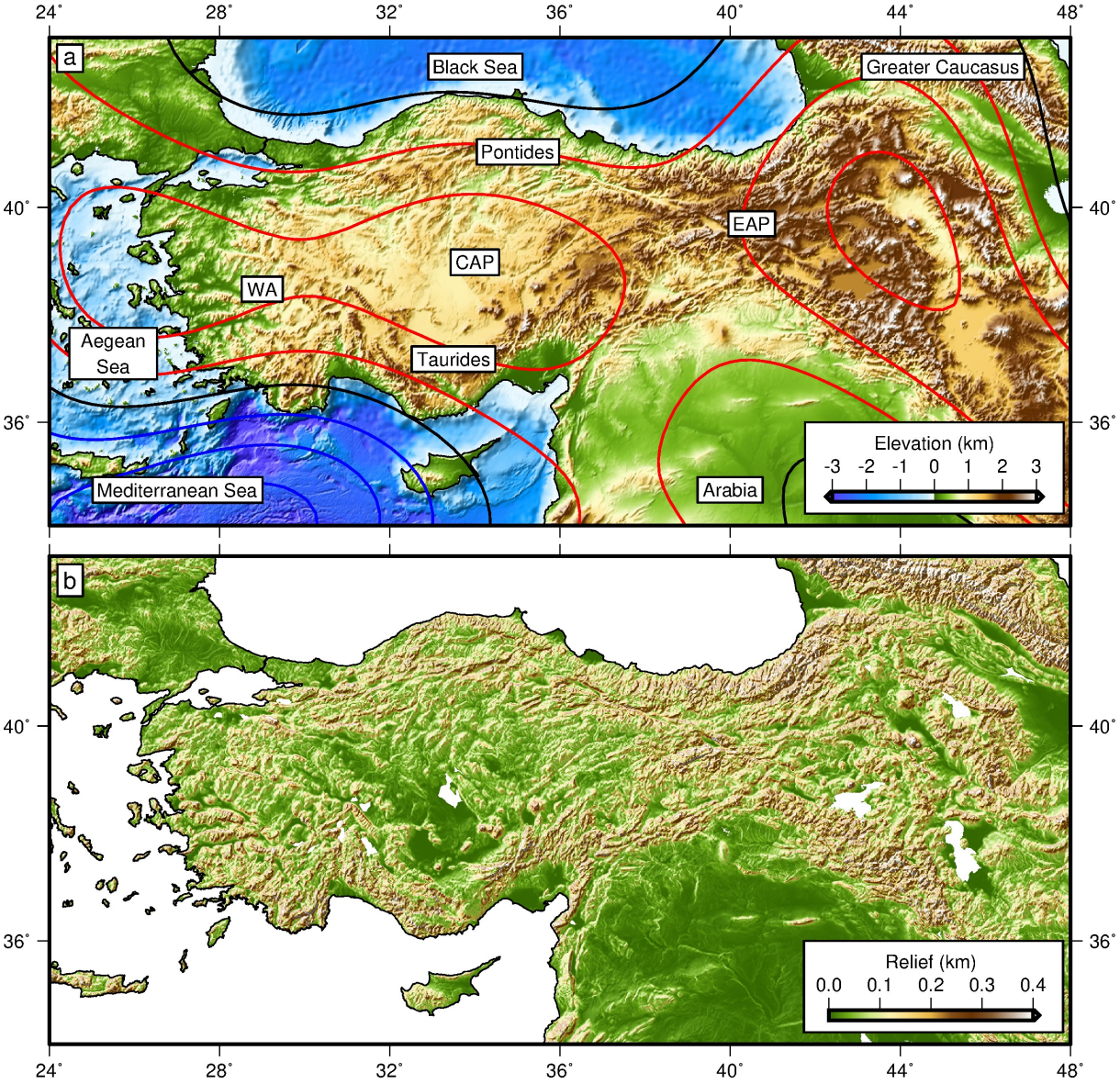

Figure 2.1: Geographic setting of Anatolia. (a) ETOPO1 shaded-relief topographic and bathymetric map of Anatolia, the Eastern Mediterranean and the Black Sea, with major geographic features labelled (Amante & Eakins, 2009). Red/black/blue contours = positive/zero/negative GGM03C free-air gravity anomalies filtered for wavelengths of 730–13,000 km and contoured at 25 mGal intervals (Tapley *et al.*, 2007); WA = Western Anatolia; CAP = Central Anatolian Plateau; EAP = Eastern Anatolian Plateau. (b) Relief map of Anatolia calculated in $1' \times 1'$ bins.

Global positioning system (GPS) measurements of crustal displacements, earthquake focal mechanisms, and the distribution of active faults confirm that north-south shortening continues in Eastern Anatolia (Figure 2.3; Reilinger *et al.*, 2006; Şengör *et al.*, 2008; Nocquet, 2012; Aktuğ *et al.*, 2013). In contrast, east-west translation and extension have dominated in Central and Western Anatolia since Miocene times (e.g. McKenzie, 1978a; Jackson & McKenzie, 1988; Aktuğ

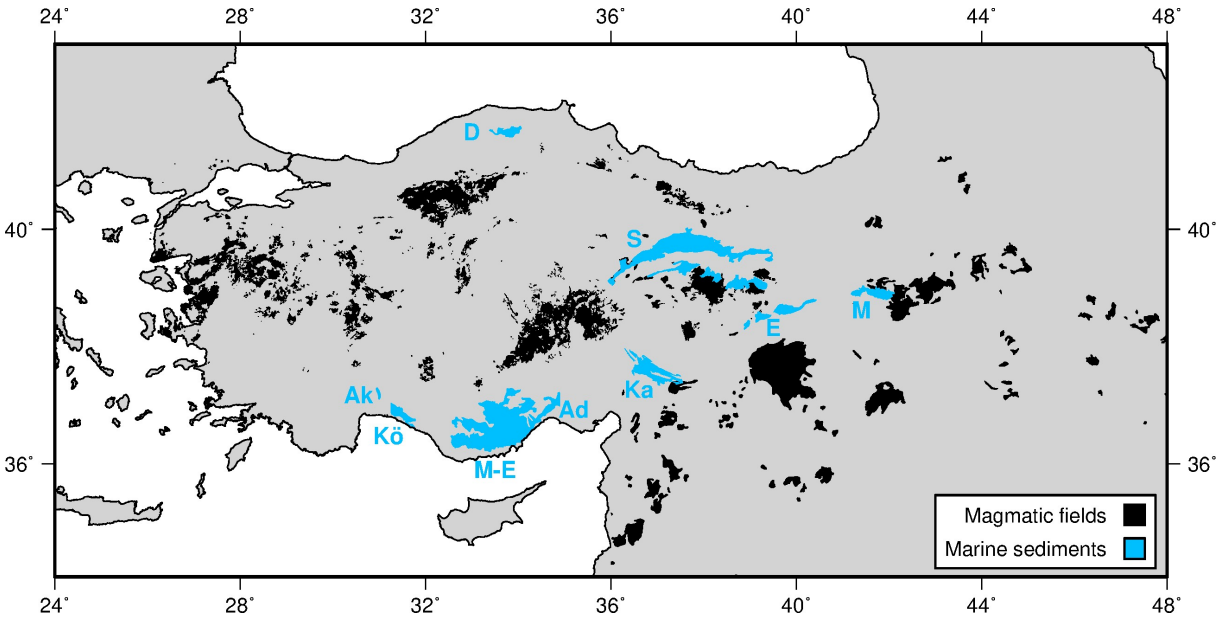

Figure 2.2: Neogene-Quaternary geologic setting of Anatolia. Outcrops of marine and volcanic rocks shown. Blue polygons = marine rocks (Table 2.1); black polygons = volcanic rocks, based on the map of Akbaş *et al.* (2011) within Turkey and on geologic maps published by United States Geological Survey elsewhere (Pawlewicz *et al.*, 2000; Pollastro *et al.*, 2000); Ak = Aksu; Ad = Adana; D = Devrekani; E = Elazig; Ka = Karamanmaraş; Kö = Köpru; M = Muş; M-E = Mut-Ermenek; S = Sivas Basins.

et al., 2009; Aktuğ *et al.*, 2013; Isik *et al.*, 2014; Yıldırım *et al.*, 2016). This interpretation is consistent with a lack of deformation within uplifted Miocene marine rocks of the southern Central Anatolia (Cosentino *et al.*, 2012; Schildgen *et al.*, 2012a,b; Cipollari *et al.*, 2012, 2013). An exception may be the western Tauride mountains, which are thought to have undergone active east-west thrust faulting in Miocene and Pliocene times (McPhee *et al.*, 2018). Evidence for north-south thrust faulting during this period has also been identified in northern Cyrprus (McPhee & van Hinsbergen, 2019). It has been proposed that westward motion of Central and Western Anatolia is a manifestation of material extrusion, accommodated largely along the right-lateral North Anatolian and left-lateral East Anatolian Faults (Figure 2.3a; Şengör *et al.*, 1985; Le Pichon & Kreemer, 2010). When rotated into an Anatolia-fixed reference frame, GPS observations suggest that Central Anatolia is currently translated westwards between these two bounding structures with limited internal deformation (Figure 2.3b; Aktuğ *et al.*, 2013). Further west, in western Anatolia and the Aegean Sea, active N-S extension becomes evident.

The tectonic configuration described above is thought to have been caused by a combination of Arabia-Eurasia collision and roll-back of the Hellenic trench. Tractions along the base of the lithosphere imposed by flow of the sub-plate mantle and gradients in gravitational potential

energy are invoked to drive these motions (Faccenna *et al.*, 2013, 2014; England *et al.*, 2016). It appears that, while crustal and lithospheric shortening probably played a role in causing regional uplift of the East Anatolian Plateau, it is less easily able to account for Late Neogene uplift of Western, and particularly Central Anatolia.

Plateau morphology and an apparent lack of pervasive crustal and lithospheric shortening have led many authors to invoke different lithospheric and asthenospheric processes in order to explain regional uplift. Examples include: steepening, tearing and breaking off of subducting African lithosphere; delamination of Anatolian lithosphere; lithospheric dripping; and upwelling asthenospheric thermal anomalies (Şengör *et al.*, 2003; Göğüş & Psyklywec, 2008; Faccenna *et al.*, 2013; Bartol & Govers, 2014; Schildgen *et al.*, 2014; Göğüş *et al.*, 2017). Each of these mechanisms involves arrival of low density asthenospheric mantle at shallow depths, where it provides isostatic and/or viscous topographic support. Positive long wavelength free-air gravity anomalies, slow P- and S-wave anomalies, together with elevated regional heat flow are all consistent with the presence of buoyant material within the uppermost mantle beneath Anatolia (Ilkışık, 1995; Dolmaz *et al.*, 2005; Biryol *et al.*, 2011; Bakırcı *et al.*, 2012; Salaün *et al.*, 2012; Chamorro *et al.*, 2014; Skolbeltsyn *et al.*, 2014; Govers & Fichtner, 2016; Balkan-Pazvantoglu & Erkan, 2019).

Coeval with this phase of Neogene-Quaternary regional uplift, basaltic magmatism has occurred throughout Anatolia (Figure 2.2; Keskin, 2003; Çoban, 2007). Geochemistry of these volcanic rocks should reflect processes involved in their generation. The most obvious feature is a clear shift from calc-alkaline (i.e. subduction related) to intra-plate alkaline magmatism during Miocene times. This shift is particularly well defined within Western Anatolia, although similar patterns have also been described in Central and Eastern Anatolia (Wilson *et al.*, 1997; Innocenti *et al.*, 2005; Agostini *et al.*, 2007; Keskin, 2007). It is widely recognized that this shift reflects a change in melt-generating processes that may be linked to growth of regional uplift.

In this chapter, I investigate the effects of Neogene-Quaternary uplift on the Anatolian landscape. First, I extract and describe an inventory of longitudinal river profiles. I then apply an inverse modelling approach to relate features of this drainage inventory to Neogene-Quaternary uplift signals. The inverse model is carefully calibrated subject to independent observations of regional uplift and inision. Finally, I discuss the implications of these results for the growth of the Anatolian Plateaux.

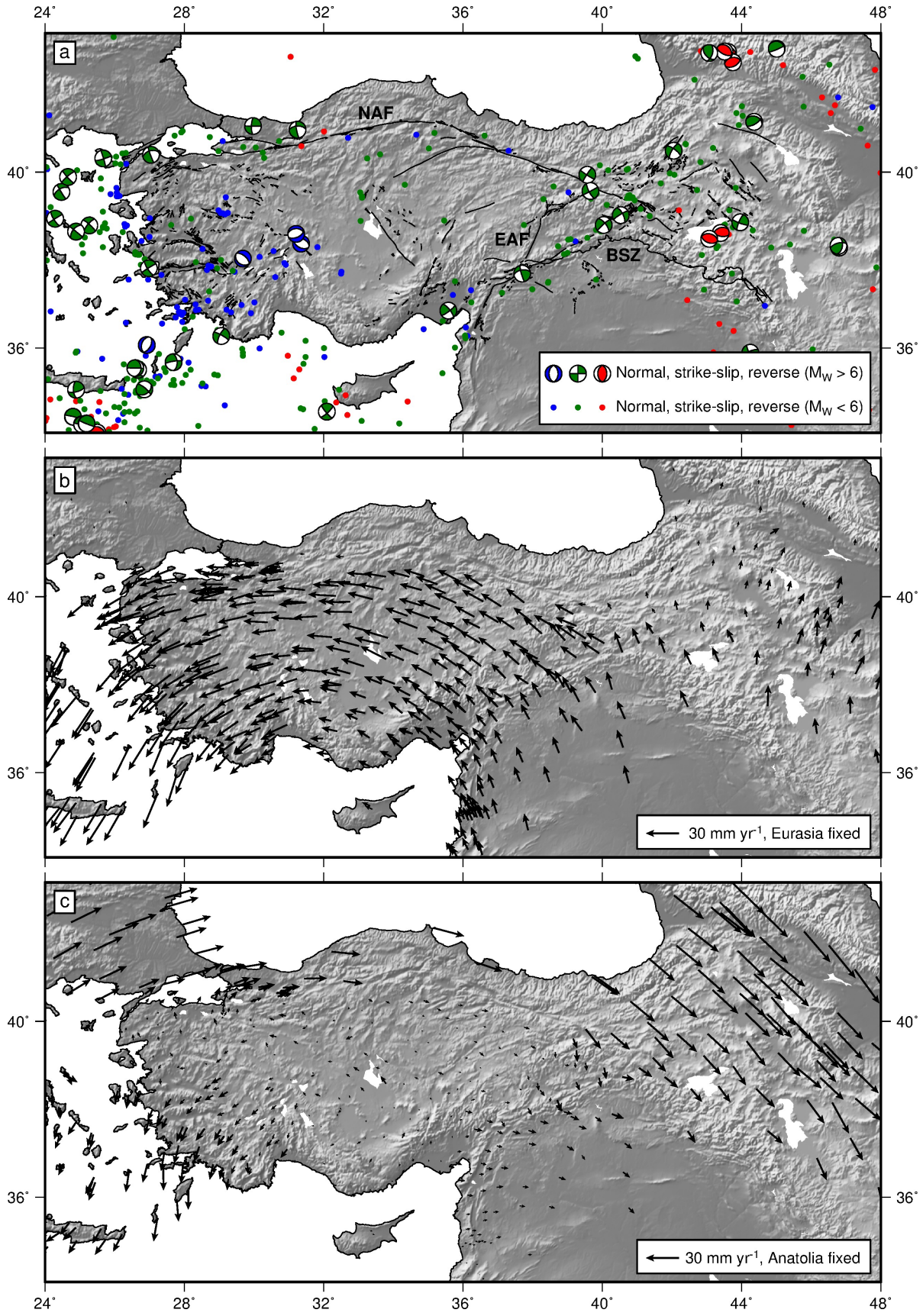

Figure 2.3: *Caption overleaf.*

2.1 Anatolian Drainage Networks

Emergent marine sedimentary rocks represent tangible evidence that specific locations throughout Anatolia have been uplifted in Neogene times (Figure 2.2; e.g. Schildgen *et al.*, 2014). Nevertheless, the spatial and temporal pattern of regional epeirogeny remains poorly constrained (Bartol & Govers, 2014). It is now recognized that fluvial landscapes are influenced in significant ways by regional tectonic forcing. An important corollary is that suites of longitudinal river profiles should indirectly record regional uplift histories (Whipple, 2009). When landscapes are in equilibrium, these profiles tend to become concave upward. When uplift exceeds erosion, convex-upward shapes develop that give rise to long-wavelength 'knickzones'.

In order to assess the impacts of Neogene-Quaternary regional uplift on the Anatolian landscape, I extracted a drainage network containing 1,844 rivers from a satelite-derived digital elevation model (Figure 2.4). I first decimated a digital elevation model from the Shuttle Radar Topography Mission (SRTM; Becker *et al.*, 2009) to reduce its horizontal resolution from 90 to 170 m, and removed and filled anomalous spikes and holes. The vertical resolution of this topographic model is typically $\sim$ 20 m away from steep valleys (Becker *et al.*, 2009). I applied routine flow-routing algorithms to recover a suite of river profiles and their associated upstream drainage areas (e.g. Tarboton, 1997). The fidelity of recovered river profiles was checked and verified using Landsat imagery (accessed via the Google Earth program), excising putative river profiles that deviated significantly from actual profiles. I also removed endorheic portions of drainage networks in the vicinity of Lakes Van, Tuz and Burdur (hashed regions in Figure 2.4).

Extracted river profiles from nine major catchments that drain the Anatolian Plateaux are presented in Figure 2.5. The shapes of these profiles deviate significantly from equilibrated profiles, which typically have concave-upward shapes. Knickpoints (i.e. short wavelength changes in slope) are primarily caused by intrinsic processes (e.g. lithologic contrasts, active faulting,

Figure 2.3: ***Previous page.*** **Active faulting and present-day surface motions of Anatolia.** (a) Distributions of active faulting and seismicity. Black lines = active faults from the database of Emre *et al.* (2013); coloured beach balls = focal mechanisms of large earthquakes ($M_W > 6$) taken from Centroid Moment Tensor Catalogue (Dziewonski *et al.*, 1981; Ekström *et al.*, 2012) where red = reverse, blue = normal, and green = strike-slip events; small colored circles = smaller earthquakes ($M_W < 6$). (b) Observed surface motions with reference to Eurasian plate determined from GPS measurements (Nocquet, 2012; Aktuğ *et al.*, 2013). (c) Observed surface motions with reference to Central Anatolia (reference frame given by Aktuğ *et al.*, 2013). Black arrows = GPS vectors.

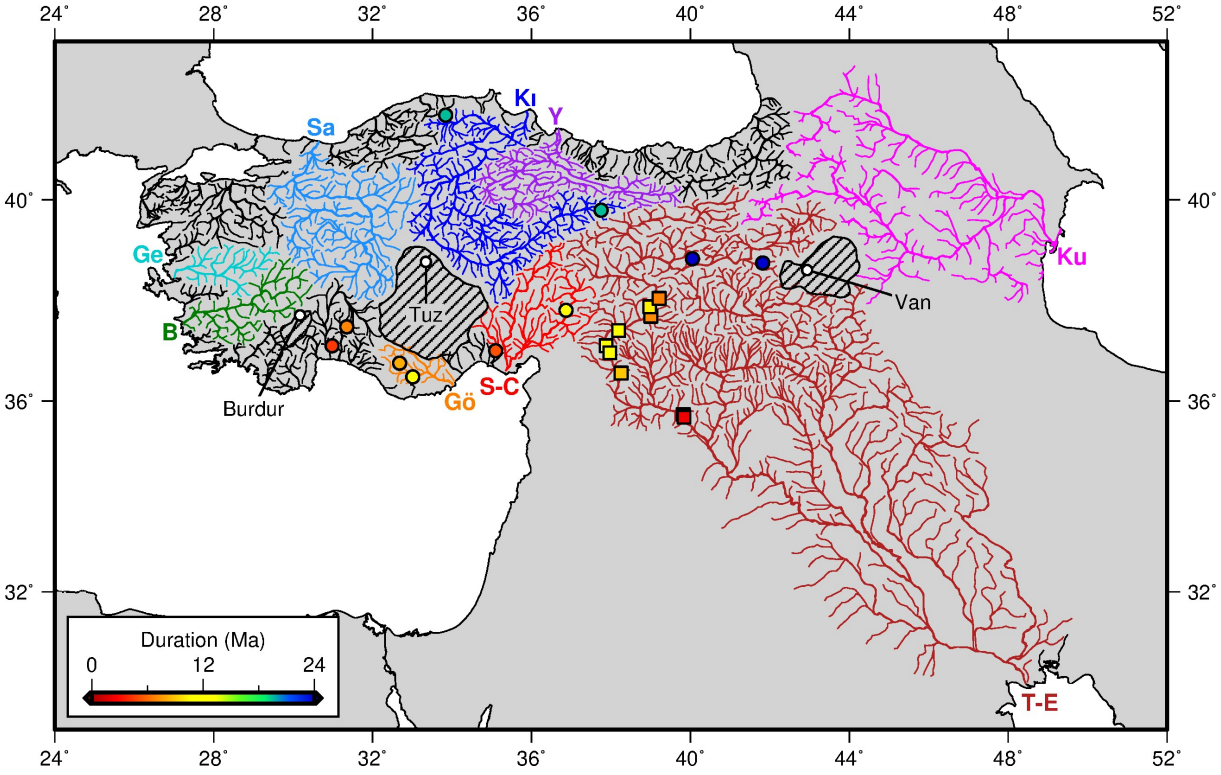

Figure 2.4: Anatolian drainage networks. Drainage pattern of Anatolia with loci of independent constraints for calibration. Büyük Menderes; Ge = Gediz; Gö = Göksu; Kı = Kızılırmak; Ku = Kura; S-C = Seyhan-Ceyhan; Sa = Sakarya; T = Tigris-Euphrates; Y = Yeşilırmak catchments; colored circles/squares = loci of observed uplift/incision rates shaded according to duration; hashed areas represent endorheic portions of drainage networks surrounding lakes Burdur, Van and Tuz.

artificial dams). However, profiles from these catchments also exhibit broad convex-upward knickzones with wavelengths of hundreds of kilometers and amplitudes of hundreds of meters. These knickzones tend to correlate within and between catchments. Examples of prominent knickzones are particularly clear near the mouths of catchments draining the Central Anatolian Plateau (e.g. Büyük Menderes, Figure 2.5a; Kızılırmak, Figure 2.5d; Seyhan-Ceyhan, Figure 2.5f). Draining the East Anatolian Plateau, the Kura catchment and upper portions of the Tigris-Euphrates catchment are also clearly disequilibrated (Figure 2.5h and 2.5i, respectively). It is generally agreed that long-wavelength knickzones are manifestations of external forcing generated by spatial and temporal patterns of regional uplift. Here, the goal is to use inventories of river profiles quantitatively to constrain these patterns.

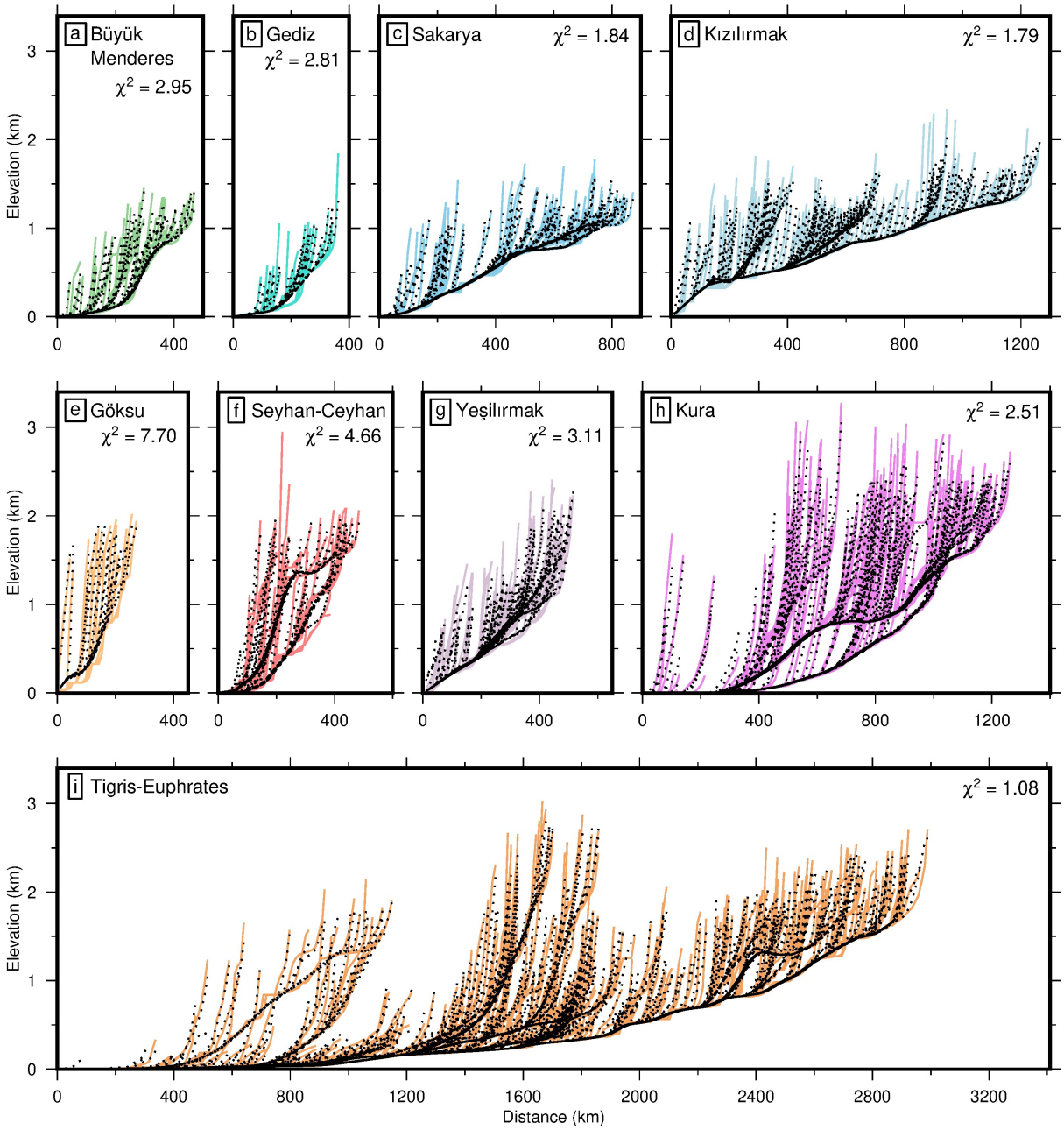

Figure 2.5: Observed and calculated river profiles for major Anatolian catchments. (a) Büyük Menderes catchment. Solid coloured lines = observed longitudinal river profiles (i.e. elevations as function of upstream distance) within each catchment; dotted lines = calculated river profiles. χ^2 misfit between observed and calculated profiles is shown. (b) Gediz, (c) Sakarya, (d) Kizilirmak, (e) Göksu, (f) Seyhan-Ceyhan, (g) Yeşilırmak, (h) Kura and (i) Tigris-Euphrates catchments.

2.2 Modelling Longitudinal River Profiles

It has been shown that the shapes of longitudinal river profiles can be exploited quantitatively by jointly inverting substantial inventories of profiles to calculate the spatial and temporal pattern

of regional uplift rate (Pritchard *et al.*, 2009; Roberts & White, 2010; Fox *et al.*, 2014; Goren *et al.*, 2014; Rudge *et al.*, 2015). In this section, I apply such an inverse modelling approach to a suite of Anatolian drainage networks.

2.2.1 Inverse modelling approach

The evolving shape of a longitudinal river profile depends upon the competing interplay between uplift rate, U, and erosion rate, E, so that

$$-\frac{\partial z}{\partial t} = E(x,t) + U(x,t), \tag{2.1}$$

where x is the distance from the river mouth along a given profile, z is elevation, and t is time before the present day. Erosion is generally parametrized using the phenomenological stream power law such that

$$E(x,t) = -vA(x)^m \left(\frac{\partial z}{\partial x}\right)^n + \kappa\frac{\partial^2 z}{\partial x^2}. \tag{2.2}$$

The first term of this equation describes the headward retreat of steeper portions of the river channel. In this detachment-limited case, v, m and n are erosional constants and A is upstream drainage area (Howard & Kerby, 1983; Whipple & Tucker, 1999). The second term describes downward erosion of the channel that is controlled by sedimentary transport. In this transport-limited case, κ represents 'erosional diffusivity' (Sklar & Dietrich, 1998; Whipple & Tucker, 2002; Tomkin *et al.*, 2003). The values of v, m, n and κ are generally not well constrained and the subject of considerable debate. Previous studies have found that, at long wavelengths, varying values of κ over several orders of magnitude within a realistic range (e.g. 10^0–10^7 m^2 Ma^{-1}) has a negligible influence on resultant uplift rate histories (Paul *et al.*, 2014). Rudge *et al.* (2015) also point out that values of κ lower than $\sim 10^7$ m^2 Ma^{-1}, which exceeds all reported estimates, will not have a resolvable affect at the lengthscales considered here (i.e. $\gtrsim 10$ km). Furthermore, Paul *et al.* (2014), Czarnota *et al.* (2014) and Rudge *et al.* (2015) demonstrate that optimal fits between observed and calculated river profiles are achieved for $n = 1$.

The stream power law can therefore be simplified so that

$$-\frac{\partial z}{\partial t} = -vA(x)^m \left(\frac{\partial z}{\partial x}\right) + U(x,t). \tag{2.3}$$

This linear kinematic wave equation can be solved using the method of characteristic curves

(Lighthill & Whitham, 1955; Weissel & Seidl, 1998; Rudge *et al.*, 2015). The solution takes the form $z(x,t) = z(x(t),t)$. Since

$$\frac{\mathrm{d}z}{\mathrm{d}t} = \frac{\partial z}{\partial t} + \frac{\mathrm{d}x}{\mathrm{d}t}\frac{\partial z}{\partial x} = \left(vA^m + \frac{\mathrm{d}x}{\mathrm{d}t}\right)\frac{\partial z}{\partial x} - U(x(t),t), \tag{2.4}$$

the solution can be written as a pair of ordinary differential equations, where

$$\frac{\mathrm{d}x}{\mathrm{d}t} = -vA^m, \tag{2.5}$$

and

$$\frac{\mathrm{d}z}{\mathrm{d}t} = -U(x(t),t). \tag{2.6}$$

Appropriate boundary conditions are

$$x = x^*,\ z = z^* \text{ at } t = 0, \tag{2.7}$$

and

$$x = 0,\ z = 0 \text{ at } t = \tau_G. \tag{2.8}$$

The first of these boundary conditions (Equation 2.7) states that, at the present day (i.e. $t = 0$), the observed elevation at a point x^* is z^*. The second boundary condition (Equation 2.8) defines a point in the past, $t = \tau_G$, at which the characteristic curve intersects the river mouth, $x = 0$, at $z = 0$. The Gilbert time, τ_G, is given by

$$\tau_G\ (x = x^*) = \int_0^{x^*} \frac{\mathrm{d}x}{vA^m}, \tag{2.9}$$

and represents the time taken for a signal inserted at the river mouth (i.e. $x = 0$) to advect upstream to a point x^*.

A general solution for Equations (2.5)–(2.9) is

$$\tau_G - t = \int_0^{x^*} \frac{\mathrm{d}x}{vA^m}, \tag{2.10}$$

and

$$z^* = z(x = x^*, t = 0) = \int_0^{\tau_G} U(x(t),t)\ \mathrm{d}t. \tag{2.11}$$

Using observed values of A at discrete positions x^* along river profiles, Equation (2.9) can

be solved using the trapezoidal rule, and as such Equation (2.10) can be used to compute characteristic curves. These curves describe the upstream adevction of a point along the river profile, such that each point x^* will have a corresponding suite of positions $x(t)$. Uplift rate histories can then be combined with these curves to solve (Equation 2.11), again using the trapezoidal rule.

A synthetic river profile calculated using this procedure is shown in Figure 2.6. Upstream drainage area as a function of distance was calculated using Hack's law (i.e. $A = (x/0.6)^{0.6}$) for an idealised profile of length 1000 km and combined with Equations (2.9) and (2.10) to compute characteristic curves (Figures 2.6d and 2.6e). Characteristic curves and the uplift history shown in Figure 2.6c were then used along with Equation (2.11) to compute elevation as a function of distance and time (Figures 2.6a and 2.6b). Uplift pulses A and B (Figure 2.6c) result in prominent knickzones which propagate and steepen upstream. These knickzones lie on characteristic curves which intersect the river mouth at times corresponding to the relevent uplift pulses (Figures 2.6c and 2.6d).

I now exploit an algorithm developed by Rudge *et al.* (2015) to pose and solve the inverse problem. Uplift values are specified at a discrete set of spatial and temporal nodes, represented by the vector $\mathbf{U}$. Spatial discretisation is achieved using a triangular mesh with nodes spaced every 50 km. Temporal discretisation is achieved using 20 time intervals spaced evenly between the maximum model Gilbert time, τ_G, and the present day. Between spatial and temporal nodes, linear interpolation of $\mathbf{U}$ is used to evaluate uplift rates at specific points along river profiles.

The procedure outlined above for using Equations (2.9)–(2.11) to compute river profiles for a given uplift history can be written in matrix form as

$$\mathbf{z} = M\mathbf{U}, \tag{2.12}$$

where $\mathbf{z}$ is the elevation at different loci along river profiles and M is the model matrix that contains the information required to translate any given uplift history into calculated river profiles. This information includes upstream drainage area together with values of the erosional constants. Equation 2.12 can be inverted to determine the uplift history, $\mathbf{U}$, which best fits a suite of observed river profiles, $\mathbf{z}$. A damped, non-negative least squares approach is used, which

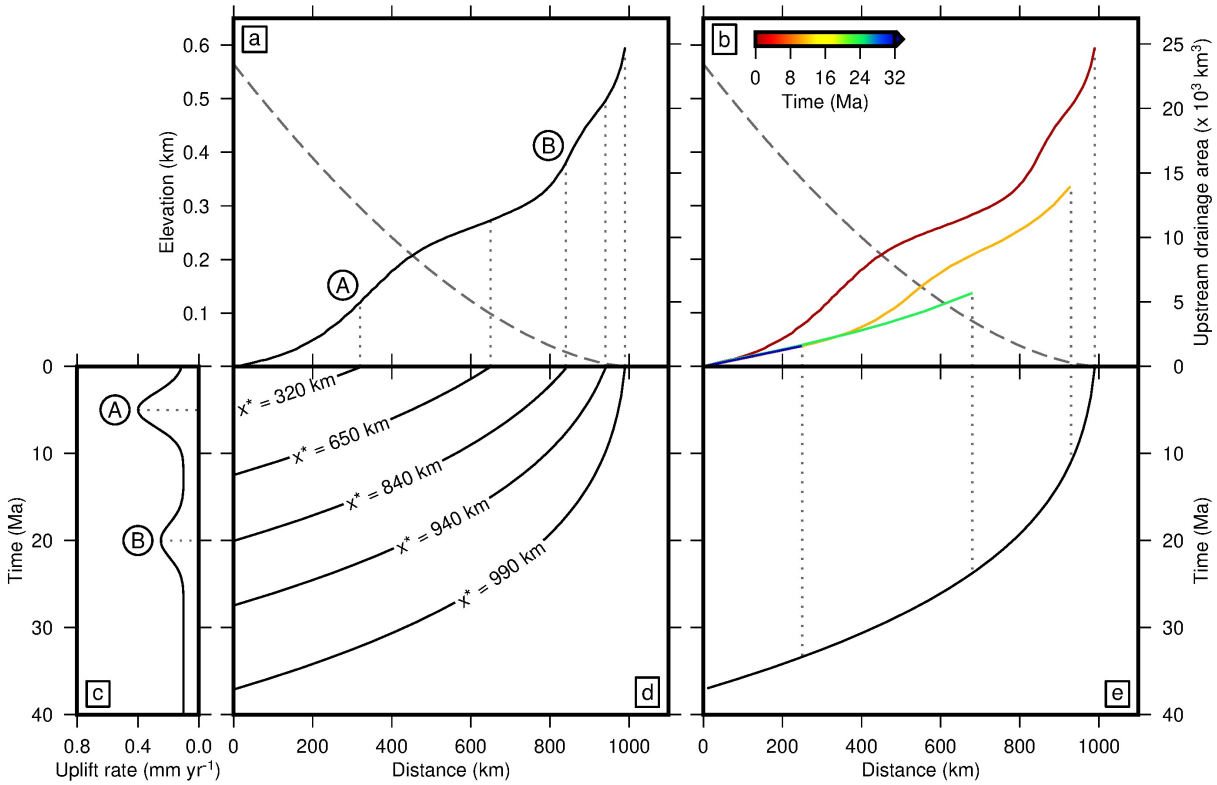

Figure 2.6: Synthetic river profile calculated using the stream power law. (a) Black line = synthetic river profile calculated from the uplift rate history shown in panel (c) using $m = 0.45$ and $v = 1.6$ m$^{0.1}$ Ma^{-1}, with labelled knickzones A and B corresponding to uplift pulses A and B; grey dashed line = upstream drainage area as function of distance, calculated using Hack's law (i.e. $A = (x/0.6)^{1/0.6}$). (b) Temporal evolution of river profile. Shaded solid lines = elevation as function of distance, where colour corresponds to time; grey dashed line = upstream drainage area as function of distance. (c) Uplift rate history used to compute river profile. (d) Characteristic curves for quoted positions x^* along river profile. (e) Characteristic curve for river head, with position of associated knickzone summit at times shown in panel (b) highlighted.

seeks to minimize

$$|M\mathbf{U} - z|^2 + \lambda_s^2 |S\mathbf{U}|^2 + \lambda_t^2 |T\mathbf{U}|^2$$
$$\text{subject to } \mathbf{U} \geq 0. \tag{2.13}$$

The non-negativity constraint is imposed to suppress positive and negative oscillations. λ_s and λ_t are spatial and temporal smoothing parameters that control regularization of this problem by penalizing spatial and temporal roughness such that

$$|S\mathbf{U}|^2 = \int_S \int_{t=0}^{t=max} |\nabla U|^2 \, \mathrm{d}t \, \mathrm{d}S, \tag{2.14}$$

and

$$|T\mathbf{U}|^2 = \int_S \int_{t=0}^{t=max} \left| \frac{\partial U}{\partial t} \right|^2 \, \mathrm{d}t \, \mathrm{d}S, \tag{2.15}$$

respectively. In this way, hundreds of river profiles can be simultaneously inverted to determine a regional uplift history.

This inverse algorithm assumes that the upstream drainage area of each river profile is invariant. In reality, river channels can change their courses, capture events probably occur, and drainage divides can migrate (Willett *et al.*, 2014). Fortunately, upstream drainage area, A, is raised to a fractional power in the stream power formulation (Equation 2.3). A significant consequence is that uplift histories calculated by inverse modeling are insensitive to substantial (e.g. $\pm$ 50 %) excursions in A (Paul *et al.*, 2014). Therefore, small-scale capture events generated by drainage divide migration at the backs of catchments are unlikely to significantly affect results of inverse modelling.

More problematic would be major rerouting events, caused by active faulting or switches in regional tilting. However, knickzones that are generated in this way are unlikely to be coherent from catchment to catchment. If so, these events may be recognizable by large values of residual misfit within particular catchments. Active faulting can also laterally displace catchments, affecting the spatial distribution of knickzones and hence the spatial planform of calculated uplift histories. However, estimates of the cumulative offset across the North Anatolian Fault, the dominant tectonic structure, range between 50 and 110 km (Hubert-Ferrari *et al.*, 2002; Akbayram *et al.*, 2016; Gürsoy *et al.*, 2017). These estimates are small compared to the length scales of regional uplift resolved by inverse modelling, and thus they are also unlikely to significantly affect its results.

2.2.2 Model calibration

This inverse approach has been used to calculate a regional uplift history of Anatolia from an inventory of 1,844 river profiles (Figures 2.7). However, calculated uplift histories are strongly dependent upon chosen values of the erosional and smoothing parameters. A total of four parameters must be determined: two erosional constants, v and m, together with two smoothing parameters, λ_s and λ_t. In general, their values are not known *a priori* and instead are calibrated using a combination of observed river profiles and independent uplift and incision constraints. Appropriate combinations of these parameters will minimise the misfit between observed and

calculated river profiles, uplift rates and incision rates while also minimising model roughness (i.e. the smoothest possible model which can satisfy the observational constraints is sought). Unlike m, λ_s and λ_t, v does not directly influence the shapes of river profiles or the spatial pattern of calculated uplift histories. Rather, v simply linearly scales the rate of erosion, and hence the length of calculated uplift histories, in time. Throughout the following sections, χ^2 misfit between a set of observed, o, and calculated, c, values will be defined as

$$\chi^2 = \sqrt{\frac{1}{N}\sum_{i=1}^{N}\frac{(o_i - c_i)^2}{{\sigma_i}^2}}, \tag{2.16}$$

where N is the number of values to be compared and σ_i is the uncertainty associated with observation o_i.

Observed river profiles

First, values of m, λ_s and λ_t are selected based upon the amount of residual misfit between observed and calculated river profiles and the roughness of calculated uplift histories. Richards *et al.* (2016) use a similar approach and report significant trade offs between these three parameters, such that, for example, optimal values of m were strongly dependent on the degree of spaitl and temporal smoothing applied. To assess the effect of these trade offs on chosen values of m, λ_s and λ_t, I performed a three parameter sweep. In this sweep, values of m, λ_s and λ_t were simultaneously varied between 0.15 and 0.75, 10^{-3} and 10^3, and 10^{-3} and 10^3, respectively (Figure 2.8). The minimum misfit between observed and calculated river profiles was obtained for a value of $m \sim 0.45$ and for values of λ_s and λ_t of 10^{-3} (i.e. the lowest values of smoothing applied). Misfit increases systematically as higher damping is applied. However, the optimal value of m is not strongly dependent on the degree of spatial or temporal smoothing that is applied (*contra* Richards *et al.*, 2016). I aim to find values of the two damping parameters that yield the smoothest possible model which still adequately fits observed river profiles, in this case choosing $\lambda_s = 1$ and $\lambda_t = 3$ (Figure 2.8). Values of λ_s and λ_t for which model roughness is minimised are not strongly dependent on the chosen value m.

Examples of river profiles from nine catchments, calculated using these chosen values of m, λ_s and λ_t, are shown as dotted lines in Figure 2.5. Misfit between observed and calculated river profiles as a function of space is shown in Figure 2.9. In general, calculated river profiles match observed profiles well: average residual root-mean-squared misfits are $\sim$ 15 m. Misfit is

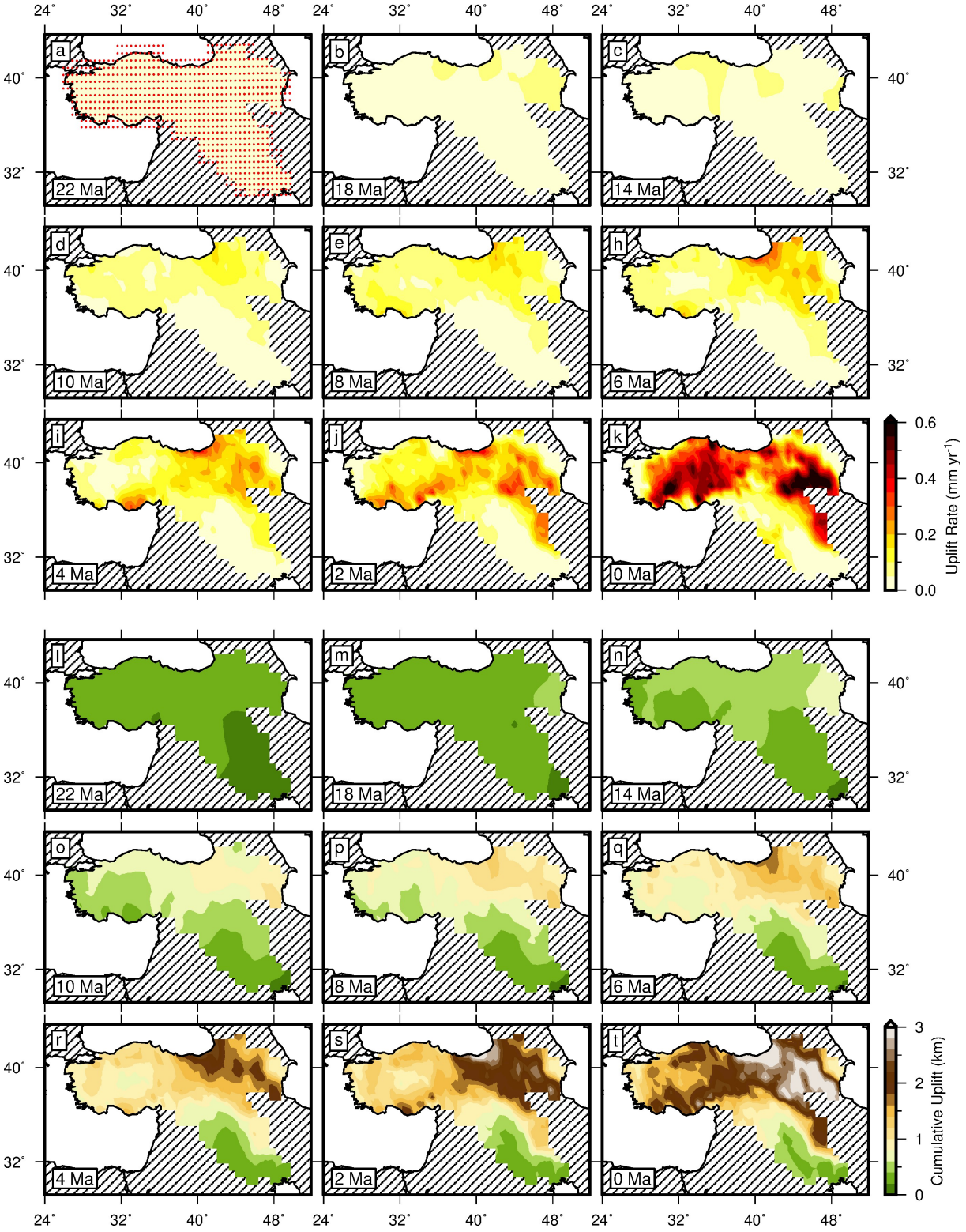

Figure 2.7: ***Caption overleaf.***

lowest in major channels and deteriorates towards the back of major catchments and in smaller catchments, where misfit can reach ~ 200 m. No catchments display exceptionally large residual misfits, which implies that the simple parameterisation of fluvial erosion used here is able to capture the major features of Anatolian drainage networks, despite not considering the effects of putative drainage reorganisation.

Observed uplift rates

Secondly, I validate the chosen values of m, λ_s and λ_t and select the value of v by calibrating against independent observations of uplift rate that are determined from the elevation of emergent marine sedimentary rocks. For example, Neogene deposits containing foraminifera and corals have been identified and biostratigraphically dated in several basins across the region (Figure 2.2; Table 2.1). At the southern margin of the Central Anatolian Plateau, sedimentary rocks within the Köprü, Mut-Ermenek and Adana basins were deposited during Tortonian to Calabrian times and are now exposed at elevations of between 1.2 and 2 km (Cosentino *et al.*, 2012; Schildgen *et al.*, 2012a,b; Cipollari *et al.*, 2012, 2013). Early to Middle Miocene marine sedimentary rocks at elevations of ~ 1 km are reported from the Devrekâni basin at the northern margin of the Central Anatolian Plateau (Tunoğlu, 1991; Schildgen *et al.*, 2014). In Eastern Anatolia, marine sedimentary rocks from the Sivas, Kahramanmaraş, Elazığ and Muş basins were deposited during Aquitanian to Tortonian times and later uplifted to elevations of 1 to 2 km (Poisson *et al.*, 1996; Hüsing *et al.*, 2009). In this way, average uplift rates over appropriate time intervals can be calculated at specific locations within Anatolia (Table 2.2). Observed uplift rates can be directly compared with corresponding uplift and incision rates calculated for a range of values of m, v, λ_s and λ_t.

Calculated uplift rates are scaled by the value of v chosen. It is therefore appropriate to choose values of v by minimising the misfit between observed and calculated uplift rates. In Figure 2.10a, this χ^2 misfit is shown as a function of v for uplift histories were calculated using the parameters of m, λ_s and λ_t determined above. The value of v was increased until the model

Figure 2.7: ***Previous page.*** **Calculated uplift history for Anatolia.** Regional uplift history calculated by minimizing misfit between observed and predicted river profiles with $\lambda_s = 1$, $\lambda_t = 3$, $m = 0.45$ and $v = 1.6$ m$^{0.1}$ Ma^{-1}. (a)–(k) Spatial pattern of regional uplift rate at selected time steps between 22 Ma and present day. Hatched regions were excluded from inverse model. Red circles in (a) = model spatial nodes. (l)–(t) Spatial pattern of cumulative uplift at selected time steps between 22 Ma and present day.

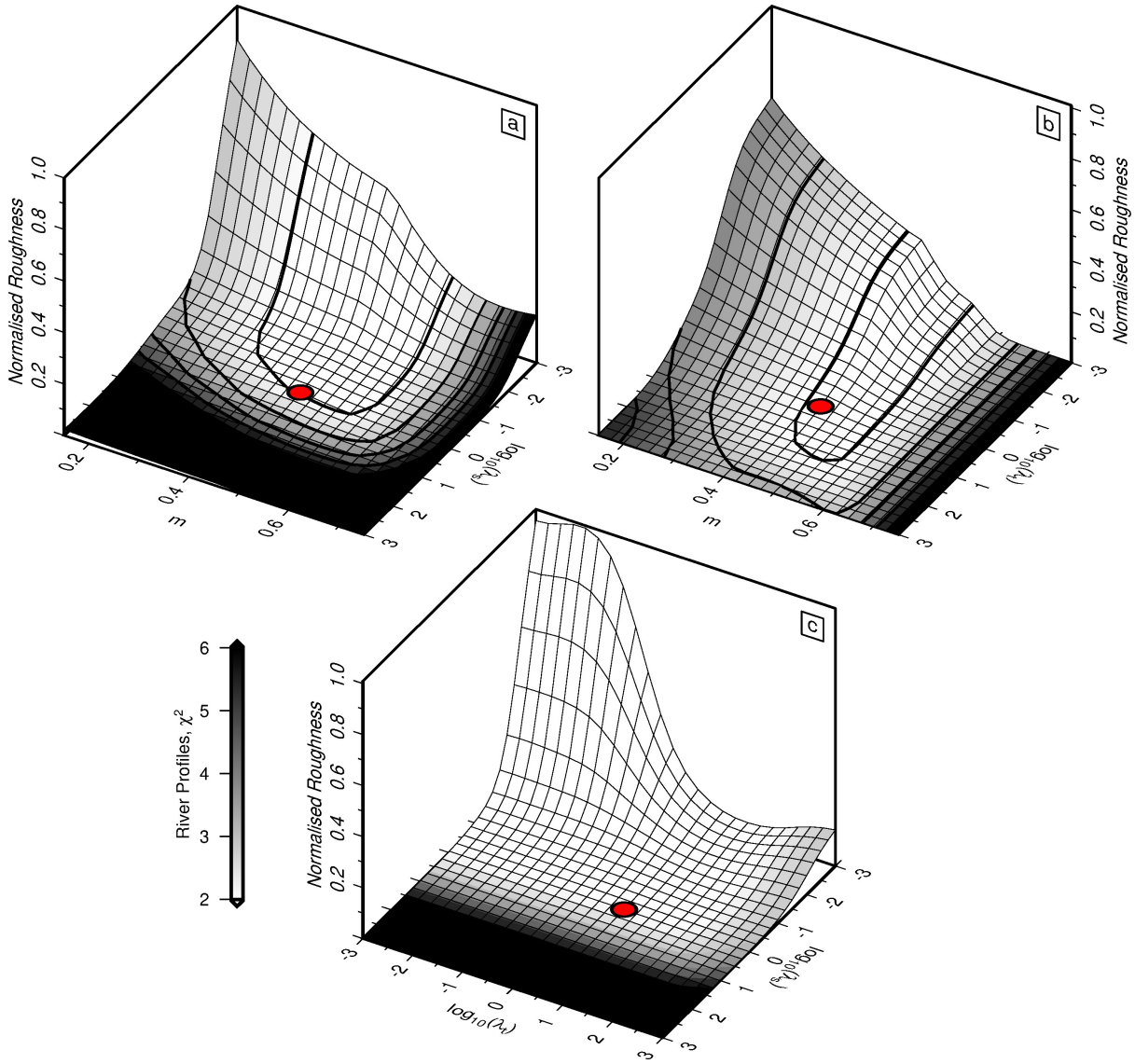

Figure 2.8: Misfit to observed profiles and model roughness as function of λ_s, λ_t and m. (a) m–λ_s space. Surface shape represents model roughness where spatial and temporal roughness are combined and normalized between 0 and 1; shading represents misfit between observed and calculated river profiles; red circle = optimal locus in model parameter space. (b) m–λ_t space and (c) λ_s–λ_t space.

Gilbert time (i.e. maximum Gilbert time of any river profile within the inventory) became shorter than the period over which independent uplift rate constraints are available, i.e. < 24 Myr. An optimal value of $v = 1.6 \pm 1.0$ m$^{0.1}$ Ma^{-1} was determined, where the upper and lower bounds correspond to values of v that yield χ^2 values that are less than double their values at the global minimum. Uplift rates calculated using this value are compared with observed uplift rates in 2.10b.

Misfit between observed and calculated uplift rates as a function of m, λ_s and λ_t is shown in

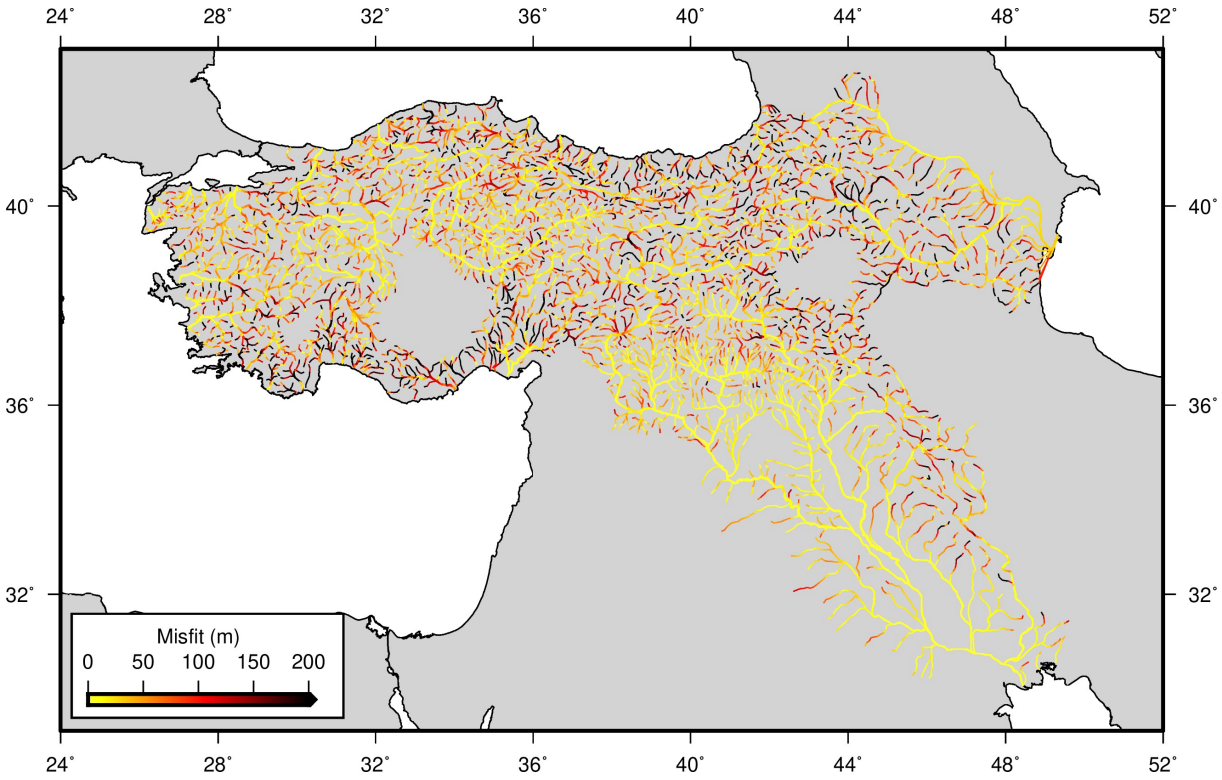

Figure 2.9: Misfit to observed river profiles in the spatial domain. Anatolian drainage network shaded by misfit between observed profiles and those calculated using $m = 0.45$, $v = 1.6$ m$^{0.1}$ Ma^{-1}, $\lambda_s = 1$ and $\lambda_t = 3$.

Figure 2.11. Optimised values of v for each combination of m, λ_s and λ_t were determined using the procedure outlined above. Values of misfit shown in Figure 2.11 were calculated using this suite of values of v. Misfits to observed uplift rates are more weakly dependent on chosen values of m, λ_s and λ_t than misfits to observed river profiles (Figure 2.11). However, there is a broad misfit minimum with $\chi^2 \sim 4$. Chosen values of $m = 0.45$, $\lambda_s = 1$ and $\lambda_t = 3$ lie within this misfit minimum, confirming that uplift histories calculated using these values are able to provide optimal fits to observed uplift rates.

Observed incision rates

In southeastern Anatolia, the Euphrates river has incised a series of flood basalt flows. $^{40}\mathrm{Ar}/^{39}\mathrm{Ar}$ dating of these flows permits long-term incision rates to be determined (squares in Figure 2.4; Demir *et al.*, 2007, 2012). These observed local rates help to corroborate the calibration of m, v, λ_s and λ_t described above.

To calculate incision rates for the Euphrates river, I first use a forward model to predict the

Table 2.2: Observed and calculated uplift and incision rates.

Location	Lon. (°)	Lat. (°)	Age Range (Ma)	Obs. Rate* (mm yr^{-1})	Calc. Rate* (mm yr^{-1})	Ref.
Uplift Constraints						
Sarıkavak	33.65	36.57	1.70 ± 0.04 – 0	0.37 ± 0.02	0.18 ± 0.25 †	a, b
Hacıahmetli	33.60	36.62	1.64 ± 0.02 – 0	0.73 ± 0.01	0.19 ± 0.24 †	a, b
Başyala	32.68	36.77	8.08 ± 0.27 – 0	0.23 ± 0.01	0.16 ± 0.04	c, d
Olukpınar	33.01	36.49	12.75 ± 0.25 – 0	0.13 ± 0.003	0.12 ± 0.03	d
Sarıalan	31.35	37.50	6.94 ± 0.24 – 0	0.22 ± 0.010	0.20 ± 0.08	e
Gebiz	30.98	37.12	4.45 ± 0.85 – 0	0.11 ± 0.03	0.12 ± 0.12	f
Avadan	35.10	37.02	5.25 ± 0.05 – 0	0.10 ± 0.03	0.10 ± 0.13	g
Borehole T-191	35.13	37.01	1.7 ± 0.9 – 0	0.15 ± 0.14	0.12 ± 0.18 †	g
C.E. Sivas	37.75	39.80	19.5 ± 3.5 – 0	0.080 ± 0.015	0.082 ± 0.009	h,i
E. Muş	41.82	38.77	24.0 ± 1.5 – 0	0.062 ± 0.004	0.089 ± 0.015	j
Gevla	40.05	38.85	25.25 ± 2.25 – 0	0.044 ± 0.004	0.068 ± 0.014	j
Avcılar	36.87	37.83	11.35 ± 1.45 – 0	0.072 ± 0.009	0.12 ± 0.05	j
Devrekani	33.84	41.62	19.5 ± 3.5 – 0	0.059 ± 0.011	0.078 ± 0.006	k, l
Incision constraints (Euphrates River)						
Halabiyeh	39.82	35.72	2.72 ± 0.02 – 0	0.040 ± 0.003	0.026 ± 0.0004	m
Zalabiyeh	39.84	35.67	2.12 ± 0.04 – 0	0.021 ± 0.0001	0.023 ± 0.0006	m
Shireen	38.26	36.57	8.9 – 0	0.007	0.025 ± 0.0013	m
Selamet	38.19	37.43	11.40 ± 0.24 – 0	0.033 ± 0.033	0.041 ± 0.0027	n
Özyurt	37.87	37.12	12.68 ± 0.27 – 0	0.027 ± 0.001	0.034 ± 0.0010	n
Asatköyü	37.97	36.98	11.11 ± 0.24 – 0	0.031 ± 0.001	0.032 ± 0.0020	n
Çaylarbaşı	39.01	37.71	7.03 ± 0.16 – 0	0.061 ± 0.001	0.046 ± 0.0053	n
Siverek İskelesi	38.98	37.90	10.24 ± 0.22 – 0	0.045 ± 0.001	0.048 ± 0.0040	n
Saltepe	39.22	38.07	6.70 ± 0.14 – 0	0.073 ± 0.002	0.061 ± 0.0014	n

* Rates are calculated as weighted mean of rates at nodes surrounding point of interest. Uncertainty is taken to be standard deviation of this weighted mean. Note that uplift rates are calculated for $v = 1.6$ and incision rates for $v = 0.9$.
† Note that constraints with durations < 2 Ma are below resolution of inverse model and are not included in misfit calculations.
[a – l] References as in Table 2.1.
[m] Demir *et al.* (2007). Estimates of incision rate from Ar-Ar dating of incised basalt lava flows.
[n] Demir *et al.* (2012). Estimates of incision rate from Ar-Ar dating of incised basalt lava flows.

evolution of its longitudinal profile as a function of time. When the stream power law is solved using the method of characteristics, elevation is predicted for a point x^* only when time, t, is less than the Gilbert time, τ_G, at that point. When comparing observed and calculated incision rates, it is useful to calculate incision rates at each point of interest throughout the model time. To do so, Equation (2.3) can be solved by finite difference. In this case, an implicit downstream finite-difference scheme was used to calculate river profiles from an uplift history previously determined by inverse modelling. It is necessary to more finely discretise the model in order to avoid numerical inaccuracies: in this case a spatial resolution of 0.5 km was used and the model time was split into 500 time steps. In Figure 2.12a, an observed river profile for a tributary of the Euphrates river is compared with profiles calculated using the method of characteristics and the finite-difference scheme described here. It is clear that both solutions agree closely and capture the long wavelength features of the observed profile. Once a suite of river profiles has been calculated, it is straightforward to estimate the amount of vertical incision, I, by using the

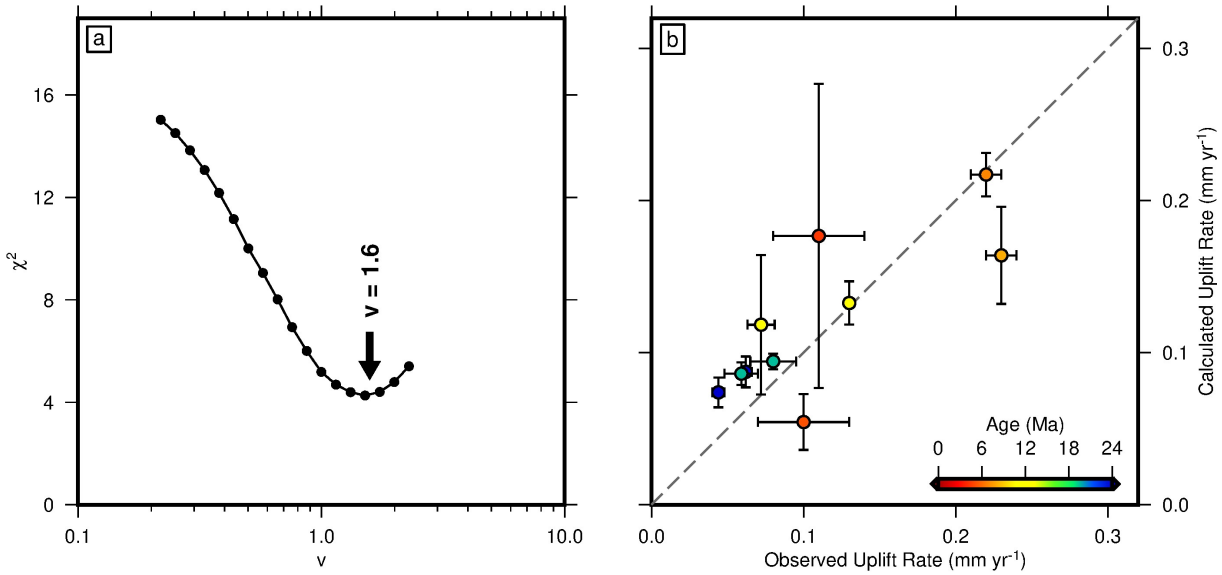

Figure 2.10: Misfit between observed and calculated uplift rates as a function of v. (a) Misfit between observed and calculated uplift rates as function of v for $\lambda_s = 1$, $\lambda_t = 3$, and $m = 0.45$. Global minimum at $v \sim 1.6$ m$^{0.1}$ Ma^{-1}. (b) Calculated uplift rate as function of observed uplift rate for $\lambda_s = 0.3$, $\lambda_t = 3$, $m = 0.45$, and $v = 1.6$ m$^{0.1}$ Ma^{-1}.

advective term of the stream power formulation such that

$$I(x,t) = vA(x)^m \frac{\partial z(x,t)}{\partial x}. \tag{2.17}$$

Incision rates are calculated for a range of values of v and can then be compared with observed incision rates (Figure 2.12b). As before, the value of v was increased until the model length became shorter than the period over which independent incision rate constraints are available, in this case < 12 Myr. An optimal value of $v = 0.9^{+0.1}_{-0.2}$ m$^{0.1}$ Ma^{-1} was obtained, where upper and lower bounds correspond to values of v that yield χ^2 values that are less than double their values at the locus of the global minimum.

The evolution of elevation and incision rates predicted by numerical modelling for the period over which independent incision rate constraints are available (12–0 Ma), using $v = 0.9$ m$^{0.1}$ Ma^{-1}, are shown in Figures 2.12c and 2.12d. Predicted incision rates are compared with observed rates at the global minimum ($v = 0.9$ m$^{0.1}$ Ma^{-1}; Figure 2.12e) and for the value of v determined by comparison of calculated and observed uplift rates ($v = 1.6$ m$^{0.1}$ Ma^{-1}; Figure 2.12f). Calculated incision rates are noisey, since gradients are necessarily computed numerically from discretely sampled profiles (Figure 2.12d). However, when integrated over periods of several million years, noise is reduced and calculated rates are relatively stable at specific locations (i.e.

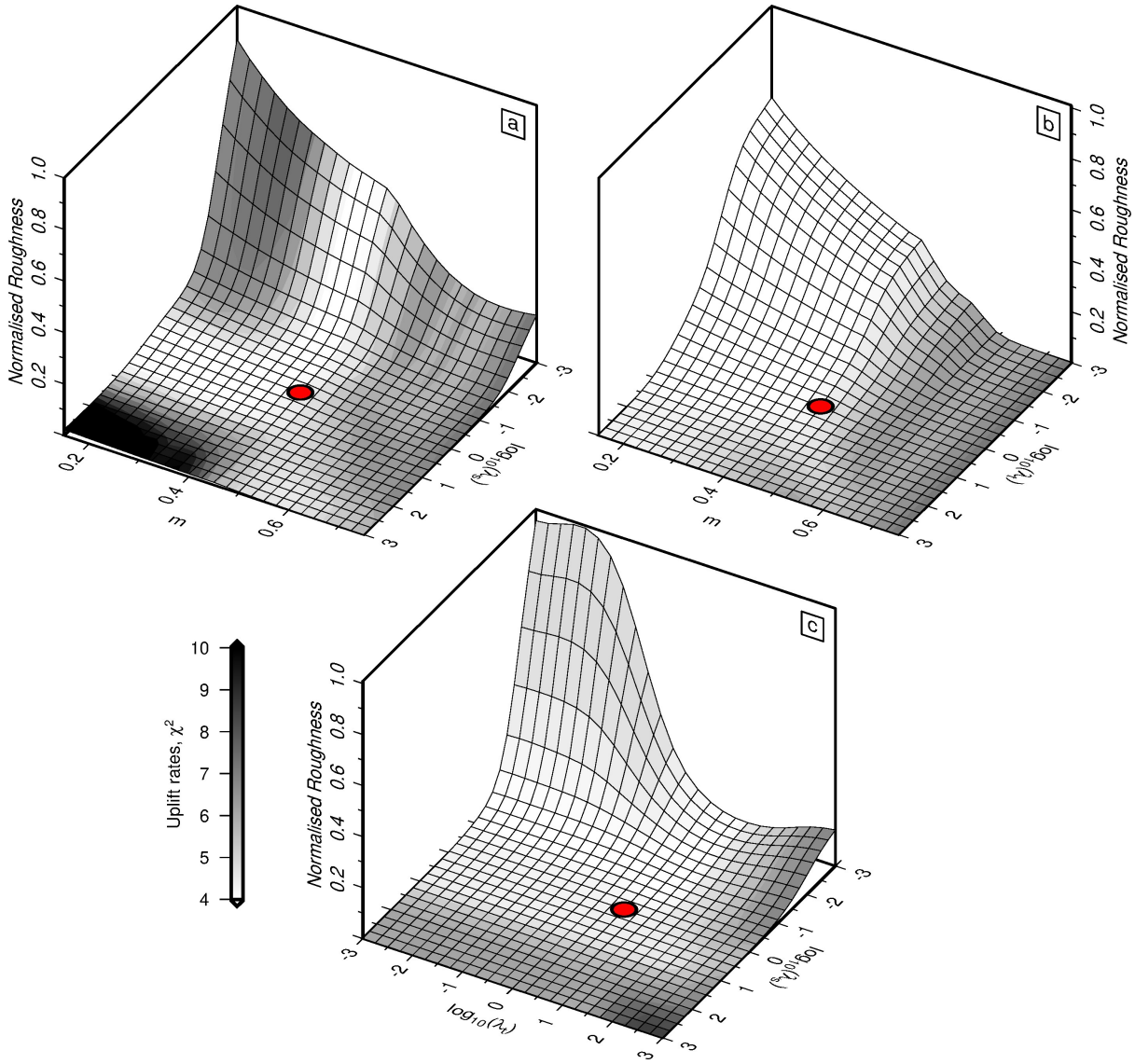

Figure 2.11: Misfit to observed uplift rates and model roughness as function of λ_s, λ_t and m. As Figure 2.8, with shading representing misfit between observed and calculated uplift rates. (a) m–λ_s space. (b) m–λ_t space and (c) λ_s–λ_t space.

$1\sigma < 0.01$ mm yr^{-1}). Incision rate predictions are able to capture the variation in long-term incision observed along the Euphrates river, with the best-fitting value of $v = 0.9^{+0.1}_{-0.2}$ m$^{0.1}$ Ma^{-1} falling within the range determined using observed and calculated regional uplift rates (Figure 2.12e). This result confirms that the range of values of v determined using observed and calculated uplift rates corresponds to geologically plausible rates of incision. It should be noted that observed incision rate constraints are spatially and temporally more restricted than the available uplift rate constraints. The wider range determined using observed and calculated uplift rates is therefore likely to be more representative of uplift and river incision across Anatolia throughout Neogene and Quaternary times, and is used for calculating uplift histories described

in the following sections. This higher value of v slightly overpredicts incision rates along the Euphrates river during the last $\sim$ 12 Ma (Figure 2.12f).

Misfit between observed and calculated incision rates as a function of m, λ_s and λ_t is shown in Figure 2.13. As above, misfit values shown in Figure 2.13 were calculated using optimised values of v for each combination of m, λ_s and λ_t. A broad misfit minimum with $\chi^2 \sim 10$ is present. Low (i.e. $m < 0.4$) and very high (i.e. $m > 0.65$) values of m provide poor fits to observed incision rates. Misfit is more weakly dependent on chosen values of λ_s and λ_t. Chosen values of m, λ_s and λ_t again return misfit values that lie within the broad misfit minimum.

2.2.3 Model coverage

The upstream propagation of kinematic waves of knickzones implies that the length of the potential 'tape recorder' that a river profile represents is strongly dependent upon longitudinal distance and upon the rate of erosion (e.g. Pritchard *et al.*, 2009). It is illuminating to consider the spatial and temporal coverage afforded by any given drainage network. The maximum length of the 'tape recorder' at a given point along a profile is given by the Gilbert time, τ_G, at that point, which represents the time taken for a signal inserted at the river mouth to propagate that distance upstream (Equation 2.9). Gilbert time for the Anatolian drainage network, calculated using $m = 0.45$ and $v = 1.6$ m$^{0.1}$ Ma^{-1}, is shown in Figure 2.14. Maximum Gilbert time for this network is $\sim$ 38 Ma at the back of the Tigris and Euphrates catchments, which suggests that information about uplift as far back as Eocene times could be retained. The East Anatolian Plateau is characterised by Gilbert times of 10–20 Ma while the remainder of the network is characterised by Gilbert times of 5–15 Ma. Late Neogene and Quaternary uplift signals should therefore be retained across the Anatolian drainage network.

A related parameter is the number of non-zero nodes in the model matrix, M, which indicates which model nodes are constrained by information from observed river profiles at a given time. Examples are shown in Figure 2.15. For early time steps, coverage is restricted to the mouths and lower reaches of major catchments (e.g. Tigris-Euphrates). Information is available for parts of the Central and East Anatolian Plateaux from about 20 Ma. Coverage is excellent across the Plateaux after $\sim$ 16 Ma. This result confirms that the Anatolian drainage network is principally sensitive to Late Neogene uplift signals and that significant features of the uplift history which are discussed here have been well resolved. An important exception may be the inner Central

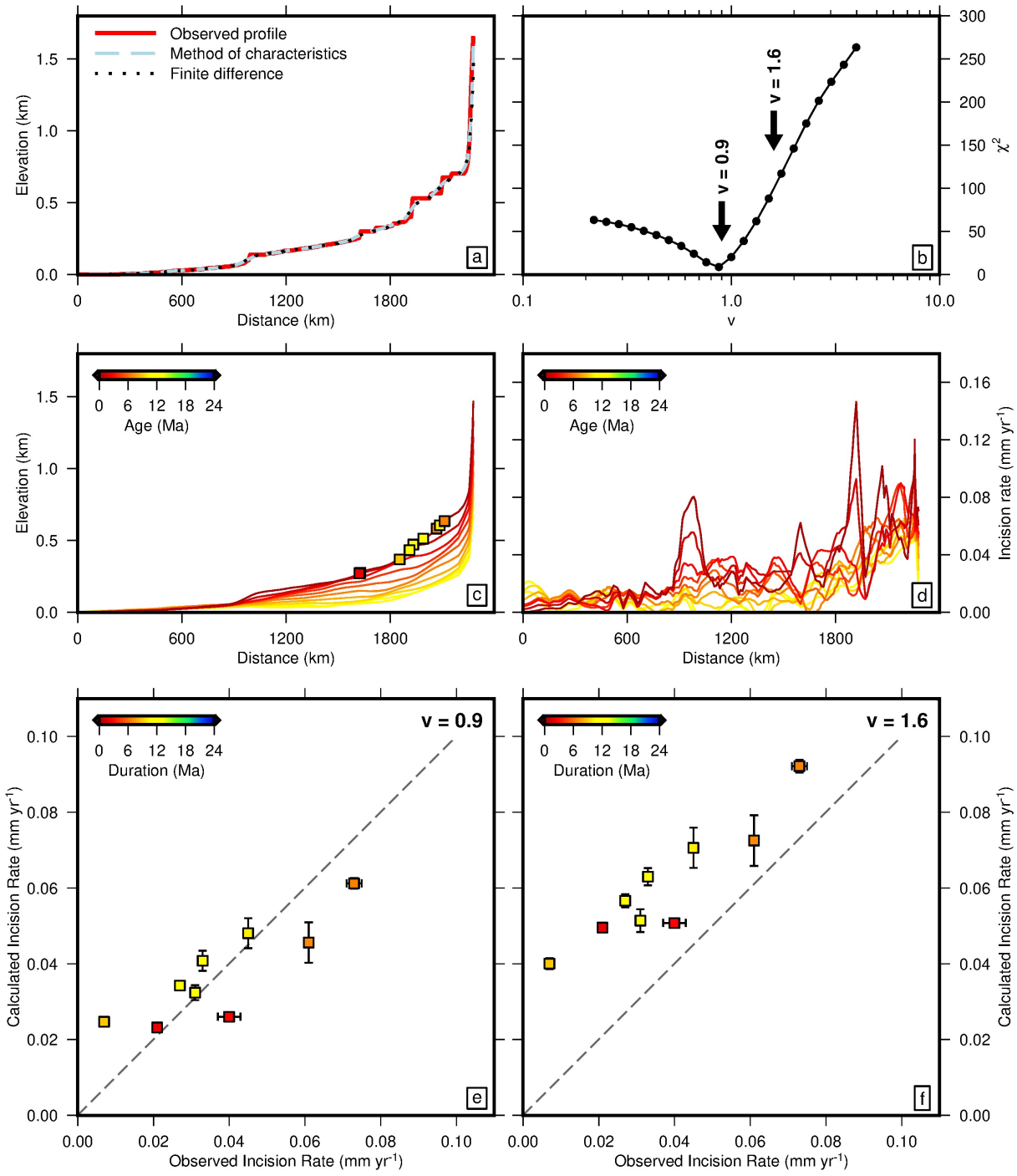

Figure 2.12: Misfit between observed and calculated incision rates as a function of v. (a) Observed and calculated profile for tributary of Euphrates river. Solid red line = observed profile, dashed blue line = profile calculated using method of characteristics, dotted black line = profile calculated using finite differences. (b) χ^2 misfit between observed and calculated uplift rates as function of v. Global minimum at $v = 0.9$ m$^{0.1}$ Ma^{-1}. (c) Predicted evolution of profile through time. Squares = locations with incision rate constraints. Shading represents age. (d) Predicted evolution of incision rate through time. (e) Calculated incision rate as function of observed incision rate for $m = 0.45$, $v = 0.9$ m$^{0.1}$ Ma^{-1}, $\lambda_s = 1$ and $\lambda_t = 3$. (f) As (e), for $v = 1.6$ m$^{0.1}$ Ma^{-1}.

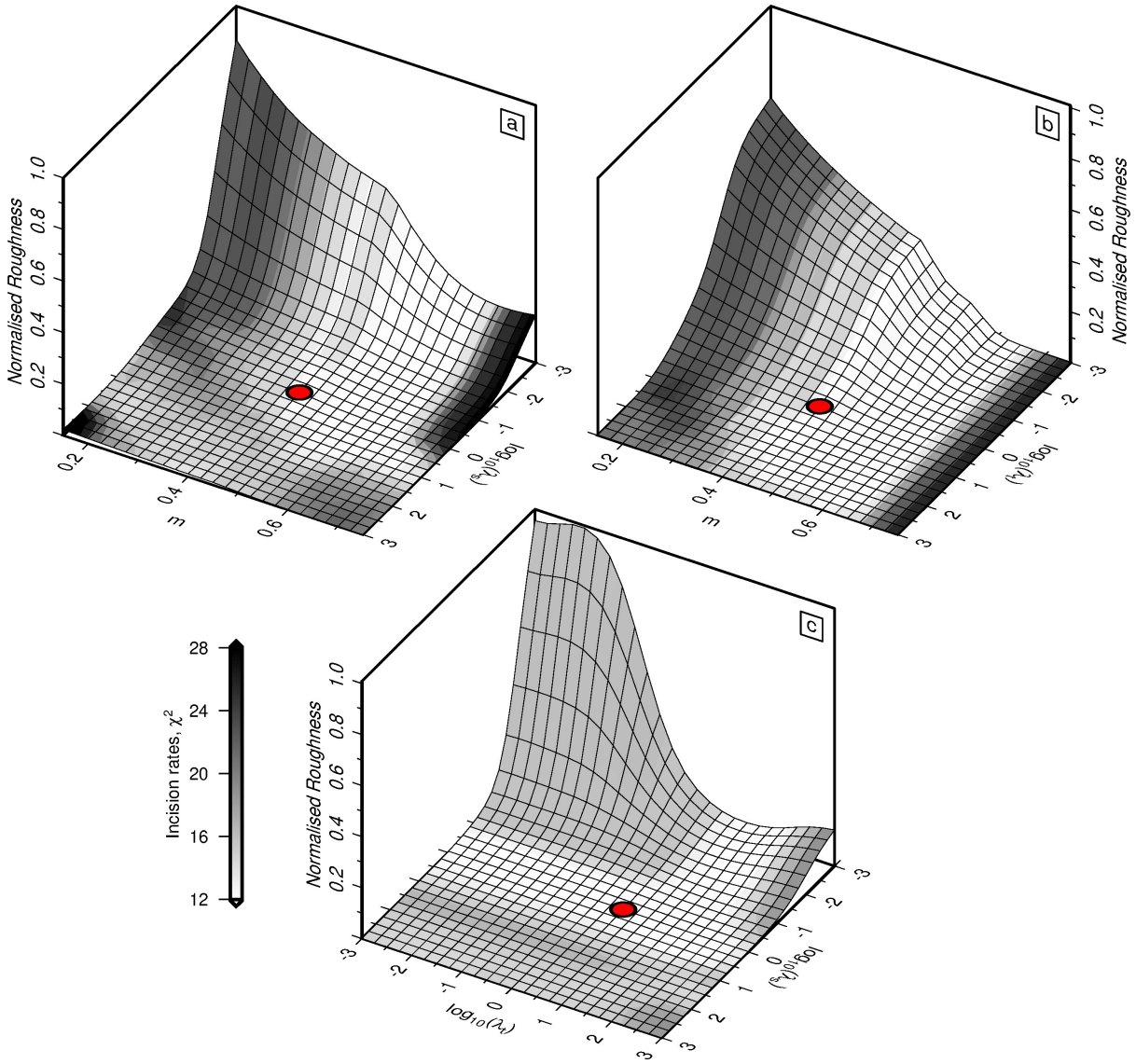

Figure 2.13: Misfit to observed incision rates and model roughness as function of λ_s, λ_t and m. As Figure 2.8, with shading representing misfit between observed and calculated incision rates. (a) m–λ_s space. (b) m–λ_t space and (c) λ_s–λ_t space.

Anatolian Plateau where endorheic drainage networks around Lake Tuz are omitted from the drainage inventory, thus leaving a gap in coverage that persists to the present day.

2.2.4 Cumulative uplift histories

Calculated uplift histories that assume $m = 0.45$ and $v = 1.6$ m$^{0.1}$ Ma^{-1} are shown in Figure 2.7 and in Figure 2.16. These uplift histories have an acceptable range which reflects permissible upper and lower bounds on m and v. In general, the suite of acceptable models agree with the chronology of uplift events to within $\sim \pm 5$ Ma. I emphasise the importance of rigorously

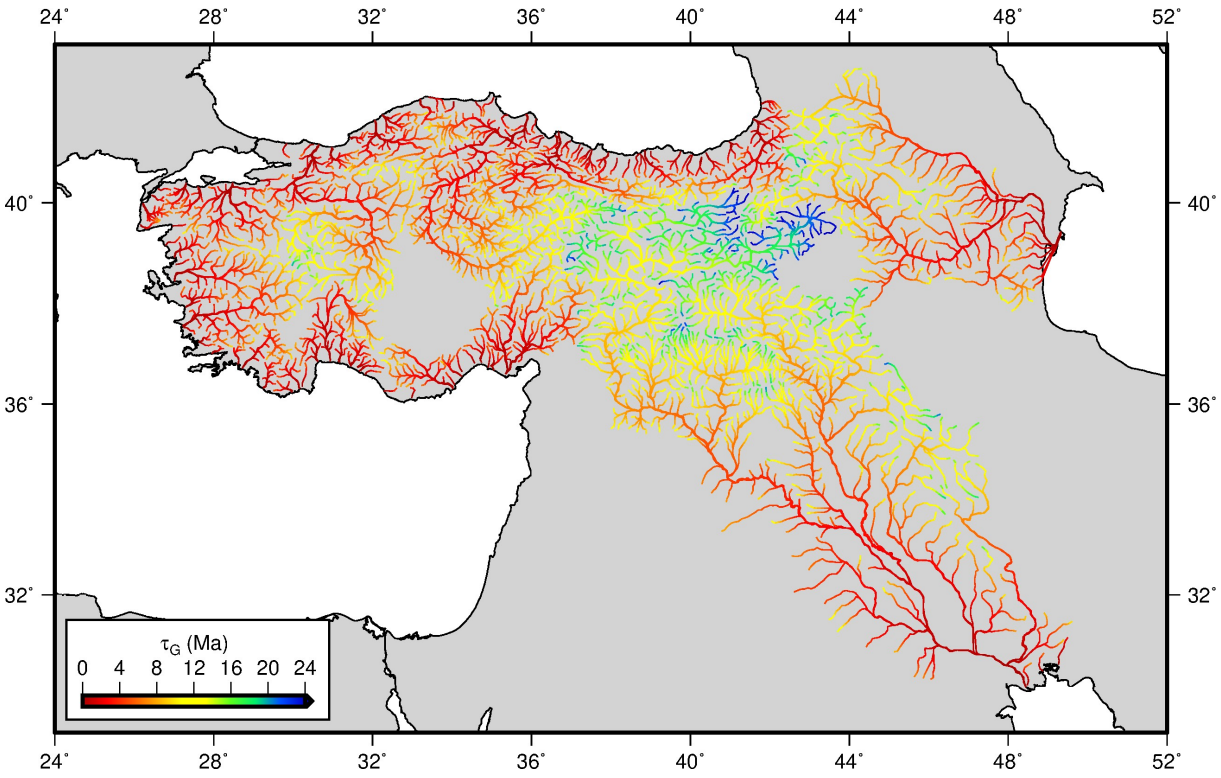

Figure 2.14: Landscape response time of Anatolian drainage networks. Gilbert time, τ_G, as a function of space for Anatolian drainage networks. Calculated using $m = 0.45$ and $v = 1.6$ m$^{0.1}$ Ma^{-1}.

testing uplift histories calculated using these chosen values of $m = 0.45$ and $v = 1.6 \pm 1.0$ m$^{0.1}$ Ma^{-1} against a range of additional independent uplift constraints from other locations across Anatolia.

Across the region, negligible uplift occurs before $\sim$ 20 Ma. Subsequently, significant regional uplift commences in the East Anatolian Plateau (Figures 2.16a and 2.16e). This timing is consistent with a transition from marine to continental deposition within the adjacent Muş basin (Hüsing *et al.*, 2009). Uplift rate increases steadily throughout Neogene times, reaching maximum values of 0.15–0.2 mm yr^{-1} by $\sim$ 10 Ma. A total of about 2–2.5 km of cumulative uplift occurs during this period. Onset of regional uplift appears to predate mafic magmatism by $\sim$ 10 Ma, as noted by Bartol & Govers (2014).

After onset of uplift in the East Anatolian Plateau, uplift rapidly migrates westward. At the transition between the East and Central Plateaux, the existence of marine sedimentary rocks in the Sivas basin suggests that uplift began after $\sim$ 20 Ma. These observations are faithfully reproduced by our inverse model (Figures 2.16b and 2.16f). In agreement with results from the East Anatolian Plateau, uplift rates increase between 15 Ma and the present day to values

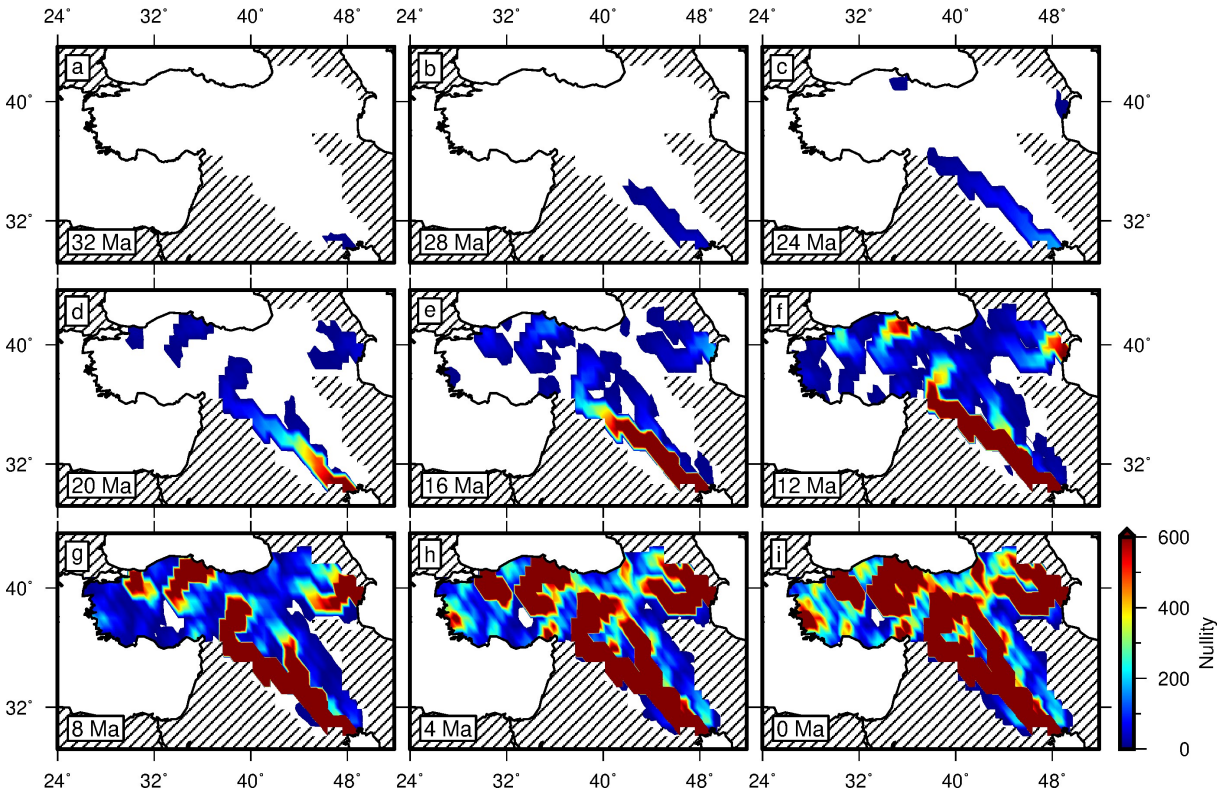

Figure 2.15: Inverse model coverage. Maps showing distribution of non-zero entries (i.e. model coverage or nullity) within model matrix, M, at selected time steps.

of $\sim$ 0.2 mm yr^{-1}. Further west, on the Central Anatolian Plateau itself, calculated uplift rates are more constant (Figure 2.16c and 2.16g). They start to increase at $\sim$ 12 Ma, before increasing rapidly from $\sim$ 6 Ma to rates that exceed 0.4 mm yr^{-1} at the present day. These calculated uplift histories are consistent with inferences made from stable isotopic compositions of sediments in continental basins surrounding the Central Anatolian Plateau, which indicate a lack of significant orographic barriers across the region until $\sim$ 15–10 Ma (Lüdecke *et al.*, 2013; Meijers *et al.*, 2018). Within the interior of the Central Anatolian Plateau, a total of 1–2 km of cumulative uplift occurs during this period. As observed for the East Anatolian Plateau, the onset of the recent phase of mafic magmatism lags the onset of uplift by $\sim$ 10 Ma.

Along the southern edge of the Central Anatolian Plateau, there are important independent constraints for the history of uplift (Figure 2.16d and 2.16h). For example, a suite of uplifted marine sedimentary rocks became emergent at about 8 Ma and record $\sim$ 2 km of regional uplift at rates of up to 0.7 mm yr^{-1} for the last 1.5 Ma (Table 2.1 Cosentino *et al.*, 2012; Schildgen *et al.*, 2012a,b; Cipollari *et al.*, 2012, 2013). It has even been suggested that uplift rates exceeded 3 mm yr^{-1} in Quaternary times (Öğretmen *et al.*, 2018). In my inverse model, uplift begins

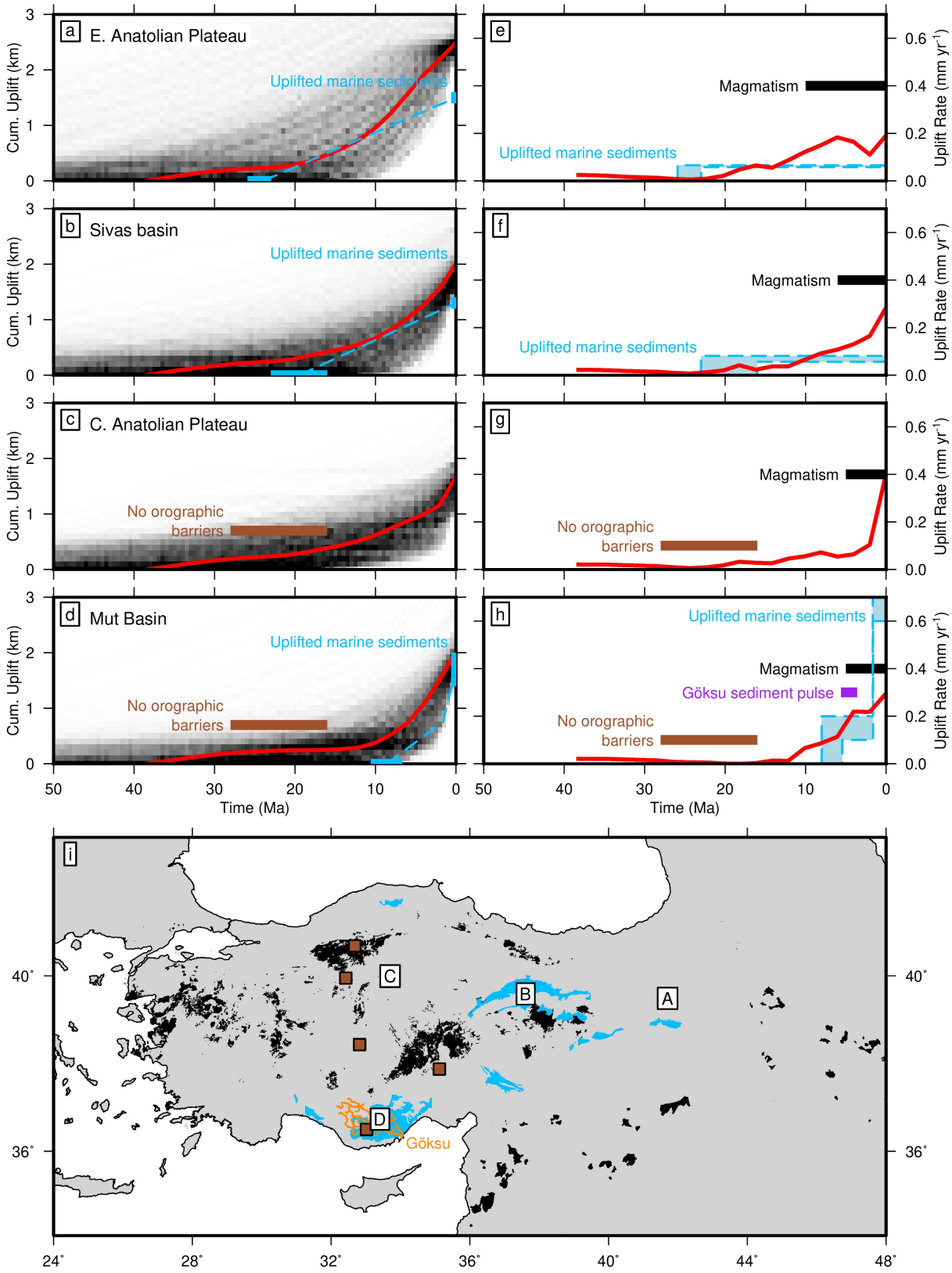

Figure 2.16: *Caption overleaf.*

slightly earlier at $\sim$ 10 Ma and such rapid uplift rates toward the present day are not resolved. Instead, calculated uplift rates steadily increase to 0.25–0.3 mm yr^{-1} by approximately 5 Ma. This discrepancy is most likely to arise from the temporal smoothing imposed upon our uplift history. Nonetheless, it is worth noting that the culmination of our calculated uplift rates corresponds to a peak in observed sedimentary flux from the Göksu catchment between 5.6 and 3.6 Ma (Walsh-Kennedy *et al.*, 2014). Between $\sim$ 10 Ma and the present-day, $\sim$ 2 km of uplift occurs in this region, $\sim$ 0.5 km more than in the Cetnral Anatolian Plateau's interior. This enhanced uplift at the plateau's southern margin is part of a topographic tongue, the Tauride mountains, which extends from the East Anatolian Plateau and is predicted to rapidly propagate westward within the last $\sim$ 5 Myr. This westward propagation has been linked to the opening of a slab tear beneath the region (Figure 2.16; Biryol *et al.*, 2011; Schildgen *et al.*, 2014).

Additional uplift between $\sim$ 5 Ma and the present day is also predicted to occur along the northern edge of the Central Anatolian Plateau. In this region, the inverse model yields an uplift rate of $\sim$ 0.2 mm yr^{-1} after $\sim$ 5 Ma. Unlike elevated regions at the plateau's southern margin, this enhanced uplift does not appear to propagate westward from the East Anatolian Plateau. These predictions are consistent with uplifted marine terraces and incised fluvial terraces in this region, which are linked with a large-scale constraining bend in the North Anatolian Fault (Yıldırım *et al.*, 2011, 2013).

England *et al.* (2016) proposed that present-day surface motions of Central Anatolia, which are dominated by westward translation between the North and East Anatolian Faults, are largely controlled by gradients in gravitational potential energy (GPE) between high topography of the East Anatolian Plateau and low topography of the Aegean Sea (Figure 2.3). Growth of the

Figure 2.16: ***Previous page.*** **Calculated uplift histories at individual nodes throughout Anatolia.** (a) Cumulative uplift history of East Anatolian Plateau. Red line = optimal cumulative uplift model with $\lambda_s = 0.3$, $\lambda_t = 3$, $m = 0.45$ and $v = 1.6$ $m^{0.1}$ Ma^{-1}; black/gray pixels = ensemble of smooth models for which χ^2 is less than twice value at global minimum. (e) Uplift rate history of East Anatolian Plateau. Red line = optimal uplift rate model; black bar = Neogene basaltic magmatism. (b) and (f) Silvas basin. Blue bar/dashed lines = marine sedimentary rocks. (c) and (g) Central Anatolian Plateau. Brown bar denotes absence of orographic barrier. (d) and (h) Mut-Erminek basin. Purple bar denotes sedimentary deposition from Göksu catchment. (i) Topographic map showing location of independent constraints. Boxes labeled A–D = loci of individual nodes; blue polygons = uplifted marine sedimentary rocks; black polygons = Neogene volcanic fields; brown squares = loci of sedimentary basins whence samples were taken for stable isotopic study reported by Lüdecke *et al.* (2013); purple lines = Göksu catchment, for which sedimentary flux history was determined by (Walsh-Kennedy *et al.*, 2014).

Anatolian Plateaux may therefore have exerted a profound influence on the tectonic configuration of the region. It is thought that displacement along the North Anatolian Fault initiated at $\sim$ 13–11 Ma in Eastern Anatolia and subsequently propagated westward, reaching the Sea of Marmara in Quaternary times (Şengör *et al.*, 2005). These timings approximately correspond to times at which regional topography is predicted to reach $\sim$ 1 km (Figures 2.7 and 2.16). Elevations of $\sim$ 1 km may therefore represent a critical threshold above which GPE gradients between Anatolia and the Aegean become unstable and westward collapse initiates. England *et al.* (2016) use present-day topography and observed surface motions to infer the effective viscosity of the lithosphere. Further analysis of the spatial and temporal evolution of surface topography together with that of the distribution of faulting may provide additional insights into the lithosphere's material properties.

2.3 Summary

In this Chapter, I have shown that Anatolian drainage networks have been strongly influenced by Neogene and Quaternary regional uplift. Longitudinal river profiles in turn contain important information about spatial and temporal uplift patterns. I applied an inverse modelling approach to extract regional uplift histories from an inventory of river profiles. Erosional and regularising parameters were carefully calibrated against observed drainage, uplift rate and incision rate data and smooth models which adequately fit these independent data selected. Results suggest that uplift initiated around 20 Ma in Eastern Anatolia and propagated westward, with uplift rates reaching ~ 0.5 mm yr^{-1}, in agreement with a range of independent constraints. Additional uplift is predicted to occur between $\sim$ 5 Ma and the present day along the northern and southern margins of the Central Anatolian Plateau. Along the plateau's southern margin, this later phase of uplift also appears to propagate westward from the East Anatolian Plateau. Uplift at the plateau's northern margin appears to be more isolated and is linked to the development of a constraining bend in the North Anatolian Fault.

Chapter 3

Neogene-Quaternary Magmatism and Mantle Dynamics of Anatolia

In Chapter 2, I presented results from calibrated inverse modelling of Anatolian drainage networks which confirmed that uplift of the Anatolian Plateaux occurred principally during Neogene and Quaternary times. Uplift appears to have initiated in eastern Anatolia at around 20 Ma and propagated westward. In this chapter, possible causes of regional uplift, and related mafic magmatism, are assessed using a range of approaches. First, I investigate the degree of isostatic support across Anatolia using a compilation of published receiver function estimates of crustal thickness. I also analyse the relationship between topography and free-air gravity anomalies to calculate the degree of flexural rigidity and to isolate long wavelength dynamic support of the Anatolian Plateaux. Secondly, an extensive database of whole-rock geochemical analyses for Neogene-Quaternary mafic magmatic rocks is compiled. This database is used to investigate the composition of the mantle source and styles of magma genesis. A combined forward and inverse modelling strategy is then used to determine the depth and degree of melting. Finally, I combine results of these analyses with those presented in Chapter 2 and discusss proposed mechanisms driving regional plateau uplift.

Table 3.1: Published receiver function analyses for Anatolia.

Study	Region	Method	Analyses
Abgarmi *et al.* (2017)	Central Anatolian Plateau	H-κ	97
Çakır & Erduran (2004)	Pontides	Joint inversion with Rayleigh-wave dispersion	1
Çakır & Erduran (2011)	Central Anatolian Plateau	Joint inversion with Rayleigh-wave dispersion	1
Erduran (2009)	Isparta	Joint inversion with Rayleigh-wave dispersion	1
Gök *et al.* (2008)	Northern Iraq	Joint inversion with Rayleigh-wave dispersion	2
Saunders *et al.* (1998)	Western Anatolia	Inversion	2
Taghizadeh-Farahmand *et al.* (2010)	East Anatolian Plateau	Inversion	8
Tezel *et al.* (2010)	Western Anatolia	Inversion	1
Tezel *et al.* (2013)	Entire region	Inversion	112
Vanacore *et al.* (2013)	Entire region	H-κ	78
van der Meijde *et al.* (2003)	Western Anatolia	Inversion	2
Zhu *et al.* (2006)	Western Anatolia	H-κ	7
Zor *et al.* (2003)	East Anatolian Plateau	Inversion	9
Zor *et al.* (2006)	Marmara	Inversion	19

3.1 Crustal and Lithospheric Template

3.1.1 Receiver function analyses

Several lines of evidence suggest that Neogene-Quaternary uplift of the Anatolian plateaux is not generated by crustal thickening alone (Chapter 2; e.g. Schildgen *et al.*, 2014). A significant consideration is the relationship between present-day elevation and crustal thickness. Here, I have assembled a database of crustal thickness estimates derived from published receiver function analyses (Table 3.1, Figure 3.1). These analyses use the recorded travel times and amplitudes of direct and converted phases from teleseismic earthquakes to constrain the shear-wave velocity structure of the crust and upper mantle. Crustal thicknesses estimated in this way increase from $\sim$ 20 km in Western Anatolia to $\sim$ 50 km on the East Anatolian Plateau (Figure 3.1a). This pattern broadly reflects the way in which present-day crustal deformation changes from northeast-southwest extension in the west to north-south shortening in the east. In general, thicker crust has greater elevation.

It is instructive to compare the observed relationship between crustal thickness and elevation with that predicted by isostatic calculations. Several recent studies have attempted to determine residual topography of Anatolia (i.e. that component of topographic elevation which is not accounted for by observed thicknesses and densities of the crust and lithospheric mantle; Boschi

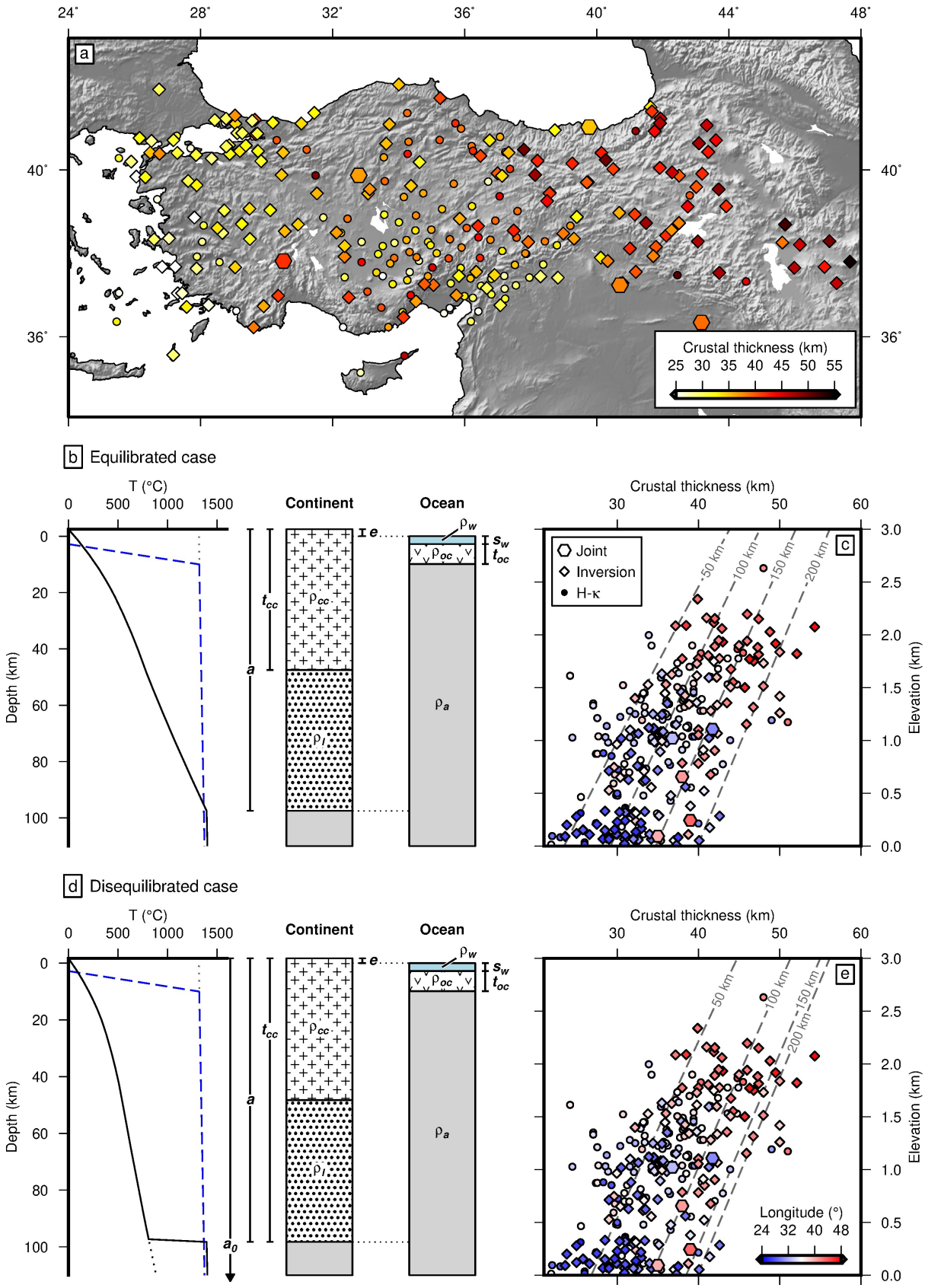

Figure 3.1: *Caption overleaf.*

et al., 2010; Komut *et al.*, 2012; Faccenna *et al.*, 2013, 2014; Komut, 2014; Uluocak *et al.*, 2016; Mahatsente *et al.*, 2018). These studies exploit different data sources and reference frames such that estimates of residual topography vary between −2 and +2 km. Here, idealized columns of continental lithosphere with different thicknesses and densities are balanced against the density structure of a mid-ocean ridge.

The elevation of a column of continental lithosphere, e, for a crustal thickness of t_{cc} is given by

$$e = t_{cc}\left(\frac{\rho_a - \rho_{cc}}{\rho_a}\right) - t_{oc}\left(\frac{\rho_a - \rho_{oc}}{\rho_a}\right) - s_w\left(\frac{\rho_a - \rho_w}{\rho_a}\right) + (a - t_{cc})\left(\frac{\rho_a - \rho_l}{\rho_a}\right), \tag{3.1}$$

where t_{oc} and ρ_{oc} are the thickness and density of oceanic crust, s_w and ρ_w are the thickness and density of water, and a is the lithospheric thickness (Figure 3.1b and 3.1d). The average density of Anatolian crust, ρ_{cc}, is 2,800 kg m^{-3} according to the EPcrust reference model (Molinari & Morelli, 2011). Key remaining parameters are densities of the continental lithospheric mantle, ρ_l, and oceanic asthenospheric mantle, ρ_a, and thickness of the continental lithosphere. All parameters used in these calculations are defined in Table 3.2.

Densities of the lithospheric and asthenospheric mantle at a given temperature, T, and pressure, P, are calculated using the relationship

$$\rho = \rho_\circ\left(1 - \alpha T + \frac{P}{K}\right), \tag{3.2}$$

which accounts for the expansivity and compressibility of mantle rocks. $\rho_\circ$ is a reference density, α is the thermal expansivity of mantle rocks and K is their compressibility.

Figure 3.1: ***Previous page.*** **Receiver function estimates of crustal thickness for Anatolia.** (a) Map showing locations of published receiver function analyses colored according to crustal thickness. Circles = crustal thicknesses determined by H-κ stacking; diamonds = crustal thicknesses determined by inverse modeling; hexagons = crustal thicknesses determined by joint inverse modeling of receiver functions and surface wave dispersion observations. (b) Pair of cartoons showing oceanic and continental columns together with continental geothermal gradient used for Airy isostatic calculation if continental lithosphere is thermal equilibrated. Solid black line = continental geotherm; dashed blue line = oceanic geotherm at mid-ocean ridge; grey dotted line = extrapolation of isentropic gradient to surface. (c) Observed crustal thicknesses plotted as function of low-pass filtered (i.e. > 30 km) elevation. Dashed lines = crustal thickness as function of elevation for the equilibrated continental lithospheric thicknesses of 50–200 km as indicated. (d) and (e) Same for thermally disequilibrated continental lithosphere, assuming an initial lithospheric thickness of 200 km. Black dotted line = extrapolation of disequilibrated continental geotherm towards original thickness.

Table 3.2: Definitions of parameters used in isostatic analysis.

Parameter	Symbol	Value	Units	Reference
Continental column				
Continental crust thickness	t_{cc}		m	
Continental upper crust thickness	t_{ucc}	$t_{cc}/2$	m	
Continental lithospheric thickness	a		m	
Continental crust density	ρ_{cc}	2,800	kg m^{-3}	Molinari & Morelli (2011)
Radiogenic heat production	H	$\begin{cases} 1.12 \text{ for } 0 < z < t_{ucc} \\ 0.4 \text{ for } t_{ucc} < z < t_{cc} \\ 0 \text{ for } t_{cc} < z < a \end{cases}$	μW m^{-3}	M^{c}Kenzie *et al.* (2005)
Oceanic column				
Mid-ocean ridge water depth	s_w	2,800	m	
Oceanic crustal thickness	t_{oc}	7,100	m	
Sea water density	ρ_w	1,030	kg m^{-3}	
Oceanic crust density	ρ_{oc}	2,860	kg m^{-3}	
Mantle rocks				
Reference density	$\rho_\circ$	3,364[a]	kg m^{-3}	Lee (2003)
Average asthenospheric mantle density	ρ_a		kg m^{-3}	
Average lithospheric mantle density	ρ_l		kg m^{-3}	
Thermal expansivity	α	3×10^{-5}	$^\circ$C^{-1}	Shorttle *et al.* (2014)
Thermal conductivity	k	$\begin{cases} 2.5 \text{ for } 0 < z < t_{cc} \\ k(T)^{\text{b}} \text{ for } t_{cc} < z < a \end{cases}$	W K^{-1} m^{-1}	M^{c}Kenzie *et al.* (2005)
Heat capacity	c_p	1,187	J kg^{-1} $^\circ$C^{-1}	Shorttle *et al.* (2014)
Gravitational acceleration	g	9.8	m s^{-1}	
Compressibility	K	115.2×10^9	Pa	
Potential temperature	T_p	1330	$^\circ$C	

[a] Value obtained using Lee's (2003) expression for peridotite density as function of Magnesium number, Mg#, where $\rho_\circ = -0.0144\text{Mg\#} + 4.66$ and $\text{Mg\#} = 100 \times (\text{Mg})/(\text{Mg} + \text{Fe})$. Mg# for ambient mantle is taken to be 90.

[b] M^{c}Kenzie *et al.*'s (2005) reparameterisation of Hofmeister's (1999) expression is given by

$$k(T) = \frac{b}{1 + cT} + \sum_{m=0}^{3} d_m (T + 273)^m$$

where $b = 5.3$, $c = 0.0015$, $d_0 = 1.753 \times 10^{-2}$, $d_1 = -1.0365 \times 10^{-4}$, $d_2 = 2.2451 \times 10^{-7}$ and $d_3 = -3.4071 \times 10^{-11}$.

To calculate T and P, the thermal structure of the lithospheric and asthenospheric mantle must first be estimated. I consider two conceivable end members for the thermal structure of the continental lithosphere. In the first case, the lithosphere is assumed to be thermally equilibrated (Figure 3.1b). M^{c}Kenzie *et al.* (2005) propose a method for calculating the temperature structure of thermally equilibrated continental lithosphere. They define a mechanical boundary layer, in which transport of heat is purely conductive, and a deeper thermal boundary layer, in which heat is increasingly transported by advection. In the mechanical boundary layer, the one-dimensional

steady-state heat flow equation,

$$-H = \frac{\partial}{\partial z}\left(k\frac{\partial T}{\partial z}\right) \tag{3.3}$$

is solved accounting for depth-dependent heat production, H, and conductivity, k, in the upper and lower crust and lithospheric mantle. In the crust, k is taken to be constant and Equation 3.3 can be solved analytically by integration. In the lithospheric mantle, the temperature dependence of k is accounted for using a modified version of Hofmeister's (1999) parameterisation (McKenzie *et al.*, 2005). Including this temperature dependence means that Equation (3.3) must be solved numerically using a Runge-Kutta scheme. For simplicity, I ignore the temperature structure of the thermal boundary layer. This simplification has a negligible affect on the integrated temperature structure of the lithospheric mantle.

In the second case, I simulate loss or thinning of lithospheric material (e.g. delamination) without any heating of the remaining lithosphere toward a steady-state geothermal gradient (Figure 3.1d). In this disequilibrated case, I first calculate an equilibrated temperature profile for some initial lithospheric thickness, $a_\circ$. This steady-state profile is then truncated at the shallower lithospheric thickness of interest. Resulting continental lithosphere is colder and denser than equilibrated lithosphere of the same thickness.

In the asthenospheric mantle, an isentropic temperature gradient is assumed so that temperature as a function of depth is given by

$$T(z) = T_p \exp\left(\frac{g\alpha z}{c_p}\right), \tag{3.4}$$

where g is the gravitational acceleration and c_p is the specific heat capacity of mantle rocks (Table 3.2; McKenzie & Bickle, 1988). Once thermal structures of the lithospheric and asthenospheric mantle have been determined, pressures and densities are calculated iteratively downwards from the base of the continental and oceanic crust using Equation (3.2).

In order to determine the degree to which changes in crustal thickness can account for observed elevation, lithospheric thickness must be estimated. Inevitably, these estimates are subject to considerable uncertainty. Reid *et al.* (2017) estimate lithospheric thicknesses of $\sim$ 60 km beneath Central Anatolia based on analysis of basaltic geochemistry. Estimates based upon receiver function analyses range between 60 and 90 km (Angus *et al.*, 2006; Çakır & Erduran, 2011; Vinnik *et al.*, 2014; Kind *et al.*, 2015). A reasonable upper bound for present-day lithospheric thickness is $\sim$ 120 km since a greater thickness would manifest itself as a substantial lithospheric root

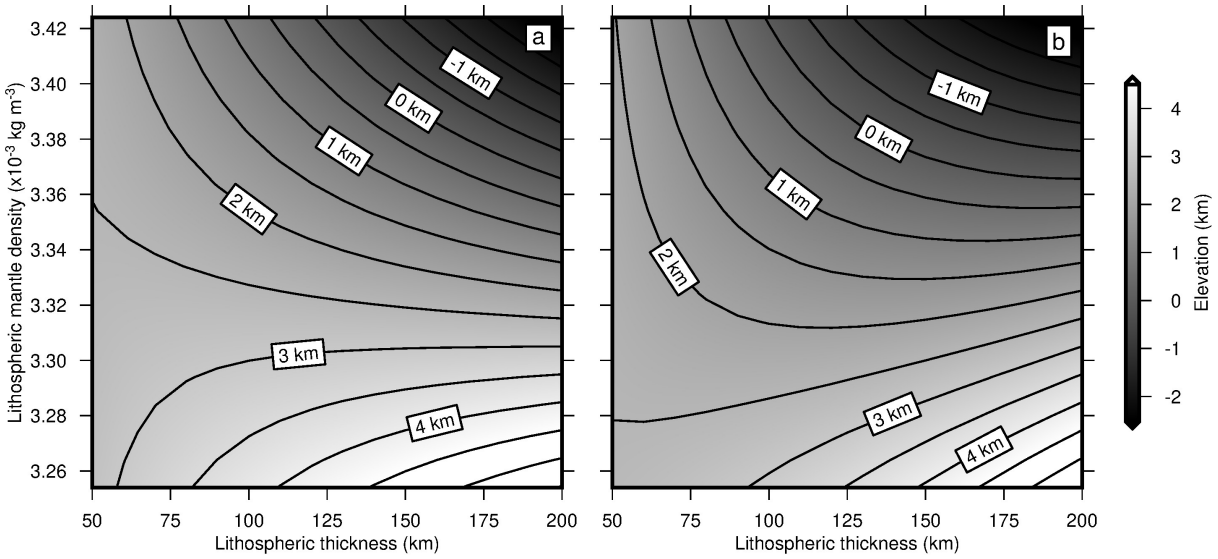

Figure 3.2: Predicted elevation as function of lithospheric thickness and density. (a) Calculated elevation plotted as function of lithospheric thickness and lithospheric mantle density for a crustal thickness of 40 km. Equilibrated case. (b) Disequilibrated case.

that should be visible in surface-wave tomographic models (Priestley & M^{c}Kenzie, 2013). For this upper bound, present-day Anatolian topography is approximately in isostatic equilibrium. If lithospheric thickness is less than 90 km, Anatolia is predicted to have residual topography of -1 km (i.e. depressed with respect to the mid-oceanic ridge). Note that if the lithosphere beneath Anatolia is thermally disequilibrated following rapid loss of the lithosphere, a thinner lithosphere is required to achieve isostatic equilibrium. I emphasise that a significant source of uncertainty in these isostatic calculations is the density of the lithospheric mantle which can be reduced through depletion (i.e. become more hartzburgitic) by up to 60 kg m^{-3} (Lee, 2003; Crosby *et al.*, 2010). Figure 3.2 shows the effects that varying the density of lithospheric mantle has upon elevation for different lithospheric thicknesses. Progressively depleted lithospheric mantle tends to increase expected elevations and hence lowers residual topographic estimates.

3.1.2 Admittance analysis

Anatolia has significant long wavelength free-air gravity anomalies of up to +50 mGal and so it is unlikely that its topography is maintained by crustal thickness and density variations alone (Figure 3.3b). In order to investigate the degree of support provided by flexural isostasy and by sub-plate density variation, the spectral relationship between topographic and gravity fields is analysed (Figure 3.3).

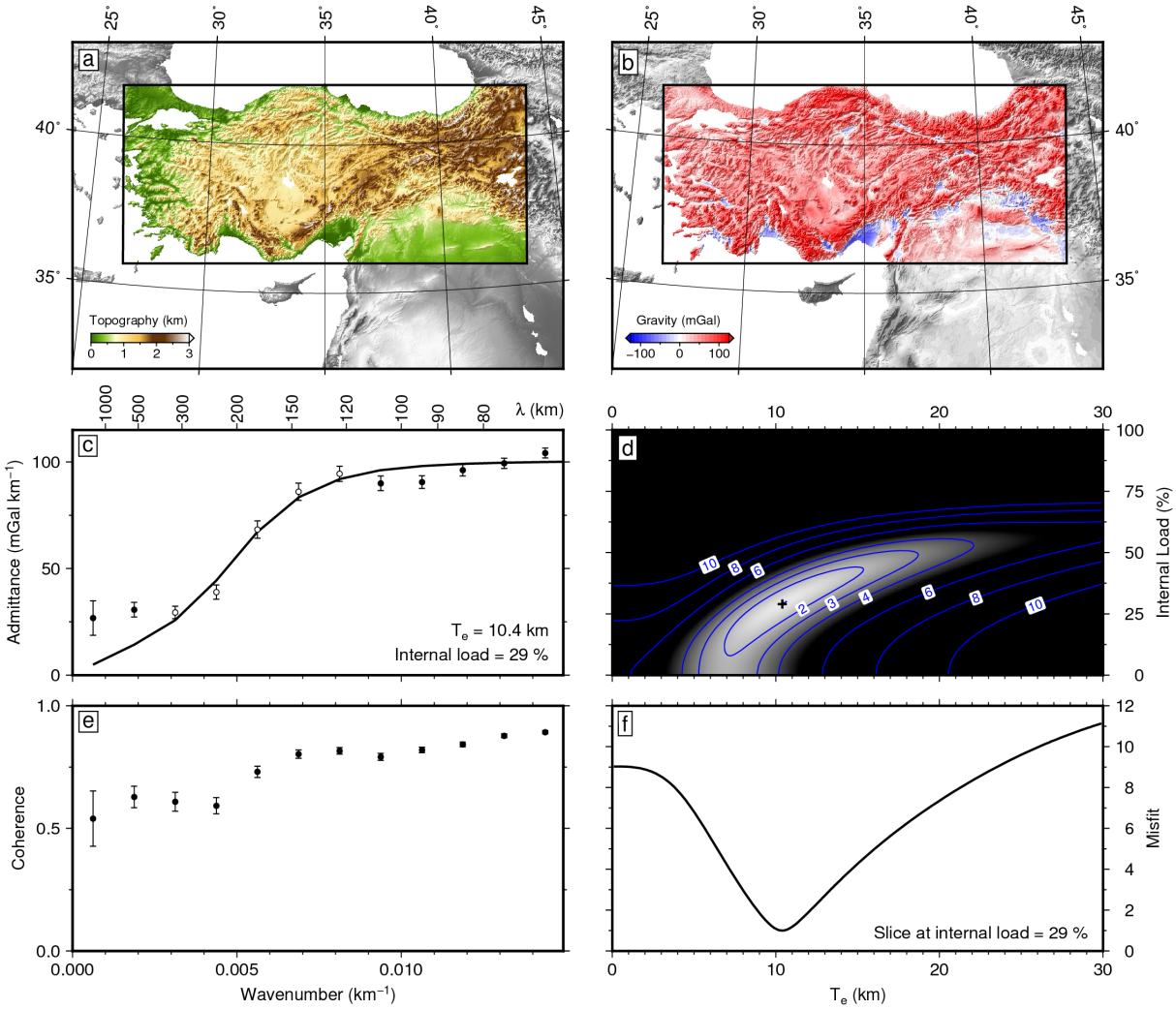

Figure 3.3: Admittance analysis of Anatolia. (a) SRTM30_PLUS topography (Becker *et al.*, 2009). Box = 650 km×1500 km window of analysis. (b) EIGEN-6C free-air gravity anomalies (Förste *et al.*, 2012). (c) Admittance for component of gravity anomalies that are coherent with topography plotted as function of wavenumber. Circles with vertical bars = observed admittance values $\pm 1\sigma$; black line = best-fitting elastic model with T_e = 10.4 km and F_2 = 29%; upper/lower crustal thicknesses and densities are 10/25 km and 2.4/2.9 Mg m^{-3}, respectively; at wavelength of 1000 km, $Z = 30 \pm 4$ mGal km^{-1}. (d) Contoured misfit to open circles plotted as function of T_e and F_2. Black cross = locus of global minimum. (e) Coherence between gravity and topography as function of wavenumber. (f) Vertical slice through global minimum at F_2 = 29%. Doubling value of minimum misfit yields uncertainty range of $T_e = 10.4^{+1.7}_{-1.5}$ km.

Admittance, $Z(k)$, is the ratio between topography and coherent free-air gravity anomalies as a function of wavenumber, $k = 2\pi/\lambda$. Here, observed values of Z are calculated from the SRTM30_PLUS topography and EIGEN-6C gravity fields within a 650 km×1500 km box using a two-dimensional multi-taper method (McKenzie & Fairhead, 1997; Becker *et al.*, 2009; Förste *et al.*, 2012). At short (i.e. < 150 km) wavelengths, Z is ∼ 100 mGal km^{-1} and at long (i.e.

$>$ 300 km) wavelengths, Z is 30 ± 4 mGal km^{-1} (Figure 3.3c). Between 150 and 300 km, Z gradually decreases. Significantly, the degree of coherence between topography and gravity is greater than 0.5 which suggests that the observed variation of Z is robust (Figure 3.3e).

The rapid decrease in Z at intermediate wavelengths can be used to estimate the effective elastic thickness, T_e. Theoretical estimates of admittance are calculated for a suite of values of T_e using an idealized two-layer crustal model overlying a mantle half-space. The upper and lower crust are assigned thicknesses of 10 km and 25 km, and densities of 2.4 Mg m^{-3} and 2.9 Mg m^{-3}, respectively. T_e together with the fraction of internal loading that correlates with surface topography, F_2, are co-varied until a satisfactory fit between observed and calculated admittance is obtained (McKenzie, 2003). A parameter sweep through T_e–F_2 space reveals a well-defined global minimum at $T_e = 10.4$ km and $F_2 = 29\%$. This value is consistent with values of $T_e < 20$ km obtained from both free-air admittance and Bouguer coherency studies, which exploited wavelet transforms (Audet, 2014).

The value of T_e, amongst other features, controls the maximum wavelength over which loads can be supported by flexural isostasy. The half-wavelength of flexural support, x_b, for a line load imposed upon an unbroken plate is given by

$$x_b = \left[\frac{4\pi^4 E T_e^3}{12g(1-\sigma^2)(\rho_m - \rho_s)} \right]^{\frac{1}{4}}, \tag{3.5}$$

where $E = 70$ GPa is Young's modulus, $g = 9.81$ m s^{-2} is gravitational acceleration, $\sigma = 0.25$ is Poisson's ratio, $\rho_m = 3.3$ Mg m^{-3} is the density of the mantle, and ρ_s is the density of infilling material (Gunn, 1943). For air-loaded topography, $T_e = 10.4^{+1.7}_{-1.5}$ km yields $x_b = 96^{+13}_{-11}$ km. This value is significantly smaller than the typical wavelengths of Anatolian plateaux, which suggests that flexural loading is unlikely to be the primary cause of this elevated interior.

A flexural isostatic model provides a good fit to observed admittance at wavelengths shorter than $\sim$ 300 km (Figure 3.3c). At longer wavelengths, Z does not tend to zero but instead approaches $+30 \pm 4$ mGal km^{-1}. This value is lower than that determined by Komut *et al.* (2012) in a study focussed on Western Anatolia ($\sim +50$ mGal km^{-1}). Positive values of long-wavelength admittance are consistent with calculations of dynamic support for convection within the upper mantle (McKenzie, 2010; Colli *et al.*, 2016).

In Figure 3.4, long wavelength free-air gravity anomalies are compared with measurements of oceanic residual depth from the compilation of Hoggard *et al.* (2017). Note that shading of

gravity and residual depth anomalies is scaled so that the two are equivalent for $Z = +30$ mGal km^{-1}. Negative long wavelength gravity anomalies and residual depths occur immediately to the north of Anatolia in the Black Sea and to the south in the East Mediterranean Sea, consistent with 1–2 km of dynamic topographic drawdown. Also shown in Figure 3.4 is the Anatolian fluvial drainage network, which is radially draped around positive long wavelength gravity anomalies. The agreement between these independent datasets is consistent with the notion that long wavelength free-air gravity anomalies reflect convective support across the region, which could have driven youthful uplift of Anatolia.

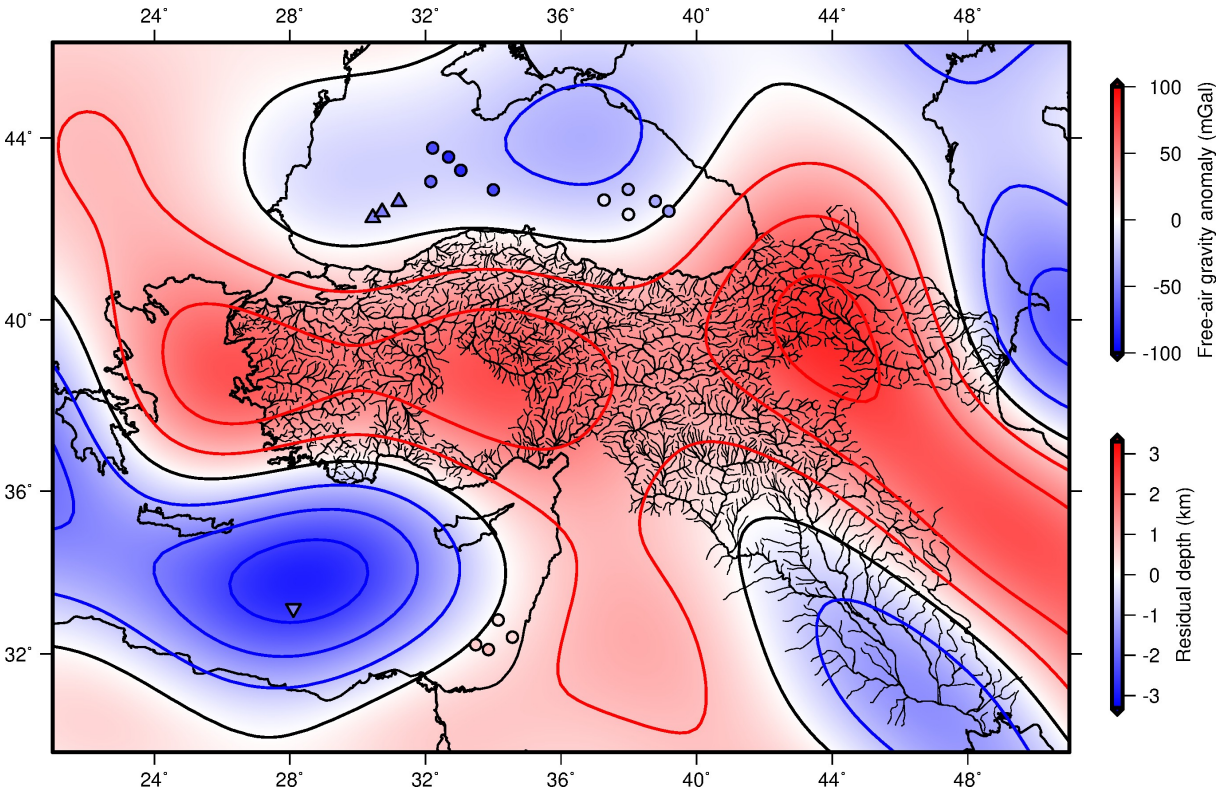

Figure 3.4: Gravity, admittance and residual depths of the Eastern Mediterranean. Map of region encompassing Anatolia showing long wavelength (i.e. 730–13,000 km) free-air gravity anomalies. Red/black/blue contours = positive/zero/negative GGM03C non-hydrostatic low-pass filtered anomalies plotted every 25 mGal (Tapley *et al.*, 2007); residual depth scale assumes $Z = 30$ mGal km^{-1}; coloured circles and upward/downward-pointing triangles = estimates and lower/upper bounds of observed oceanic residual depths (Hoggard *et al.*, 2017); irregular network of black lines = river drainage pattern.

3.2 Magmatism

Abundant Neogene-Quaternary magmatism occurs throughout Anatolia and its existence is often linked with the geodynamic evolution of this region. A range of processes have been proposed to explain this magmatism that include: subduction of oceanic lithosphere (Aldanmaz *et al.*, 2000; Ersoy *et al.*, 2012); slab break-off, fragmentation or roll back (e.g. Keskin, 2003; Şengör *et al.*, 2003; Innocenti *et al.*, 2005; Agostini *et al.*, 2007; Reid *et al.*, 2017); extension and delamination of continental lithosphere (e.g. Pearce *et al.*, 1990; Şengör *et al.*, 2008); and elevated asthenospheric temperatures (e.g. Şengör *et al.*, 2003; Prelević *et al.*, 2012). Each of these processes could generate different surface expressions and thus modify the evolving landscape in different ways. It is often remarked that there is a significant transition from calc-alkaline to alkaline magmatism in Neogene times, which has been interpreted as a shift from subduction zone to intraplate magmatic generation (e.g. Wilson *et al.*, 1997; Innocenti *et al.*, 2005; Agostini *et al.*, 2007; Keskin, 2007). The timing, nature and significance of this transition are poorly understood.

To assess the relative importance of subduction and intraplate processes in generating Anatolian magmatism throughout Neogene-Quaternary times, I compiled a comprehensive database of published geochemical analyses of mafic samples that have been assigned either radiometric or inferred chronostratigraphic ages (Table 3.3, Figure 3.5). Major and trace-element analyses and/or isotopic measurements of samples with MgO $>$ 5 wt% are presented. For the sake of completeness, this database includes previously unpublished geochemical analyses from Western Anatolia (Richardson-Bunbury, 1992; Paton, 1992).

3.2.1 Styles of magma genesis

The composition of mafic magmas directly reflects processes involved in their generation and emplacement. Magmas produced by subduction zones are geochemically distinct from those that are derived from either passively or actively upwelling asthenosphere. Above a subducting slab, the mantle wedge is considerably altered by fluids released by dehydration processes within the slab. Thus the wedge becomes enriched in fluid mobile elements, such as large ion lithophiles (e.g. K, Pb, Ba; Elliott, 2003; Bebout, 2007). The degree of enrichment can be gauged by taking the ratio of these elements with respect to insoluble equivalents which behave similarly during melting processes (e.g. Nb, Ce). Melts derived from subduction-influenced mantle will therefore

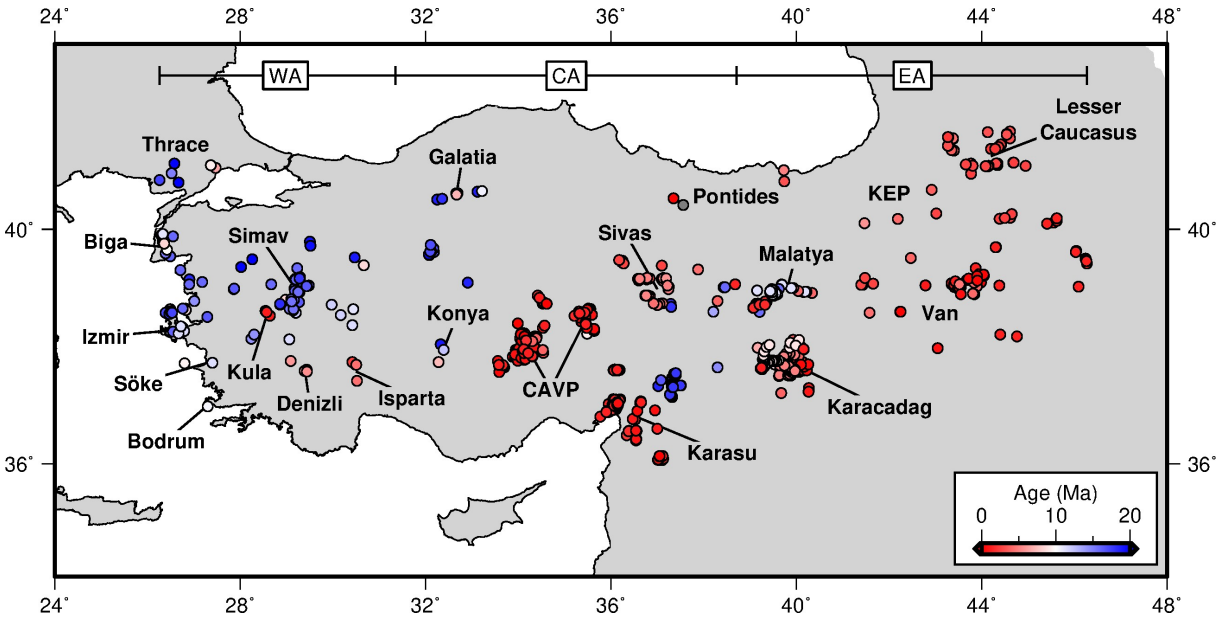

Figure 3.5: Neogene-Quaternary mafic magmatism of Anatolia. Map of Anatolia showing distribution of Neogene basaltic volcanism. Colored circles = sample locations according to age (see Table 3.3). Labels refer to locations described in text; WA = Western Anatolia, CA = Central Anatolia, EA = Eastern Anatolia, CAVP = Central Anatolian Volcanic Province, KEP = Kars-Erzurum Plateau.

have higher values of K/Nb, Pb/Ce and Ba/Nb than those derived from unenriched mantle.

Subduction processes can also modify the isotopic composition of the mantle wedge. Isotopic ratios are not thought to be affected by melting or by fractionation processes and the isotopic composition of a sample will directly reflect that of its source material. During formation of continental crust, the upper mantle became depleted in the incompatible elements Rb and Nd, relative to the more compatible Sr and Sm. Subsequently, decay of radioactive ^{87}Rb and ^{147}Sm resulted in concentration of radiogenic isotopes ^{87}Sr within the crust and ^{144}Nd within the upper mantle. Continental crust therefore has high $^{87}Sr/^{86}Sr$ and low $^{143}Nd/^{144}Nd$ relative to mantle rocks (Zindler & Hart, 1986). Oceanic sediments are partly derived from the continental crust and so they also acquire elevated $^{87}Sr/^{86}Sr$ and reduced $^{143}Nd/^{144}Nd$ values. Incorporation of subducted continental sediments into the mantle wedge therefore raises the $^{87}Sr/^{86}Sr$ values and lowers the $^{143}Nd/^{144}Nd$ values of melts generated in subduction zone settings (Plank & Langmuir, 1998).

These elemental and isotopic systems can be used to track the influence of subduction processes in generating Anatolian magmatism (Figure 3.6). Here, I exploit an online compilation to determine average values for Ocean Island Basalts for comparison (OIB; `http://www.georoc.edu`).

Table 3.3: Published geochemical analyses of mafic igneous rocks of Anatolia.

Province	Age range (Ma)	Analyses	References
Western Anatolia			
Thrace	21.7–6.5	40	Aldanmaz *et al.* (2006), Ersoy *et al.* (2014), Paton (1992)
Biga–Bodrum coast	18.5–7.1	97	Agostini *et al.* (2007), Altunkaynak & Genç (2008), Aldanmaz *et al.* (2000), Aldanmaz *et al.* (2006), Helvacı *et al.* (2009), Paton (1992)
Simav & surroundings	21.3–6	97	Bozkurt *et al.* (2008), Chakrabarti *et al.* (2012), Çoban *et al.* (2012), Dilek & Altunkaynak (2010), Erkül *et al.* (2019, 2005), Ersoy & Helvacı (2016), Ersoy *et al.* (2008, 2010, 2012), Francalanci *et al.* (2000), Innocenti *et al.* (2005), Karaoğlu *et al.* (2010), Paton (1992), Prelević *et al.* (2012, 2015), Semiz *et al.* (2015); Seyitoğlu *et al.* (1997)
Kula	1.7–0.2	53	Agostini *et al.* (2007), Alıcı *et al.* (2002), Aldanmaz *et al.* (2015), Chakrabarti *et al.* (2012), Dilek & Altunkaynak (2010), Grützner *et al.* (2013), Innocenti *et al.* (2005), Richardson-Bunbury (1992), Robert *et al.* (1992)
Denizli & Isparta	7.54–0	66	Çoban & Flower (2007), Francalanci *et al.* (2000), Paton (1992), Platevoet *et al.* (2014), Prelević *et al.* (2012), Yılmaz (2010)
Central Anatolia			
Konya	22–5	15	Asan & Ertürk (2013), Gençoğlu Korkmaz *et al.* (2017), Temel *et al.* (1998)
Galatia & surroundings	21.3–6.2	48	Adiyaman *et al.* (2001), Asan & Kurt (2011), Temel *et al.* (2010), Tankut *et al.* (1998), Wilson *et al.* (1997)
CAVP	5.3–0	208	Alıcı Şen *et al.* (2004), Aydar & Gourgaud (2002), Aydin (2008), Aydin *et al.* (2014), Deniel *et al.* (1998), Ercan *et al.* (1992), di Giuseppe *et al.* (2018), Gencalioglu-Kuscu & Geneli (2010), Gencalioglu-Kuscu (2011), Güçtekin & Köprübaşı (2009), Kürkcüglu (2010), Kürkcüglu *et al.* (1998), Notsu *et al.* (1995), Reid *et al.* (2017), Uslular & Gençalioğlu-Kuşcu (2019)
Karasu Valley	19.1–0	260	Alıcı *et al.* (2001), Alpaslan (2007), Arger *et al.* (2000), Bağcı *et al.* (2011), Italiano *et al.* (2017), Oyan (2018a), Parlak *et al.* (1998, 2000), Polat *et al.* (1997), Varol & Alpaslan (2012), Yurtmen *et al.* (2000, 2002)
Sivas	18–0	52	Alpaslan *et al.* (2004), Kocaarslan & Ersoy (2018), Kürkçüoğlu *et al.* (2015)
Pontides	6.4–0	8	Adiyaman *et al.* (2001), Aydin *et al.* (2008), Ekici (2016b)
Eastern Anatolia			
Malatya	19.2–1.4	82	Aktağ *et al.* (2019), Arger *et al.* (2000), Ekici (2016a), Ekici *et al.* (2007, 2009), Kürüm *et al.* (2008), Kürüm & Tanyıldızı (2017), Di Giuseppe *et al.* (2017)
Karacadağ	11–0	154	Alıcı Şen *et al.* (2004), Ekici *et al.* (2012, 2014), Lustrino *et al.* (2010, 2012), Notsu *et al.* (1995), Pearce *et al.* (1990)
Van, KEP & surroundings	11.6–0	168	Buket & Temel (1998), Keskin *et al.* (1998), Kheirkhah *et al.* (2009), Lebedev *et al.* (2016a,b), Neill *et al.* (2015), Notsu *et al.* (1995), Oyan (2018b,c), Oyan *et al.* (2016a,b), Özdemir *et al.* (2006, 2011, 2019), Özdemir & Güleç (2014), Pearce *et al.* (1990), Sugden *et al.* (2019)
Lesser Caucasus	5.4–0	67	Lebedev *et al.* (2007, 2008a,b), Neill *et al.* (2013, 2015)

The mean and standard deviations for OIB samples are shown as grey boxes in Figure 3.6. There are significant geochemical differences between Western, Central and Eastern Anatolia.

In Western Anatolia, a dramatic transition is evident at about 10 Ma (Figure 3.6a–3.6e). Prior to 10 Ma, magmatism occurred over a wide area encompassing volcanic centres around, for example, Simav, İzmir, Thrace, and the Biga Peninsula (Figure 3.5). All five systems show a wide range of values, greatly exceeding those observed for the majority of OIB samples. These values are largely consistent with subduction zone magmatism. Since 10 Ma, these values are much more uniform and fall within one standard deviation of the mean observed for OIB samples. This period includes Late Miocene magmatism across the region as well as a renewed phase of activity

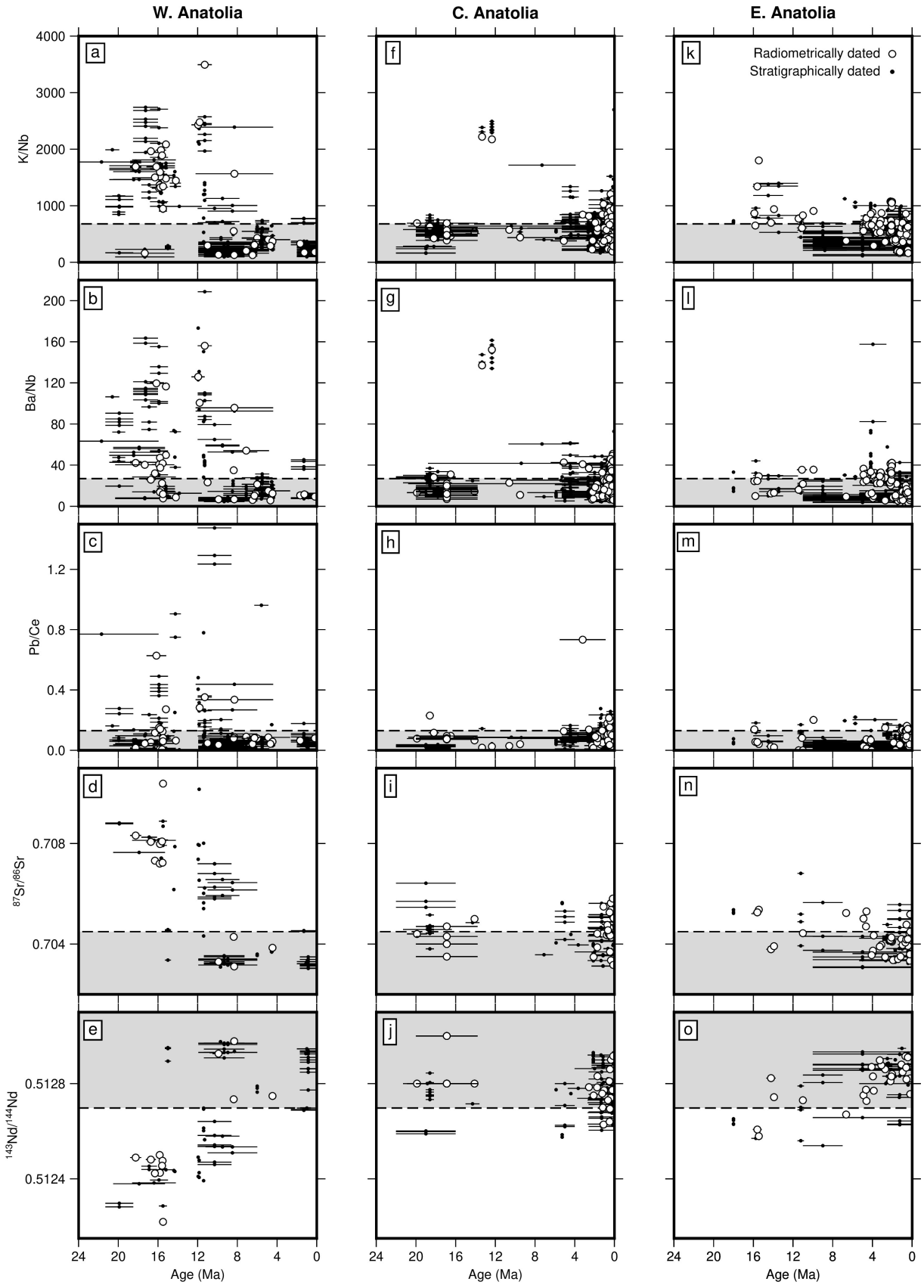

Figure 3.6: *Caption overleaf.*

at the Kula volcanic field in Quaternary times (Figure 3.5). The transition from subduction to intraplate style magmatism is well established and has been linked to the development of a 'slab window' and to the consequent arrival of uncontaminated, sub-slab asthenosphere (Innocenti *et al.*, 2005; Agostini *et al.*, 2007).

In Central Anatolia, there are two distinct magmatic phases (Figure 3.6f–3.6j). No significant geochemical transition exists between these two phases. The first phase lasted from 20–14 Ma and principally occurred within the Galatia province and around the Karasu Valley, which are northwest and southeast of the Central Anatolian Plateau, respectively (Figure 3.5). A small number of samples of this age have also been reported from the Sivas region, on the eastern Central Anatolian Plateau. The second phase lasted from about 5 Ma to the present day and occurs in central and eastern Central Anatolia (e.g. Central Anatolian Volcanic Province, Sivas, Karasu Valley). Throughout Neogene and Quaternary times, the range of values for each of the subduction-sensitive parameters is significantly lower than that observed within subduction zone settings and within Western Anatolia prior to 10 Ma. A small number of exceptional analyses from the Konya province of Central Anatolia do have significantly elevated ratios of K/Nb and Ba/Nb (Asan & Ertürk, 2013). However, these lamprophyric rocks probably represent small melt fractions from an enriched source and their low Pb/Ce ratios as well as a lack of isotopic measurements mean that it is difficult to determine whether they are the products of arc volcanism or lithospheric contamination. Overall, the majority of samples from Central Anatolia exhibit a modest subduction zone signature compared with the majority of OIB samples.

Values of each of the subduction-sensitive parameters similar to those of Central Anatolia are obtained for Eastern Anatolia, where mafic magmatism has occurred continuously since $\sim$ 12 Ma across an extensive region including the Karacadağ stratovolcano (Figures 3.5 and 3.6k–3.6o). The absence of a switch from subduction-influenced to intraplate-style magmatism in Neogene times for Central and Eastern Anatolia does not agree with the results of several earlier studies (Wilson *et al.*, 1997; Keskin, 2007). In order to mitigate sensitivity to the effects of fractionation

Figure 3.6: ***Previous page.*** **Enrichment of mafic magmatic rocks of Anatolia as function of time.** White circles with horizontal bars = radiometrically dated samples $\pm 1\sigma$; black circles with horizontal bars = chronostratigraphically dated samples $\pm 1\sigma$; grey boxes with dashed lines = mean and standard deviation of ocean island basalts from GEOROC database (OIB; `http://www.georoc.edu`). (a-e) Western Anatolia, note dramatic change in composition at $\sim$ 10 Ma; (f-j) Central Anatolia; (k-o) Eastern Anatolia. Regions as defined in Figure 3.5.

and contamination, I only include samples with MgO > 5 wt%. These previously described switches are predicated upon samples that do not pass our chosen cut-off value of MgO. It is difficult to assess the relevance of these more fractionated samples as a guide to the composition of the mantle source. When only high-MgO samples are considered, any regional Neogene-Quaternary shift away from subduction-influenced magmatism in Central and Eastern Anatolia is not apparent.

$^{87}Sr/^{86}Sr$ and $^{143}Nd/^{144}Nd$ are independent systems that can be combined to more closely constrain the nature of the putative source region. Several different mantle reservoirs can been defined within $^{87}Sr/^{86}Sr$–$^{143}Nd/^{144}Nd$ space. The isotopic composition of primitive mantle is thought to be that of the bulk Earth, which has a present-day average composition of $^{87}Sr/^{86}Sr = 0.7047$ and $^{143}Nd/^{144}Nd = 0.51265$ (Figure 3.7; Philpotts & Ague, 2009). Fractional melting of primitive mantle raises the $^{143}Nd/^{144}Nd$ ratio and lowers the $^{87}Sr/^{86}Sr$ ratio of the source rock. Reservoirs that are thought to represent uncontaminated mantle, including those invoked as potential sources for OIB-style magmatism (e.g. CMR: common mantle reservoir; HIMU: high-μ reservoir; FOZO: focal zone reservoir), lie along a 'mantle array' between bulk Earth and a significantly depleted end-member known as Depleted Mid-Ocean Ridge Basalt Mantle (DMM; Figure 3.7; Zindler & Hart, 1986; Hart *et al.*, 1992; Stracke *et al.*, 2005; Lustrino & Wilson, 2007). Fractional melting of primitive mantle also generates enriched products. Examples include reservoirs that are thought to be representative of lower crust (e.g. EM1; Enriched Mantle 1), upper crust (e.g. EM2; Enriched Mantle 2), or oceanic sediments (e.g. EMS; Eastern Mediterranean Sediments) and that have higher values of $^{87}Sr/^{86}Sr$ and lower values of $^{144}Nd/^{145}Nd$, relative to the bulk Earth (Zindler & Hart, 1986; Klaver *et al.*, 2015).

In general, Anatolian mafic rocks lie along a simple binary mixing line between a partially depleted OIB-like source (e.g. CMR, HIMU, FOZO) and an enriched oceanic sediment or upper crustal source (e.g. EM2, EMS; Figure 3.7). There is no requirement to invoke significant depletion of the mantle source or contamination by lower crustal material. K/Nb, Pb/Ce and Ba/Nb ratios all correlate well with the relative importance of the EM2/EMS sources, implying that variations in the isotopic composition of Anatolian mafic rocks are primarily controlled by the degree of source contamination by subducted oceanic sediments. At high values of $^{143}Nd/^{144}Nd$, there is a systematic shift to higher values of $^{87}Sr/^{86}Sr$ from west to east. To assess the potential influence of contamination by continental crust, I calculate mixing lines between the least enriched mafic sample and Neoproterozoic basement material from Western

Anatolia (Augen gneiss; Gürsu, 2016). The observed shift to higher $^{87}Sr/^{86}Sr$ values in Eastern Anatolia is consistent with up to 10% of crustal contamination and probably reflects increasing crustal thickness from west to east.

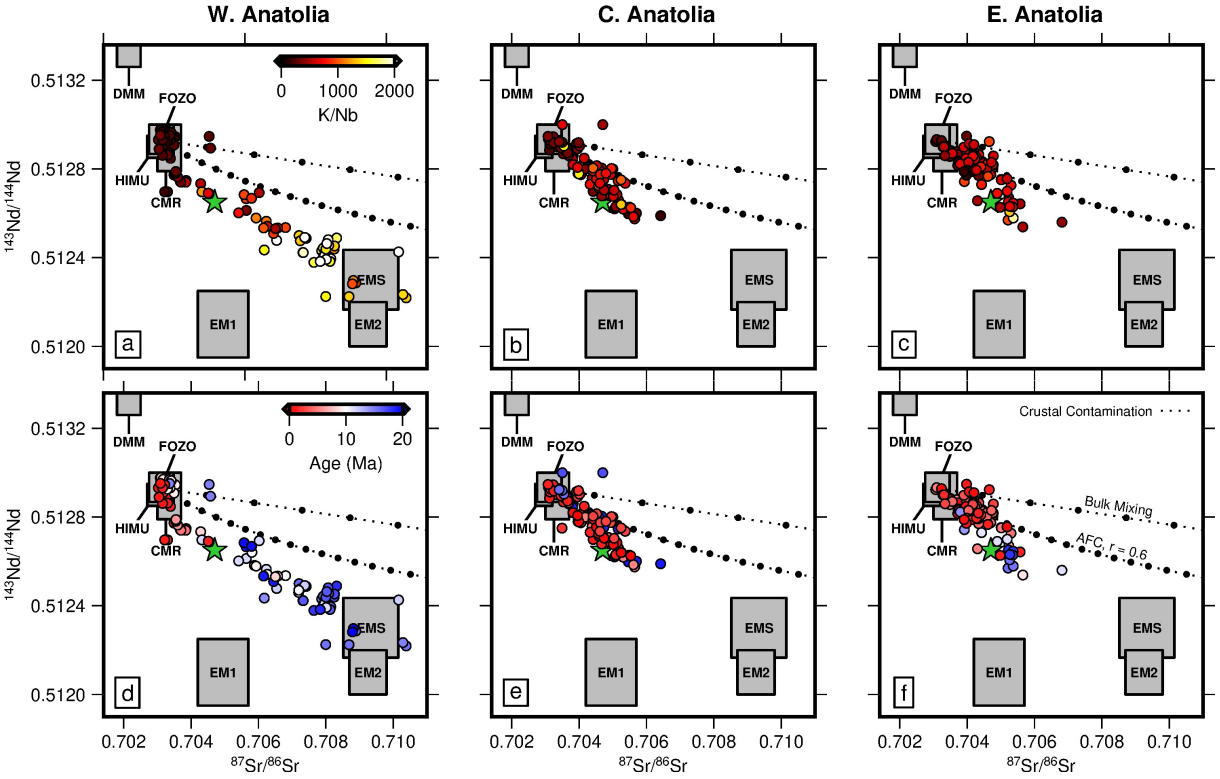

Figure 3.7: Isotopic compositions of Neogene-Quaternary mafic magmatic rocks from Anatolia. (a) $^{143}Nd/^{144}Nd$ plotted as function of $^{87}Sr/^{86}Sr$ for Western Anatolia. Circles are colored according to K/Nb ratio; green star = bulk Earth composition (Philpotts & Ague, 2009); labeled grey polygons = mantle reservoirs where HIMU is high-μ mantle, FOZO is the focal zone reservoir; DMM is depleted MORB mantle; EM1/EM2 is enriched mantle 1 and 2 (Zindler & Hart, 1986), CMR is common mantle reservoir (Lustrino & Wilson, 2007), EMS is Eastern Mediterranean sediments (Klaver *et al.*, 2015); upper/lower dotted lines = bulk mixing/assimilation and fractional crystallization (AFC) trends between most primitive basalts and average composition of augen gneisses that are representative of Anatolian basement (Gürsu, 2016). AFC trends are calculated using DePaulo (1981) mixing equations. (b) Isotopic plot for Central Anatolia. (c) Isotopic plot for Eastern Anatolia. (d)–(f) Isotopic plots where circles are colored according to radiometric age.

In Western Anatolia, mafic samples span the full range of isotopic compositions from OIB-like mantle to oceanic sediments (Figure 3.7a and 3.7d). As observed on Figure 3.6, there is a clear age progression, with the degree of enrichment decreasing towards the present day. The most recent basaltic products fall entirely within the observed ranges of uncontaminated mantle reservoirs and require no enrichment by subduction. In Central and Eastern Anatolia, samples require significantly less enrichment than the older (i.e. pre-10 Ma) samples from

Western Anatolia (Figures 3.7b and 3.7e, and 3.7c and 3.7f). However, unlike the youngest Western Anatolian rocks, all samples are enriched to some degree. This enrichment could reflect residual/continued contamination of the asthenosphere by subduction processes or melting of previously contaminated lithospheric material.

3.2.2 Mantle potential temperatures and lithospheric thicknesses

It is evident that subduction processes are not responsible for the generation of basaltic magmatism for the last 10 Ma in Western Anatolia and throughout Neogene and Quaternary times in Central and Eastern Anatolia. Instead, melting of an OIB-like or partially enriched source region could be accounted for by passive upwelling caused by lithospheric extension, by lithospheric delamination or slab fragmentation, or by elevated asthenospheric temperatures. I now investigate these potential mechanisms by applying two independent schemes for estimating mantle potential temperature, T_p, and lithospheric thickness. First, I use the major-element thermobarometer developed by Plank & Forsyth (2016). Secondly, inverse modelling of rare-earth element concentrations is carried out (McKenzie & O'Nions, 1991). Both of these methods can be used to model high-Mg basalts generated from peridotitic mantle and account for fractionation of olivine. I exploit a subset of samples with MgO $>$ 8.5 wt% that are suitable for modelling and focus on the youngest, post-10 Ma, phase of magmatism (Figure 3.8).

It is useful to compare estimates of T_p with the potential temperature of ambient convecting mantle. Estimates of this ambient value vary depending upon methodology (e.g. Katsura *et al.*, 2004; Herzberg *et al.*, 2007; Dalton *et al.*, 2014; Matthews *et al.*, 2016b). Hirschmann & Stolper (1996) noted that an important constraint is the global mean oceanic crustal thickness, since values of T_p can be combined with melting models to predict melt fractions and hence crustal thicknesses generated by adiabatic decompression. Throughout the following sections, I exploit the adiabatic melting models of Katz *et al.* (2003) with updated material properties from Shorttle *et al.* (2014). The value of T_p required to produce the mean thickness of oceanic crust, 6.9 $\pm$ 2.2 km, by adiabatic decompression melting using these parameterizations is 1331 $\pm$ 35 °C (White *et al.*, 1992; Hoggard *et al.*, 2017; Richards *et al.*, 2018). A suitable reference value of T_p for ambient mantle is therefore $\sim$ 1330 °C.

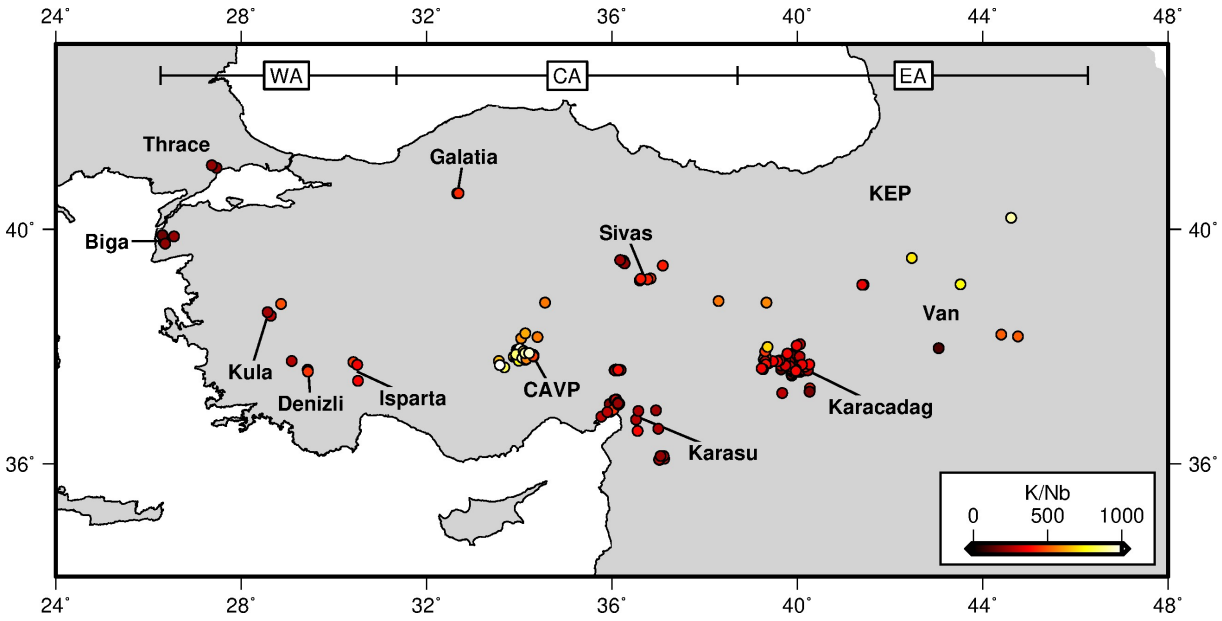

Figure 3.8: Samples selected for estimating mantle potential temperatures. Map of Anatolia showing distribution of post-10 Ma, MgO > 8.5 wt% samples used for estimating mantle potential temperatures and lithospheric thicknesses. Coloured circles = sample locations according to K/Nb (see Table 3.3). Labels refer to locations described in text; WA = Western Anatolia, CA = Central Anatolia, EA = Eastern Anatolia, CAVP = Central Anatolian Volcanic Province, KEP = Kars-Erzurum Plateau.

Major-element thermobarometry

Building upon the pioneering work of Lee *et al.* (2009), Plank & Forsyth (2016) developed parameterizations of source temperature and pressure using an extensive compilation of experimental melt equilibration datasets. Their approach exploits the fact that partitioning of major elements during melting is dependent on pressure and temperature. First, observed major element compositions of high-Mg basalts are corrected for olivine fractionation to estimate primary melt compositions. Olivine in equilibrium with melt is incrementally added until melt compositions reach equilibrium with mantle that has an assumed olivine forsterite content. For each of sample, I back-calculate to a melt Mg number, Mg# = Mg/Mg + Fe = 0.9 in olivine. This value of Mg# is considered to be a reasonable average value for partially depleted mantle (Lee *et al.*, 2009). This correction, together with the following pressure and temperature calculations, are also dependent upon the ratio of Fe^{3+} to Fe^{2+}, and upon the water content of the melt.

Once primary melt compositions have been estimated, temperature, T, and pressure, P, are

calculated using an emprically derived parameterisation, in which

$$T\ (\mathrm{K}) = 1264.5 + 7.85(\mathrm{Mg_4Si_2O_8}) + \frac{8545}{\mathrm{Si_4O_8}} - 5.96(\mathrm{Al_{16.3}O_8}) - \Delta T_{\mathrm{H_2O}} - \Delta T_{\mathrm{CO_2}}, \tag{3.6}$$

and

$$P\ (\mathrm{GPa}) = \frac{\ln(\mathrm{Si_4O_8}) - 4.045 + 0.0114(\mathrm{Fe_4Si_2O_8}) + 0.00052(\mathrm{Ca_4Si_2O_8})^2 + 0.0024(\mathrm{Mg_4Si_2O_8})}{-336.3T^{-1} + 0.0007T^{1/2}}, \tag{3.7}$$

where

$$\Delta T_{\mathrm{H_2O}} = 40.4(\mathrm{H_2O}) - 2.97(\mathrm{H_2O})^2 + 0.0761(\mathrm{H_2O})^3. \tag{3.8}$$

Compositional components are reported in mole%, as defined by Lee *et al.* (2009), with the exception of H_2O which is reported in wt%. A correction is applied to any samples which initially give equilibrium pressures in excess of 2 GPa in order to account for the effects of undersaturated CO_2. Thus

$$\text{if } P > 2.0 \text{ GPa, then } \Delta T_{\mathrm{CO_2}} = \frac{\mathrm{SiO_2} - 50.3}{0.128}, \text{ else } \Delta T_{\mathrm{CO_2}} = 0, \tag{3.9}$$

where SiO_2 is in wt%. For these particular samples, pressure is then recalculated using the revised temperature.

Temperature and pressure estimates clearly depend upon variations in major elemental concentrations. Changes in melt composition can also arise as a result of fractionation and heterogeneities in source composition and mineralogy. I have already highlighted the fact that K/Nb can be used as a proxy for enrichment by subduction processes across Anatolia. Major element compositions are shown as a function of MgO and shaded by K/Nb in Figure 3.9. There is little systematic variation with MgO content which implies that fractionation is not a dominant control on major element compositions. However, significant variation does occur with K/Nb. For K/Nb values greater than $\sim$ 500, samples generally shift to higher values of SiO_2, Al_2O_3 and CaO, and to lower values of FeO_t (i.e. combined FeO and Fe_2O_3). Indeed, high K/Nb begin to form a distinct population in MgO–Al_2O_3 and MgO–FeO_t space. Magnitudes of these shifts are unlikely to be caused by subduction enrichment. Rather, they probably reflect distinct equilibration conditions for both populations. These trends act consistently to reduce temperature and pressure estimates for high K/Nb samples.

Thermobarometric calculations for Western, Central and Eastern Anatolia are shown in Figure

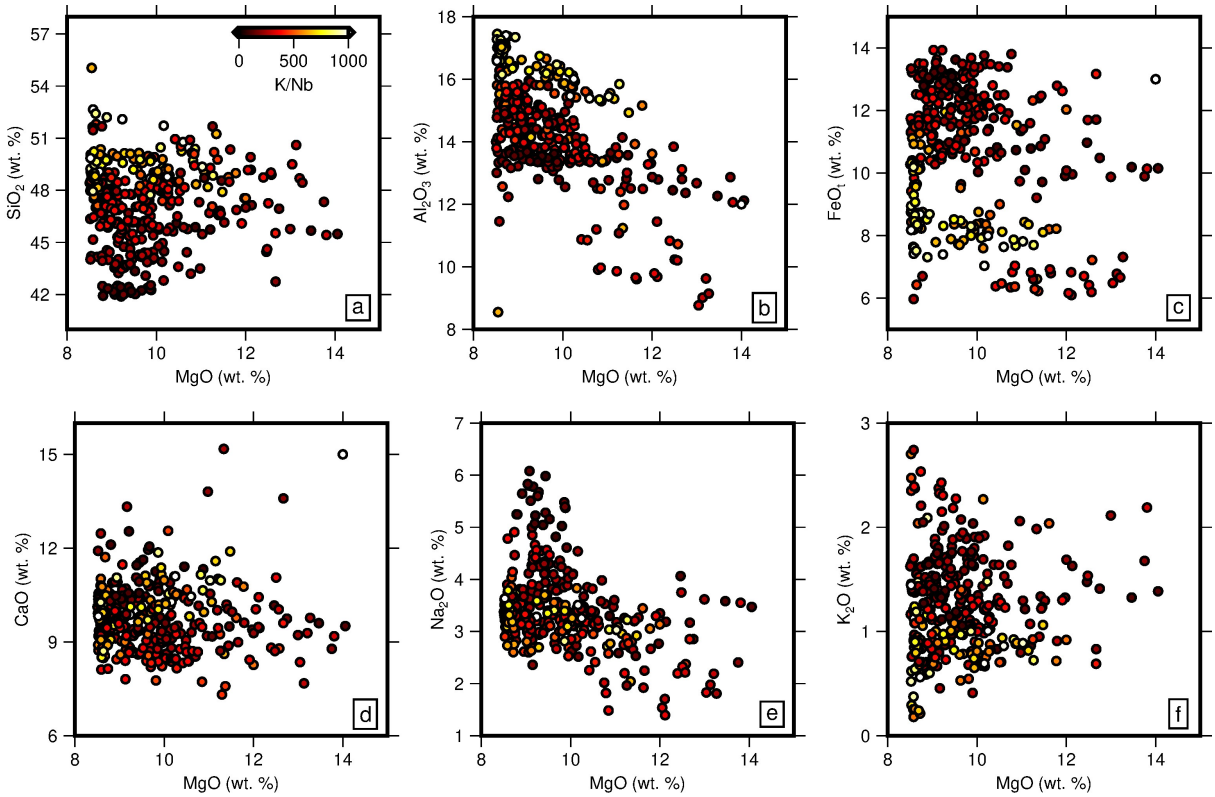

Figure 3.9: Major element compositions of selected Anatolian mafic magmatic rocks. (a) SiO_2, (b) Al_2O_3, (c) FeO_t (i.e. combined FeO and Fe_2O_3), (d) CaO, (e) Na_2O and (f) K_2O as function of MgO for samples with MgO $>$ 8.5 wt% and ages $<$ 10 Ma, shaded by K/Nb.

3.10. Note that these results are strongly dependent upon the chosen value of $Fe^{3+}/\Sigma Fe$, which is controlled by oxidation state, and upon the assumed water content. In Anatolia, direct measurements of $Fe^{3+}/\Sigma Fe$ and of water concentrations within melts are scarce. Globally, it is observed that $Fe^{3+}/\Sigma Fe$ varies between about 0.1 for mid-ocean ridge basalts (MORB) and 0.3 for arc settings (Cottrell & Kelley, 2011; Brounce *et al.*, 2014). Average estimates for the Basin and Range province of western North America are ~ 0.2 (Plank & Forsyth, 2016). This value is assumed to be appropriate for Anatolia, given the similarities of these regions, which both combine recently active subduction processes and subsequent generation of mafic melts with OIB affinities (Fitton *et al.*, 1991; Kempton *et al.*, 1991). H_2O is known to scale with Ce for MORB samples so that $H_2O/Ce = 200 \pm 100$ (Michael, 1995; Dixon *et al.*, 2002). The results shown in Figure 3.10a–3.10c assume that $Fe^{3+}/\Sigma Fe = 0.2$ and that $H_2O/Ce = 200$.

In order to relate these results to mantle potential temperature, T_p, I have fitted adiabatic decompression melting paths to calculated equilibration temperatures and pressures. Melting paths are determined using the anhydrous parameterisation of Katz *et al.* (2003), with values

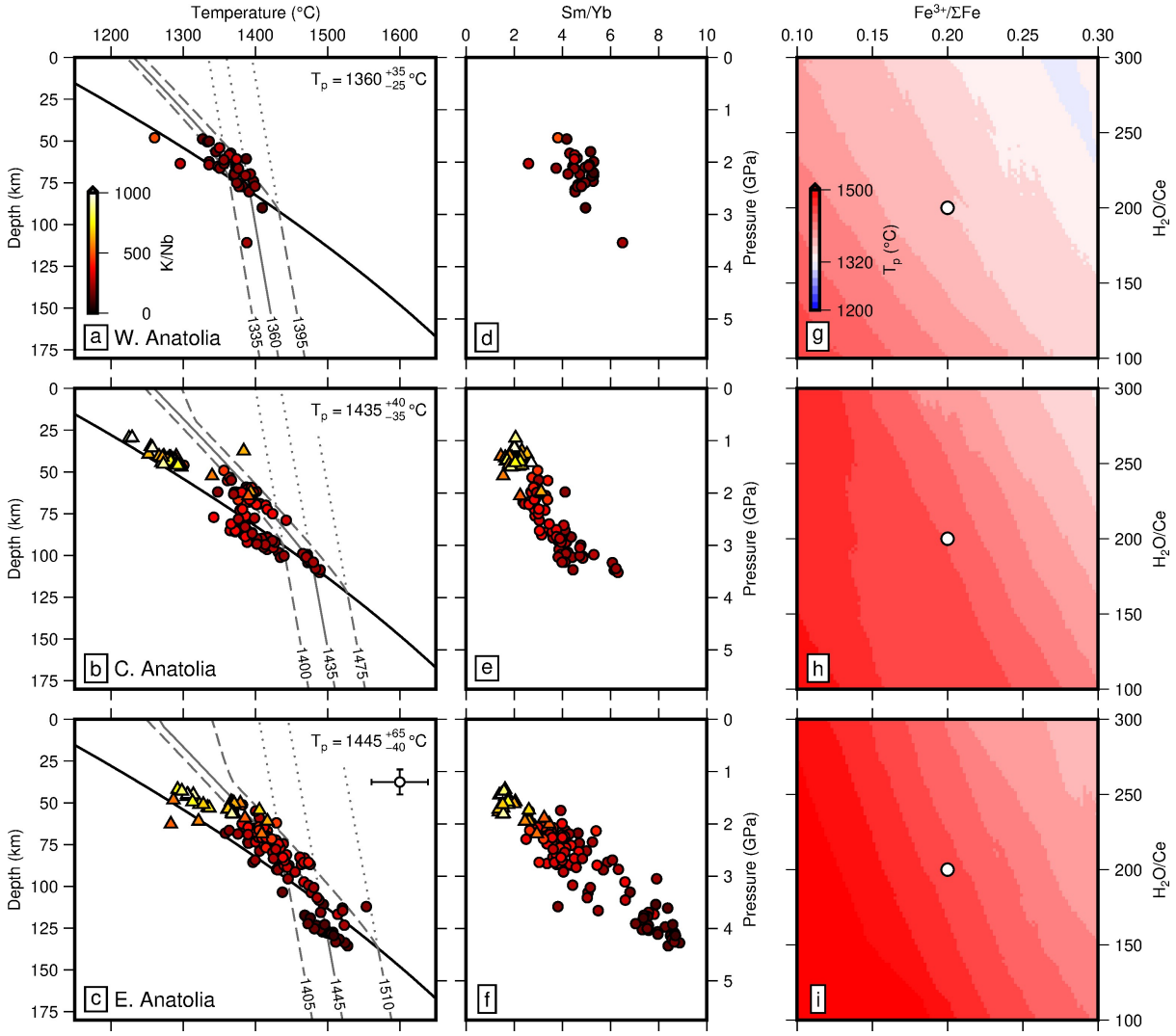

Figure 3.10: Major-element thermobarometry of Anatolian mafic magmatic rocks. (a) Temperature plotted as function of depth/pressure. Colored circles = Equilibration pressures and temperature estimates determined for mafic samples (MgO > 8.5 wt%) from Western Anatolia with K/Nb < 500 using $Fe^{3+}/\Sigma Fe = 0.2$ and $H_2O/Ce = 200$; black line = anhydrous solidus; grey line = best-fit melt pathway; dashed grey lines = minimum and maximum melt pathways; dotted grey lines = adiabatic gradients corresponding to loci of intersection between melt pathways and anhydrous solidus (Katz *et al.*, 2003); optimal value of potential temperature, T_p, given in top right-hand corner. (b) Estimates for Central Anatolia. Triangles = samples with K/Nb > 500. (c) Estimates for Eastern Anatolia. (d–f) Sm/Yb as function of equilibration pressure estimates. (g)–(i) Distribution of potential temperatures obtained by varying $Fe^{3+}/\Sigma Fe$ and H_2O/Ce. In each case, white circle = values used for thermobarometric calculations shown in panels (a)–(c).

of material properties updated to those of Shorttle *et al.* (2014) where appropriate, assuming a modal clinopyroxene value of 0.15. The misfit between melting paths and calculated equilibration conditions is calculated using a least squares approach, where temperature and pressure are normalized by their respective formal uncertainties of ± 39 °C and ± 0.24 GPa, as quoted by

Plank & Forsyth (2016).

Two distinct magmatic populations exist in Central and Eastern Anatolia: calculated equilibration pressures and temperatures for high K/Nb samples are consistently colder and shallower than those for low K/Nb samples. The latter samples lie along regionally consistent melt paths that require varying mantle potential temperatures. Temperatures are highest in Eastern Anatolia and decrease toward the west. Best-fit melting paths for low K/Nb samples that lie above the solidus, along with a range of paths that can equally fit these data, are shown in Figures 3.10a–3.10c. These melting paths correspond to mantle potential temperatures of $T_p = 1360^{+35}_{-20}$ °C for Western Anatolia, $T_p = 1435^{+40}_{-35}$ °C for Central Anatolia, and $T_p = 1445^{+85}_{-40}$ °C for Eastern Anatolia. In general, the top of the melting column is at about 50 km depth. Quoted upper and lower bounds correspond to values of T_p that yield misfit values that are less than twice those at the global minima. Average melt fractions along these melting paths are 3.4 ± 2.7 %, 4.8 ± 4.4 % and 7.2 ± 4.7 % for Western, Central and Eastern Anatolia, respectively. In contrast, high K/Nb populations do not lie along consistent melt paths. Instead, they cluster near the solidus at depths shallower than 50 km. I suggest that samples from these populations probably reflect melting of, or contamination by, lithospheric material partially enriched during earlier episodes of subduction. This more complex evolution means that fitting adiabatic decompression melting paths is not reasonable.

Equilibration pressure estimates are compared to values of Sm/Yb in Figures 3.10d–3.10f. Sm and Yb are rare earth elements (REEs) which are strongly incompatible during melting. Both elements behave similiarly during melting of spinel peridotite, but, Yb, a heavy REE, is retained within garnet peridotite during melting. Since there is a pressure-dependent transition from spinel to garnet peridotite at about 65 km depth within the Earth's mantle, Sm/Yb can be used as a proxy for the depth of melting, with higher values reflecting deeper melting (e.g. Jennings & Holland, 2015). There is a strong correlation between calculated melt equilibration pressures and Sm/Yb values, particularly in Central and Eastern Anatolia, which implies that the Plank & Forsyth (2016) scheme is performing well in this region (Figures 3.10d and 3.10e).

To assess the influence of uncertainties in water content and oxidation state, I repeated the modelling procedure for the full range of globally observed values (Michael, 1995; Dixon *et al.*, 2002; Cottrell & Kelley, 2011; Brounce *et al.*, 2014). The revised results for each region are shown in Figures 3.10g–3.10i. Higher values of $Fe^{3+}/\Sigma Fe$ and H_2O/Ce tend to reduce estimates of potential temperatures. For Western Anatolia, calculated temperatures through much of the

parameter space are at or below that of ambient mantle. For the chosen values of $Fe^{3+}/\Sigma Fe = 0.2$ and $H_2O/Ce = 200$, the estimated potential temperature is within the range of uncertainty of that for ambient mantle. For Central Anatolia, our estimates of mantle potential temperature approach those for ambient mantle only for the highest values $Fe^{3+}/\Sigma Fe$ and H_2O/Ce. For Eastern Anatolia, excess temperatures are required for all reasonable values of $Fe^{3+}/\Sigma Fe$ and H_2O/Ce.

Inverse modelling of rare earth element concentrations

Partitioning of rare earth elements (REEs) is also sensitive to both the depth and degree of melting. During mantle melting, the REEs are incompatible so that their abundance is reduced with increasing melt fraction. Compatibility of the heavy REEs is dependent upon the aluminous phase that is present. Since there is a pressure-dependent transition from spinel to garnet in the uppermost mantle, the relative abundance of light and heavy REEs is dependent upon the depth of melting. Heavy REEs are more compatible in garnet than in spinel so that melting of garnet-bearing peridotite will lead to a relative depletion of these elements. McKenzie & O'Nions (1991) developed the INVMEL algorithm for adiabatic decompression of peridotite, which exploits these relationships by inverting REE distributions in order to calculate melt fraction as a function of depth. Here, the INVMEL-v12.0 scheme is used.

The INVMEL scheme inverts observed REE concentrations by summing fractional melts over incremental depths to determine cumulative melt fraction as a function of depth. Mantle potential temperature is then estimated by comparing resultant melt-fraction-with-depth distributions to parameterised mantle adiabats. Spinel-garnet transition-zone depths are fixed in advance. Here, I have chosen a transition at 63–72 km, in agreement with the thermodynamic modeling results of Jennings & Holland (2015). The lower limit of their transition zone has been increased from 68.1 km to 72 km in order to stabilise the inversion procedure. Source compositions for each inversion run are estimated by mixing components of depleted (i.e. $\epsilon Nd = 10$) and primitive (i.e. $\epsilon Nd = 0$) mantle compositions to match the observed average value of ϵNd for each sample suite (McKenzie & O'Nions, 1991). Partition coefficients are calculated using the parameterisation of Blundy & Wood (2003). Melt paths are specified at 3 km depth increments and melting is assumed to cease at the base of the lithospheric column. The inverse model iteratively calculates melt compositions for different melt-fraction-with-depth curves using the relationships of Shaw (1970). The root-mean-squared misfit between calculated and observed compositions is

minimised using Powell's conjugate gradient search algorithm (Press *et al.*, 1992). The top of the melting column and the starting melt-fraction-with-depth model are varied until an optimal fit to the observed REE distribution is achieved for a smooth output melt-fraction-with-depth curve.

Once a best-fitting curve of melt fraction as a function of depth has been determined, a forward model is produced for the complete element suite in order to test the extent to which the optimal result matches major and other trace element observations. Olivine fractionation does not significantly affect REE concentrations within the melt. It does, however, contribute to variations in Mg and Fe concentrations, which results in a disparity between observed and modelled values of these elements. The amount of olivine addition required to explain this disparity is straightforward to calculate. The final melt fraction is given by $1/(1-F)$, where F is the estimated weight fraction of crystallised material. Starting models, best-fit models, and fractionation-corrected models are all presented in Figure 3.11. Inverse modelling of enriched samples (i.e. K/Nb $>$ 500) using simple melting models results in larger misfits to observed trace element concentrations. Acceptable fits can only be achieved with a strongly modified mantle source, the characterisation of which introduces a significant degree of uncertainty. Samples with K/Nb $>$ 500 were therefore omitted.

In Western Anatolia, very low melt fractions (i.e. $< 2\%$) are required to replicate high REE concentrations. This melting must occur within both the garnet and spinel stability fields. Consequently, the resultant melting path spans a broad depth range and does not track a calculated isentropic melting path. Optimal fits to observed REE concentrations are achieved with the top of the melting column at 62 km. At these depths, low melt fractions require potential temperatures of less than $\sim$ 1330 °C (Figure 3.11a–3.11c). Observed REE concentrations decrease eastward, so that calculated melt fractions increase to 2.1% for Central and 3.9% for Eastern Anatolia. The best-fitting depths at which melting ceases are 58 km and 59 km, respectively. At shallow depths, calculated melting paths approximately follow theoretical isentropic decompression melting paths that correspond to mantle potential temperatures of $\sim$ 1340 °C and $\sim$ 1355 °C (Figure 3.11d–3.11i).

In all three regions, the majority of observed REE and trace element concentrations can be accurately matched. In Central and Eastern Anatolia, the forward model tends to overpredict concentrations of Cs, Rb and Ba. These large-ion-lithophile elements are highly soluble and so any discrepancies may reflect leaching during the weathering process. REE concentrations are

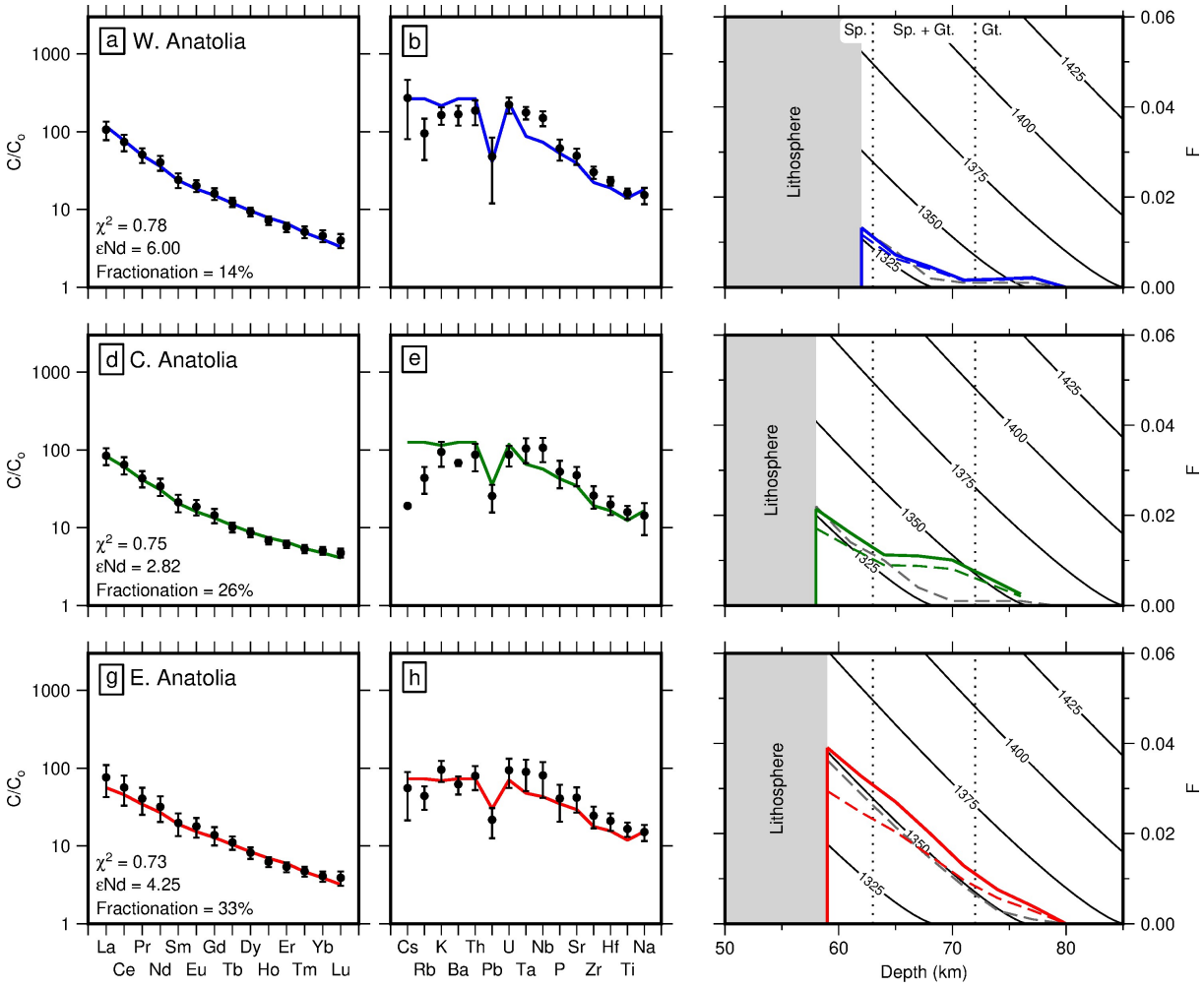

Figure 3.11: Inverse modelling of REEs distributions for Anatolian mafic magmatic rocks. (a) Western Anatolia. Black circles with error bars = average observed concentrations of rare earth elements normalized with respect to mixed mantle source $\pm 1\sigma$; blue line = best-fitting calculated concentrations obtained by inverse modeling. (b) Black circles = trace element concentrations; blue line = predicted concentrations; (c) Cumulative melt fraction, F, as function of depth. Dashed blue line = distribution of F obtained using calculated concentrations of rare earth elements shown in panel (a); solid blue line = same corrected for fractionation of olivine; dashed grey line = starting distribution of F; shaded box = lithosphere; vertical dotted lines = spinel-garnet (Sp-Gt) transition zone; solid labeled lines = isentropic melting paths for different potential temperatures (Katz *et al.*, 2003). (d)–(f) Central Anatolia. (g)–(i) Eastern Anatolia.

far less sensitive to the weathering process, which suggests that the results of inverse modeling are less affected. The forward model also consistently underpredicts concentrations of Ta and Nb, possibly as a consequence of uncertainties in partition coefficients and/or source composition for these particular elements. In general, calculated melting paths exhibit long, low melt-fraction tails because observed REE concentrations require small-degree melting within the garnet stability field before the onset of adiabatic decompression at shallower depths. Similar low melt

fraction tails have been reported for the Potrillo Volcanic Field of North America and for the Galápagos islands (Thompson *et al.*, 2005; Gibson & Geist, 2010).

3.2.3 Magmatic insights

Both modelling techniques show that there is an asthenospheric temperature gradient across Anatolia. Temperatures increase by $\sim$ 30–80 °C from west to east and the top of the melting column for low K/Nb samples lies at a depth of about 50–60 km. Although regional patterns in melt fraction and potential temperature estimates from both approaches generally agree, there are systematic differences in their optimal values. Melt fractions and temperatures estimated using the Plank & Forsyth (2016) parameterization are consistently 2–4% and 50–100 °C higher than those calculated using the INVMEL algorithm. Both techniques are subject to different uncertainties and approximations that can affect estimates of melt fraction and mantle T_p.

Effects of source composition and water content

A general assumption in both major-element thermobarometry and REE inversion is that melts are derived from unenriched lherzolitic mantle. Anatolia has undergone a complex and protracted geodynamic history. Long-lived subduction of African lithosphere throughout closure of the Neotethys Ocean could have significantly altered the composition of the underlying mantle, as is manifest, for example, by compositions of Early to Middle Miocene magmatic rocks exposed in Western Anatolia. Analysis presented in Section 3.2.1 suggests that after $\sim$ 10 Ma, subduction processes have had a limited influence on basaltic compositions with the exception of some partially enriched samples that are thought to be derived from melting of, or contamination by, enriched lithospheric material. By excluding samples with values of K/Nb $>$ 500, it is likely that the assumed mantle composition is a reasonable one. However, it is important to note that concentrations of REEs are more sensitive to source enrichment than major elements due to their lower concentrations. For inverse modelling, an underestimation of REE concentrations within the source region results in underprediction of melt fraction and asthenospheric T_p. This underprediction probably accounts for at least some of the difference between the results of major-element thermobarometry and REE inverse modelling.

Methods for estimating mantle T_p generally used here rely on anhydrous melting models. In reality, source materials are likely to contain at least a small amount of water. Source water

concentrations are not well known but, given relatively low concentrations within the melts ($\sim 1.5\pm0.8$ wt%), they are unlikely to be greater than $\sim 0.1\pm0.05$ wt% for $H_2O/Ce = 200$ at 5% melting. This value is consistent with estimates from OIBs and is at the lower end of estimates for a subduction-modified mantle wedge (i.e. ~ 0.075 wt% and 0.1-1 wt%, respectively; Dixon *et al.*, 2002; Karato, 2011). It is possible to incorporate hydrous melting into parameterisations of mantle melting (e.g. Ghiorso *et al.*, 2002; Katz *et al.*, 2003; Langmuir *et al.*, 2006; Hirschmann, 2010; Kelley *et al.*, 2010). The addition of water shifts the solidus to greater depths. I note that hydrous melting parameterisations vary significantly and are often only constrained by experimental data limited to pressures equivalent to depths < 60 km (Katz *et al.*, 2003).

Melting models are required to relate estimates of melt equilibration pressure and temperature derived from major-element thermobarometry to T_p. Incorporating hydrous melting would require higher T_p melt paths to fit the melt equilibration data. If there are significant amounts of water in the source region, my estimates of T_p are minima. Using the hydrous melting model of Katz *et al.* (2003), adding 0.1 wt% of water yields T_p estimates that are up to ~ 40 °C hotter. Due to the concave-upward shape of the solidus, this effect becomes greater as temperature increases. In this way, the observed gradient of potential temperature across Anatolia would be steepened by incorporating hydrous melting. Unlike the major element parametrisation, the INVMEL algorithm explicitly incorporates a melting model as part of the calculation. In this case, addition of water will lower the calculated value of T_P since melting will necessarily occur deeper and at lower temperatures. Nonetheless, water is extremely incompatible and readily enters the melt so that its supply is rapidly diminished. The cooling effect is therefore greater at lower melt fractions, which means that the observed gradient of T_p across Anatolia is likely to be preserved by incorporating hydrous melting.

It is conceivable that geographical variations in source composition and oxidation state could influence the robustness of the observed gradient in T_p across Anatolia. Although source composition is allowed to vary regionally for REE inverse modelling, all other parameters in the analyses are kept fixed. Reconciling the estimated temperature differences would require extreme variations in these parameters. Given similarities in isotopic and elemental compositions for high-Mg samples from the region, such large variations are unlikely. I conclude that the estimated temperature gradient is a robust reflection of the asthenospheric temperature pattern beneath Anatolia.

A potential challenge in relating melt equilibration conditions to asthenospheric potential tem-

perature identified by Plank & Forsyth (2016) concerns the pooling and conductive cooling of melts at the base of the lithosphere. These authors have invoked this phenomenon to account for melt equilibration estimates at locations from western North America that lie parallel to the solidus. Distributions of Anatolian melt equilibration estimates for low K/Nb samples are steeper than the solidus and can be approximated by adiabatic decompression melting paths. Therefore, there is no requirement to invoke conductive cooling. If a degree of conductive cooling has affected estimated melt equilibration conditions, T_p estimates would be minima. In contrast, the majority of high K/Nb samples presented here do cluster close to the solidus at depths < 50 km (i.e. shallower than the top of the low K/Nb distribution and shallower than the top of the melting column estimated from REE inverse modelling). Their distribution is more consistent with the effects of conductive cooling at the base of the lithosphere. This observation is also consistent with the interpretation that their enrichment derives from the melting of, or contamination by, an enriched lithospheric source.

Comparisons with published T_p estimates

In their study of the rocks from the Central Anatolian Volcanic Province, Reid *et al.* (2017) also estimated mantle potential temperatures using the Plank & Forsyth (2016) thermobarometer. They conclude that melt equilibration beneath the Hasan field was significantly shallower and colder than to the west and east. Analysis of our more comprehensive database reproduces this result. However, the majority of Hasan samples have K/Nb values that exceed 500 which places them within the enriched population identified above. Elevated potential temperatures are estimated for unenriched samples from the nearby Sivas and Karasu Valley lava fields. I therefore infer that these volcanic rocks are not necessarily representative of asthenospheric melting beneath Central Anatolia. Instead, my results imply that asthenospheric temperatures beneath Central Anatolia are indeed anomalously elevated.

Reid *et al.* (2017) also report elevated temperatures across Western and Eastern Anatolia. For Eastern Anatolia, their maximum temperature estimates range from 1380 to 1430 °C, in broad agreement with results presented here. Notably, they do not recover a westward temperature decrease. Instead, their maximum temperature estimates of ~ 1450 °C occur in Western Anatolia where my estimates are much closer to those of ambient mantle. Minor disparities in melt equilibration estimates can arise due to differences in chosen parameters. Significantly, Reid *et al.* (2017) chose to correct for the effects of latent heat by employing the scheme described

by Putirka *et al.* (2007). This scheme relies on an estimate of melt fraction that carries a large degree of uncertainty. The scheme returns high melt fraction estimates of $\sim 10\%$ for Western Anatolia, which requires a significant latent heat correction (i.e. $\sim +70$ °C). The procedure used here of fitting melting paths through suites of melt equilibration estimates combined with REE inverse modeling yields much lower estimates of melt fraction for Western Anatolia (i.e. ~ 3 and $\sim 2\%$, respectively), and thus cooler temperatures. Applying the latent heat correction of Putirka *et al.* (2007) to these lower melt fraction estimates would also result in significantly cooler calculated temperatures, accounting for most of the difference between my results and those of Reid *et al.* (2017). In summary, a wealth of disparate evidence supports the presence of a westward decrease in asthenospheric potential temperature across Anatolia.

3.3 Independent Constraints from Tomographic Models

Earthquake tomographic models provide useful additional constraints on the thermal structure of the sub-plate mantle because seismic wave speeds, especially those of shear waves, are strongly dependent on temperature (Faul & Jackson, 2005). Several studies have built tomographic models of the mantle beneath Anatolia using a range of datasets and techniques (e.g. Bakırcı *et al.*, 2012; Salaün *et al.*, 2012; Chamorro *et al.*, 2014; Skolbeltsyn *et al.*, 2014; Govers & Fichtner, 2016). In Figure 3.12, results from two studies are summarised: a regional P-wave model (Biryol *et al.*, 2011); and part of a global upper-mantle shear-wave model (Schaeffer & Lebedev, 2013). Both models suggest that mantle material that lies immediately beneath the Anatolian lithospheric plate (i.e. shallower than ~ 250 km) is anomalously slow. The relative sizes and magnitudes of these anomalies are largest beneath Eastern Anatolia and decrease westward. Beneath a depth of 250 km, a continuous fast anomaly extends across most of Anatolia, which has been interpreted as subducted African lithosphere. This anomaly is clearest in the P-wave model, which is particularly sensitive to cold temperatures.

The nature of the relationship between shear-wave velocities and mantle temperature has received considerable attention in recent years (see, e.g., Takei, 2017). At low temperatures, mantle rocks behave elastically and V_s steadily decreases with increasing temperature as the rock density decreases due to thermal expansion (e.g. Faul & Jackson, 2005). As temperatures approach the solidus, grain boundary sliding can introduce significant anelasticity and V_s decreases more rapidly. Priestley & McKenzie (2006) developed a parameterisation for converting

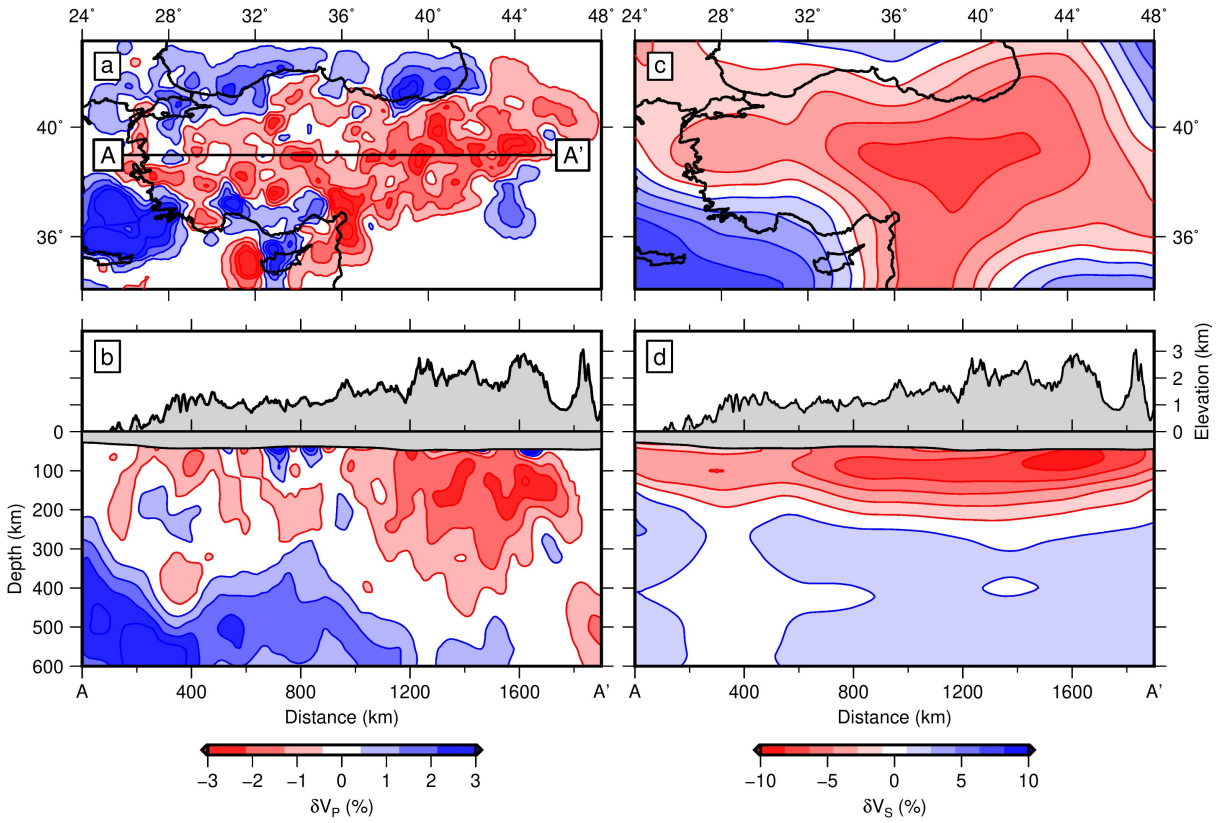

Figure 3.12: Tomographic models of Anatolia. (a) 130 km depth slice through regional earthquake tomographic model of Anatolia based upon P-wave arrivals (Biryol *et al.*, 2011). (b) East-west vertical slice at 39°N through model shown in panel (a). Black line with grey band = topographic and crustal thickness profile from EPcrust reference model of Molinari & Morelli (2011). Note that blobby/streaky appearance of both map and vertical slice probably reflects sub-optimal ray coverage. (c) 125 km depth slice through global surface wave tomographic model (Schaeffer & Lebedev, 2013). (d) East-west vertical slice.

V_s to temperature which includes the effects of anelasticity. This parameterisation contains empirical constants which must be calibrated. Priestley & M^{c}Kenzie (2006) do so by comparing V_s obtained for oceanic lithosphere, stacked as a function of plate age, to the predictions of a plate cooling model. They also include temperature estimates from lithospheric xenoliths in the continents. Priestley & M^{c}Kenzie's (2006) procedure has subsequently been updated to include the results of recent mineral physics experiments and updated plate cooling models (Priestley & M^{c}Kenzie, 2013; Yamauchi & Takei, 2016; Richards, 2018).

Here, I apply the revised parameterisation of Richards (2018) to the upper mantle shear-wave model of Schaeffer & Lebedev (2013). The eastward decrease in shear-wave velocity is reflected in the resulting T_p model (Figure 3.13a and 3.13b). Note that at depths shallower than 100 km, tomographic models may be affected by artefacts related to uncertainties in crustal structure

(Priestley & McKenzie, 2013). Beneath 100 km, a long wavelength high temperature feature is recovered beneath Eastern Anatolia, extending to depths of ∼ 200 km and with asthenospheric potential temperatures up to ∼ 1400 °C. The magnitude and extent of this high temperature feature decrease westward.

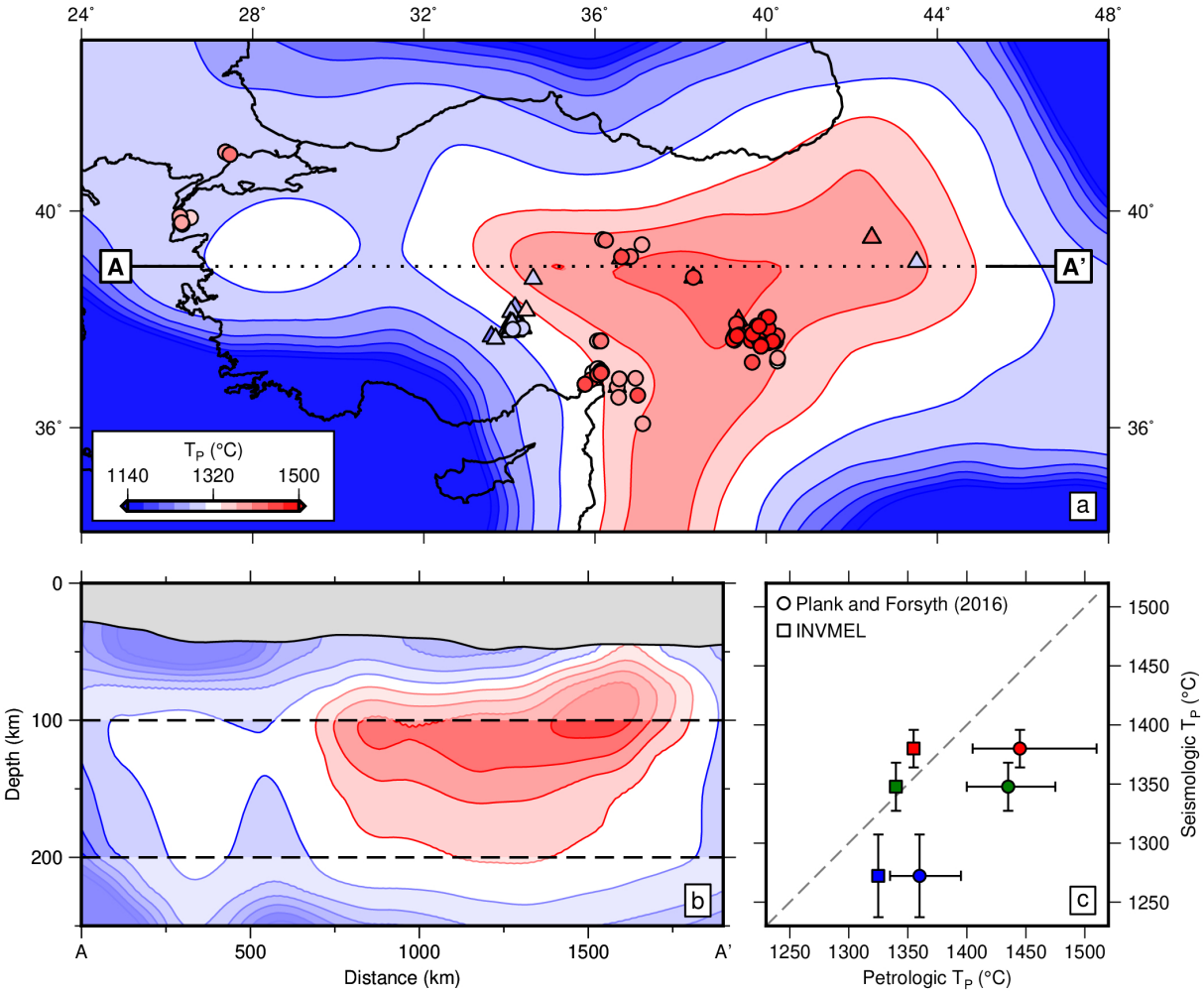

Figure 3.13: Tomographic mantle potential temperature estimates. (a) Map of Anatolia showing average potential temperatures between depths of 100 and 200 km, calculated from shear-wave velocity model of Schaeffer & Lebedev (2013) using parametrization of Richards (2018). Circles/triangles = potential temperature estimates determined from major-element thermobarometry for individual basaltic samples with K/Nb < 500 and > 500, respectively. (b) Vertical slice through potential temperature model at 39 °N. Pair of dashed lines = depth range over which average T_p was estimated. (c) Relationship between estimates of potential temperature from geochemical and seismological techniques. Blue/green/red squares and circles = potential temperature estimates for Western/Central/Eastern Anatolia from inverse modeling of REE concentrations and major-element thermobarometry, respectively (McKenzie & O'Nions, 1991; Plank & Forsyth, 2016).

In Figure 3.13c, average potential temperatures between depths of 100 and 200 km that have

been calculated from the shear-wave velocity model are compared with temperatures obtained by both petrologic approaches. T_p estimates for each region are calculated by averaging T_p estimates at locations with petrological constraints. Although uncertainties in seismologic T_p are quoted in terms of standard deviations of mean values, I must emphasise that larger, but less easily quantifiable, uncertainties are associated with the tomographic model and with the temperature parameterisation. There is a reasonable correlation between potential temperatures estimated using petrological and seismological approaches. This agreement strengthens the notion that sub-plate mantle temperatures are highest beneath Eastern Anatolia and decrease westward.

3.4 Uplift Mechanisms

I have exploited a range of diverse approaches to investigate the causes of Neogene-Quaternary uplift and magmatism across Anatolia. In Chapter 2, I discussed how calibrated inverse modelling of large inventories of longitudinal profiles can be used to extract quantitative information about the spatial and temporal evolution of regional topography. In this Chapter, a compilation of published receiver function analyses was used to investigate the isostatic relationship between crustal and lithospheric thickness and elevation (Section 3.1.1). Admittance analysis was then used to elucidate the relationship between gravity and topography as a function of wavelength, confirming that, at long wavelengths, Anatolian topography is not entirely supported by flexural isostasy (Section 3.1.2). In Section 3.2, I used a database of published geochemical analyses for Anatolian mafic igneous rocks to investigate their genesis and to make quantitative estimates of lithospheric thickness and asthenospheric potential temperature. These results were then compared with estimates from seismic tomography. The results of each of these analyses have important implications for the geodynamic evolution of the region. In the following sections, I will critically discuss potential mechanisms driving regional uplift and magmatism in light of these results.

3.4.1 Asthenospheric flow

It has been proposed that flow within the asthenospheric mantle could account for the Neogene-Quaternary growth of the Anatolian Plateaux and associated magmatism (e.g. Boschi *et al.*, 2010; Faccenna *et al.*, 2013, 2014). The arrival of hot, bouyant mantle beneath the plate could

drive upift through isostatic and/or viscous support. Major-element thermobarometric calculations and inverse modelling of REEs for recent high-MgO mafic rocks, along with slow shear-wave anomalies, suggest that asthenospheric material beneath Anatolia is anomolously hot. Asthenospheric potential temperature appears to be highest beneath Eastern Anatolia, decreasing from up to $\sim$ 1400 °C there to approximately that of ambient mantle beneath Western Anatolia, in line with decreasing elevation. The most recent phase of mafic intraplate volcanism initiated at $\sim$ 12 Ma beneath Eastern Anatolia and propagated westward. A westward propagation is also inferred for regional uplift on the basis of inverse modelling of longitudinal river profiles, initiating in Eastern Anatolia $\sim$ 10 Ma earlier than mafic volcanism. Consistent patterns linking onset and migration of uplift and magmatism together with the magnitude of uplift and size of temperature excess all point toward a common cause.

It is informative to calculate amounts of uplift generated by excess asthenospheric temperatures beneath Anatolia. Rudge *et al.* (2008) provide an expression for calculating isostatic uplift, U, generated by the emplacement of a layer of hot asthenospheric material with thickness, H, where

$$U = \frac{H\alpha\Delta\overline{T}}{1 - \alpha T_{base}}. \tag{3.10}$$

α is the thermal expansivity, T_{base} the temperature at the base of the column, and $\Delta\overline{T}$ the average temperature difference between the hot and ambient layers (Figure 3.14a). $\Delta\overline{T}$ is calculated by integrating an isentropic temperature profile over the depth range a to $a + H$ and setting T_p equal to ΔT_p (Equation 3.4).

Predicted uplift as a function of layer thickness and anomalous temperature is shown in Figure 3.14b. Petrologic and tomographic evidence suggests that asthenospheric temperatures are raised by up to $\sim$ 50–100 °C in a $\sim$ 100–150 km thick channel beneath Anatolia. These values correspond to $\sim$ 0.2–0.6 km of predicted uplift, although additional uplift could be driven by viscous support if the asthenospheric mantle is actively upwelling. This analysis therefore suggests that some, but not all, of the observed regional uplift can be explained by high mantle temperatures immediately beneath the lithosphere.

3.4.2 Lithospheric thinning

It has also been suggested that removal of Anatolian lithosphere could drive uplift and magmatism (Göğüş & Psyklywec, 2008; Bartol & Govers, 2014; Göğüş *et al.*, 2017). In this case, uplift

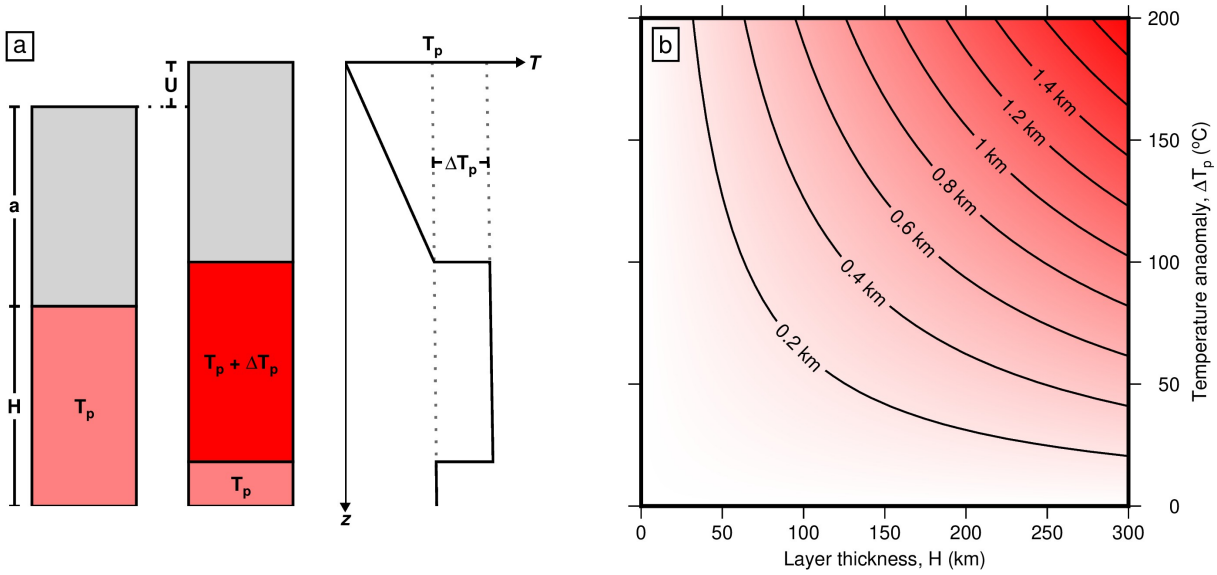

Figure 3.14: Uplift generated by asthenospheric thermal anomalies. (a) Cartoon outlining isostatic balance used to calculate uplift, U, associated with a temperature anomaly, ΔT_p, is a channel of thickness H below lithosphere of thickness a. On the temperature profile, black solid line = geotherm with asthenospheric temperature anomaly, grey dotted lines = isentropic temperature profiles for ambient and anomalously hot mantle. Not to scale. (b) Predicted uplift as function of H and ΔT_p, where ΔT_p is the excess potential temperature.

and magmatism are thought to have been caused by upwelling of buoyant asthenospheric mantle in response to removal of dense lithospheric material. Several mechanisms have been proposed as triggers for lithospheric removal. Göğüş & Psyklywec (2008) investigated the peeling off and detachment of coherent blocks of lithospheric mantle from the base of the plate, with particular reference to Eastern Anatolia. Bartol & Govers (2014) suggested that such a process could have resulted from subducted African lithosphere steepening and migrating trenchward following a period of flat-slab subduction, and that such a model could explain the evolution of both the Central and East Anatolian Plateaux. In contrast, in a study focussed on the Central Anatolian Plateau, Göğüş *et al.* (2017) proposed that a thickened lithospheric root, which developed during a Cretaceous period of shortening and arc magmatism, could have become gravitationally unstable and 'dripped' into the underlying asthenosphere.

Several lines of evidence suggest that the present-day lithospheric thickness beneath Anatolia is anomalously thin. Estimates of lithospheric thickness from S-to-P receiver function analyses are generally $\sim$ 60–90 km (Angus *et al.*, 2006; Çakır & Erduran, 2011; Vinnik *et al.*, 2014; Kind *et al.*, 2015). In magmatic regions, the top of the melting column is generally assumed to coincide with the base of the conducting lithospheric lid. Estimates from major-element thermobarometry and inverse modelling of REEs both suggest that the top of the melting column lies at around

$\sim$ 60 km beneath volcanic centres throughout Anatolia (Section 3.2; Reid *et al.*, 2017). These values are considerably lower than typical estimates of steady-state thicknesses of undepleted lithosphere, which are $\sim$ 125 km (e.g. the thickness at which the oceanic lithosphere appears to stabilise; Parsons & Sclater, 1977; Parsons & McKenize, 1978; Richards *et al.*, 2018). Thus, it is likely that present-day lithospheric thicknesses of $<$ 100 km beneath Anatolia reflect a recent phase of thinning or removal which could have contributed to regional uplift in Neogene and Quaternary times.

Numerous recent studies have predicted amounts of uplift generated by lithospheric thinning, exploiting complex numerical simulations that include viscous effects of downwelling lithosheric material and compensatory upwelling asthenosphere (e.g. Göğüş & Psyklywec, 2008; Bartol & Govers, 2014; Göğüş *et al.*, 2017). These authors suggest that, in some cases, lithospheric thinning is capable of generating $\sim$ 1 km of regional uplift at appropriate rates to explain observations from the Anatolian Plateaux. However, the results of these numerical simulations are strongly dependent on a wide range of chosen model parameters, such as initial density structure and mantle viscosities. Alternatively, a simple isostatic approach can place useful bounds on amounts of uplift generated by lithospheric thinning and requires fewer parameters to be chosen. The isostatic component of uplift generated by thinning lithospheric mantle of thickness a by an amount Δa is given by

$$U = (a - t_c)\Big(\frac{\rho_{l,0} - \rho_{l,1}}{\rho_{base}}\Big) - \Delta a\Big(\frac{\rho_a - \rho_{l,1}}{\rho_{base}}\Big), \tag{3.11}$$

where t_c is crustal thickness, ρ_a asthenospheric density and ρ_{base} the density at the base of the column (Figure 3.15a). As in Section 3.1.1, the initial lithospheric density, $\rho_{l,0}$ is calculated using a steady-state geotherm for lithosphere of thickness a, and this equlibrated profile is truncated by an amount Δa to calculate the lithospheric density following thinning, $\rho_{l,1}$.

Predicted uplift as a function of lithospheric thinning, Δa, and present-day, thinned thickness (i.e. $a - \Delta a$) is shown in Figure 3.15b. Estimates of lithospheric thickness for Anatolia at the present day are $\sim$ 60–90 km. $\sim$ 0.5–1.5 km of regional uplift cannot be accounted for by the presence of hot asthenosphere at the base of the plate. This remaining uplift could be explained by lithospheric thinning of 50–125 km. It is conceivable that loss of lithospheric material of this magnitude could occur due to peeling off and detachment of African oceanic lithopshere following a period of flat-slab subduction, as proposed by Bartol & Govers (2014), since mature oceanic lithosphere appears to stabilise at thicknesses of $\sim$ 125 km (e.g. Parsons & Sclater, 1977; Parsons

& McKenize, 1978; Richards *et al.*, 2018). Göğüş *et al.* (2017) suggest that similar magnitudes could result from gravitational instability of a thickened lithospheric root.

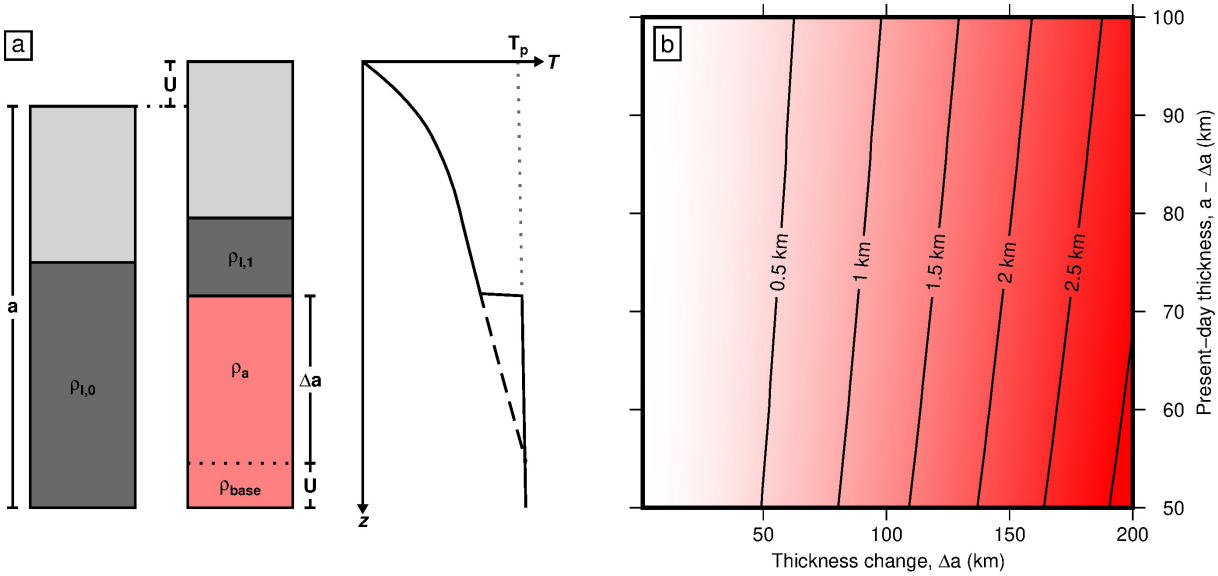

Figure 3.15: Uplift generated by thinning of the lithospheric mantle. (a) Cartoon outlining isostatic balance used to calculate uplift, U, associated with lithospheric thinning, Δa, from an initial lithospheric thickness a. On the temperature profile, black solid line = geotherm following lithospheric thinning, black dashed line = initial steady-state geotherm, grey dotted line = isentropic temperature profile for ambient mantle. Not to scale. (b) Predicted uplift as function of Δa and present-day lithospheric thickness (i.e. $a - \Delta a$).

An alternative way in which the lithospheric mantle could be thinned is thermal erosion due to enhanced small-scale convection. Indeed, a range of laboratory and numerical experiments suggest that significant loss of lithospheric material may occur in this way in the presence of anomalously hot asthenosphere (e.g. Yuen & Fleitout, 1985; Olson *et al.*, 1988). Davies (1994) suggests that this process could generate lithospheric thinning of several tens of kilometres over time scales of $\sim$ 10–20 Myr. Thus, the westward propagation of warm asthenospheric material with associated thermal erosion of the lithospheric mantle could provide a parsimonious explanation for patterns of Neogene-Quaternary uplift and magmatism across Anatolia.

3.4.3 Slab fragmentation

Slab fragmentation, including tearing and/or detachment of the subducting slab, is also often invoked to explain specific features of the topographic and magmatic evolution of Anatolia (e.g. Wilson *et al.*, 1997; Keskin, 2003; Biryol *et al.*, 2011; Schildgen *et al.*, 2014). In this hypothesis, uplift occurs in response to the loss of viscous draw down associated with coupling

between the slab and the over-riding plate. This effect is enhanced by the replacement at shallow depths of dense slab material with upwelling asthenosphere of low density, which can decompress sufficiently to undergo partial melting. Numerical modelling indicates that uplift rates of 0.1 to 0.8 mm yr^{-1} and extension of the overriding plate can occur following detachment of subducting slabs, consistent with regional uplift histories obtained from linear inverse modelling of drainage networks (Duretz *et al.*, 2011; van Hunen & Allen, 2011). Slab fragmentation may therefore be a plausible mechanism for generating Neogene and Quaternary uplift across Anatolia.

Within Western Anatolia, the occurrence of a Miocene transition from calc-alkaline to alkaline magmatism is well established. Recently, several authors have linked this transition to the opening of a 'slab window' within the subducting African lithosphere (Innocenti *et al.*, 2005; Agostini *et al.*, 2007; Klaver *et al.*, 2016). Such a window is purported to have been imaged in several tomographic models (Biryol *et al.*, 2011; Govers & Fichtner, 2016). Geochemical analyses confirm a clear shift from arc to intraplate-style magmatism, culminating at about 10 Ma (Figure 3.6a–3.6e). After this time, basaltic compositions are similar to those derived from an unenriched mantle source. Major element thermobarometric calculations and inverse modelling of REEs suggest low degree decompression melting at approximately ambient mantle temperatures. Both sets of observations are consistent with passive upwelling of sub-slab asthenospheric mantle, possibly in response to slab fragmentation.

Slab tearing and detachment has also been invoked to explain Neogene-Quaternary uplift and magmatism in Central and Eastern Anatolia (Keskin, 2003; Şengör *et al.*, 2003; Keskin, 2007; Biryol *et al.*, 2011; Schildgen *et al.*, 2014; Neill *et al.*, 2015; Lebedev *et al.*, 2016b). These models are supported by observations of a continuous high velocity anomaly at transition-zone depths beneath Anatolia, interpreted as remnant subducted lithosphere (Figure 3.12; e.g. Biryol *et al.*, 2011). Beneath Eastern Anatolia, this high velocity anomaly does not continue to the surface and is thought to represent a completely detached portion of African lithosphere. Keskin (2003) and Keskin (2007) suggested that slab detachment occurred beneath Eastern Anatolia at $\sim$ 10 Ma, on the basis of an observed transition from subduction-related (i.e. calc-alkaline) to intraplate-style magmatism at that time. However, these studies relied on geochemical analyses of large numbers of low-MgO rocks, and there is little evidence for this transition in the database of high-Mg rocks used here. It therefore appears that, if slab detachment occurred beneath Eastern Anatolia, it did so prior to Neogene times, and could have contributed to the onset of plateau uplift at $\sim$ 20 Ma.

High velocity anomalies at transition zone depths beneath Central Anatolia are connected to the Hellenic Trench at the surface by a series of northward dipping high velocity structures thought to represent actively subducting lithosphere (Biryol *et al.*, 2011). Biryol *et al.* (2011) identify a slab 'tear' beneath the southern edge of the Central Anatolian Plateau, the opening of which may be linked to enhanced uplift rates in the region: emergent marine sedimentary rocks and disequilibrated river profiles both attest to regional uplift rates up to 0.7 mm yr^{-1} during the last 7 Ma (Schildgen *et al.*, 2014). Indeed, this enhanced uplift appears to have rapidly propagated from east to west in since $\sim$ 5–10 Ma, consistent with an inferred westward propagation of slab tearing (Biryol *et al.*, 2011; Schildgen *et al.*, 2014). The nearby Central Anatolian Volcanic Province is anomalous since the composition of its basalts suggests that melting is occurring at shallow depths with cool temperatures, unlike the majority of other Anatolian provinces whose mafic igneous rocks appear to sample adiabatic decompression melting paths. These shallow and cool equilibration estimates possibly reflect a combination of conductive cooling and contamination at the base of the lithosphere. Relationships between putative slab tearing and magmatism within the Central Anatolian Volcanic Province are therefore unclear.

3.5 Summary

I have combined geomorphic and geochemical observations to investigate the geodynamic evolution of Anatolia. Analysis of Anatolian drainage networks provides additional insights into the spatial and temporal evolution of regional epeirogeny (Chapter 2). The bulk of Anatolia became emergent in Neogene times when regional uplift initiated in the east and propagated westward. This uplift pattern cannot be explained by the geometry of active deformation alone, by crustal thickness variations, or by flexural processes. Mafic magmatism that occurred over the last $\sim$ 10 Ma is of OIB affinity, requires melting of anomalously hot asthenospheric mantle beneath the high plateaux, and also propagated from east to west.

Slab detachment/fragmentation and lithospheric delamination are often invoked to account for Neogene uplift and magmatism across Anatolia. Regional lithospheric thickness estimates of 60–90 km imply that recent lithospheric thinning has occurred. There is strong evidence to suggest that slab fragmentation occurred in western Anatolia at $\sim$ 10 Ma, but such evidence does not exist for Central or Eastern Anatolia. Neither of these mechanisms can generate elevated asthenospheric temperatures that are observed. In contrast, the arrival and westward

propagation of anomalously hot asthenospheric material can account for observed spatial and temporal patterns of regional uplift and magmatism, particularly if combined with thermal erosion of the lithospheric mantle. Slab tearing may have contributed to enhanced uplift along the southern margin of the Central Anatolian Plateau since $\sim$ 10 Ma, and a constraining bend in the North Anatolian Fault is likely to have generated additional uplift at the plateau's northern margin (Biryol *et al.*, 2011; Yıldırım *et al.*, 2011, 2013; Schildgen *et al.*, 2014).

What is the cause of the elevated asthenospheric temperatures inferred beneath Central and Eastern Anatolia? Recent global studies of oceanic residual depths and their correlation with a range of geophysical and geologic observations suggest that significant thermal anomalies are a common feature of the sub-plate asthenosphere (Hoggard *et al.*, 2016, 2017). Faccenna *et al.* (2013) invoke material upwelling beneath Afar and spreading laterally beneath Arabia and

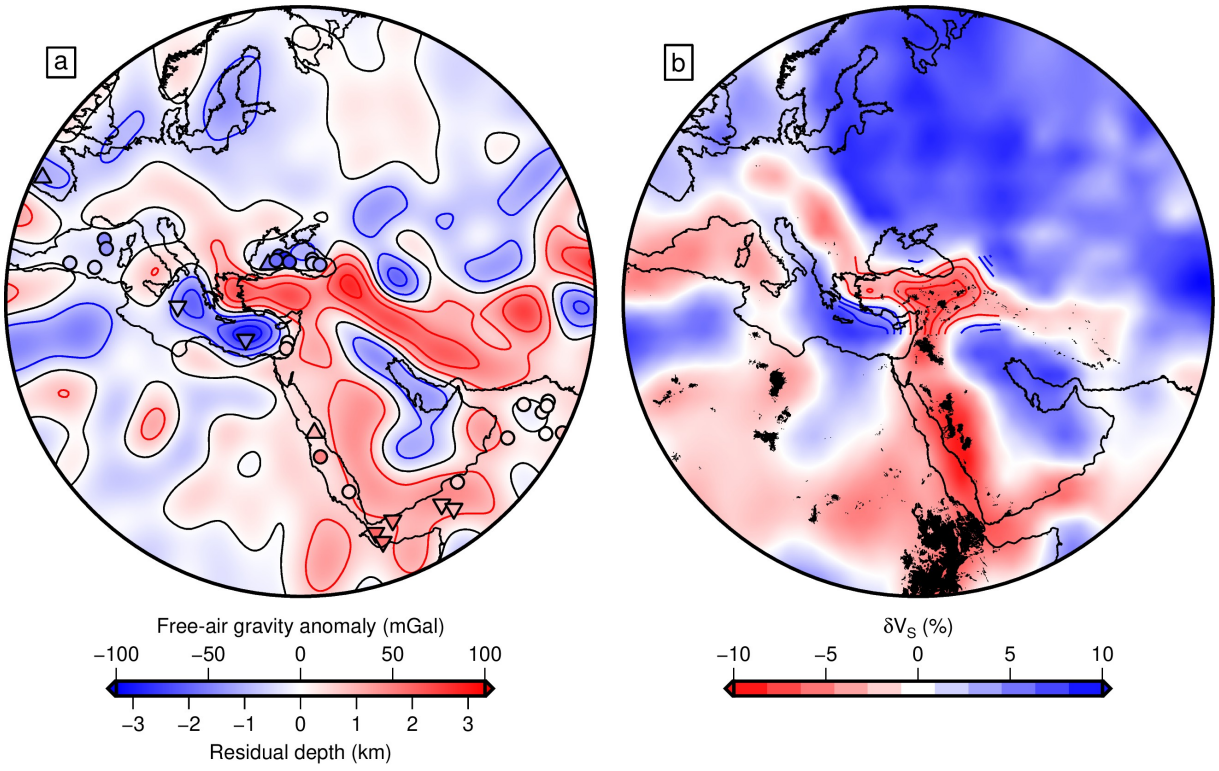

Figure 3.16: Free air gravity and shear-wave velocity of Afar-Arabia-Anatolia region. (a) Long wavelength (i.e. 730 – 13,000 km) free-air gravity anomalies. Red/black/blue contours = positive/zero/negative GGM03C non-hydrostatic low-pass filtered anomalies plotted every 25 mGal (Tapley *et al.*, 2007); residual depth scale assumes Z = 30 mGal km^{-1}; colored circles and upward/downward-pointing triangles = estimates and lower/upper bounds of observed oceanic residual depths (Hoggard *et al.*, 2017). (b) 125 km depth slice through global surface wave tomographic model (Schaeffer & Lebedev, 2013). Black polygons = outcrops of Cenozoic mafic magmatic rocks based on geologic maps published by United States Geological Survey (Pawlewicz *et al.*, 2000; Pollastro *et al.*, 2000; Persits *et al.*, 2002).

Anatolia to explain a range of regional observations. Figure 3.16 shows long wavelength free-air gravity anomalies and upper mantle shear-wave velocity anomalies for the Anatolia-Arabia-Afar region. Positive gravity and slow shear-wave velocity anomalies run continuously from Afar, along the western Arabian margin to Anatolia. These anomalies coincide with high topography and centres of intraplate magmatism onshore, and positive residual depth estimates in the Red Sea (Hoggard *et al.*, 2017). Wilson *et al.* (2014) analyse drainage networks and patterns of mafic magmatism in Arabia, and describe a northward progression of uplift and magmatism throughout Cenozoic times consistent with the movement of asthenospheric thermal anomalies. Lateral displacement of hot plume material from beneath Afar would therefore appear to be a plausible mechanism for generating elevated asthenospheric temperatures beneath Anatolia.

Chapter 4

A Buried Transient Landscape from Carboniferous Times

The Surprise Canyon Formation is a rock unit exposed throughout the Grand Canyon region of Arizona, North America (Figure 4.1). It was deposited during Carboniferous times in isolated channels that are incised into shelfal carbonate rocks of the underlying Redwall Limestone, and it is overlain by mixed marine and terrestrial rocks of the Supai Group (Figure 4.2; Billingsley & Beus, 1984, 1999). Channels are up to 122 m thick and filled with heterogenous deposits including conglomerates, sandstones and limestones (Figures 4.2 and 4.3). At their bases, they contain abundant terrestrial flora (e.g. *Calamites*, *Lepidodendron*, *Stigmaria*) that are absent from underlying marine successions (Billingsley & Beus, 1984; Billingsley *et al.*, 1999). Marine conditions returned during deposition of the upper Surprise Canyon Formation and continued while the overlying Supai Group was deposited. These relationships require a period base-level fall, incision and subsequent resubmergence. Potential mechanisms driving this transient base-level fall have so far not been comprehensively discussed, although tectonic uplift and eustatic sea-level fluctuations have been proposed (Billingsley & Beus, 1984; Martin, 1992; Billingsley & Beus, 1999).

The stratigraphic relationships described above are reminiscent of those recently identified in

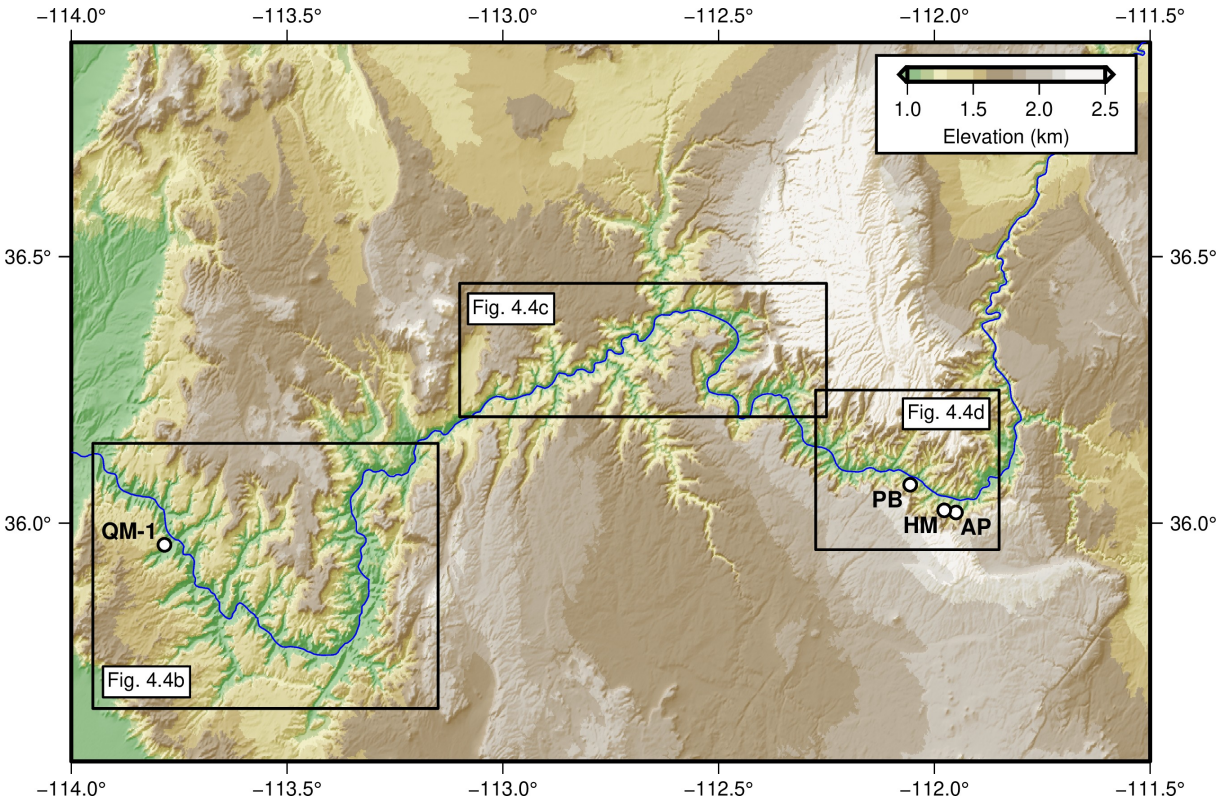

Figure 4.1: Overview of the Grand Canyon region. Shaded relief topographic map of the Grand Canyon region. Boxes refer to areas shown in Figure 4.4b-d. Blue line = Colorado River, white circles = loci of outcrops shown in Figures 4.2 and 4.3. QM-1 = Quartermaster 1, PB = Pattie's Butee, HM = Horseshoe Mesa, AP = Ayer Point.

the Faroe-Shetland Basin and the North Sea using three-dimensional seismic surveys (Rudge *et al.*, 2008; Shaw Champion *et al.*, 2008; Hartley *et al.*, 2011; Stucky de Quay *et al.*, 2017). For example, in the Faroe-Shetland Basin, channels incised into the marine Lamba Formation are infilled by continental deposits of the Flett and Balder Formations, which contain lignite (Shaw Champion *et al.*, 2008; Hartley *et al.*, 2011). Subsequently, marine deposition resumed, represented by the Stronsay Group. Careful mapping of these Paleogene unconformities revealed detailed fluvial landscapes with amplitudes of up to 800 m. They are also associated with perturbations to regional patterns of tectonic subsidence. Their formation in Paleocene times is attributed to transient variations in convective support associated with the Icelandic plume (Hartley *et al.*, 2011). Similarities between these ancient landscapes and that recorded by the Surprise Canyon Formation suggest that the latter may also have a convective origin.

Here, I investigate possible causes and consequences of transient base-level fall associated with the Surprise Canyon Formation using a variety of approaches. First, I review published stratigraphic and chronologic information relating to the Surprise Canyon Formation, the underlying

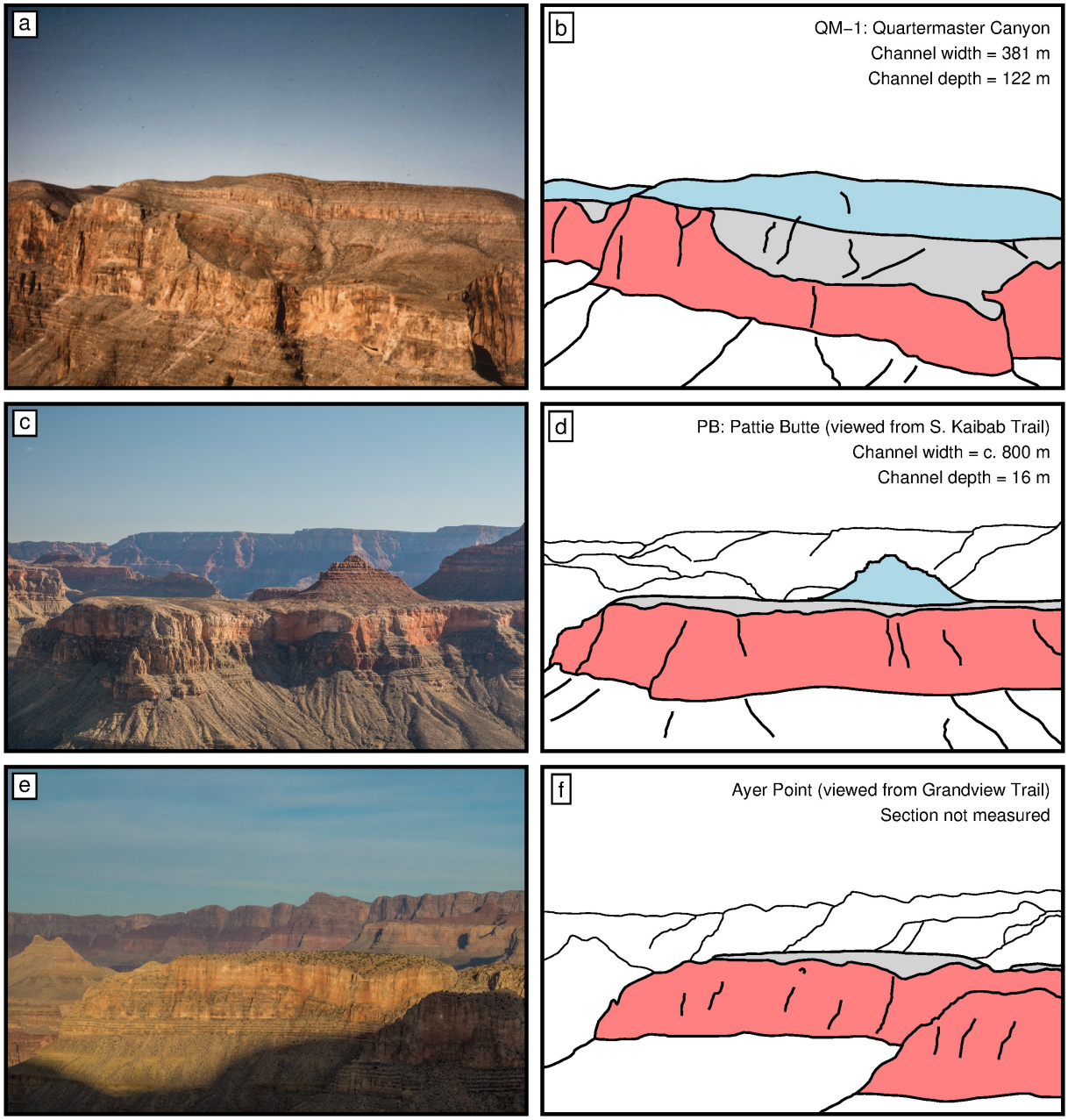

Figure 4.2: Examples of Surprise Canyon Formation paleovalleys. (a) Photograph of Surprise Canyon Formation outcrop QM-1 at Quartermaster Canyon. Image from Grover (1989). (b) Interpretation of (a). Red polygons = Redwall Limestone, grey polygons = Surprise Canyon Formation, blue polygons = Supai Group. Outcrop data from Billingsley & Beus (1999). (c, d) As (a, b) for outcrop PB at Patties Butte. (e, f) As (a, b) for unmeasured outcrop at Ayer Point.

Redwall Limestone and the overlying Supai Group. Next, I explore possible pertubations to tectonic subsidence patterns by compiling a regional database of water-loaded subsidence curves and comparing them to the predictions of flexural and thermal models. Finally, I critically discuss a range of possible causal mechanisms.

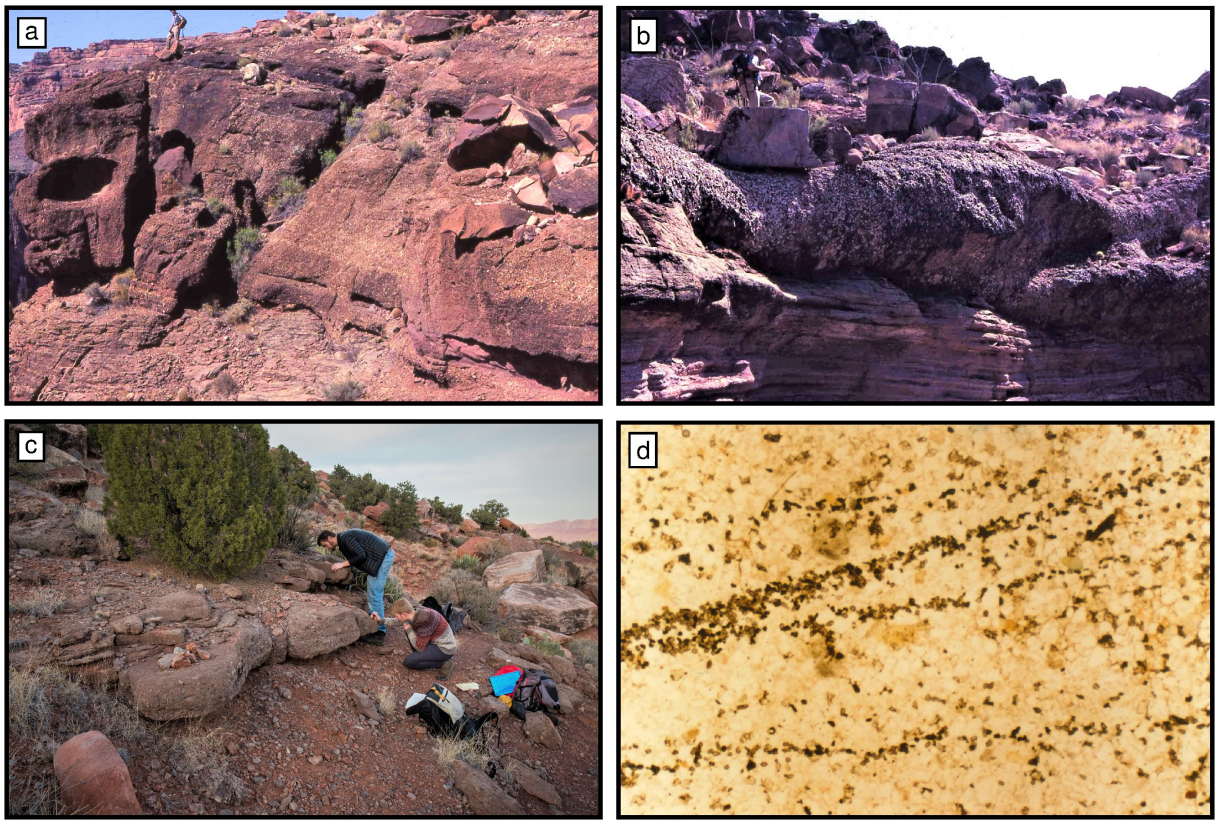

Figure 4.3: Examples of Surprise Canyon Formation outcrops. (a) and (b) Photographs of Surprise Canyon Formation outcrops courtesy of L. Middleton. Note thick packages of poorly sorted conglomeratic material with erosive bases. (c) Photograph of Surprise Canyon Formation outcrop at Horsehoe Mesa. (d) Thin section of Surprise Canyon Formation sandstone from Quatermaster Canyon with heavy mineral assemblage. Image from Grover (1989).

4.1 Stratigraphic relationships

The spectactular stratigraphic record exposed in the Grand Canyon is summarized in Figure 4.4a. The record begins with the Unkar and Chuar Groups, deposited during the Proterozoic Eon, which are separated from overlying rocks by a prominent angular unconformity. Relatively flat-lying Paleozoic rocks comprise most of the remaining section. My discussion will focus on Carboniferous times, represented by the Redwall Limestone, Surprise Canyon Formation and Supai Group. However, it is worth noting that the Devonian Temple Butte Formation, deposited in isolated channels incised into the Cambrian Muav Limestone, shares many of the characteristics of the Surprise Canyon Formation and may also represent a period of transient base-level fall.

The presence of significant erosional relief at the top of the marine Redwall Limestone has been recognised for some time (e.g. Noble, 1922; McKee, 1963; McKee & Gutschick, 1969).. Related

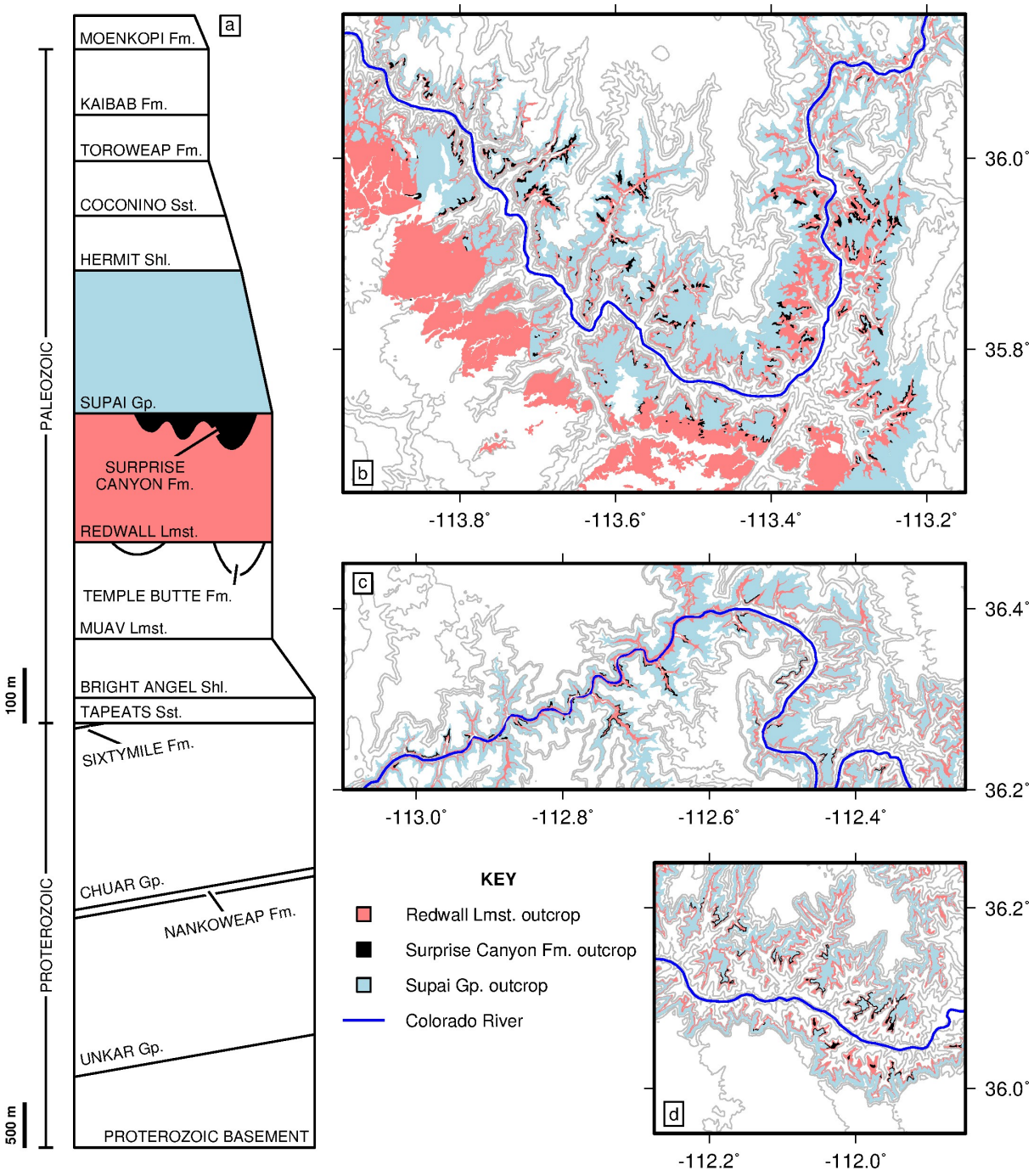

Figure 4.4: Stratigraphy of the Grand Canyon region. (a) Stratigraphic column for the Grand Canyon, after Hintze (1988). Note seperate scales for Proterozoic and Paleozoic rocks. (b), (c) and (d) Simplified geological maps of areas specified in Figure 4.1. Red polygons = outcrops of Redwall Limestone, black polygons = outcrops of Surprise Canyon Formation, blue polygons = outcrops of Supai Group, black dotted lines = inferred Surprise Canyon paleovalleys from Grover (1989) and Billingsley (1999), blue lines = Colorado River. Outcrop data based on Billingsley (2000), Billingsley & Wellmeyer (2003) and Billingsley *et al.* (2006a,b, 2007, 2012), courtesy of R. Clark (`http://rclark.github.io/grand-canyon-geology/`).

channel fill deposits were later described by Billingsley & McKee (1982) and Billingsley & Beus (1984), the latter defining the Surprise Canyon Formation as a distinct and mappable rock unit. Subsequently, a series of contributions, summarised by Billingsley & Beus (1999), addressed sedimentologic, paleontologic and stratigraphic features of the Formation (e.g. Shirley, 1989; Grover, 1989; Martin, 1992). In the following sections, I summarise key observations for the Surprise Canyon Formation and surrounding rock units.

4.1.1 Redwall Limestone

The Redwall Limestone is divided into the Whitmore Wash, Thunder Springs, Mooney Falls and Horeshoe Mesa Members (McKee, 1963; McKee & Gutschick, 1969). The dominant lithologies are limestone and dolostone, with locally abundant chert. Each Member contains a diverse and definitively marine faunal assemblage, including foraminifera, corals, bryzoa, cephalapods, crinoids and rare trilobites (McKee & Gutschick, 1969; Bezinski, 2017). Several facies are identified including bioclastic, pelletal and oolitic limestones. Based on facies variations and disconformities between each member, a series of transgressions and regressions has been identified (McKee & Gutschick, 1969). Kent & Rawson (1980) also propose a general shift from earlier open marine to later intratidal conditions.

4.1.2 Surprise Canyon Formation

The Surprise Canyon Formation itself is generally divided into three informal units: a lower conglomerate and sandstone, a middle limestone, and an upper siltstone unit (Billingsley & McKee, 1982). Detailed descriptions of outcrops measured by geologists from Northern Arizona University during field campaigns between 1976 and 1990 are given by Grover (1989) and Billingsley *et al.* (1999).

The lower unit is dominated by pebble to boulder conglomerate and sandstones (Figure 4.3a and 4.3b; Grover, 1989; Billingsley *et al.*, 1999). Conglomerate clasts are predominantly composed of chert and limestone derived from the upper members of the Redwall Limestone. Sands are generally composed of mature quartz arenite. Conglomerates are channelised or massive, and sandstones display a range of sedimentary structures and bedforms including channelisation, cross stratification and rippling. Paleo-current estimates suggest that westward (i.e. downhill)

flow was dominant (Grover, 1989). The sandstone facies also frequently contains lignite, palynomorphs (e.g. spores and pollen grains), carbonaceous plant and wood fragments (e.g. ferns), and *Lepidodendron* impressions (Billingsley & McKee, 1982; Billingsley & Beus, 1984; Grover, 1989; Billingsley *et al.*, 1999). This evidence strongly suggests that the lower unit was deposited in a terrestrial fluvial environment.

The middle unit is generally represented by a cliff-forming limestone. It is seperated from the lower unit by an erosional unconformity and contains marine fauna such as foraminifera, corals, cephalopods and echinoderms (Billingsley & McKee, 1982; Billingsley & Beus, 1984; Grover, 1989; Billingsley *et al.*, 1999). Where present, trough cross stratification records bimodal paleocurrent directions, dominanted by eastward flow (i.e. upstream). The middle unit is thickest in the western Grand Canyon, thinning and eventually pinching out towards the east (Billingsley *et al.*, 1999). The upper unit is largely composed of siltstones, which are commonly ripple laminated and occasionally contain mudcracks. Contact with the middle unit is gradational. Plant debris and *Lepidodendron* impressions are found (Grover, 1989; Billingsley *et al.*, 1999).

Careful stratigraphic correlation between Surprise Canyon Formation outcrops and consideration of a paleo-flow direction estimates allowed the reconstruction of a westward draining 'paleovalley' system (Grover, 1989; Billingsley, 1999). This ancient drainage network is shown in Figure 4.5a, along with measured channel thicknesses and widths (Figure 4.5b; Billingsley, 1999). Channel thicknesses are largest in the west (i.e. downstream) and decrease towards the east (i.e. upstream). Channel widths are up to $\sim$ 400 m in the west and initially decrease eastward. However, the largest channel widths are found in the eastern Grand Canyon (up to 800 m). These patterns are consistent with the headward propagation of a wave of incision into an exposed platform, in which downstream valleys are broad and deep. At the wave front, rapid incision results in narrow channels which quickly shallow upstream onto the platform. Upstream of this wave of incision, on the preserved platform, valleys are shallow and diffuse.

Although outcrops of the Surprise Canyon Formation are heterogeneous and largely variable, these general descriptions apply to the majority of paleovalley systems identified by Grover (1989) and Billingsley (1999). An important exception is a series of outcrops around Quartermaster Canyon and Burnt Canyon in the western Grand Canyon region. In contrast to mature quartz-arenite sandstones exposed elsewhere, channels in this area contain a heavy mineral suite comprising olivines, pyroxenes (including pristine augite crystals) and hornblendes (Figure 4.3d; Grover, 1989, pp. 170–173). Such an assemblage is not identified in the Redwall Limestone, or

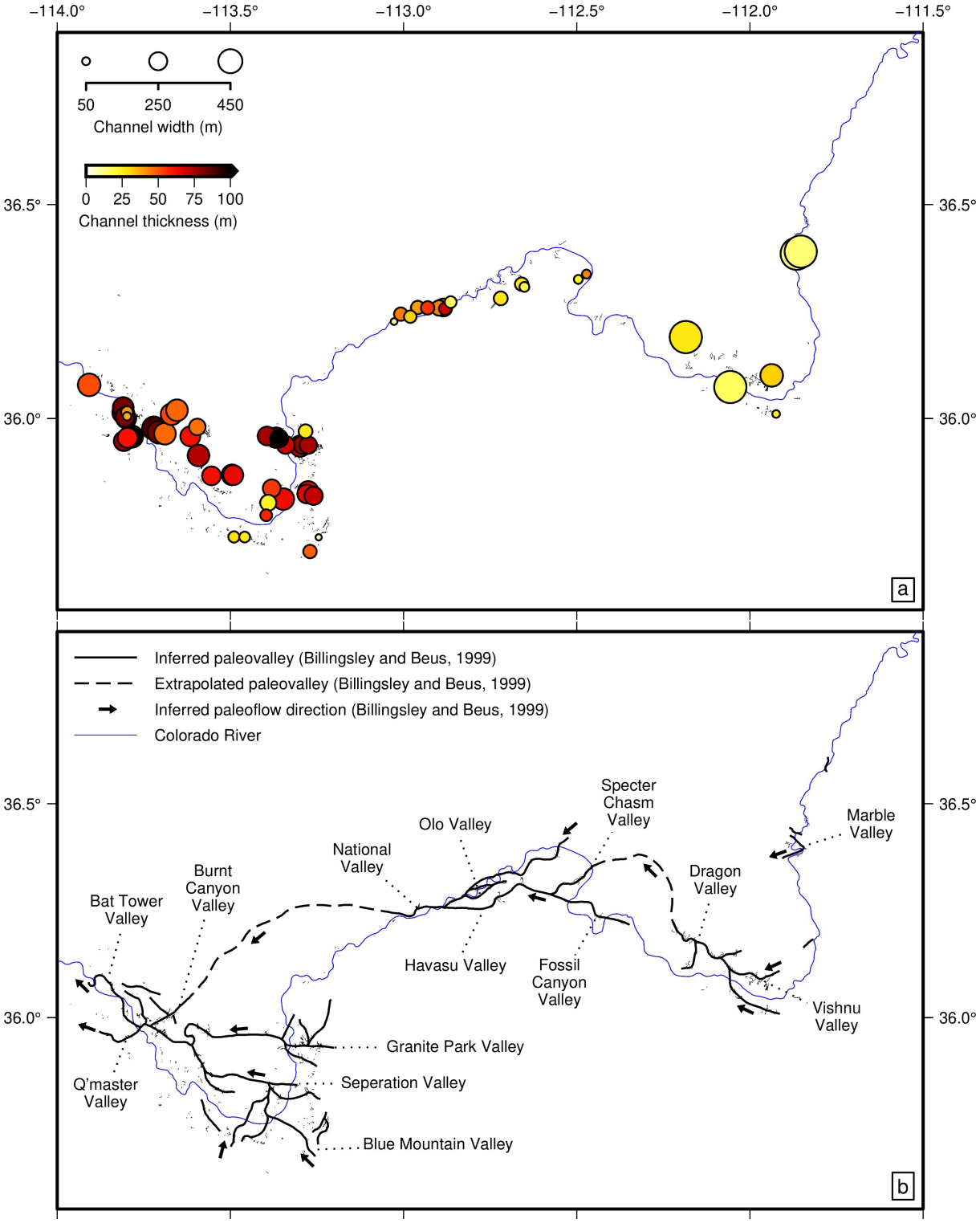

Figure 4.5: Outcrops and paleovalleys of the Surprise Canyon Formation. (a) Measured outcrops of Surprise Canyon Formation (Billingsley, 1999). Shading reflects channel thickness, size reflects channel width. (b) Surprise Canyon Formation paleovalleys (Grover, 1989; Billingsley, 1999). Black solid and dashed lines = inferred and extrapolated paleovalleys, black arrows = inferred paleoflow direction, blue line = Colorado River.

any other Surprise Canyon Formation channel. This absence, along with the crystals' pristine nature (despite a tendency to rapidly break down under weathering), introduces the intriguing possibility that local mafic volcanism occurred during or immediately prior to deposition of the Surprise Canyon Formation.

4.1.3 Supai Group

The Supai Group is generally subdivided into the Watahomigi, Manakacha and Wescogame Formations and Esplanade Sandstone (McKee, 1975, 1982). The Watahomigi Formation consists of interbedded mudstones, siltsones, conglomerates and limestones. Limestones contain an abundant marine faunal assemblage, including foraminifera, bryzoa and crinoids. In contrast, mudstones and siltstones contain plant debris and desiccation cracks consistent with a terrestrial depositional environment. Similar lithologies are found in the higher formations, along with increasingly predominant cross-bedded sandstones and some evaporitic bodies. Each formation is bounded by channelised erosional unconformities with local relief of up to 30 m, overlain by basal gravels and conglomerates. The Supai Group is thought to represent a coastal environment in which marine and terrestrial conditions interchanged in response to a series of transgressions and regressions (McKee, 1982).

In contrast to the Redwall Limestone, which, in the Grand Canyon region, gradually thickens northwestwards, the lower formations of the Supai Group appear to have infilled a bathymetric low known as the 'Watahomigi Embayment' (Figure 4.6; McKee & Gutschick, 1969; Peirce, 1981; McKee, 1982; Martin, 1992, pp. 79–86). This embayment is expressed as a tongue of thickened marine sediments of the Watahomigi Formation which extends in a southwest-northeast orientation across the region, with amplitudes of ~ 50 m. Its geometry closely matches the distribution of Surprise Canyon Formation outcrops. It is directly underlain by Surprise Canyon channels which contain marine limestone, while Surprise Canyon channels containing exclusively terrestrial material lie beneath its margins (Martin, 1992). These observations are consistent with the existence of additional longer-wavelength erosional relief of at least 50 m at the top of the Redwall Limestone that is not captured by infilled channels of the Surprise Canyon Formation. Rather, this relief persisted into Supai times as a bathymetric low.

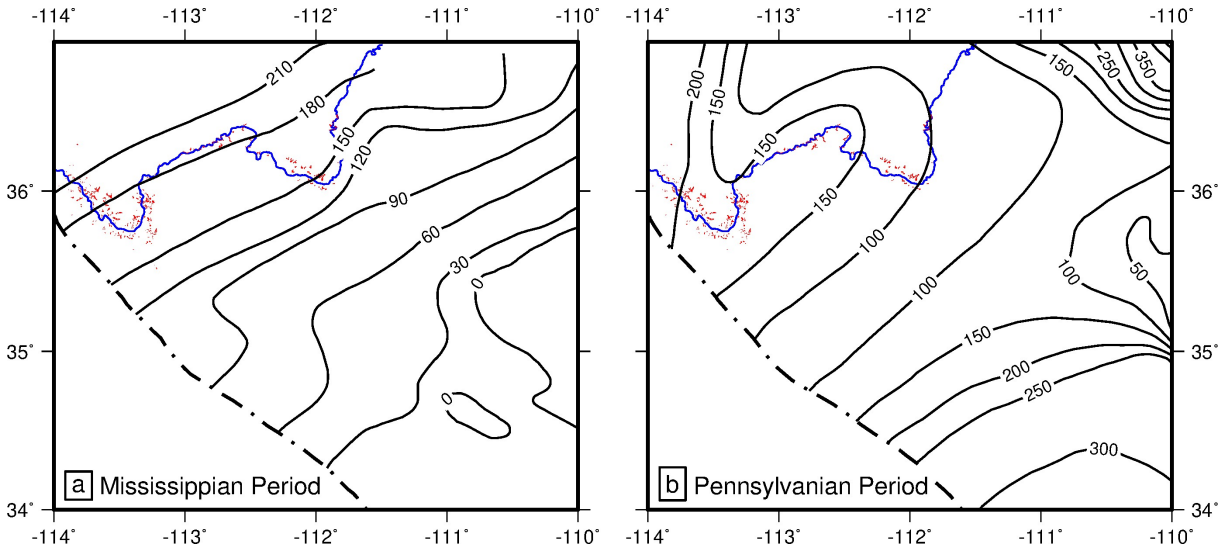

Figure 4.6: Carboniferous sediment thickness distributions. Sediment thickness contours from Peirce (1981). Black lines = sediment thickness contours in metres, blue line = Colorado River, red polygons = Surprise Canyon Formation outcrops. No Carboniferous stratigraphy is preserved in blank region in bottom left-hand corner. (a) Mississippian period (i.e. lower Carboniferous). Contours every 30 m. (b) Pennsylvanian period (i.e. upper Carboniferous) isopach map of Grand Canyon region. Contours every 50 m. Note prominent tongue of thickened sediment corresponding to region of transient landscape development, known as the 'Watahomigi Embayment' (Martin, 1992).

4.1.4 Magnitude of base-level fall

There is therefore clear stratigraphic evidence that the Surprise Canyon Formation records a period of transient base-level fall, emergence and incision of the Redwall Limestone, and subsequent resubmergence. A key question is the magnitude of base-level fall required to explain these stratigraphic observations. A minimum estimate is given by the maximum depth of erosional channels, which is 122 m (Billingsley & Beus, 1999). If the Watahomigi Embayment is taken to reflect further erosional relief at the top of the Redwall Limestone, an additional $\sim$ 50 m of base-level fall is required. However, several important lines of evidence suggest the true value must be somewhat larger than these minimum bounds.

Since sediments of the Redwall Limestone, Surprise Canyon Formation and Supai Group have been buried to significant depths, they will have undergone some degree of compaction. Sediment porosity, ϕ, as a function of burial depth, z, is usually parameterised by

$$\phi(z) = \phi_\circ \exp\left(\frac{-z}{\lambda}\right), \tag{4.1}$$

where $\phi_\circ$ is an initial porosity and λ is a compaction decay length (Sclater & Christie, 1980).

Since the solid (i.e. incompressible) mass of any layer must be conserved,

$$\int_{z_1}^{z_2} (1 - \phi(z))\, dz = \int_{0}^{z_3} (1 - \phi(z))\, dz, \tag{4.2}$$

where z_1 and z_2 are depths of the top and bottom of a compacted layer, respectively, and z_3 is the base of the corresponding uncompacted layer (Figures 4.7a and 4.7b). Substituting Equation (4.1) for $\phi(z)$, integrating and rearranging gives

$$z_3 = z_2 - z_1 + \phi_\circ \lambda \left(\exp\left(\frac{-z_2}{\lambda}\right) - \exp\left(\frac{-z_1}{\lambda}\right) - \exp\left(\frac{-z_3}{\lambda}\right) + 1 \right). \tag{4.3}$$

Since z_3 appears on both sides of Equation (4.3), this equation must be solved by iteration. In this case a Newton-Raphson scheme was employed. As such, original depositional thicknesses of sedimentary units can be estimated.

Sediments of the upper Redwall Limestone, Surprise Canyon Formation and Supai Group are strongly heterogeneous and contain a mixture of limestone, sandstone and shale. Porosity as a function of depth for these lithologies is shown in Figure 4.7c, calculated using Equation (4.1) and values of $\phi_\circ$ and λ from Sclater & Christie (1980). These values can also be used along with Equation (4.3) to calculate original depositional thickness, z_3, as a function of maximum burial depth, z_2, as shown in Figure 4.7d for an observed thickness of 122 m. At present, Surprise Canyon paleovalleys lie beneath 0.4–1.3 km of younger Paleozoic sediments (e.g. Hintze, 1988; Beus & Morales, 2003). Based on apatite fission track thermochronology, Dumitru *et al.* (1994) estimated that $\sim$ 2.7–4.5 km of Mesozoic strata were deposited over the Grand Canyon region and subsequently removed, consistent with thicknesses of $\sim$2.5–3.5 km preserved in nearby southern Utah. These values suggest that Surprise Canyon paleovalleys were buried to depths of $\sim$ 3.1–5.8 km, which corresponds to original depositional thicknesses of $\sim$ 190–270 m for Surprise Canyon Formation outcrops (grey region in Figure 4.7d). If the Watahomigi Embayment is taken to reflect additional erosional relief at the top of the Redwall Limestone, the total base-level fall required increases to $\sim$ 260–370 m. A reasonable minimum bound on the amount of base-level fall required to explain the stratigraphic relationships described here is therefore $\sim 280 \pm 90$ m.

These values still probably reflect minimum bounds on base-level fall that occurred during incision of the Redwall Limestone for two reasons. First, shelfal carbonate rocks of the Redwall Limestone were deposited in shallow marine conditions, probably within the euphotic zone (i.e.

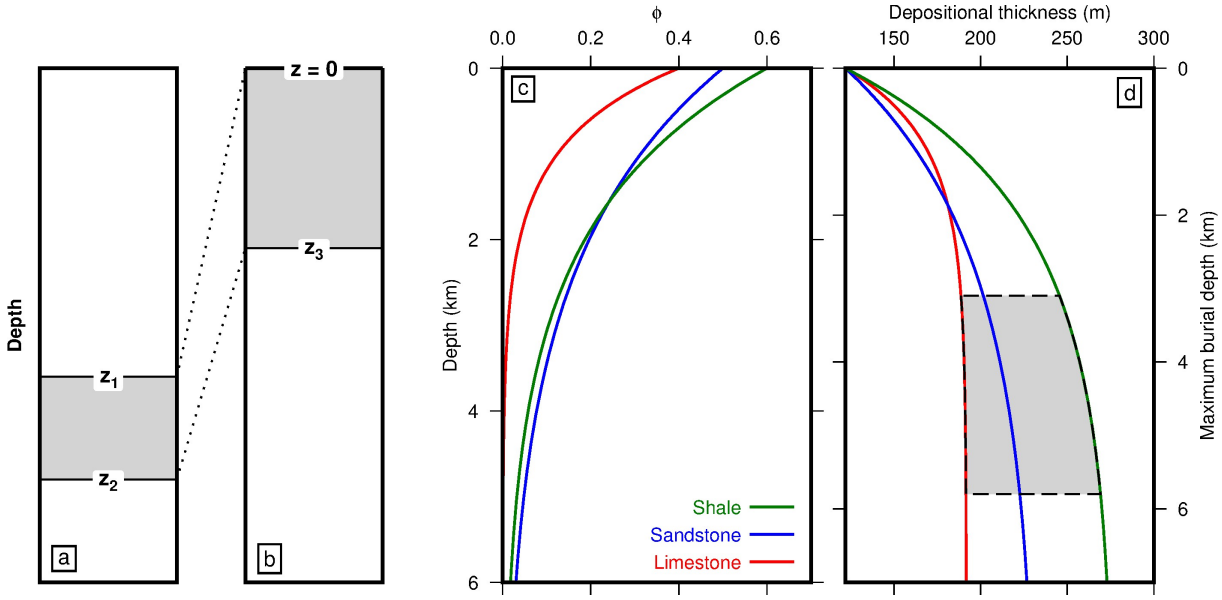

Figure 4.7: Decompacting Surprise Canyon paleovalleys. (a) and (b) Cartoons outlining decompaction procedure. A compacted layer at depth z_1 to z_2 is corrected to its original depositional thickness, z_3. (c) Porosity, ϕ, as a function of depth for relevent lithologies. (d) Original depositional thickness as a function of maximum burial depth for a compacted layer of thickness 122 m. Grey box highlights parameter space relevent to Surprise Canyon paleovalleys.

up to $\sim$ 100 m water depth; McKee & Gutschick, 1969; Kent & Rawson, 1980). Several tens of metres of base-level fall must therefore have occurred prior to any sub-aerial incision in order to overcome this initial water depth. Secondly, contact between the Surprise Canyon Formation and the overlying Supai Group is disconformable (McKee, 1982). This relationship implies that a period of erosion seperated deposition of these units, and that amplitudes of preserved channels were reduced by an unknown amount. Further erosional unconformities exist in sediments of the Supai Group which infilled the Watahomigi Embayment. These arguments suggest that significantly more than 280 $\pm$ 90 m base level fall is required to explain the stratigraphic record associated with Surprise Canyon paleovalleys.

4.2 Chronology and regional setting

In this section, I re-evaluate age estimates of Carboniferous rocks from the Grand Canyon region. The calibrated Carboniferous time scale and biozones of Davydov *et al.* (2012) was used as a framework, with additional information relating to foraminiferal, ammonoid and conodont biostratigraphy from Mamet & Skipp (1970), Ramsbottom & Saunders (1985), Ross & Ross (1988), Lane & Brenckle (2005) and Korn (2006). Alongside age estimates I discuss regional strati-

Table 4.1: Carboniferous biostratigraphy of the Grand Canyon.

Formation	Reported fauna	Zone[a]	Stage	Age (Ma)
Redwall Limestone	**Base**		Tournaisian –	353 –
	Conodonts[b]:	Mc7		
	Polygnathus communis communis, *Pseudopolygnathis multistratus*, *P. oxypageus*, *P. nudus*.			
	Foraminifera[c]:	Mf6		
	Septaglomospiranella primaeva, *Tuberendothyra tuberculata*.			
	Top		– Visean	– 337
	Foraminifera[c]:	Mf11		
	Endothyra scitula, *E. pauciseptata*.			
Surprise Canyon	Conodonts[d,e,f]:		Serpukhovian	327 – 325
	Adetognathus unicornis, *A. spathus*, *A. lautus*, *A. gigantus*, *Cavusgnathus naviculus*, *C. unicornis*, *Gnathodus billineatus*, *Rachistognathus muricatus*, *R. primus*.	Mc16		
	Foraminifera[e,g,h]:			
	Eosigmolina explicata, *E. rugosa*, *E. robertsoni* or *Brencklеina rugosa*.	Mf18		
Watahomigi (Supai Group)	**Base**		Bashkirian	323 –
	Conodonts[e,i]:	Mc17		
	Adetognathus lautus, *A. spathus*, *Rachistognathus muricatus*, *R. websteri*, *R. proxilus*.			
	Foraminifera[i]:			
	Asteroarchaediscus sp.			
			– Moscovian?[j]	– ∼ 310

[a]Davydov *et al.* (2012), global correlation of the Carboniferous time scale and biozones; [b]Ritter (1991), conodont biostratigraphy of the Redwall Limestone at Iceberg Ridge; [c]Skipp (1969), foraminifera of the Redwall Limestone; [d]Grover (1989), conodonts of the Surprise Canyon Formation; [e]Martin (1992), biostratigraphy of Surprise Canyon Formation and Watahomigi Formation outcrops throughout the Grand Canyon; [f]Martin & Barrick (1999), summary of conodont biostratigraphy for the Surprise Canyon Formation; [g]Billingsley & McKee (1982); [h]Beus & Martin (1999), summary of age estimates and correlations for the Surprise Canyon Formation; [i]McKee (1982), summary of fossil content and age estimates for the Supai Group; [j]Limited biostratigraphic information is available for the upper Watahomigi Formation, McKee (1982) estimates an Atokan (i.e. Bashkhirian–Moscovian) age on the basis of brachiopod fauna.

graphic correlations and paleogeographic interpretations. Relevant conodont and foraminiferal species reported for Carboniferous rocks in the Grand Canyon are summarised in Table 4.1, along with subsequently assigned zones and ages, and shown graphically in Figure 4.8. Regional paleogeographic reconstructions, based on the maps of Poole & Sandberg (1977), Sando (1985), Sando *et al.* (1990) and Leary *et al.* (2017), are shown in Figure 4.9.

4.2.1 Redwall Limestone

Foraminifera and conodonts of the Redwall Limestone are consistent with a middle Tournaisian to middle Visean age (i.e. ∼ 355–337 Ma; Table 4.1, Figure 4.8; Skipp, 1969; Ritter, 1991). Shelf-carbonate deposition is also recorded at the well-known Arrow Canyon section in southern Nevada, west of the Grand Canyon region (Figures 4.8 and 4.9a). Sediments of the Monte Cristo Group, including the Anchor Limestone, Bullion, Yellowpine and lower Battleship Wash

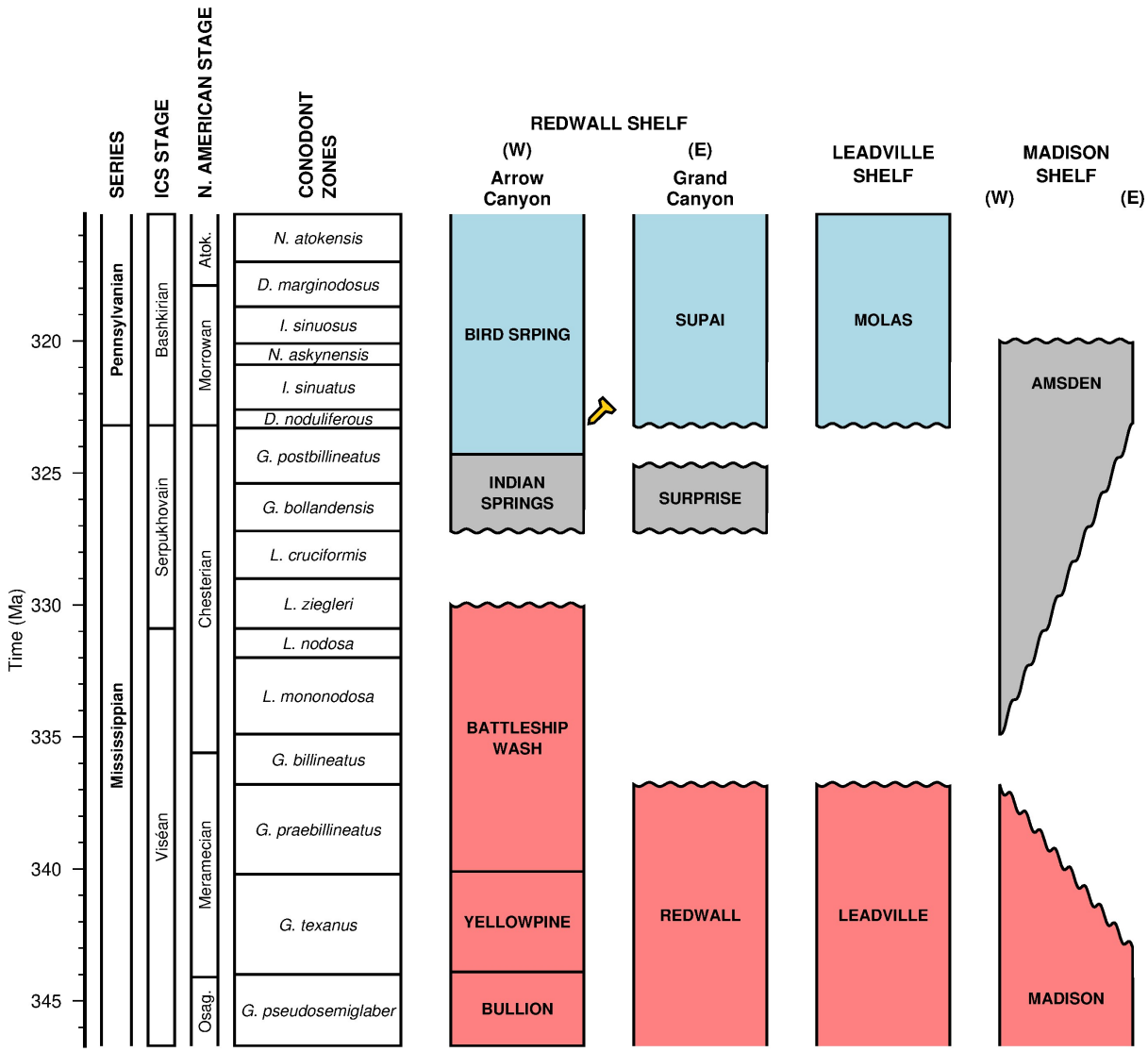

Figure 4.8: Mid-Carboniferous chronology of the Grand Canyon and surrounding regions. See Table 4.1 for details. Golden pin = Global Boundary Stratotype Point (Lane *et al.*, 1999). See Figure 4.9 for locations. Red polygons = units approximately correlating with the Redwall Limestone; grey polygons = units approximately correlating with the Surprise Canyon Formation; blue polygons = units approximately correlating with the Supai Group.

Formations, were deposited contemporaneously with the Redwall Limestone. Deposition is thought to have occurred in slightly deeper waters than rocks of the Redwall Limestone, beneath the photic zone, reflecting Arrow Canyon's more distal position (Bishop *et al.*, 2009). During this period, shelf-carbonate deposition is also recorded by the Madison Limestone of Wyoming, Idaho and Montana, and the Leadville Limestone of Utah and Colorado (Figure 4.9a; e.g. Rose, 1976; Poole & Sandberg, 1977; Gutschick & Sandberg, 1983). Together, these limestones represent an extensive shelf-carbonate system which developed in shallow seas along a passive margin running approximately north-south through western North America. East of this platform, deposition

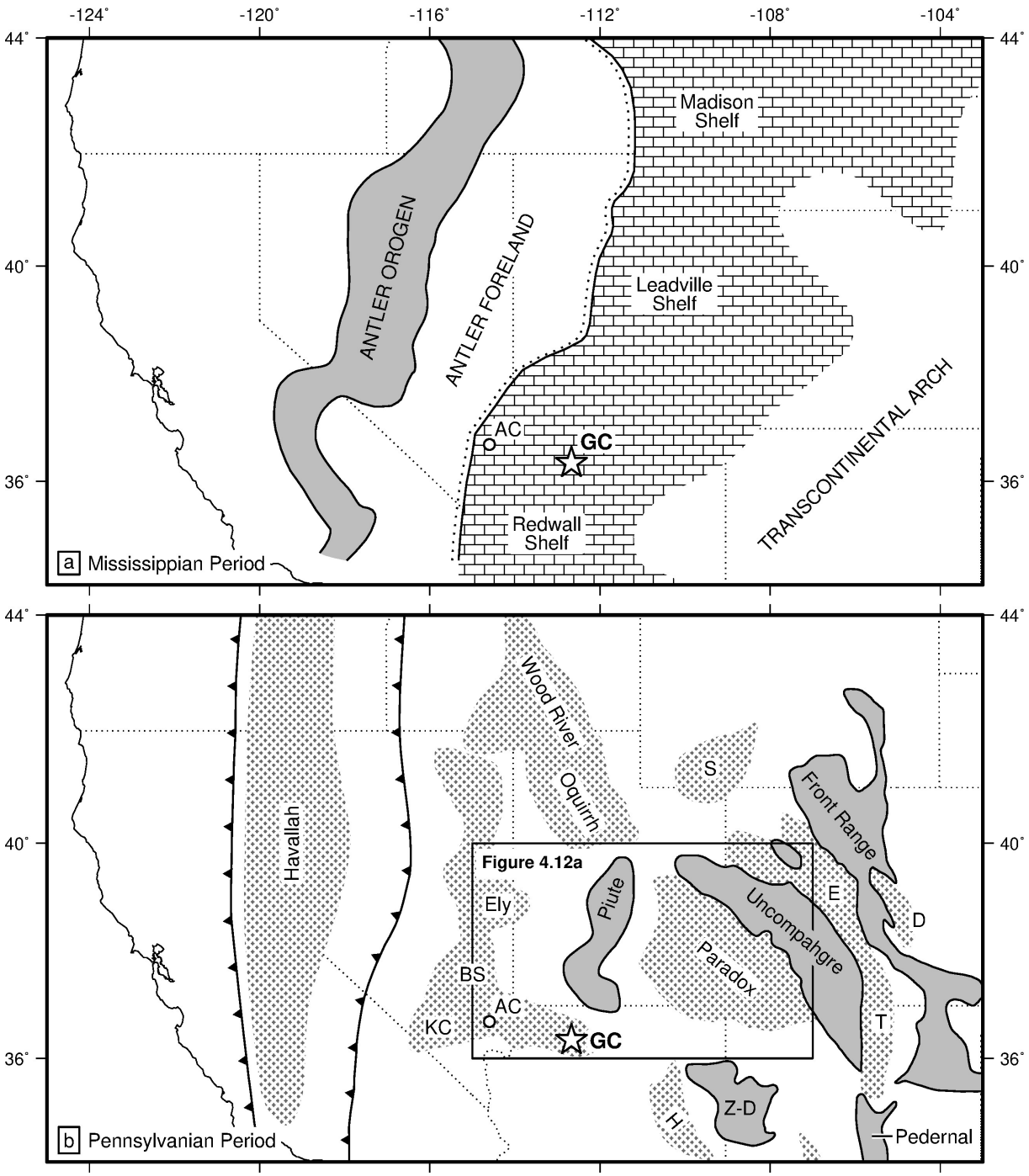

Figure 4.9: Carboniferous paleogeography of western North America. Note that all locations are approximate and based on present-day outcrops which have been affected by Mesozoic and Cenozoic deformation. (a) Paleogeographic reconstruction of western North America for lower Carboniferous (i.e. Mississippian) times, after Poole & Sandberg (1977), Sando (1985) and Sando *et al.* (1990). Bricked region = carbonate deposition on cratonic platform, AC = Arrow Canyon, GC = Grand Canyon. (b) Paleogeographic reconstruction of western North America for upper Carboniferous (i.e. Pennsylvanian) times, after Leary *et al.* (2017). Solid grey regions = Ancestral Rocky Mountains uplifts, Z-D = Zuni-Defiance; stippled grey regions = basins, BS = Bird Spring, D = Denver, E = Eagle, H = Holbrook, KC = Keeler Canyon, S = Sweetwater Trough = Taos Trough.

ceased along a southwest-northeast trending topographic high known as the 'Transcontinental Arch' (Figure 4.9a).

West of this carbonate platform, water depths increased rapidly into the Antler Trough, a series foreland basins that developed in response to loading by highlands of the Antler orogeny further west (Figure 4.9a; e.g. Poole & Sandberg, 1977; Miller *et al.*, 1992). The Antler orogeny is thought to have been the result of a complex arc-continent collision that occurred during closure of the Rheic ocean and the assembly of Pangaea (e.g. Nilsen & Stewart, 1980; Miller *et al.*, 1992; Colpron & Nelson, 2009; Lawton *et al.*, 2017).

The tops of the Leadville and Madison Limestones are marked by prominent karst surfaces, developed during late Visean times, which approximately correlate with that observed in the Grand Canyon region at the top of the Redwall Limestone (e.g. Sando, 1988; De Voto, 1988; Meyers, 1988). On the Madison Shelf, karst features include enlarged joints, sinkholes and caves (Sando, 1974, 1988; Palmer & Palmer, 1995). Maximum relief is up to 60 m, and a westward flowing fluvial network has been identified. Age estimates for the uppermost Madison Limestones are youngest at the western shelf edge, and increase inland to the east, reflecting longer exposure and deeper incision of more proximal deposits (Figure 4.8; Sando, 1974, 1988). Similar features are described for the Leadville Shelf, where erosional relief of up to 200 m is reported (Maslyn, 1977; De Voto, 1988).

At the more distal Arrow Canyon section, carbonate deposition continued until early Serpukhovian times, represented by the Battleship Wash Formation. Bishop *et al.* (2009) suggest that water depths shallowed throughout this period, culminating in a depositional hiatus and phase of paleosol development. Saltzman (2003) and Dyer *et al.* (2015) identify a coincident progressive negative perturbation to regional sea-water $\delta^{13}C$, which they link to weathering of exposed proximal carbonate platforms.

4.2.2 Surprise Canyon Formation

The Surprise Canyon Formation contains conodonts, such as *Adeotognathus unicornis*, restricted to the middle Serpukhovian stage (Table 4.1, Figure 4.8; Martin, 1992; Martin & Barrick, 1999). This age, which is consistent with the floral assemblage described by Tidwell *et al.* (1992) and brachiopods identified by Beus (1999) and Beus & Martin (1999), implies a < 10 Myr period of landscape development between deposition the Redwall Limestone and that of the Surprise

Canyon Formation. The Surprise Canyon Formation was then deposited over a period of up to ~ 3 Myr. This period overlaps with deposition of the Indian Springs Formation at Arrow Canyon in Middle to Late Serpukhovian times. The Indian Springs Formation consists of limestones and shales, containing several paleosol layers that represent periods of sub-aerial exposure and weathering (Bishop *et al.*, 2009).

No sediments of Serpukhovian age have been identified above the Leadville Limestone, but deposition of the Amsden Formation, overlying the Madison Limestone, does appear to be overlap with that of the Surprise Canyon Formation (Sando *et al.*, 1975). The lowermost Amsden Formation, the Darwin Sandstone Member, consists of conglomerates and sandstones and is thought to have been deposited in a fluviatile to coastal environment. Mirroring distributions of the Madison Limestone, the Amsden Formation thins and youngs from west to east, consistent with progressive eastward marine transgression (Figure 4.8; Sando *et al.*, 1975; Sando, 1988). It is worth noting that deposition of the lowermost supra-karst Amsden Formation in Late Visean times appears to overlap with deposition of the sub-karst Battleship Wash Formation at Arrow Canyon. These relationships imply that transient base-level fall affected the more northern Madison shelf slightly earlier than the Redwall shelf in the Grand Canyon region (Figure 4.8).

4.2.3 Supai Group

The basal Supai Group (Watahomigi Formation) contains a conodont assemblage consistent with a latest Serpukhovian or earliest Bashkirian age, a few metres above which the diagnostic earliest Bashkirian *Declinognathodus noduliferous* is reported (Table 4.1, Figure 4.8; McKee, 1982; Martin, 1992). This age implies that a hiatus of up to ~ 2 Myr occurred between deposition of the Surprise Canyon Formation and the onset of deposition of the Supai Group. Deposition continued until Early Permian times McKee (1982). The Supai Group correlates with the Bird Spring Formation at Arrow Canyon (Lane *et al.*, 1999; Bishop *et al.*, 2009, 2010). The Bird Spring Formation lies conformably over the Indian Springs Formation and predominantly consists of sands and carbonates deposited in a shelf setting. Thin conglomeratic units with erosional bases also occur. The Formation contains the Global Boundary Stratotype Point for the Serpukhovian–Bashkirian (i.e. Mississppian–Pennsylvanian) boundary, 7.6 m above its base (Figure 4.8; Lane *et al.*, 1999).

During this period, western North America became influenced by collision of Gondwana and Laurentia along the Marathon-Ouchita-Appalachian suture, southeast of the Grand Canyon

region. Together with a left-lateral transpressional boundary to the southwest, this collision generated a complex pattern of intraplate deformation which resulted in the growth of a series of basement-cored uplifts known as the Ancestral Rocky Mountains (Figure 4.9b; e.g. Kluth & Coney, 1981; Dickinson & Lawton, 2003; Leary *et al.*, 2017). Examples in the vicinity of the Grand Canyon include the Uncompahgre and Zuni-Defiance uplifts. Foreland basins such as the Paradox and Holbrook developed alongside these mountain ranges (Figure 4.9b; e.g. Barbeau, 2003; Dickinson & Lawton, 2003; Sturmer *et al.*, 2018).

4.3 Regional subsidence patterns

Useful insights into the evolution of sedimentary basins can be obtained from their subsidence histories. Knowledge of the long-term behaviour of subsidence in the Grand Canyon region is essential if the causes and consequences of Carboniferous transient landscape development are to be understood. Here, I present a subsidence curve for the Grand Canyon based on stratigraphic information from Hintze (1988) and Beus & Morales (2003). Updated chronologic information is used for the Proterozoic Unkar and Chuar groups, and the Cambrian Sixtymile Formation and Tonto Group (Weil *et al.*, 2003; Timmons *et al.*, 2005, 2012; Dehler *et al.*, 2017; Rooney *et al.*, 2017; Karlstrom *et al.*, 2018). Observed sediment thicknesses are backstripped to remove the effects of compaction and sediment loading and obtain an estimate of water-loaded, or tectonic, subsidence, following the procedure of Sclater & Christie (1980). This procedure involves progressively removing sedimentary layers, finding decompacted thicknesses and densities of remaining layers, and hence calculating their equivalent water load. In this way, the growth of water-loaded accommodation space as a function of time is determined. The resulting water-loaded subsidence curve is shown in Figure 4.10.

Subsidence recorded by sedimentary rocks exposed in the Grand Canyon is strongly episodic. The earliest preserved subsidence occurred during Mesoproterozoic times, represented by the Unkar Group ($\sim$ 1255–1100 Ma). Subsidence was initially steady but accelerated rapidly throughout the Group's deposition. This pattern, along with syn-sedimentary monoclinal structures in lower units, is consistent with deposition in a compressional, foreland-basin setting associated with the Grenville orogen and the assembly of Rodinia (Timmons *et al.*, 2005, 2012; Mulder *et al.*, 2017). Upper units of the Unkar Group are characterised by extensional faulting and basaltic magmatism (Timmons *et al.*, 2001).

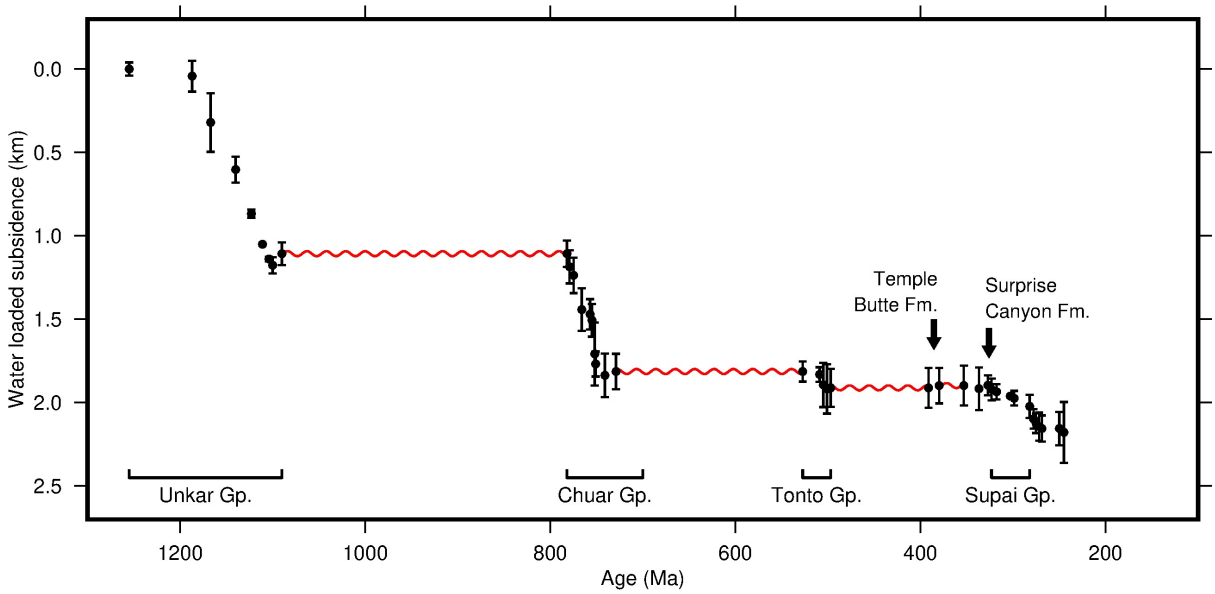

Figure 4.10: Water-loaded subsidence curve for the Grand Canyon region. Black circles = water-loaded subsidence estimates as function of time, where error bars reflect uncertainties in depositional water depths and variations in depositional thickness; red sinusoids = major erosional unconformaties.

A ∼ 300 Myr stratigraphic gap, which could represent a lack of deposition or removal of deposited material, is followed by the Neoproterozoic Chuar Group (∼ 780–730 Ma). Subsidence rates were relatively constant throughout. Syn-sedimentary extensional faulting is consistent with deposition in a rift setting associated with the break up of Rodinia (Karlstrom *et al.*, 2000; Timmons *et al.*, 2001; Dehler *et al.*, 2017; Rooney *et al.*, 2017). Another gap of ∼ 200 Myr preceeded Cambrian deposition of the recently reclassified Sixtymile Formation (∼ 530–510 Ma; Karlstrom *et al.*, 2018) and the Tonto Group (∼ 510–500 Ma; Rose, 2006; Karlstrom *et al.*, 2018). This smaller pulse of subsidence may represent a later stage of rifting in southern Rodinia (Karlstrom *et al.*, 2018).

No sediment is preserved from Ordovician and Silurian times. The Devonian Temple Butte formation was deposited in thin channels incised into the top of the Tonto Group, and subsequently the Carboniferous Redwall Limestone was deposited in a passive margin shelf setting (Section 4.2.1; Beus & Morales, 2003). Neither of these units record significant water-loaded subsidence.

The Surprise Canyon Formation is represented by a small negative subsidence excursion (i.e. uplift) and marks the onset of a significant subsidence pulse recorded by rocks of the Supai Group and subsequent units. This period is not associated with syn-sedimentary faulting or regional rifting (McKee, 1982; Beus & Morales, 2003). It is therefore possible that transient landscape development recorded by the Surprise Canyon Formation and subsequent subsidence

are intrinsically linked.

It is useful to compare calculated water-loaded subsidence in the Grand Canyon with that on a regional scale. I therefore also present subsidence histories calculated at locations in Arizona, Utah and Colorado for which appropriate stratigraphic information is available (Figure 4.11). Stratigraphic information was primarily obtained from Hintze (1988), then updated and refined as necessary (Table 4.2). Together, these curves provide a record of regional subsidence stretching from Cambrian times to the present day. Many features of the Grand Canyon subsidence curve described above are also present in this regional database, including a phase of subsidence associated with putative Cambrian rifting followed by a long-lived unconformity. Several curves also contain a prominent kink and subsequent increase in subsidence rate at the time of Surprise Canyon Formation deposition. The post-Redwall subsidence pulse observed in the Grand Canyon therefore appears to be manifest on a regional scale. In the following sections, I investigate two possible explanations for this pulse in subsidence: flexural effects of progressive lithospheric loading by active mountain ranges, and thermal effects of convective circulation in the asthenospheric mantle.

4.3.1 Flexural modelling

Patterns of water-loaded subsidence in western North America during Carboniferous times are often attributed to the flexural affects of mountain ranges associated with the Antler Orogeny and the Ancestral Rocky Mountains (Figure 4.9b, Section 4.2.3; e.g. Barbeau, 2003; Sturmer *et al.*, 2018). The extent to which flexural loading of the lithosphere can explain the post-Redwall pulse in subsidence observed in the Grand Canyon region depends on the proximity of potential loads and the lithosphere's effective elastic thickness, T_e.

The Uncompahgre Uplift of eastern Utah and western Colorado was a major mountain range located near to the Grand Canyon region (Figures 4.9b and 4.12a; e.g. Barbeau, 2003; Dickinson & Lawton, 2003; Leary *et al.*, 2017). The extensive Carboniferous and Permian stratigraphic record preserved in southern Utah allows subsidence patterns between the Uncompahgre and the Grand Canyon to be characterised. In Figures 4.12a and 4.12b, cumulative water-loaded subsidence between 330–250 Ma is shown as a function of distance from the Uncompahgre Uplift. This period corresponds to that of the post-Redwall record in the Grand Canyon region. Subsidence increases rapidly up to > 1.5 km within ~ 200 km of the Uncompahgre Uplift. At greater distances, subsidence tends to an approximately constant value of around 0.5 km.

Table 4.2: Subsidence histories of Grand Canyon region and surroundings.

Location[a]	Lat.(°)	Lon. (°)	Age	Subsidence[b] (km) Total	ℙ–P	References
Cedar City, Ce	37.7	-113.32	Cambrian — Quaternary	$2.45^{+0.58}_{-0.61}$	$0.394^{+0.032}_{-0.024}$	Hintze (1988)
Zion, Z	37.45	-112.95	Cambrian — Quaternary	$2.08^{+0.27}_{-0.28}$	$0.456^{+0.016}_{-0.012}$	Hintze (1988)
Grand Canyon region, GC	36.35	-112.67	Precambrian — Triassic	$2.84^{+0.48}_{-0.49}$	$0.312^{+0.162}_{-0.158}$	Hintze (1988), Beus & Morales (2003)
Kanab, K	37.23	-112.52	Cambrian — Paleogene	$1.84^{+0.26}_{-0.27}$	$0.476^{+0.011}_{-0.009}$	Hintze (1988)
Antimony, A	38.02	-111.98	Cambrian — Quaternary	$1.59^{+0.21}_{-0.21}$	$0.185^{+0.006}_{-0.004}$	Hintze (1988)
Bryce Canyon, BC	37.5	-111.96	Cambrian — Neogene	$2.24^{+0.50}_{-0.55}$	$0.581^{+0.107}_{-0.088}$	Hintze (1988)
Fish Lake, FL	38.58	-111.74	Devonian — Neogene	$1.37^{+0.08}_{-0.09}$	$0.168^{+0.002}_{-0.002}$	Hintze (1988)
Upper Salina Canyon, SC	38.89	-111.61	Cambrian — Paleogene	$2.37^{+0.09}_{-0.09}$	$0.126^{+0.001}_{-0.001}$	Hintze (1988)
Capitol Reef, CR	38.4	-111.27	Cambrian — Neogene	$1.63^{+0.22}_{-0.23}$	$0.458^{+0.048}_{-0.044}$	Hintze (1988)
Huntington, Hu	39.16	-111.13	Carboniferous — Paleogene	$2.03^{+0.46}_{-0.52}$	$0.219^{+0.011}_{-0.009}$	Hintze (1988)
Circle Cliffs, Ci	38.04	-110.98	Cambrian — Cretaceous	$1.69^{+0.26}_{-0.28}$	$0.448^{+0.102}_{-0.097}$	Hintze (1988)
San Rafael, SR	38.82	-110.87	Cambrian — Cretaceous	$1.51^{+0.25}_{-0.28}$	$0.342^{+0.057}_{-0.051}$	Hintze (1988)
Glen Canyon, Gl	37.35	-110.84	Cambrian — Cretaceous	$1.71^{+0.23}_{-0.24}$	$0.507^{+0.099}_{-0.093}$	Hintze (1988)
Hanksville, Ha	38.39	-110.71	Cambrian — Cretaceous	$1.24^{+0.15}_{-0.15}$	$0.518^{+0.090}_{-0.093}$	Hintze (1988)
Sunnyside, Su	39.41	-110.37	Cambrian — Paleogene	$2.06^{+0.34}_{-0.36}$	$0.300^{+0.040}_{-0.059}$	Hintze (1988)
Monument Valley, MV	37.01	-110.23	Cambrian — Jurassic	$1.09^{+0.21}_{-0.22}$	$0.506^{+0.140}_{-0.132}$	Hintze (1988)
Green River, GR	39.03	-110.15	Cambrian — Cretaceous	$1.91^{+0.30}_{-0.31}$	$0.622^{+0.156}_{-0.131}$	Hintze (1988)
Canyonlands, Ca	38.34	-109.88	Cambrian — Cretaceous	$1.26^{+0.42}_{-0.48}$	$0.663^{+0.301}_{-0.247}$	Hintze (1988)
Crescent Junction, CJ	38.91	-109.73	Carboniferous — Paleogene	$2.20^{+0.29}_{-0.30}$	$1.302^{+0.026}_{-0.016}$	Frahme & Vaughn (1983), Hintze (1988)
Northern Paradox, NP	38.63	-109.60	Carboniferous — Permian	—	1.33[c]	Sturmer *et al.* (2018)
Elba Flats, EF	38.99	-109.5	Cambrian — Paleogene	$2.70^{+0.28}_{-0.29}$	$1.657^{+0.026}_{-0.016}$	Frahme & Vaughn (1983), Hintze (1988)
Moab, Mo	38.57	-109.44	Cambrian — Paleogene	$1.67^{+0.68}_{-0.78}$	$1.016^{+0.462}_{-0.390}$	Hintze (1988)
Monticello, Mc	37.55	-109.31	Cambrian — Cretaceous	$1.40^{+0.66}_{-0.81}$	$0.716^{+0.357}_{-0.257}$	Hintze (1988)
Onion Creek, OC	38.8	-109.29	Devonian — Paleogene	$2.60^{+0.28}_{-0.28}$	$1.626^{+0.025}_{-0.016}$	Frahme & Vaughn (1983), Hintze (1988)
Lisbon Valley, LV	38.16	-109.15	Cambrian — Paleogene	$1.39^{+0.17}_{-0.17}$	$0.784^{+0.036}_{-0.044}$	Bohn (1977), Hintze (1988)
Durango, D	37.33	-107.95	Cambrian — Cretaceous	$2.14^{+0.14}_{-0.14}$	$0.814^{+0.107}_{-0.094}$	Huffman & Condon (1993), Lucas & Heckert (2005), McBride (2016)

[a] Location abbreviations are used on Figure 4.12a.
[b] Water loaded. Error bounds reflect variations in depositional thickness and uncertainties in water depth. ℙ = Pennyslvanian (i.e. upper Carboniferous), P = Permian.
[c] Published subsidence estimate.

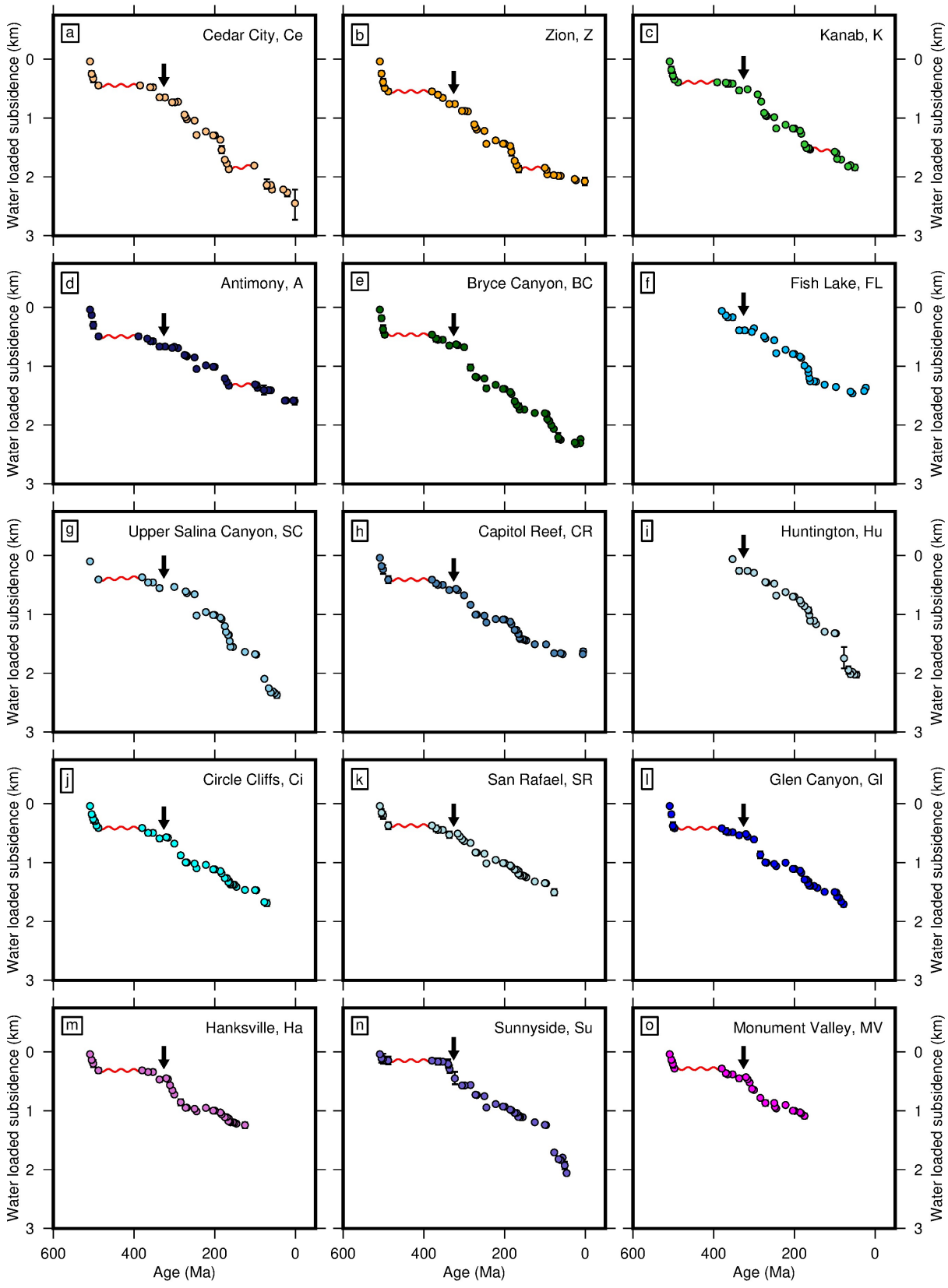

Figure 4.11: *Continued overleaf.*

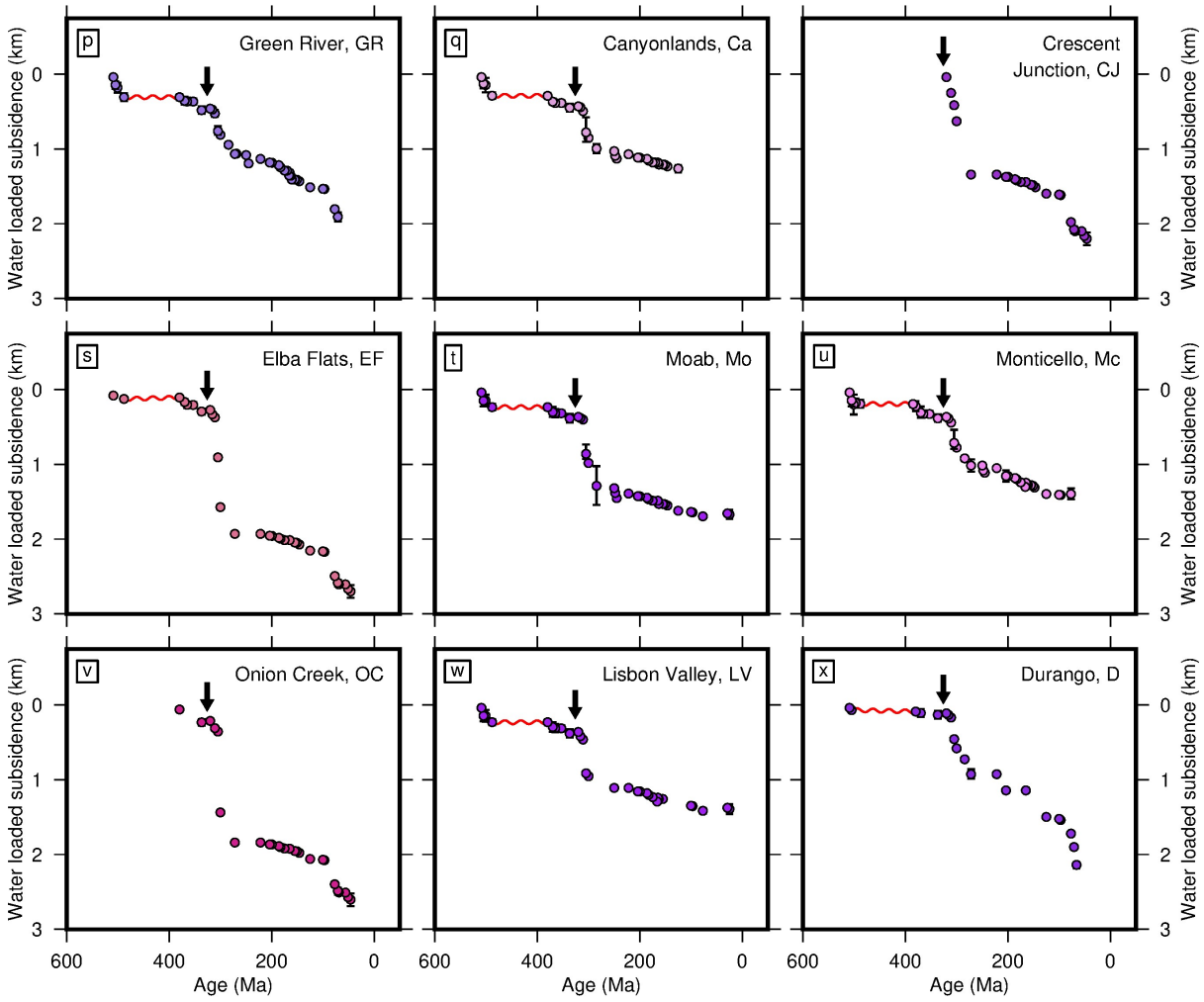

Figure 4.11: ***Continued from previous page.*** **Water-loaded subsidence curves for regions surrounding the Grand Canyon.** See text and Table 4.2 for details. Circles = water-loaded subsidence estimates; black arrows = timing of Surprise Canyon Formation in the Grand Canyon region; red sinusoids = major unconformities. Location abbreviations are used on Figure 4.12a.

Here, I model subsidence as a function of distance from the Uncompahgre Uplift using equations for flexure of an unbroken elastic plate (Gunn, 1943; Watts, 2001; Turcotte & Schubert, 2014). Water-loaded subsidence generated by flexure of an infinite elastic plate, S_f, in response to a line load, $V_\circ$, as a function of distance from the load, x, is given by

$$S_f(x) = \frac{V_\circ \alpha^3}{8D} \exp\left(-\frac{x}{\alpha}\right)\left[\cos\left(\frac{x}{\alpha}\right) + \sin\left(\frac{x}{\alpha}\right)\right], \tag{4.4}$$

where the flexural parameter, α, is defined as

$$\alpha = \left[\frac{4D}{(\rho_m - \rho_w)g}\right]^{\frac{1}{4}}, \tag{4.5}$$

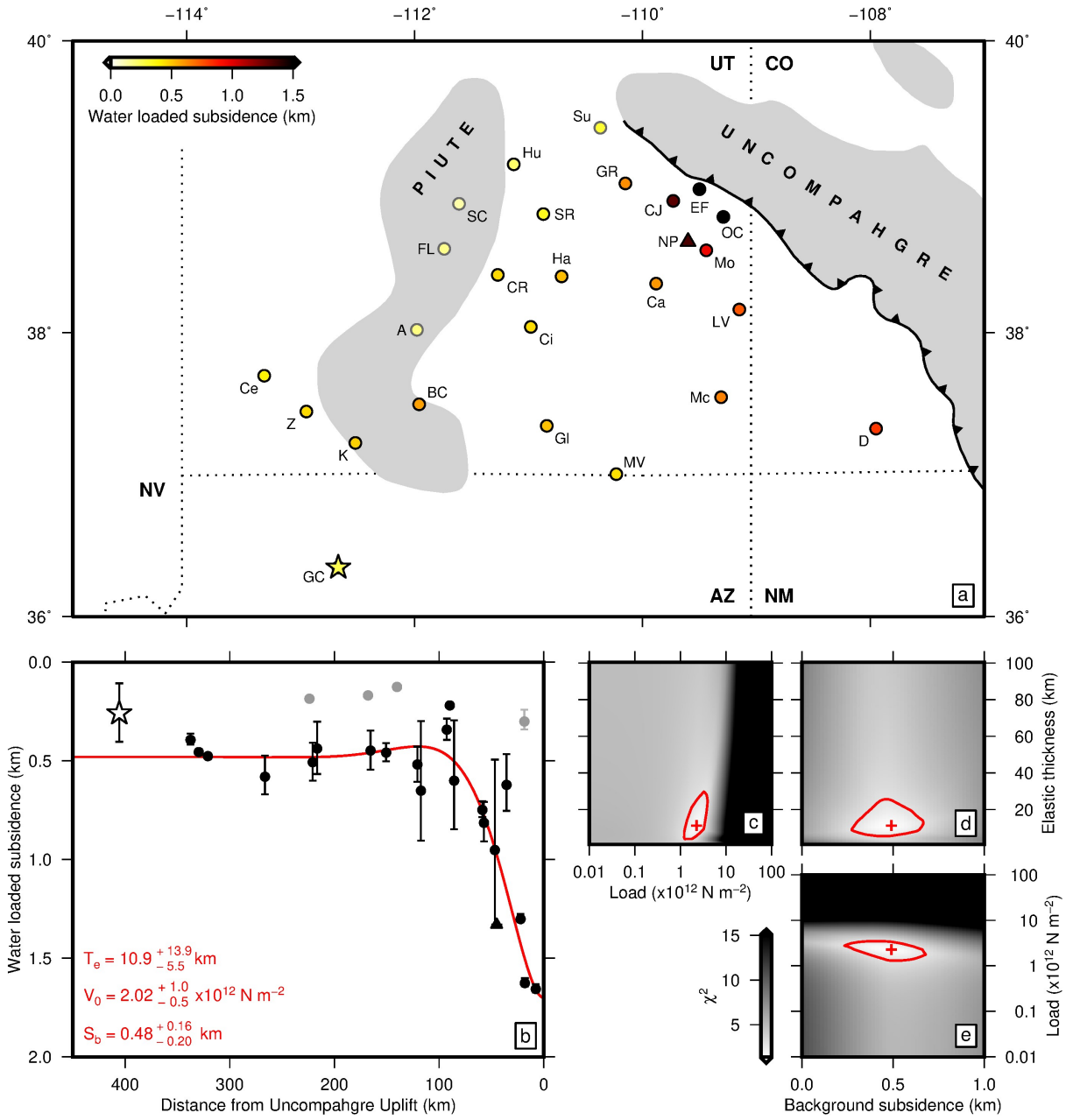

Figure 4.12: Regional flexural subsidence analysis. (a) Cumulative water-loaded subsidence in the Grand Canyon region for the period 330–250 Ma. Shaded star = Grand Canyon; shaded circles = loci with estimated water-loaded subsidence from this study, those with grey outlines are not included in optimisation procedure; shaded triangles = loci with published estimates of water-loaded susbidence; grey polygon = uplifts from Leary *et al.* (2017). Locations labelled with letter codes corresponding to those in Table 4.2 and Figure 4.11. (b) Cumulative water-loaded subsidence as a function of distance from Uncompahgre Uplift, for period 330–240 Ma. Black circles = cumulative water-loaded subsidence for sections calculated in this study, star = cumulative water-loaded subsidence for the Grand Canyon, black triangles = published estimates of water-loaded subsidence. Error bars reflect uncertainties in depositional water depths and thickness variations. Red line = water-loaded subsidence for best-fitting flexural model. (c) Slice through misfit space at global minimum, varying T_e as function of $V_\circ$. Red cross = global minimum, red line = misfit contour for values twice that at global minimum. (d) T_e as function of S_b, (e) $V_\circ$ as function of S_b.

and flexural rigidity, D, as

$$D = \frac{E{T_e}^3}{12(1-\nu^2)}. \tag{4.6}$$

ρ_m and ρ_w are densities of the mantle and water respectively, E is Young's modulus and ν is Poisson's ratio. I also allow for a regional, background component of subsidence, S_b, so that the total water-loaded subsidence, S_w, is given by

$$S_w = S_f + S_b. \tag{4.7}$$

Water-loaded subsidence predicted using these equations is compared with observed subsidence patterns in Figures 4.12b–4.12e. I performed a three-parameter sweep in which T_e, $V_\circ$ and S_b were varied and a χ^2 misfit between predicted and observed subsidence was calculated (Figures 4.12c–4.12e). Best-fitting values are $T_e = 10.9^{+13.9}_{-5.5}$ km, $V_\circ = 2.02^{+1.0}_{-0.5} \times 10^{12}$ N m^{-2} and $S_b = 0.48^{+0.16}_{-0.20}$ km. The best-fitting model is shown as a red line in Figure 4.12b. Upper and lower bounds correspond to values that yield χ^2 misfit values that are less than double the misfit value at the global minimum. These bounds are illustrated by red contours in Figures 4.12c–4.12e. The value of $T_e = 10.9^{+13.9}_{-5.5}$ km is broadly consistent with the results of Barbeau (2003), who estimated $T_e =$ 25 km using a sediment-loaded analysis.

Four locations, shown as grey points on Figure 4.12b, were not included in the optimisation calculations described above. The first three locations, Antimony, Fish Lake and Salina Canyon, are located on the Piute Uplift, a paleo-topographic high that extended for some distance across central southern Utah (Figure 4.9b; Hintze, 1988; Leary *et al.*, 2017). Their Carboniferous and Permian sections contain frequent unconformities and some key regional formations are significantly thinned or absent, resulting in significantly lower recorded subisdence than at more complete nearby sections (Figures 4.12a and 4.12b; Hintze, 1988). It is likely that this lower value of recorded subsidence is a result of reduced sedimentation and removal of sediment during sub-aerial exposure, due to the location of these sections on a topographic high. As such, these points would bias the optimisation towards artificially low values of background subisdence. The fourth location, Sunnyside, is located near to the Uncompahgre Front (Figure 4.12a; Hintze, 1988). It also records significantly reduced subsidence when compared to nearby locations. Its location close to the Front means that it has a significant influence on the optimisation procedure. However, the exact position of the Front varies between different paleogeographic reconstructions (e.g. Hintze, 1988; Dickinson & Lawton, 2003; Leary *et al.*, 2017), and the simple one-dimensional modelling used here does not allow for along-strike variation in load, which would probably have

reduced towards the range's northwestern end. For these reasons, particularly given its strong influence on the result, subsidence data from Sunnyside were not used in the optimisation but are shown for reference. Best-fitting values of T_e = 10.9 km, $V_\circ$ = 2.02 × 10^{12} N m^{-2} and S_b = 0.48 km are not greatly altered by including these four points, but ranges of acceptable values are significantly increased.

These results have two important implications. First, estimates of elastic thickness place limits on the distance over which any load can exert an influence. A useful parameter is the distance to the forebulge, x_b, which demarcates the limits of a flexural foreland basin and is equal to $\pi\alpha$ (Gunn, 1943; Watts, 2001; Turcotte & Schubert, 2014). For $T_e = 10.9^{+13.9}_{-5.5}$ km, $x_b = 120.5^{+101.9}_{-49.6}$ km. The Uncompahgre Uplift was located > 400 km from the Grand Canyon. The remnant Antler orogen was probably located ∼ 400 km to the west (Figure 4.9). The smaller Zuni-Defiance Uplift to the southeast was closer, but, at ∼ 300 km distance, also unlikely to generate significant vertical motions in the Grand Canyon region (Figure 4.9b). There are therefore no obvious lithospheric loads that could have produced the post-Redwall pulse of subsidence observed in the Grand Canyon region. Secondly, significant background subsidence of ∼ 300–700 m is required to fit observed regional subsidence patterns. It therefore appears that post-Redwall subsidence in the Grand Canyon region is associated with a component of regional subsidence, on length-scales greater than 100s of kilometres, which cannot be attributed to flexural affects of the Uncompahgre Uplift or any other known Carboniferous mountain range.

4.3.2 Thermal modelling

Since flexural subsidence as a result of loading by mountain ranges of the Ancestral Rocky Mountains and the Antler Orogeny appears unable to account fully for patterns of post-Redwall subsidence in the Grand Canyon region and its surroundings, an alternative explanation is sought. One possibility is a thermal process operating in the lithospheric and/or asthenospheric mantle, which could also contribute to transient uplift associated with the Surprise Canyon Formation. Several recent studies have highlighted the importance of asthenospheric thermal anomalies, likely existing in a thin channel directly beneath the lithospheric plate, in generating and maintaining dynamic topography at the present day (e.g. Hoggard *et al.*, 2016, 2017). The lateral propagation of such anomalies outwards from the Icelandic plume has been invoked to explain rapid uplift and subsidence associated with Cenozoic ancient landscapes preserved in the Faroe-Shetland Basin and the North Sea (Hartley *et al.*, 2011; Stucky de Quay *et al.*,

2017). Elsewhere, however, asthenospheric thermal anomalies have also been invoked to explain longer-term vertical motions (e.g. Anatolia, India, North America, North Africa; Chapter 3, Richards *et al.*, 2016; Klöcking *et al.*, 2018b; Ball *et al.*, 2019). In these cases, the arrival of anomalously hot asthenospheric material appears to coincide with significant thinning of the lithospheric mantle. These regions would be expected to subside as thermal anomalies cool and the lithosphere rethickens. Here, I investigate such a process as a possible explanation for patterns of Carboniferous uplift and subsidence observed in the Grand Canyon region.

Modelling strategy

The evolution of temperature, T, as a function of depth, z, and time, t, for the lithosphere can be described using the one-dimensional heat-flow equation for an internally heated conductive layer, in which

$$\rho c_p \frac{\partial T}{\partial t} = \frac{\partial}{\partial z}\left(k\frac{\partial T}{\partial z}\right) + H, \tag{4.8}$$

where ρ is density, c_p is specific heat capacity, k is thermal conductivity and H is the rate of heat production. ρ, c_p, k and H are likely to vary significantly with depth in the lithosphere as a result of temperature dependence and compositional differences between the crust and mantle. This variability with depth and temperature has been shown to have a significant effect on the thermal evolution of the oceanic lithosphere (McKenzie *et al.*, 2005; Richards *et al.*, 2018). To properly account for this depth dependence, a numerical scheme must be used to solve Equation 4.8. In this case, I used a Crank-Nicolson scheme where Equation 4.8 was approximated by

$$\begin{aligned}\rho_i^{n-\frac{1}{2}} c_{pi}^{\,n-\frac{1}{2}}\ \frac{T_i^n - T_i^{n-1}}{\delta t} = \frac{1}{2}\Bigg[&\frac{k_{i-\frac{1}{2}}^n T_{i-1}^n - \left(k_{i-\frac{1}{2}}^n + k_{i+\frac{1}{2}}^n\right)T_i^n + k_{i+\frac{1}{2}}^n T_{i+1}^n}{\delta z^2} + \\ &\frac{k_{i-\frac{1}{2}}^{n-1} T_{i-1}^{n-1} - \left(k_{i-\frac{1}{2}}^{n-1} + k_{i+\frac{1}{2}}^{n-1}\right)T_i^{n-1} + k_{i+\frac{1}{2}}^{n-1} T_{i+1}^{n-1}}{\delta z^2}\Bigg] + H_i^{n-\frac{1}{2}}.\end{aligned} \tag{4.9}$$

δt and δz are time and depth increments, respectively, and superscripts represent position in time while subscripts represent position in space. Equation (4.9) can be solved solved for T^n using a tridiagonal matrix algorithm (e.g. Press *et al.*, 1992). Values of material properties at timestep n were initially approximated using the temperature structure of the previous timestep, $n-1$, and subsequently updated iteratively once an estimate of the temperature structure at timestep n was obtained. Solutions typically converged within three iterations. Initial and

boundary conditions are given by

$$T(z, t=0) = \begin{cases} T_{ss} \text{ for } 0 < z < a - \Delta a \\ T_I(z,\ T_p + \Delta T_p) \text{ for } a - \Delta a < z < a \end{cases}, \tag{4.10}$$

$$T(z = 0, t) = 0\ ^\circ\text{C, and} \tag{4.11}$$

$$T(z = a, t) = T_I(z = a). \tag{4.12}$$

Equation (4.10) describes an initial temperature profile, in which the steady-state geotherm, T_{ss} for lithosphere of thickness a, is instantaneously thinned by an amount Δa and replaced with anomalously hot asthenosheric material. T_{ss} is calculated using the procedure outlined in Section 3.1.1 (McKenzie *et al.*, 2005). T_{ss} is then truncated at a depth $a - \Delta a$ and replaced with an isentropic temperature profile, T_I, raised by an amount ΔT_p (Equation 3.4; McKenzie & Bickle, 1988). Equation (4.11) states that the temperature is fixed to 0 °C at the surface and Equation (4.12) that it is fixed to the isentropic temperature at its base.

Once temperature as a function of time and depth has been calculated, corresponding subsidence as a function of time can be determined. If lithospheric thinning and emplacement of hot asthenosphere occur alone, the column will initially be uplifted and subsequently subside back to its original elevation with no net increase in accommodation space. However, if denudation occurs as a result of uplift, extra accommodation space can be created. If denudation is taken to occur instantaneously along with lithospheric thinning and emplacement of hot asthenosphere, the total water-loaded subsidence, S_w, can be written as a combination of thermal effects, S_T, and those associated with denudation, S_D, so that

$$S_w(t) = S_T(t) + S_D. \tag{4.13}$$

Thermally driven subsidence, S_T, is given by

$$S_T(t) = \frac{(a - t_c)\left[\rho_m(t=0) - \rho_m(t)\right]}{\rho_w - \rho_{base}} \tag{4.14}$$

where t_c is the crustal thickness, ρ_w the density of water and ρ_{base} the density at the base of the column. The density of the mantle, ρ_m, evolves through time as the column re-equilibrates and thermally contracts. Removal of some thickness of material, D, by denudation will result in a

water-loaded increase in accommodation space, S_D, given by

$$S_D = \frac{D(\rho_s - \rho_{base})}{\rho_w - \rho_{base}}, \tag{4.15}$$

where ρ_s is the density of denuded material, taken to be sediment. To simulate removal of Redwall Limestone during uplift and erosion, ρ_s is calculated using the compaction relationship for limestone described in Section 4.1.4.

Model benchmarking

In certain cases, analytical solutions to Equation (4.8) can be obtained and used to test the accuracy of the numerical model developed in the previous section. If material properties do not vary as a function of depth or temperature and there is no internal heat production, Equation (4.8) can be written as

$$\frac{\partial T}{\partial t} = \kappa \frac{\partial^2 T}{\partial z^2}, \tag{4.16}$$

where the thermal diffusivity, $\kappa = k/\rho c_p$, and solved analytically by Fourier expansion (e.g. Carslow & Jaeger, 1959). Comparisons between analytical and numerical calculations for two different sets of starting and boundary conditions are shown in Figure 4.13.

In the first case, cooling of a Gaussian temperature anomaly is shown. With an initial condition, $T(z, t_0) = \exp(-z^2/4\kappa t_0)$, temperature as a function of depth and time is given by

$$T(z, t) = \sqrt{\frac{t_0}{t}} \exp\left(\frac{-z^2}{4\kappa t}\right), \tag{4.17}$$

where the initial time, t_0, must be greater than zero. An excellent fit between analytical and numerical solutions is obtained, confirming that the numerical scheme is performing well (Figure 4.13a).

In the second case, lithospheric thinning and emplacement of hot asthenospheric material is simulated in a simplified way, where crustal heat production is neglected, material properties do not vary with depth and the asthenospheric mantle is assumed to be at a constant temperature. A general solution to Equation (4.16) takes the form

$$T(z, t) = T_{ss} + \sum_{n=1}^{\infty} A_n \sin\left(\frac{n\pi z}{a}\right) \exp\left(-\frac{n^2 t}{\tau}\right), \tag{4.18}$$

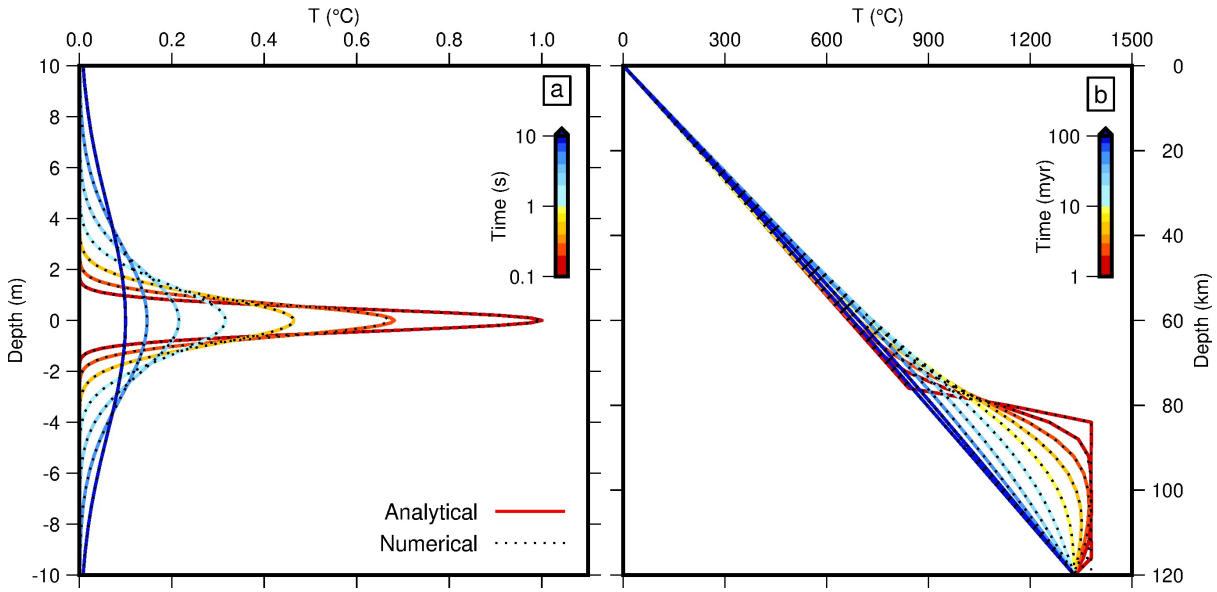

Figure 4.13: Analytical and numerical solutions to the heat flow equation. (a) Cooling of a Gaussian anomaly. Solid lines = temperature as a function of depth, shaded by time, calculated using analytical solution (Equation 4.17, $\kappa = 1$ m^2 s^{-1}); dotted lines = numerical solution, $\delta z = 0.1$ m, $\delta t = 0.1$ s. (b) Cooling of a simplified lithospheric column following thinning and emplacent of hot asthenospheric material. Solid lines = analytical solution (Equations 4.18 and 4.20); dotted lines = numerical solution, $\delta z = 4$ km, $\delta t = 1$ Myr.

where T_{ss} is the steady-state temperature profile and the thermal time constant, $\tau = a^2/\pi^2\kappa$. The initial condition is specified within the coefficient A_n, given by

$$A_n = \frac{2}{a}\int_0^a \left(T(z,0) - T_{ss}\right)\ \sin\left(\frac{n\pi z}{a}\right)\ \mathrm{d}z. \tag{4.19}$$

In this simple case, the steady-state geotherm becomes linear so that $T_{ss} = T_p z/a$. The initial condition is given by truncating this steady-state geotherm at a certain depth and setting the temperature below this depth to $T_p + \Delta T_p$. Equation (4.19) yields

$$\begin{aligned} A_n = \frac{2T_p}{an\pi}\Bigg[a\left(1+\frac{\Delta T_p}{T_p}\right)\left(\cos\left(\frac{n\pi(a-\Delta a)}{a}\right) - (-1)^n\right) + \\ a(-1)^n + \frac{a}{n\pi}\sin\left(\frac{n\pi(a-\Delta a)}{a}\right) - (a-\Delta a)\cos\left(\frac{n\pi(a-\Delta a)}{a}\right)\Bigg]. \end{aligned} \tag{4.20}$$

This analysis is essentially a modified version of that used by McKenzie (1978b) to model thermal relaxation of the lithosphere following instantaneous stretching and Bird (1979) to investigate the effects of delamination beneath the Colorado Plateau. Again, an excellent fit between analytical and numerical solutions is obtained (Figure 4.13b).

Calculated subsidence histories

Subsidence histories calculated using the scheme described above are now compared with observed patterns of subsidence in the Grand Canyon region. Instantaneous lithospheric thinning, emplacement of asthenospheric material and denudation are inserted at a time corresponding to the top of the Redwall Limestone (i.e. $\sim$ 335 Ma). Predicted subsidence is then compared to the observed subsidence pulse represented by the Surprise Canyon Formation, Supai Group and subsequent rock units. The record ends with the Triassic Moenkopi Formation. Observed subsidence is shown as black circles in Figure 4.14a. I performed a three parameter sweep through Δa, ΔT_p and D space to determine best-fitting values and their trade offs.

The best-fitting model, where Δa = 36 km, ΔT_p = 30 °C and D = 0.65 km, is shown as a red line in Figure 4.14a. The corresponding evolution of temperature as a function of depth and time is shown in Figure 4.14b. Slices through the misfit space at the global minimum are shown in Figures 4.14c–4.14e. It is clear that best-fitting values of Δa, ΔT_p and D are not well constrained, with significant trade offs existing between each parameter.

Estimated lithospheric thinning of 30–40 km and replacement by asthenospheric material with potential temperatures a few tens of degrees above that of ambient mantle is consistent with estimates from several regions experiencing active or recent epeirogenic uplift at the present-day (e.g. Chapter 3; Richards *et al.*, 2016; Klöcking *et al.*, 2018b; Ball *et al.*, 2019). However, to reproduce the $\sim$ 300 m increase in water-loaded accommodation space observed, removal of about 650 m of loosely compacted limestone is required. This value corresponds to roughly twice the thickness of Redwall Limestone preserved today, which is thought to have accumulated over a $\sim$ 20 Myr period. Deposition and removal of such a thick package of sediment within the $\sim$ 10 Myr stratigraphic gap between the youngest preserved Redwall Limestone rocks and the Surprise Canyon Formation would require a dramatic increase in sedimentation rate followed by rapid erosion and may therefore be unlikely.

One plausible way to reconcile these discrepancies is if the region was experiencing some amount of background subsidence during Carboniferous and Permian times. For example, thermal relaxation of the lithosphere may have been ongoing following putative phases of rifting in Neoproterozoic and Cambrian times (Karlstrom *et al.*, 2000, 2018; Timmons *et al.*, 2001; Dehler *et al.*, 2017; Rooney *et al.*, 2017). If a fraction of the subsidence pulse observed following deposition of the Redwall Limestone was a result of some background process, lower values of

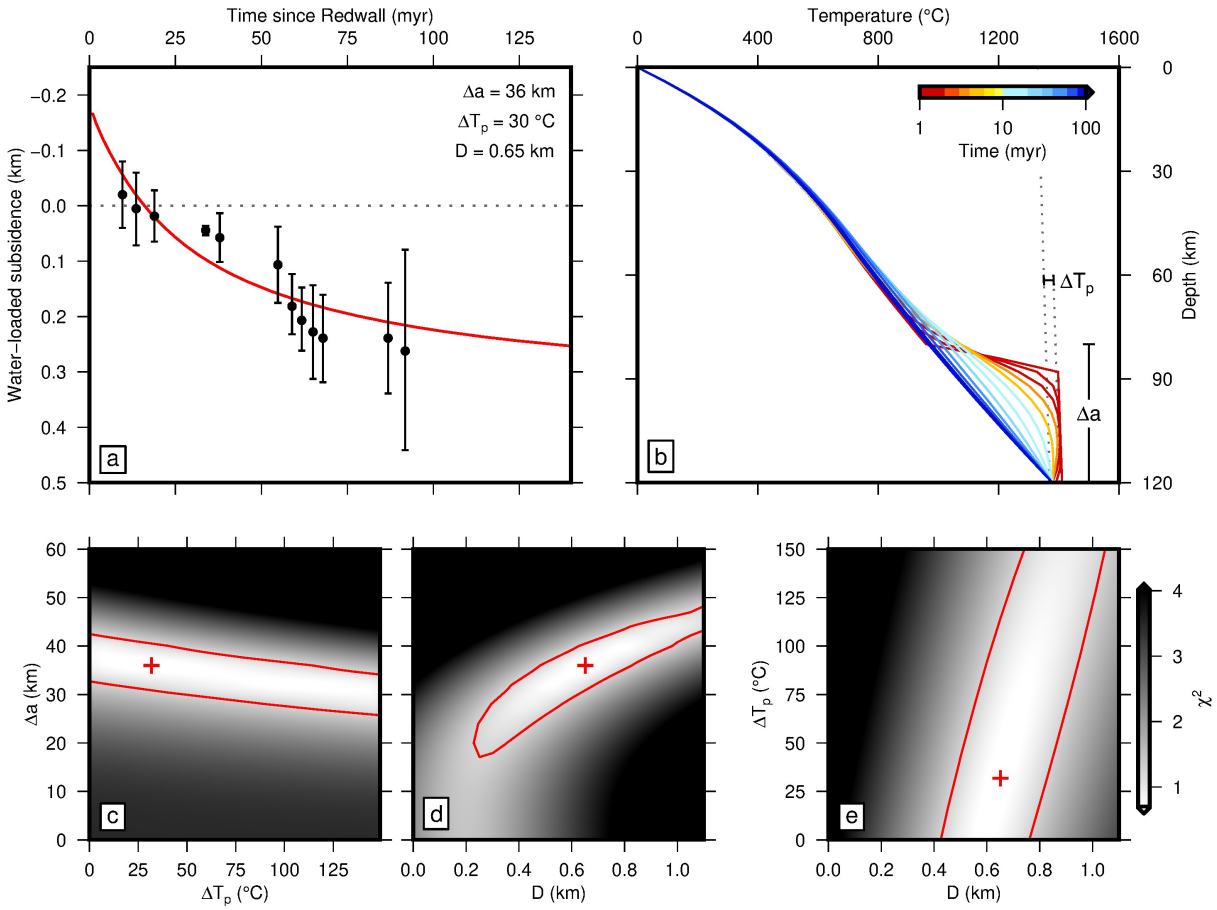

Figure 4.14: Thermal subsidence analysis. (a) Observed and calculated subsidence as function of time following Redwall Limestone deposition. Red line = predicted subsidence when $\Delta a = 36$ km, $\Delta T_p = 30$ °C and $D = 0.65$ km; black circles = observed subsidence in the Grand Canyon region, where error bars reflect uncertainty in depositional water depths and thickness variations; grey dotted line = 0 km subsidence (b) Evolution of temperature as a function of depth, shaded by time, for best-fitting thermal model. Grey dotted lines = isentropic temperature profile for T_p and $T_p + \Delta T_p$. (c–e) Slices through Δa-ΔT_p-D misfit space at global minimum. Red cross = global minimum, red line = misfit contour where misfit is twice that at the global minimum.

lithospheric thinning, asthenospheric heating and, crucially, denudation would be required to fit the data. Unfortunately, the incomplete Paleozoic subsidence record available in the Grand Canyon region makes accurately correcting for any background process challenging. However, steady subsidence throughout Devonian and Carboniferous times recorded in nearby regions with more complete records (e.g. southeastern Utah, Figure 4.11) suggests that such a process may have been occurring. If so, the best-fitting parameters of $\Delta a = 36$ km, $\Delta T_p = 30$ °C and $D = 0.65$ km represent upper bounds.

Another significant unknown is the steady-state lithospheric thickness. At the present day, regional lithospheric thicknesses are thought to be low (i.e. $\sim$ 60 km), although it has been

suggested that these low thicknesses are the result of lithospheric thinning in Cenozoic times associated with uplift of the Colorado Plateau (e.g. Bird, 1979; Klöcking *et al.*, 2018b). In the analysis described above, each model was performed using an initial thickness, a, of 120 km, which is typical of mature oceanic lithosphere and passive margins at the present day (e.g. Parsons & Sclater, 1977; Parsons & McKenize, 1978; Richards *et al.*, 2018). However, continental lithospheric thicknesses can vary considerably. For example, cratonic lithosphere east of the Colorado Plateau is thought to reach thicknesses of $\sim$ 200 km (Priestley & M^{c}Kenzie, 2013). In general, larger anomalies and more denudation are required to fit observed subsidence histories. If the steady-state lithospheric thickness is increased to cratonic values, larger values of Δa, ΔT_p and D are required and subsidence is predicted to continue long after the record in the Grand Canyon region ends. These effects are a result of the fact that the time scale of thermal diffusion increases with the square of lithospheric thickness.

4.4 Discussion

I have presented reviews of stratigraphic and chronologic observations relating to the Surprise Canyon Formation, along with flexural and thermal analyses of regional subsidence patterns. Here, I discuss potential driving mechanisms and their regional consequences in light of these results.

4.4.1 Eustatic sea-level variations

One conceivable mechanism for generating base-level fall associated with the Surprise Canyon Formation is eustatic sea-level change: the Carboniferous period was a time of considerable glaciation and hence eustatic sea-level fluctuation (e.g. Ross & Ross, 1985; Veevers & Powell, 1987; Fielding *et al.*, 2008). Indeed, a major eustatic event, represented by an unconformity or regression in global stratigraphic sequences, is inferred to have occurred during late Mississippian to early Pennsylvanian times (Saunders & Ramsbottom, 1986). This event has been linked to the development of a transient landscape in the central Appalachian Basin of eastern North America (Beuthin, 1994; Blake & Beuthin, 2008). Key questions are whether a global eustatic event can be shown to coincide with incision of the Redwall Limestone and deposition of the Surprise Canyon Formation and generate observed base-level fall of $\sim 280 \pm 90$ m.

The exact nature of late Paleozoic glaciation is the subject of considerable debate. Reconstructions are generally based on the distribution and extent of glacial deposits, particulary across southern Gondwana (i.e. present-day Antarctica, South America, southern Africa, Australia; at the time centered near the South Pole); relative sea-level variations observed in far-field sedimentary basins (e.g. in present-day North America, Eurasia); and geochemical proxies. Veevers & Powell (1987) argued for short, small-scale periods of glaciation in late Devonian and Visean times, followed by major and protracted glaciation which initiated in Serpukhovian times and lasted until early Permian times. More recently, it has been argued instead that the latter, protracted period of glaciation could be divided into a series of distinct, shorter glaciations (e.g. Fielding *et al.*, 2008; Montañez & Poulsen, 2013). In particular, the growth of small, localized ice centers is thought to have begun during middle Visean to Serpukhovian times, followed by a major increase in ice extent and volume towards the beginning of the Bashkirian stage (Figure 4.15).

Saunders & Ramsbottom (1986) compared stratigraphic sections from across North America, northern Africa and Eurasia and identified a prominent unconformity that developed in many locations during middle Carboniferous times and which they termed the 'mid-Carboniferous eustatic event'. Their event was defined using ammonoid zones, beginning in the uppermost *Eumorphoceras* zone ('E_2c') and lasting until the early *Reticuloceras* zone ('R_1'), although the exact timing and duration of hiatuses varies with location. These zones correspond to an upper Serpukhovian to lower Bashkirian age, spanning the Mississippian–Pennsylvanian boundary (Figure 4.15; Ramsbottom & Saunders, 1985; Korn, 2006; Davydov *et al.*, 2012). Saunders & Ramsbottom (1986) identified conglomeratic beds and short-lived hiatuses within the Indian Springs and Bird Spring formations at Arrow Canyon, which they associated with the onset and termination of the eustatic event, respectively. The event has also been linked to the development of a transient landscape in the central Appalachian basin (Beuthin, 1994; Blake & Beuthin, 2008). There, marine limestones, shales and sandstones of the Serpukhovian Mauch Chunk Group and Bluestone Formation are incised and overlain by sandstones of the New River and Pocahontas Formations. A series of south-westward draining paleovalleys have been identified, running parallel to the Appalachian range front and extending over Virgnia, West Virginia, Kentucky, Indiana, Illinois and Arkansas (Siever, 1951; Bristol & Howard, 1971; Rice, 1984, 1985; Howard & Whitaker, 1988; Droste & Keller, 1989; Beuthin, 1994; Webb, 1994; Archer & Greb, 1995). Local relief of up to $\sim$ 100 m is reported, although base-level fall may have been amplified by flexural uplift (e.g. Ettensohn, 1994).

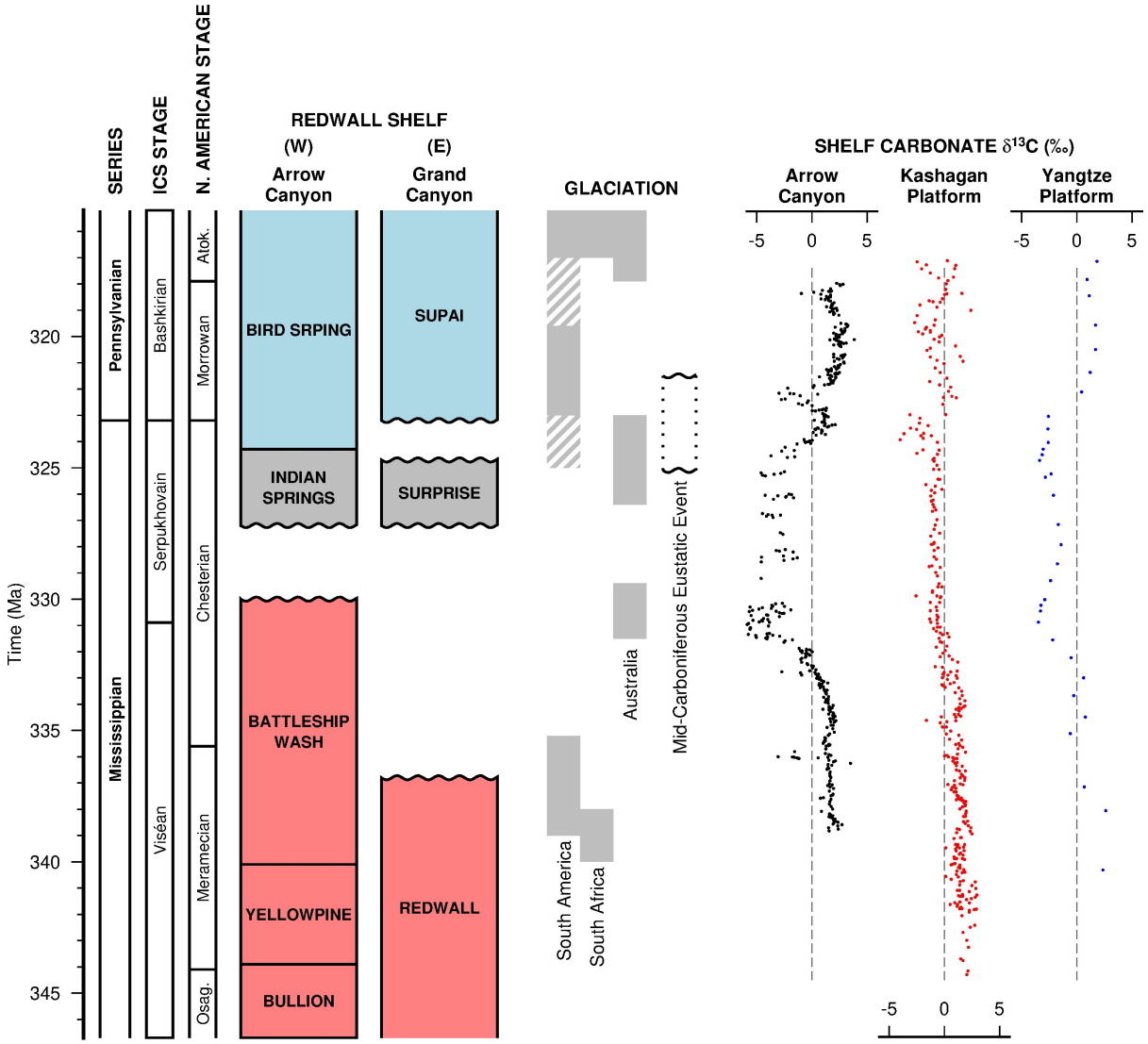

Figure 4.15: Redwall Shelf chronology and global eustatic sea level. Redwall Shelf stratigraphy as in Figure 4.8 and Table 4.1. Global glaciation record after Montañez & Poulsen (2013). Solid bars = periods of continental glaciation, hashed bars = possible glaciation. Mid-Carboniferous Eustatic Event from Ramsbottom & Saunders (1985) using the Davydov *et al.* (2012) time scale. δ^{13}C data from Dyer *et al.* (2015). Data from Kashagan (Kazakhstan) and Yangtze (China) originally from Ronchi *et al.* (2010) and Zhao & Zheng (2014), respectively.

The glacial chronology described above is broadly consistent with sea-water δ^{18}O records which increase through Serpukhovian times into early Bashkirian times (Mii *et al.*, 1999, 2001; Grossman *et al.*, 2008). However, the δ^{13}C record is more complicated. In western North America, a strong negative excursion is observed in the upper Battleship Wash Formation at Arrow Canyon, and in equivalent sections along the Leadville and Madison Shelves (Figure 4.15; Saltzman, 2003; Bishop *et al.*, 2009; Dyer *et al.*, 2015). Similar late Visean to early Serpukhovian excursions are observed in platform carbonates of Kazakhstan and China, where negative excursions also occur in upper Serpukhovian times (Figure 4.15; Ronchi *et al.*, 2010; Zhao & Zheng, 2014). Meanwhile,

in deep-water basins which appear to have avoided meteroic diagenesis (e.g. northern Spain), δ^{13}C gradually increases throughout late Visean and Serpukhovian times (Campion *et al.*, 2018). This positive trend is also recovered for western North American, European and Russian basins when pristine brachiopod shells, a more faithful recorder of sea-water δ^{13}C than bulk carbonate, are used (Bruckschen *et al.*, 1999; Mii *et al.*, 1999; Bishop *et al.*, 2009; Dyer *et al.*, 2015). The cause of this positive δ^{13}C shift is the subject of debate, but could be related to an increase in organic carbon burial or extensive meterioc diagenesis of sub-aerially exposed carbonate rocks (Mii *et al.*, 1999; Dyer *et al.*, 2015; Campion *et al.*, 2018). δ^{13}C records therefore appear to be consistent with periods of glaciation and an eustatic sea-level fall in late Visean to early Serpukhovian times and in late Serpukhovian times.

In the Grand Canyon region, the unconformity associated with incision of the Redwall Limestone begins in middle Visean times and continues until middle Serpukhovian times, when deposition of the Surprise Canyon Formation began (Figures 4.8 and 4.15). At the more distal Arrow Canyon section, the depositional hiatus was delayed until early Serpukhovian times. Base-level fall and incision of the Redwall Shelf therefore seems to correlate with the onset of localized glaciation in middle Visean to early Serpukhovian times (e.g. Veevers & Powell, 1987; Fielding *et al.*, 2008; Montañez & Poulsen, 2013). However, while in the Grand Canyon region base-level fall appears to have ceased and deposition to have resumed during middle Serpukhovian times (represented by the Surprise Canyon and Indian Springs Formations), ice-sheet growth is thought to have reached its maximum extent in late Serpukhovian to early Bashkirian times (Veevers & Powell, 1987; Fielding *et al.*, 2008; Montañez & Poulsen, 2013). At the Redwall Shelf, unconformities between the Surprise Canyon Formation and Supai Group and within the Indian Springs and Bird Spring Formations occur at this time, as does the development of a globally recognized middle Carboniferous unconformity identified by Saunders & Ramsbottom (1986). Therefore, while ice-sheet histories, the isotopic record, and the presence of a globally recognized unconformity point to a peak in ice-sheet coverage and eustatic sea-level low stand around the Mississippian-Pennsylvanian boundary, its effect in the Grand Canyon region is subtle compared to dramatic early Serpukhovian base-level fall recorded by the Surprise Canyon Formation. I therefore argue that existing reconstructions of late Paleozoic glaciation are inconsistent with a eustatic cause for observed incision of the Redwall Limestone and the formation of paleovalleys preserved by the Surprise Canyon Formation.

The arguments outlined above rely on sparse local biostratigraphic information as well as global

biostratigraphic correlations and global glacial reconstructions that are based on an incomplete record and necessarily uncertain. A more straightforward question may be, regardless of timing, whether Carboniferous glacioeustatic variations could have generated the minimum $\sim 280 \pm 90$ m of base-level fall required by the stratigraphic relationships observed in the Grand Canyon region (Section 4.1.4). For the Cenozoic era, estimates of eustatic sea level vary from $\sim +$ 70–100 m for early Cenozoic times, when ice extent was minimal, to $\sim -$ 120 m for periods of maximum ice extent, relative to the present day (e.g. Miller *et al.*, 2005). There is therefore some precedent for invoking glacially-forced eustatic sea-level variations with peak-to-peak amplitudes of $\sim$ 200 m. However, there is a growing consensus that, unlike during the Cenozoic era, glaciation in middle Carboniferous times was restricted to localised ice centres rather than forming a single extensive ice sheet (e.g. Fielding *et al.*, 2008; Montañez & Poulsen, 2013). As a result, despite the compilation of Rygel *et al.* (2008) containing estimates of middle Carboniferous eustatic fluctuations of up to $\sim$ 150 m, many authors now treat estimates over $\sim$ 50 m with skepticism, citing, for example, inaccurate facies-based water-depth estimates and incomplete geochemical proxies as potential sources of over estimation (e.g. Montañez & Poulsen, 2013). Indeed, recent attempts to simulate late Paleozoic glaciations suggest that, in order to maintain localised ice sheets, ice volumes equivalent to $<$ 50 m eustatic sea level are required (Horton *et al.*, 2010, 2012).

In summary, I have reviewed existing reconstructions of middle Carboniferous glaciation and eustatic sea level. The distribution of glacial deposits, development of globally synchronous unconformities and isotopic records are all consistent with the development of localised ice centres and a eustatic sea-level fall in late Visean to early Serpukhovian times, followed by the development of more extensive ice sheets in late Serpukhovian to early Bashkirian times (i.e. around the Mississippian-Pennsylvanian boundary). It seems unlikely that eustatic sea-level changes associated with these glaciations exceeded a few tens of metres. This timeline is at odds with observations from the Grand Canyon region which require $\sim 280 \pm 90$ m base-level fall in early Serpukhovian times, followed by apparently more modest base-level fall at the Mississippian-Pennsylvanian boundary. I therefore argue that either some component of transient uplift or significant revision of middle Carboniferous glacial and sea-level reconstructions are required to explain the generation of Surprise Canyon Formation paleovalleys.

4.4.2 Transient convective uplift

An alternative explanation for Carboniferous base-level fall and landscape development in the Grand Canyon region is uplift of the lithospheric column. The transient nature of base-level fall and the apparent lack of syn-sedimentary deformation (e.g. faulting, folding) suggests that crustal thickening could not have generated this uplift. A flexural origin is also unlikely given an absence of nearby lithospheric loads (for example, major Ancestral Rocky Mountains ranges were located at least $\sim$ 300 km away; Section 4.3.1).

Convective support may be a more plausible mechanism for generating transient uplift and subsidence. Indeed, such a process has been invoked to explain the formation of Paleogene transient landscapes now buried in the Faroe-Shetland Basin and North Sea and identified on seismic reflection data (Shaw Champion *et al.*, 2008; Hartley *et al.*, 2011; Stucky de Quay *et al.*, 2017). In these cases, uplift and subsidence of $\sim$ 800 m occurred over a period of a few million years. Hartley *et al.* (2011) proposed that such rapid phases of uplift and subsidence could be explained by lateral advection of hot blobs of asthenospheric mantle within the broader Icelandic plume.

Uplift and subsidence recorded by the Surprise Canyon Formation and overlying units is considerably slower than that observed in Paleogene times around the Icelandic plume, with uplift and incision occurring within $\sim$ 10 Myr and subsequent subsidence apparently continuing for up to $\sim$ 100 Myr. Furthermore, there were no known mantle plumes in the vicinity of the Grand Canyon region in Carboniferous times. However, several lines of evidence suggest that thermal anomalies capable of supporting 100s of metres of topography are a pervasive feature of the upper mantle at the present day. Global analyses of oceanic residual depth anomalies reveal a complex planform of convective support with amplitudes of $\sim \pm$ 1 km and wavelengths of $\sim$ 1,000 km (Menard, 1973; Cochran & Talwani, 1977; Winterbourne *et al.*, 2014; Hoggard *et al.*, 2016, 2017). On the continents, Cenozoic growth of magmatic domes and plateaux has also been attributed to the presence of hot asthenospheric material immediately beneath the plate, in many cases linked with significant thinning of the lithospheric mantle (e.g. Anatolia, Africa, Arabia; Chapter 3; Paul *et al.*, 2014; Wilson *et al.*, 2014; Ball *et al.*, 2019). Such processes have also been invoked to explain recent uplift of the Colorado Plateau, of which the Grand Canyon region forms a part (Bird, 1979; Roberts *et al.*, 2012; Klöcking *et al.*, 2018b). Exact mechanisms of lithospheric thinning are unclear, but could involve thermal erosion by small-scale convection, 'dripping' of gravitationally unstable lithosphere or delamination of large lithospheric blocks

(Bird, 1979; Houseman *et al.*, 1981; Yuen & Fleitout, 1985; Davies, 1994; Göğüş & Ueda, 2018). Estimates of anomalous asthenospheric temperature and amounts of lithospheric thinning associated with these topographic and bathymetric features, based on basaltic geochemistry and surface-wave tomography, are generally of the order a few tens of degrees and a few tens of kilometres, respectively (e.g. Chapter 3; Klöcking *et al.*, 2018b; Richards, 2018; Ball *et al.*, 2019)

Several lines of evidence suggest that a convective process of the kind described above could have generated transient uplift, denudation and subsidence recorded by the Surprise Canyon Formation and subsequent units. Such processes can generate vertical motions of appropriate amplitudes, are not associated with significant crustal deformation and appear to occur relatively frequently, at least througout Cenozoic times. In Section 4.3.2, I showed that the magnitude and timescale of subsidence following deposition of the Surprise Canyon Formation can be adequately reproduced by cooling and re-thickening of the lithospheric mantle following thinning and emplacement of hot asthenospheric material (Figure 4.14). Best-fitting values of $\Delta a = 36$ km, $\Delta T_p = 30$ °C are well within the range estimated for modern equivalents. The large amount of denudation required by best-fitting models could be a result of a background component of subsidence, in which case lower values of Δa and ΔT_p would be required. The localised occurrence of a heavy-mineral assemblage, including pristine olivine, pyroxene and hornblende grains, in one Surprise Canyon Formation paleovalley implies that there was a local source of mafic magmatic material (Section 4.1.2, Figure 4.3d; Grover, 1989, pp. 170–173). Including approximately contemporaneous exposure and incision of the Leadville and Madison Shelves, the affected length of the passive margin was $\sim$ 1,500 km, again consistent with equivalent features observed at the present day (Cochran & Talwani, 1977; De Voto, 1988; Sando, 1988; Hoggard *et al.*, 2016, 2017). Furthermore, if existing age estimates for these sequences are accurate, base-level fall and incision appears to have affected the more northern Madison Shelf a few million years earlier than Redwall Shelf of the Grand Canyon Region (Figure 4.8, Section 4.2). This apparent southward migration cannot be explained by glacio-eustatic variations, but would be consistent with the lateral advection of an asthenospheric thermal anomaly beneath the plate, movement of the plate over a stationary anomaly, or a combination of the two.

There is also evidence that Carboniferous transient base-level fall in the Grand Canyon region was linked to changes in drainage patterns on a regional scale. A recent study by Gehrels *et al.* (2011) provided detailed detrital zircon geochronologic data for the Paleozoic sequence at the

Grand Canyon. They collected zircon grains from each sandstone unit and obtained Uranium-Lead (U-Pb) ages and uncertainties for each grain. Resulting suites of U-Pb ages reflect the age composition of the sands' source region, or regions. As such, this technique is a useful way of investigating sediment provenance.

In Figure 4.16, the results of Gehrels *et al.* (2011) are shown as normalised probability density functions along with ages of prominent North American sediment source regions. Throughout early Paleozoic formations (the Cambrian Tapeats Sandstone and Bright Angel Shale, and Devonian Temple Butte), a remarkably consistent age distribution is obtained, with broad peaks at ~ 1.45 and ~ 1.73 Ga. The origins of grains with these ages are thought to be the widespread granitic '1.34–1.48 Ga Province', and the Yavapai and Mazatzal Provinces, respectively (Anderson & Morrison, 1992; Karlstrom & Bowring, 1993; Gehrels *et al.*, 2011). Each of these sediment sources is thought to be located in central North America, east of and including the Grand Canyon region. The age distribution of sands from the Surprise Canyon Formation is strikingly different to those of the Cambrian–Devonian rocks that precede it. Previously dominant age peaks at ~ 1.45 and ~ 1.73 Ga are significantly reduced, while a diffuse peak at ages ~ 1.0–1.3 Ga dominates. This younger age peak is associated with the magmatism of the Grenville orogenic belt of eastern North America. A small cluster of Paleozoic ages is associated with Appalachian magmatism, also derived from eastern North America. In the upper Suprise Canyon Formation and subsequent units, the Grenville peak is more subdued and the Yavapai/Mazatzal peak becomes more prominent again. This broad pattern is then maintained for the majority of the remiaing Paleozoic sequence.

The dramatic changes in age distributions observed prior to and during deposition of the Surprise Canyon Formation must reflect re-organisation of drainage patterns on a regional, and possibly continental scale. Uncertainties in the source locations for the ~ 1.45 and ~ 1.73 Ga peaks that dominated prior to deposition of the Surprise Canyon Formation make understanding this re-organisation and its relation to Carboniferous base-level fall in the Grand Canyon region difficult. The ~ 50 Myr gap in the record between the Devonian Temple Butte Formation and Carboniferous Surprise Canyon Formation means that the initial change to a Grenville-dominated distribution could have occurred some time before deposition of the Surprise Canyon Formation. Furthermore, the shift to a more eastern sediment source could have been a result of active Appalachian orogenisis in that region. However, the return of a significant peak at ~ 1.45 Ga within the upper Surprise Canyon Formation does imply that drainage re-organisation

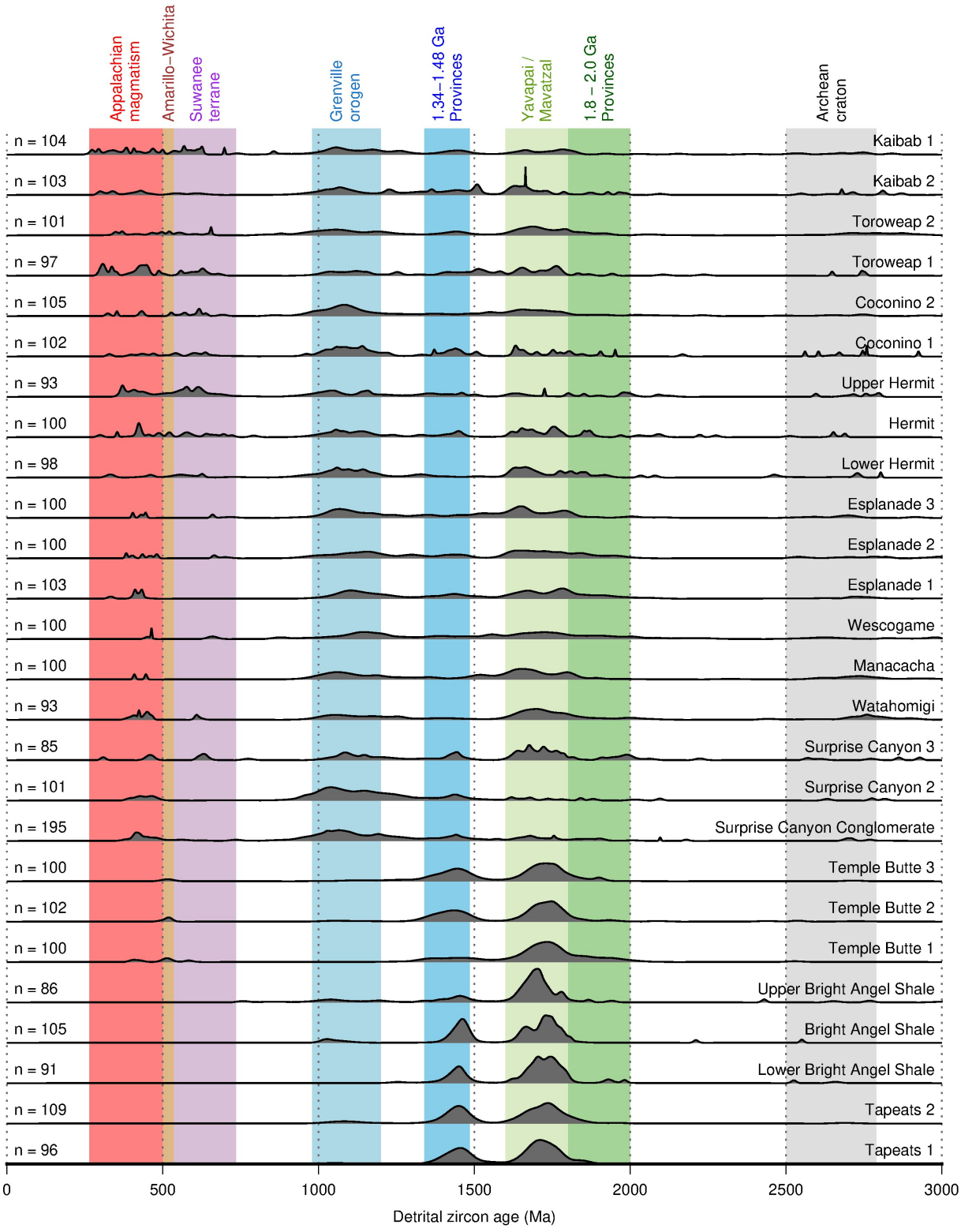

Figure 4.16: Paleozoic detriral zircon age distributions for the Grand Canyon. Based on data from Gehrels *et al.* (2011). Probability density functions generated by combining normal distributions calculated from each U-Pb age and its uncertainty, then normalising so that the total area under the curve is one. Coloured bars represent dominant ages of zircons derived from potential source regions, also based on information from Gehrels *et al.* (2011).

was, at least to an extent, transient and linked to processes that led to base-level fall and landscape development in the Grand Canyon region. Such a re-organisation is unlikely to have been produced by eustatic sea-level variations but would be an expected consequence of regional transient uplift.

4.5 Summary

The Carboniferous Surprise Canyon Formation of the Grand Canyon region represents a dramatic period of transient base-level fall. It is underlain by carbonates of the Redwall Limestone, which form part of an extensive shelf system that covered much of western North America in Mississippian times. Over a period of < 10 Myr, $\sim 280 \pm 90$ m base-level fall resulted in the exposure, karstification and incision of this carbonate platform. Subsequent base-level rise brought resumed deposition, in an initially terrestrial and later marine environment. A prolonged period of subsidence followed, apparently not related to regional rifting or flexural effects of the Ancestral Rocky Mountains. The timing and magnitude of required base-level fall makes eustatic sea-level changes an unlikley cause, at least within the framework of the most recent Carboniferous glacial reconstructions. Rather, a regional transient uplift event appears to be required. Such an uplift event could be driven by the arrival of hot asthenospheric material and subsequent lithospheric thinning, a process linked to epeirogenic uplift in various locations at the present day. Plausible amounts of anomalous temperature and lithospheric thinning are able to reproduce the magnitude of initial uplift, and the magnitude and timescale of subsequent subsidence. The apparent occurrence of contemporaneous mafic magamtism, and the possible migration of uplift and landscape development from north to south, are both consistent with this conceptual model. Detrital zircon geochronologies from Gehrels *et al.* (2011) also imply that transient uplift may have caused a re-organisation of regional drainage networks, resulting in an arrangement which, at least in part, persisted for the remainder of Paleozoic times. Following work by Shaw Champion *et al.* (2008), Hartley *et al.* (2011) and Stucky de Quay *et al.* (2017) on Paleogene landscapes buried in the Faroe-Shetland Basin and North Sea, these results provide further evidence that ancient transient landscapes can record important information about lithospheric and asthenospheric processes throughout geologic time.

Chapter 5

Origin and Evolution of Congo Basin

The origin and evolution of intracratonic basins— thick piles of sediment lying on cratonic lithosphere far away from plate boundaries— represent a significant outstanding problem in geodynamics. Classic examples include the Michigan, Illinois, Williston and Hudson basins of North America, and the Congo basin of central Africa, the latter of which is the focus of this chapter. These basins are typically large, $O(10^5$–$10^6)$ km^2, sub-circular in shape and contain several kilometres of shallow marine and continental sediment representing several hundred million years of subsidence (Xie & Heller, 2009; Allen & Armitage, 2012). Their stratigraphic record tends to consist of thick sediment packages, or 'megasequences', bounded by basin-wide unconformities (Sloss, 1963). It has been proposed that phases of subsidence and erosion recorded by these sequences and their bounding unconformities could reflect changing patterns of convective support beneath these basins (Rodríguez Tribaldos & White, 2018).

Many conceptual models have been proposed to explain the protracted subsidence histories of intracratonic basins, which include: lithospheric stretching at low strain rates followed by thermal relaxation (e.g. Klein & Hsui, 1987; Xie & Heller, 2009; Armitage & Allen, 2010; Allen & Armitage, 2012); the presence of density anomalies in the crust and/or lithospheric mantle due to phase changes or melt intrusion (e.g. Klein & Hsui, 1987; Hamdani *et al.*, 1991; Klein, 1991; Fowler & Nisbet, 1995; Downey & Gurnis, 2009); lithospheric thickening, heating, denudation,

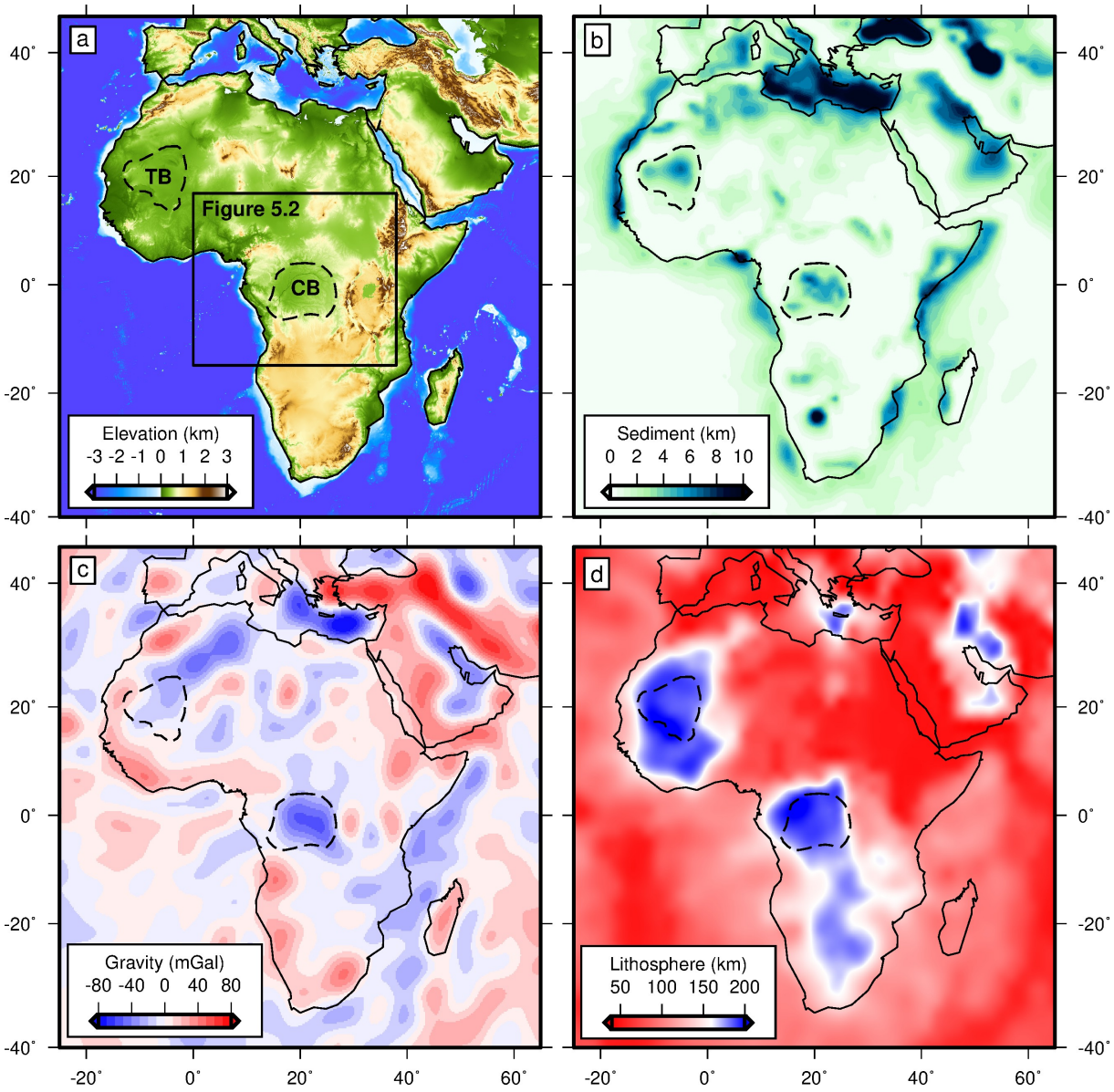

Figure 5.1: Geological and geophysical setting of Congo basin within Africa. (a) ETOPO1 topographic and bathymetric map of Africa (Amante & Eakins, 2009). Dashed lines = outlines of Congo (CB) and Taoudeni (TB) basins, box = region shown in Figure 5.2. (b) Sedimentary thicknesses from Laske & Masters (1997) contoured every 0.5 km. (c) GGM03C free-air gravity anomalies filtered for wavelengths of 730–13,000 km and contoured at 10 mGal intervals (Tapley *et al.*, 2007). (d) CAM2016Litho lithospheric thickness model from Priestley *et al.* (2019). Note that red–blue transition occurs at 160 km and thus approximately represents boundary between cratonic and non-cratonic lithosphere.

and subsequent cooling (McKenzie & Priestley, 2016; McKenzie & Rodríguez Tribaldos, 2018); and convective drawdown (e.g. Middleton, 1989; Hartley & Allen, 1994; Heine *et al.*, 2008; Downey & Gurnis, 2009). Support for basin initiation in a rift setting largely originates from basin subsidence histories, which often include an initial phase of relatively rapid subsidence

followed by a prolonged phase of more modest subsidence (Klein & Hsui, 1987; Xie & Heller, 2009). It has also been noted that basin initition often coincides with periods of continental dispersion (Klein & Hsui, 1987; Armitage & Allen, 2010). Nevertheless, a lack of high-quality seismic imaging often precludes identification of associated rifting structures at the base of these basins (Allen & Armitage, 2012). Basin formation by convective downwelling is supported by the presence of prominent negative long-wavelength free-air gravity anomalies over many intracratonic basins (Figure 5.1c; Peltier *et al.*, 1992; Hartley & Allen, 1994). This hypothesis, however, requires convective downwelling beneath these basins to be continuous for several hundred million years, despite significant plate motion, which is probably unrealistic (Hanne *et al.*, 2004). Few attempts have been made to quantitatively test the predictions of these conceptual models against a full range of geological and geophysical observations.

The Congo basin, or Cuvette Centrale, located in Central Africa, is in many ways a typical intracratonic basin (Figure 5.1). Its large size, with a diameter of $\sim$ 1,600 km and area of $\sim$ 1.4×10^6 km^2, constitutes approximately one tenth of the African continent (Figure 5.1a; Daly *et al.*, 1992). Sediment thicknesses are generally $\sim$ 5 km but locally reach up to 9 km (Figure 5.1b; e.g. Lawrence & Makazu, 1988; Daly *et al.*, 1992; Kadima *et al.*, 2011). The stratigraphic record spans Neoproterozoic to Quaternary times, and consists of thick packages of sediment bounded by basin-wide unconformities (Lawrence & Makazu, 1988; Daly *et al.*, 1991, 1992; Kadima Kabongo *et al.*, 2011). A prominent negative long wavelength free-air gravity anomaly of ~ -30 mGal is centred on the basin (Figure 5.1c). Lithospheric thickness estimates based on surface-wave tomographic models are generally > 200 km, which suggests that the basin is underlain by a thick cratonic root (Figure 5.1d; e.g. Ritsema & van Heijst, 2000; Crosby *et al.*, 2010; Priestley & M^{c}Kenzie, 2013; Priestley *et al.*, 2019).

Attempts to reconstruct and understand the evolution on the Congo basin have been hindered by a lack of observational constraints. Limited exposure within the basin means that geological investigations have been restricted to its margins. Geophysical and borehole data were acquired in two phases during the 1950s and 1970s. On the basis of these data, Daly *et al.* (1991, 1992) suggested that the basin initiated during a phase of rifting and that subsequent thermal relaxation could explain subsidence until Mesozoic times. They proposed that regional unconformities developed during periods of continent-wide compression imposed at far-field plate boundaries. However, they were unable to explain continued subsidence in Mesozoic and Cenozoic times. Several authors then suggested that this 'anomalous' subsidence could be generated by con-

vective downwelling beneath the plate (Hartley & Allen, 1994; Downey & Gurnis, 2009; Forte *et al.*, 2010). More recently it has been pointed out that the large thermal time constant of thick cratonic lithosphere means that Neoproterozoic stretching could account for protracted subsidence throughout Phanerozoic times (Crosby *et al.*, 2010; Kadima Kabongo *et al.*, 2011; Lucazeau *et al.*, 2015).

To date, no single model proposed for the Congo basin satisfies all of the available observational constraints. In this Chapter, I investigate the origin and evolution of the basin using a range of approaches. First, available outcrop and borehole stratigraphic information is reviewed. Newly digitised seismic reflection profiles acquired during the 1970s are also re-interpreted to characterise basin architecture. Secondly, crustal and lithospheric thicknesses and compositions are constrained using published receiver function analyses, earthquake tomographic models and geochemical analyses of peridotite xenoliths. Thirdly, the extent to which stretching of thick lithosphere and subsequent thermal relaxation can explain the basin's long-term subsidence history is investigated. I also explore whether convective processes at the base of the plate can explain the formation of basin-wide unconformities and subsequent pulses of tectonic subsidence. Fourthly, the basin is compared to two other intracratonic basins: Taoudeni, West Africa; and Parnaíba, Brazil.

5.1 Stratigraphy and basin Architecture

5.1.1 Exposure and well data

Dense vegetation and limited exposure means that stratigraphic information from within the Congo basin can only be obtained from well data and comparison with outcrops around the basin's margins. Two shallow wells, Samba and Dekese, were drilled in the 1950s by the Synidcat pour l'Étude Géologique et Minière de la Cuvette Congolaise (Figure 5.2; Cahen *et al.*, 1959, 1960). In 1981, two deep exploration wells, Mbandaka and Gilson, were drilled by an industrial consortium. This well data was combined with outcrop observations by Energy Consultants Limited (ECL, 1988), Lawrence & Makazu (1988) and later Daly *et al.* (1991, 1992) in order to develop a regional stratigraphic framework. This framework was subsequently updated by Kadima *et al.* (2011). These authors identified three major stratigraphic sequences, bounded by regional unconformities (named U0–U3; Kadima *et al.*, 2011), and spanning Neoproterozoic to Quaternary times. Details of these sequences are discussed in the following sections and

summarised in Figure 5.3. Also shown in Figure 5.3 is a portion of the seismic reflection profile L52, which coincides with the Samba well (Figure 5.2).

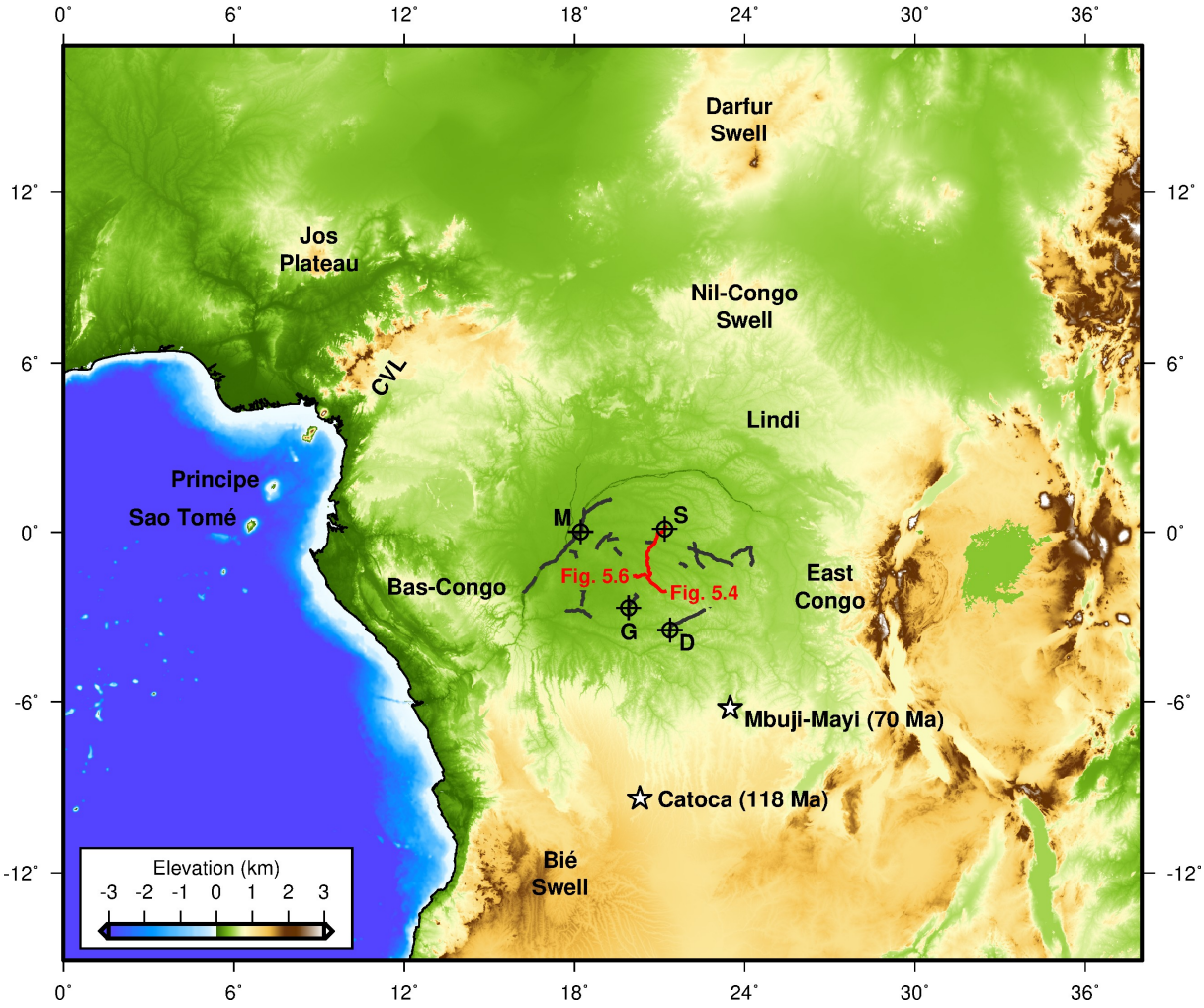

Figure 5.2: Overview of the Congo basin and its surroundings. ETOPO1 topographic and bathymetric map of the region surrounding the Congo basin (Amante & Eakins, 2009). Geographic features referred to in main text are labelled. Circles with crosses = wells, where M = Mbandaka, G = Gilson, S = Samba and D = Dekese; grey lines = reflection seismic profiles collected with Congo basin; red lines = reflection seismic profiles shown in Figures 5.4 and 5.6; stars = Mbuji-Mayi and Catoca kimberlite pipes.

Carbonate-Evaporite Sequence

ECL (1988) used the term 'Carbonate-Evaporite Sequence' (CES) to describe basal sediments recovered from the Mbandaka and Gilson wells. The sequence is bounded by unconformities U0 and U1, where U0 represents the sediment-basement interface. Limited chronostratigraphic information was recovered from the Mbandaka and Gilson wells. Age estimates are therefore

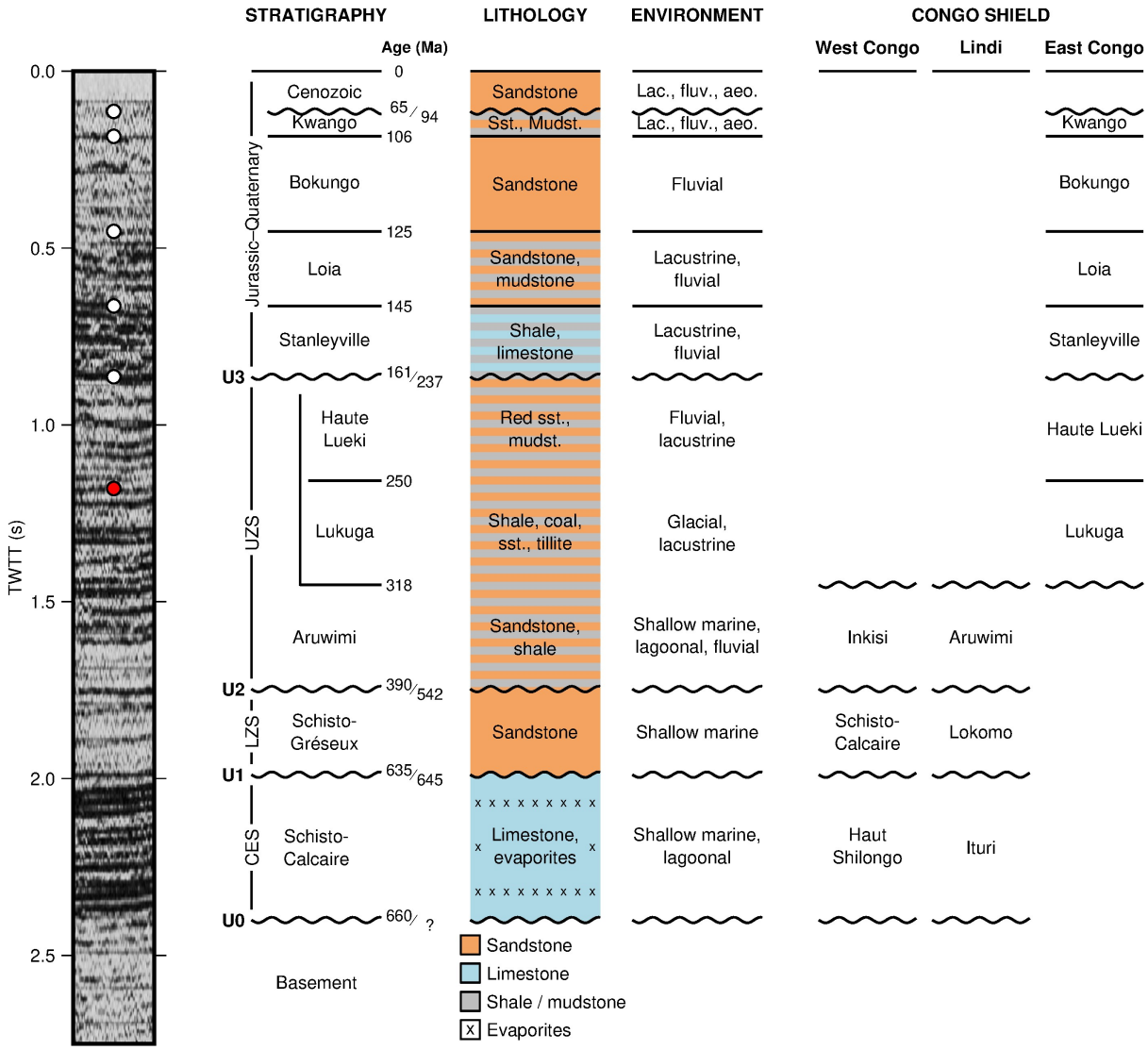

Figure 5.3: Stratigraphy of the Congo basin. Part of seismic reflection profile L52 corresponding to Samba well shown on the left-hand side (see Figures 5.2 and 5.4 for location). White circles = major stratigraphic horizons; red circle = base of well (ECL, 1988). Note that Lukuga and Haute Lueki groups are not reported from Samba well but are shown for reference. Stratigraphic information compiled primarily from information presented by ECL (1988), Daly *et al.* (1992) and Kadima *et al.* (2011). Note that all numerical ages are approximate. CES = Carbonate-Evaporite Sequence; LZS = Lower Zaire Sequence; UZS = Upper Zaire Sequence; Sst. = sandstone; Mudst. = mudstone; Lac. = lacustrine; fluv. = fluvial; aeo. = aeolian.

mainly based on regional correlation, particularly with the West Congo and Lindi supergroups exposed at the western and northeastern basin margins, respectively (Figure 5.2). The CES, also referred to as the 'Schisto-Calcaire', consists of stromatolitic carbonates and evaporites which form a thick band of bright reflections in the seismic reflection profile (Figure 5.3). Daly *et al.* (1992) suggested that these carbonates are equivalent to the Ituri group, which comprises similar lithologies and unconformably overlies basement rocks in the Lindi basin (Verbeek, 1970;

Tait *et al.*, 2011). Poidevin (2007) inferred an Early Neoproterozoic age for the Ituri group on the basis of strontium isotopic chronologies and microfauna assemblages. This sequence is also correlated with carbonates of the Haut Shiloango group of the West Congo basin (Frimmel *et al.*, 2006; Tait *et al.*, 2011; Kadima *et al.*, 2011). Both the Ituri and Haut Shiloango groups are bounded by diamictite deposits associated with the Sturtian and Marinoan glaciations. If these glaciations are assumed to be globally synchronous, resonable bounds can be placed on their ages. Radiometric dating of deposits in, for example, Africa, Australia, Canada, China and Mongolia yielded age estimates for the Sturtian and Marinoan glaciation of $\sim$ 720–660 Ma, and $\sim$ 645–635 Ma, respectively (e.g. Hoffman *et al.*, 2004; Condon *et al.*, 2005; Rooney *et al.*, 2015; Prave *et al.*, 2016). An appropriate age estimate for the CES would therefore appear to be $\sim$ 660–645 Ma (i.e. the Cryogenian period).

Lower Zaire Sequence

The unit overlying unconformity U1 and underlying unconformity U2, referred to as the 'Lower Zaire Sequence' (LVS) or the 'Schisto-Gréseux', comprises carbonates and siliciclastic rocks and generally appears weakly banded in seismic reflection profiles (Figure 5.3). ECL (1988) and Daly *et al.* (1992) preferred an Early Cambrian age for the sequence, citing unpublished sphaeromorph acritarch data, and suggested that it correlated with the Lokomo Group of the Lindi basin (Verbeek, 1970; Tait *et al.*, 2011). Kadima *et al.* (2011) suggest the sequence also correlates with the Schisto-Calcaire group of the West Congo basin. The Lokomo and Schisto-Calcaire groups both overlie diamactite and characteristic 'cap-carbonate' deposits associated with the Marinoan glaciation ($\sim$ 660–645 Ma; e.g. Hoffman *et al.*, 2004; Condon *et al.*, 2005; Rooney *et al.*, 2015; Prave *et al.*, 2016). These relationships suggest that the unconformity seperating this sequence from the underlying carbonates represents a $\sim$ 15 Myr period corresponding to the Marinoan glaciation, and that deposition then continued through Ediacaran and possibly into early Cambrian times. I note here that a recent study by Linol *et al.* (2015a) re-assigned these sediments to Permo-Carboniferous times, on the basis of unpublished palynological data and comparison with an exposed section along the Kwango river at the southwestern margin of the Congo basin. This interpretation contradicts established correlations with sediments of the West Congo and Lindi basins and quoted acritarch ages. It is probably unlikely, but cannot necessarily be ruled out.

Upper Zaire Sequence

Sediments bounded by unconformities U2 and U3 were named the 'Upper Zaire Sequence' by ECL (1988). This sequence is represented by a series of moderately bright reflections in seismic reflection profiles (Figure 5.3). The lower part of the UZS is generally correlated with red sandstones of the Aruwimi group in the Lindi basin, and with the similar Inkisi Redbeds of the West Congo basin (ECL, 1988; Daly *et al.*, 1992; Kadima *et al.*, 2011). Age control for these sandstones is poor. They lie above the so-called 'Pan-African' unconformity, thought to be related to the culmination of the Pan-African orogeny in late Neoproterozoic times (e.g. Tohver *et al.*, 2006). They are therefore generally assigned broadly to the lower-to-middle Paleozoic era (e.g. ECL, 1988; Daly *et al.*, 1992). ECL (1988) recovered undiagnostic sphaeromorph bodies from the Lindian section which they considered to predate late Silurian times. Elsewhere in the Congo Shield, placoderm fish remnants have been reported from similar redbeds and tentatively assigned a Devonian age (Tack *et al.*, 2008). The Aruwimi group is thought to represent deposition in shallow marine (tidal), lagoonal and fluvial conditions.

The upper part of the UZS is thought to correspond to the Lukuga and Haute Lueki groups, best exposed along the eastern margin of the Congo basin and considered contemporaneous with the Karoo Group of southern Africa (Figure 5.2; ECL, 1988; Daly *et al.*, 1992; Kadima *et al.*, 2011). The Lower Lukuga group consists of interbedded glacial tillites and lacustrine shales (ECL, 1988; Linol *et al.*, 2015a). Above these glacial deposits, the Upper Lukuga group includes coal bearing mudstones and sandstones that are considered to be lacustrine. Bose & Kar (1978) proposed an upper Carboniferous to Permian age for the Lukuga group on the basis of paleobotanical observations, which is consistent with the history of Paleozoic glaciation elsewhere in Africa (e.g. Montañez & Poulsen, 2013). Above the Lukuga group, red sandstones and mudstones of the Haute Lueki group are found (ECL, 1988; Linol *et al.*, 2015a). These siliciclastic rocks are thought to represent a continuation of lacustrine and fluvial environments. Plant remains and spores recovered from the bottom part of the group yielded a Triassic age (Bose & Kar, 1976).

There has been some debate concerning the nature of the contact between the Aruwimi and Lukuga groups within the Congo basin. Original descriptions of cored sediments suggested that the contact was unconformable, leading some authors to infer an Early Paleozoic age for the Aruwimi group and a significant depositional hiatus between it and the overlying Lukuga group (Cahen *et al.*, 1960; Daly *et al.*, 1992). However, this contact appears conformable on seismic reflection surveys and Kadima *et al.* (2011) questioned the interpretation of Cahen *et al.* (1960)

having re-examined the cores. On this basis, and considering anectodal evidence of Devonian fish remains cited by Tack *et al.* (2008), a Middle Paleozoic age for the Aruwimi group and relative continuity with the Lukuga group is preferred here. Note that neither the Aruwimi nor Lukuga-Haute Lukei groups are found throughout the Congo basin. For example, only the Aruwimi group is reported in the Samba well, whereas conglomerates of the Lukuga group are reported immediately above unconformity U2 in the Mbandaka well (ECL, 1988). Finally, I acknowledge that in the statigraphic framework proposed by Linol *et al.* (2015a), rocks of the UVZ are assigned entirely to the Triassic period.

Jurassic–Quaternary Sequence

Above unconformity U3, a thick and uniform sequence of Mesozoic to Cenozoic sedimentary rocks are found (ECL, 1988; Daly *et al.*, 1992; Giresse, 2005; Kadima *et al.*, 2011). Reasonable age control is available for these rocks, particularly on the basis of fish fossils and palynology (e.g. ECL, 1988). At the base of this sequence, the upper Jurassic Stanleyville formation consists of lacustrine shales and limestones (ECL, 1988; Caillaud *et al.*, 2017). This formation is imaged as a package of bright reflections in seismic reflection profiles (Figure 5.3). Subsequently, continental deposition continued throughout Cretaceous times, represented by sandstones and mudstones of the Loia, Bokungo and Kwango formations. A conglomeratic unit at the base of the Kwango formation could record a brief period of uplift and erosion between it and the underlying Bokungo formation (ECL, 1988). These formations and the overlying Cenozoic basin cover are separated by a minor unconformity.

5.1.2 Seismic reflection data

Between 1974 and 1976, an industrial consortium acquired $\sim$ 2,900 km of seismic reflection lines within the Congo basin (Figure 5.2). These data have been the subject of extensive interpretation in the intervening years (e.g. ECL, 1988; Daly *et al.*, 1991, 1992; Kadima *et al.*, 2011; Kadima Kabongo *et al.*, 2011). However, some controversy remains, particularly regarding the relative importance of extensional and shortening structures. Here, high resolution scanned images of processed seismic data provided by the Royal Museum for Central Africa, Tervuren (Belgium) were digitised and transferred into native SEG-Y format (J. Winterbourne, 2019, written comm.). This procedure allowed detailed examination and re-interpretation of the seismic

lines. Raw and interpreted data for lines L50, L51, L52, L62 and L63 are shown in Figures 5.4–5.6 (see Figure 5.2 for locations). In general, these images reveal a stratigraphic architecture typical of intracratonic basins. In particular, the upper part of the basin consists of thick, relatively uniform and undeformed packages of sediment bounded by unconformities, reminiscent of the 'layer-cake' stratigraphy described in North American intracratonic basins (Figures 5.4 and 5.6; e.g. Sloss, 1963; Allen & Armitage, 2012). In contrast, significant structure can be discerned below unconformity U2 (i.e. TWTT $\gtrsim$ 1.5 s). For example, profile L50 crosses a fault-bounded basement uplift known as the Kiri High (Figures 5.4b and 5.4f). In this section, I will first describe the nature of stratigraphic contacts before discussing the structural evolution of the basin.

Unconformity U0 represents the base of the acoustically imaged stratigraphy and is generally considered to represent the sediment-basement interface. Above unconformity U0, bright reflections of the Cryogenian Carbonate-Evaporite Sequence can be traced across each profile (Figures 5.4 and 5.6a). Thickening of these reflections towards the right-hand side of profile L50 is interpreted as a result of salt deformation (Figures 5.5c and 5.5d; ECL, 1988; Daly *et al.*, 1992). The CES is separated from the overlying Lower Zaire Sequence by a subtle unconformity, U1. This unconformity can be identified on the left-hand side of profile L50, where dipping reflections of the overlying LZS onlap a fold structure within the CES (Figures 5.5a and 5.5b). Incidentally, these onlapping relationships and the subtlety of unconformity U1 elsewhere are consistent with a short depositional hiatus with limited erosion separating the CES and LZS, as is generally believed, rather than the age difference of 100s of millions of years proposed by Linol *et al.* (2015a, see Section 5.1.1).

Unconformity U2, between the Lower and Upper Zaire Sequences, can be seen clearly truncating dipping reflections of the CES and LZS in several locations across the profiles, but is relatively subtle elsewhere (Figures 5.4, 5.5a and 5.5b, 5.5c and 5.5d, and 5.6c and 5.6d). It separates deformed Neoproterozoic rocks from relatively flat-lying and uniform Paleozoic sequences. Finally, unconformity U3 divides the UZS from the overlying Jurassic-Quaternary sequence. This boundary appears conformable across significant portions of the seismic reflection profiles but can be identified truncating gently dippng reflections of the UZS in some locations (Figures 5.5e, 5.5f, 5.6e and 5.6f).

The nature of tectonic deformation throughout the history of the Congo basin has been the subject of considerable debate. Lawrence & Makazu (1988) and Daly *et al.* (1991, 1992) suggested

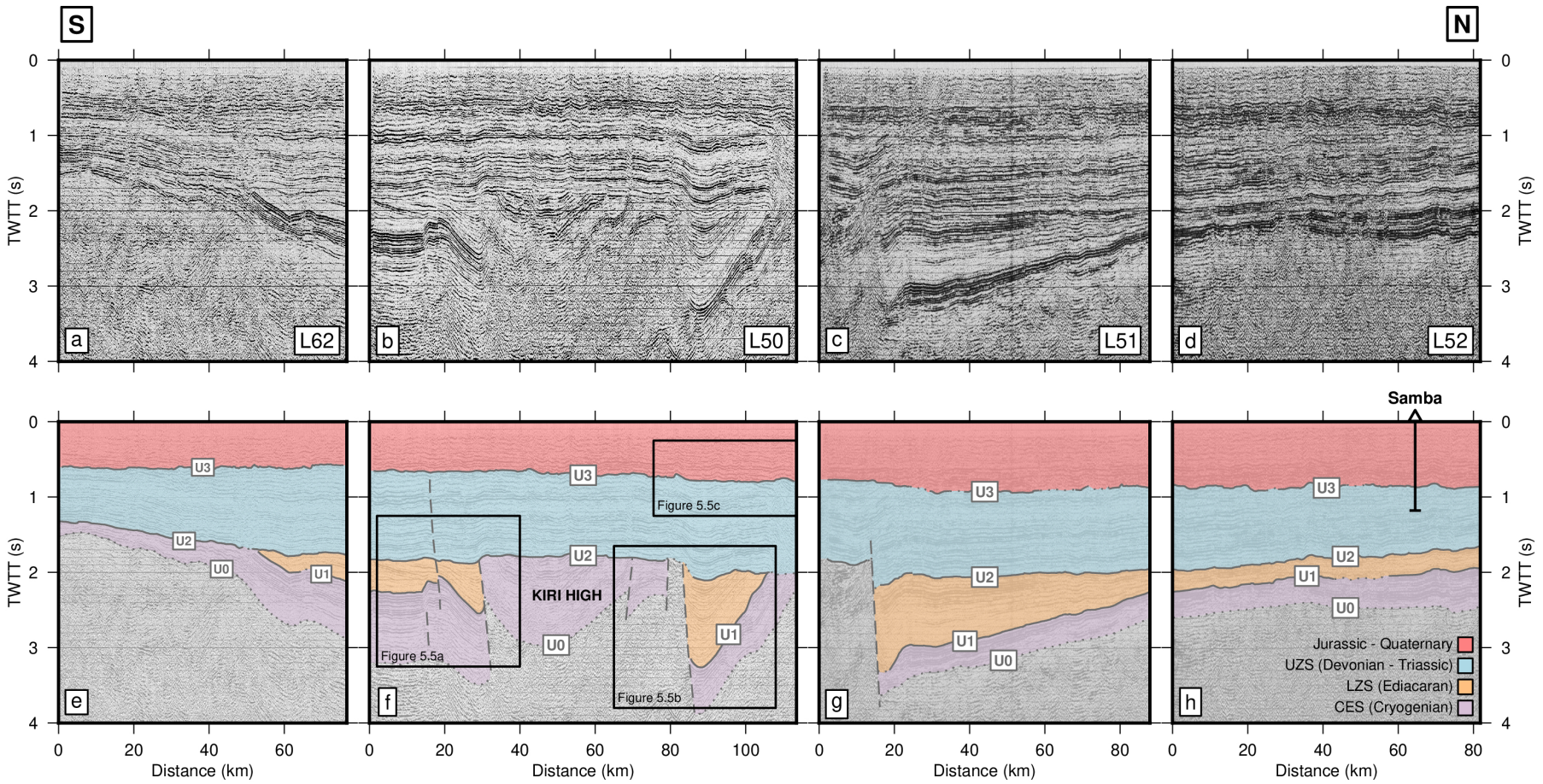

Figure 5.4: Seismic reflection profiles of the Congo basin. Lines (a) L62, (b) L50, (c) L51 and (d) L52. (e–h) Interpretation of seismic reflection profiles shown in (a–d), highlighting major sedimentary packages separated by unconformities U0–U3. Solid lines = unconformities identified using sedimentary structure or well data and extrapolated along continuous reflections; dotted lines = extrapolated or approximate unconformities; dashed lines = faults; TWTT = two-way travel time. Location of Samba well shown in (h).

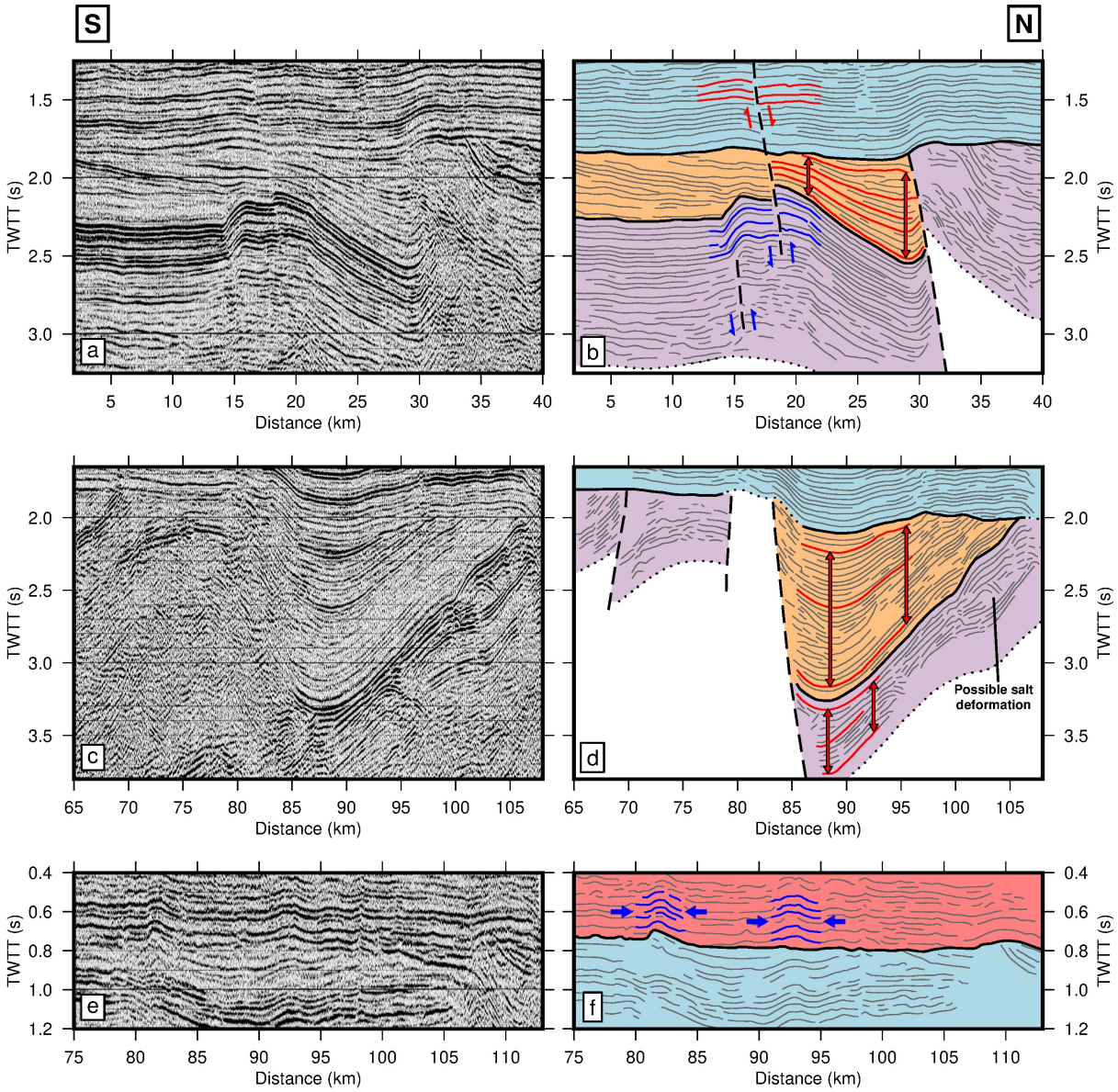

Figure 5.5: Detailed interpretations of seismic reflection profile L50. (a, c, e) Portions of seismic reflection profile L50. Locations shown in Figure 5.4f. (b, d, f) Interpretations of subsections shown in (a, c, e). Black solid lines = major unconformities; black dotted lines = major unconformities where extrapolated or less certain; black dashed lines = faults; grey lines = other horizons; red lines highlight structure related to extensional deformation; blue lines highlight structure related to compressional deformation; background colour scheme as in Figure 5.4.

that the basin initiated in a rift setting but subsequently experienced significant shortening. They attributed an initial phase of shortening to the 'Pan-African' orogenic event and the assembly of Gondwana, and also identified a subsequent phase of shortening in Late Paleozoic times. As such, they interpret much of the basin's deep structure, such as the prominent Kiri High, in terms of folding and reverse faulting. More recently, Crosby *et al.* (2010) and

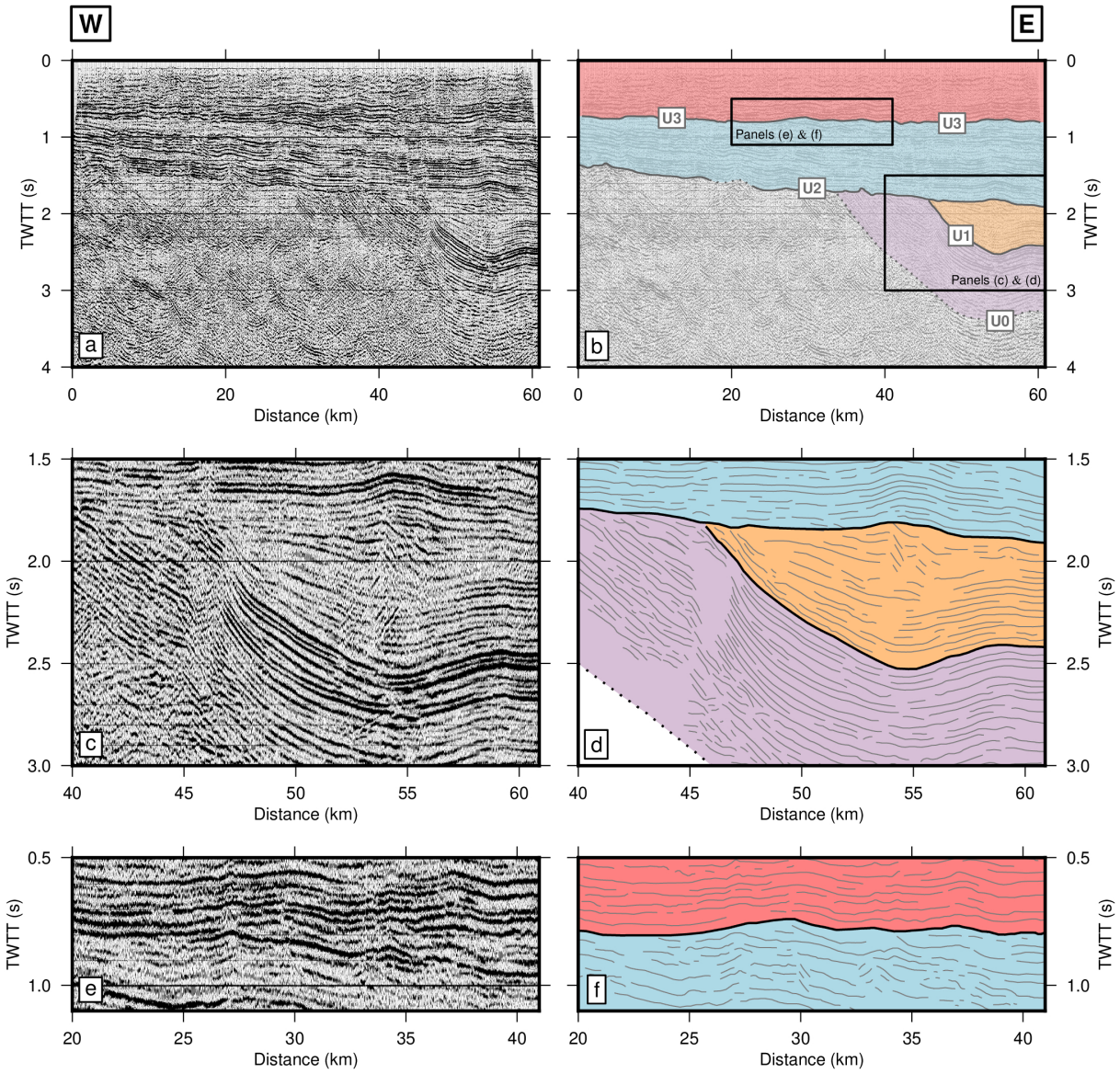

Figure 5.6: Seismic reflection profile L63. (a) Full-length profile L63. (b) Interpretation of full-length profile shown in (a). (c, e) Portions of seismic reflection profile L63, locations shown in (b). Black solid lines = major unconformities; black dotted lines = major unconformities where extrapolated or uncertain; grey lines = other horizons; background colour scheme as in Figure 5.4.

Kadima Kabongo *et al.* (2011) suggested that extensional faulting could explain the majority of imaged structure. Portions of profile L50 which illustrate key structural features are shown and interpreted in Figure 5.5.

At the right-hand side of profile L50, a thick package of CES and LZS reflections can be seen dipping from north to south towards an acoustically transparent region at the edge of the Kiri High (along-profile distances of $\sim$ 80–85 km; Figures 5.5c and 5.5d). South of this relatively

transparent zone a bright package of reflections interpreted as the CES can be seen at shallower depths (TWTT $\sim$ 2–2.5 s). Daly *et al.* (1991, 1992) interpret this structure as a large-scale northward-verging fold. However, as highlighted in Figure 5.5d, reflections of the CES and particularly the LZS gradually thicken southwards into the transparent zone. This thickening, or stratigraphic growth, is characteristic of deposition in the hanging wall of an active normal fault (e.g. Allen & Allen, 1990; Miall, 1997). Downwarping of reflections within the UZS overlying this structure can be explained by progressive compaction of thickened sedimentary packages in the fault's hanging wall. This structure is therefore interpreted here as a simple normal fault and associated half graben, although some reactivation as a reverse fault cannot be ruled out.

A similar structure can be seen at the opposite side of the Kiri High, where northward dipping reflections within the the LZS thicken substantially into a seismic discontinuity at a range of $\sim$ 30 km (Figure 5.5a and 5.5b). Again, reflections within the overlying UZS are downwarped above thickened hanging-wall deposits. This structure therefore also appears to have formed as a half graben bounded by a normal fault, although in this case the orientation of the mapped fault suggests it may have been rotated and reactivated in a reverse sense. Nearby, a prominent fold and associated reverse faults can be seen to displace bright reflections of the CES (Figures 5.5a and 5.5b). These structures provide unequivocal evidence that the basin experienced a period of shortening, although total displacements are small. Onlapping relationships between the LZS and underlying CES imply that shortening occured between deposition of the two sequences, while continued folding of the LZS implies some shortening also occurred following its deposition.

Unlike the older CES and LZS, sediments of the overlying UZS and Jurassic-Quaternary Sequence appear to be relatively undeformed. At the left-hand side of profile L50, one fault can be seen propagating through the CES and LZS, where it displaces reflections in a reverse sense, into the overlying UZS, where it displaces younger reflections in a normal sense (Figures 5.5a and 5.5b). However, elsewhere, reflections of the UZS and and particularly the Jurassic-Quaternary Sequence are folded into gentle monoclines (e.g. Figures 5.5e and 5.5f). These structures suggest that the basin has experienced phases of minor extension and compression throughout Phanerozoic times. Indeed, source mechanisms of recent moderate-magnitude earthquakes from within the basin indicate that a transpressional regime exists at the present day (Foster & Jackson, 1998; Ayele, 2002; Crosby *et al.*, 2010; Craig *et al.*, 2011). On the profiles analysed in this study, no evidence is seen for a major deformational episode in late Paleozoic times, as suggested by Daly *et al.* (1991, 1992) and Kadima *et al.* (2011).

In summary, it appears that the basin's deep structure imaged in the lines examined here can largely be explained in terms of extensional faulting. In this interpretation, the Kiri High essentially forms an uplifted horst block bounded by normal faults. Some shortening is required, between deposition and of the CES and LZS, and following deposition of the LZS, but it appears to be relatively localised with small total displacements. The overlying UZS and Jurrasic-Quaternary sequence are relatively underformed and define a 'layer-cake' stratigraphy, typical of intracratonic basins (e.g. Sloss, 1963; Allen & Armitage, 2012). While these sediments have been affected by minor extensional and compressional deformation, there is limited structural evidence for major deformational episodes on the profiles examined here. Such episodes have been inferred to generate basin-wide sequence-bounding unconformities by uplift and denudation (e.g. Daly *et al.*, 1991, 1992; Kadima *et al.*, 2011). An alternative mechanism may therefore be required to explain the formation of these regional unconformities.

5.2 Crustal and Lithospheric Template

An understanding of the structure of the lithosphere is essential for estimating the isostatic state of the Congo basin and for testing different models of its evolution. In the following sections, published receiver function, xenolith, tomographic and gravity data are compiled and modelled in order to constrain the thickness and composition of the crust and lithospheric mantle.

5.2.1 Receiver function analyses

By measuring travel-time differences between direct and converted phases, receiver function analyses can provide useful information about the one-dimensional velocity structure directly beneath a seismometer. This technique is often used to estimate crustal thicknesses. A recent study by Globig *et al.* (2016) compiled receiver function estimates of crustal thickness from across Africa, a subset of which is shown in Figure 5.7. No measurements have been made within the Congo basin itself, but some useful information is available from around the basin's surroundings.

Spatial variations in crustal thickness are compared with topographic and lithospheric thickness varations in Figures 5.7a and 5.7b. On areas of thin lithosphere (i.e. $\lesssim$ 120 km), such as around the Cameroon Volcanic Line, northwest of the Congo basin, and the East and West

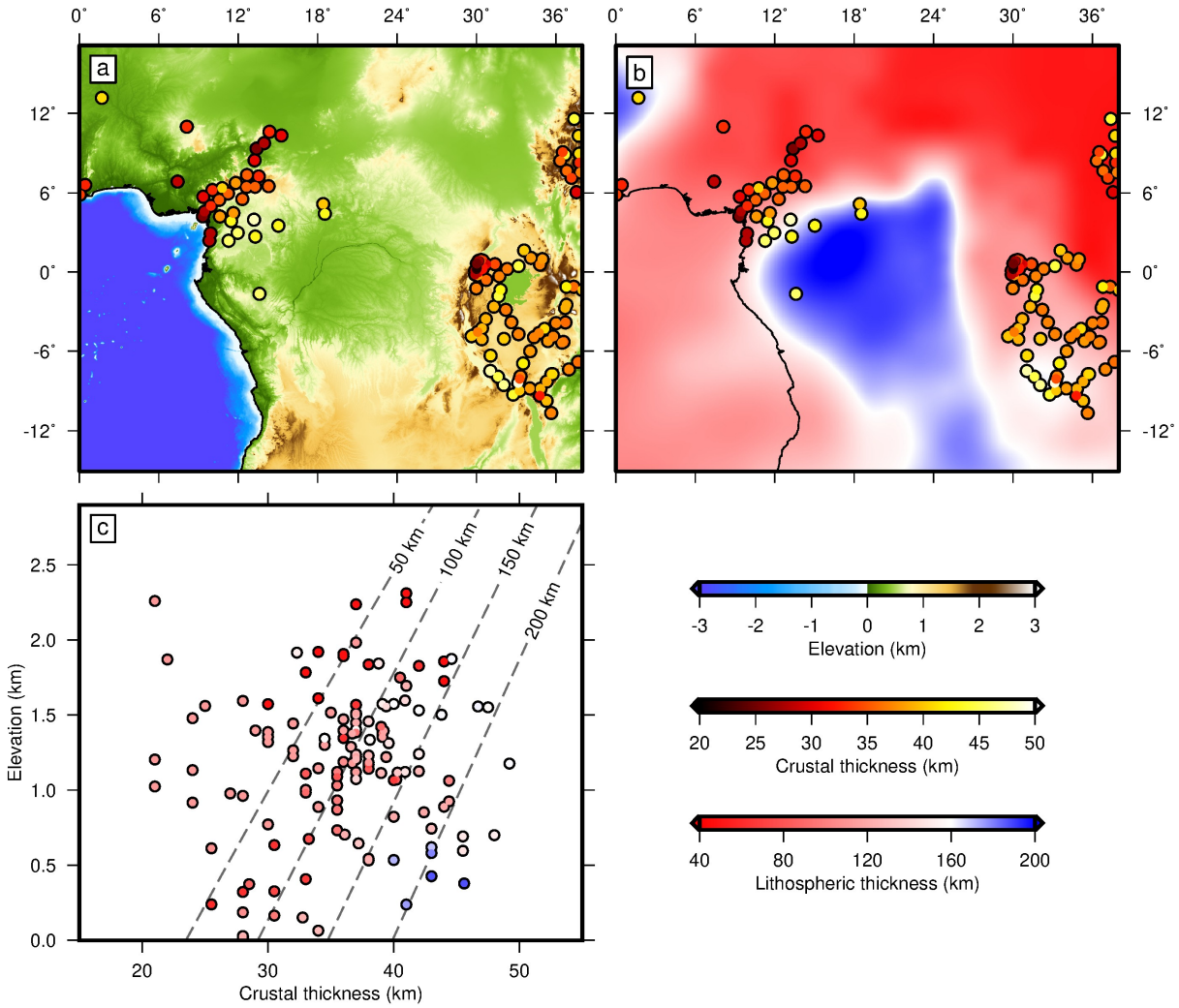

Figure 5.7: Crustal thickness estimates for the Congo-Kasai Craton and surroundings. (a) ETOPO1 topographic and bathymetric map of the region surrounding the Congo basin. Shaded circles = receiver function estimates of crustal thickness. (b) CAM2016Litho lithospheric thickness model from Priestley *et al.* (2019). Note that red–blue transition occurs at 160 km and thus approximately represents boundary between cratonic and non-cratonic lithosphere. (c) Crustal thickness as function of elevation. Circles = observed crustal thicknesses and elevations shaded by lithospheric thickness; dashed lines = crustal thickness as function of elevation for the equilibrated undepleted continental lithospheric thicknesses of 50–200 km, calculated using the procedure outlined in Section 3.1.1.

African Rifts, east of the Congo basin, crustal thicknesses vary significantly between $\sim$ 20–40 km. Information from cratonic lithosphere (i.e. $\gtrsim$ 160 km) is sparse, but suggests that the cratonic crust is thicker and more uniform, with crustal thickness estimates consistently lying within the range of 40–50 km (Sandvol *et al.*, 1998; Kosarian, 2006; Hansen *et al.*, 2009; Tokam *et al.*, 2010). The transition from non-cratonic to cratonic crust is particularly clear in Cameroon, northwest of the Congo basin, where crustal thicknesses rapidly increase from

$\sim$ 30 km to $>$ 40 km across the 160 km lithospheric thickness contour (Figure 5.7b; Tokam *et al.*, 2010). Tokam *et al.* (2010), who employed joint inversion of receiver function and surface-wave dispersion data, reported unusually fast velocities of 4.0–4.2 km s^{-1} for the lowermost 20 km of the crust on the Congo-Kasai Craton, which they interpreted as a dense, mafic layer. They report average crustal shear-wave velocites of $\sim$ 3.9 km s^{-1}, which corresponds to a mean crustal density of $\sim$ 2890 kg m^3 using the relationships of Brocher (2005). Overall, the available data are consistent with a mean crustal thickness of 45 $\pm$ 0.5 km, including a thick, dense lower crust.

Elevation as a function of estimated crustal thickness is shown in Figure 5.7c, and compared with predicted relationships for different lithospheric thicknesses calculated using the procedure outlined in Section 3.1.1. No clear relationship exists between crustal thickness and elevation, probably reflecting a large range in lithospheric thicknesses and possibly convective support for topography in the Afar region. However, in general, cratonic regions sit lower than non-cratonic regions with equivalent crustal thicknesses, consistent with the presence of a thick lithospheric root beneath the cratons.

5.2.2 Constraints from peridotite xenoliths

Important information about the composition and structure of the cratonic mantle lithosphere can be obtained from peridotite xenocrysts and xenoliths exhumed in kimberlite pipes. Appropriate analyses are available for two Cretaceous kimberlite clusters on the Congo-Kasai Craton: the Mbuji-Mayi cluster in the Democratic Republic of Congo and the Catoca cluster in Angola (Figure 5.2).

Lithospheric composition and density

It is widely believed that cratonic lithosphere is chemically distinct from ambient convecting mantle. It is thought that progressive partial melting during growth of the continents left a mantle residue depeleted in incompatible elements. It has been proposed that such depletion, which acts to lower lithospheric density, is necessary to stabilise thick cratonic roots observed at the present day (e.g. Jordan, 1978). However, the nature and extent of chemical depletion within the continental lithosphere remains poorly constrained. An understanding of the composition, and thus density, of lithospheric mantle beneath the Congo-Kasai Craton is required

if its isostatic state and evolution are to be estimated.

Crosby *et al.* (2010) estimated mean density of cratonic lithosphere using a global database of crustal thickness and density and lithospheric thickness observations. Their approach was to determine lithospheric densities for which continental columns were in isostatic equilibrium with an idealised mid-oceanic ridge. They estimated that, for regions where lithospheric thicknesses exceed 150 km, the lithospheric mantle density was 33 ± 16 kg m^{-3} lower than that of ambient convecting mantle. This value is consistent with estimates from gravity modelling (Kaban *et al.*, 2003).

Since xenoliths and xenocrysts exhumed in kimberlite pipes directly sample lithospheric mantle, their composition can be used to be infer its bulk composition. Of particular use are olivine xenocrysts, since their magnesium number, Mg# = Mg/(Mg+Fe), closesly reflects that of the bulk rock. Few such data are available for the Congo-Kasai Craton, but Kosman *et al.* (2016) provide analyses of ~ 100 olivine inclusions in alluvial diamonds extracted from the Kasai River. These diamonds were probably sourced from the adjacent Mbuji-Mayi and/or Catoca kimberlite clusters (Figure 5.2). Mean Mg# ($\pm 1\sigma$) of these inclusions is 0.928 ± 0.075, which implies that lithospheric mantle of the Congo-Kasai Craton is significantly depleted with respect to ambient convecting mantle, which is thought to have Mg# ~ 0.9. Lee (2003) provides an empirical relationship for estimating bulk standard-pressure-temperature (STP) density, ρ_0, from olivine Mg#, where $\rho_0 = -1,520\text{Mg\#} + 4740$, which yields a value of $3{,}329 \pm 11$ kg m^{-3}. This value is equivalent to depletion of ~ 35 kg m^{-3} relative to ambient mantle with Mg# ~ 0.9, which lies within the global bounds estimated by Crosby *et al.* (2010).

Lithospheric thermal structure

Since element partitioning between mineral phases is pressure and temperature dependent, mineral compositions of mantle xenoliths and xenocrysts are dependent on the depth at which they equilibrated. Several schemes have been developed for calculating equilibration pressures and temperatures from the compositions of peridotite xenoliths and xenocrysts (see e.g. Grutter, 2009; Nimis & Grütter, 2010). It is generally believed that the most reliable schemes are those which estimate temperatures based on calcium-magnesium exchange between pyroxenes and aluminium exchange between garnet and orthopyroxene (Taylor, 1998; Grutter, 2009; Nimis & Grütter, 2010). The available data from the Congo-Kasai Craton consist mainly of individual

clinopyroxene analyses (Pivin *et al.*, 2009, 2011; Ashchepkov *et al.*, 2012). Nimis & Taylor (2000) developed a single-clinopyroxene scheme, which is of comparable accuracy to the two-pyroxene and garnet-orthopyroxene schemes scheme (i.e. $\sim \pm$ 2.3 kbar and $\sim \pm$ 30 °C; Grutter, 2009; Nimis & Grütter, 2010). In this scheme, pressure, P, and temperature, T, are parameterised by

$$P(\text{kbar}) = -\frac{T(\text{K})}{126.9} \ln\left(a^{\text{Cpx}}_{\text{CaCrTs}}\right) + 15.483\left(\frac{\text{Cr}\#^{\text{Cpx}}}{T}\right) + \frac{T(\text{K})}{71.38} + 107.8, \tag{5.1}$$

and

$$T(\text{K}) = \frac{23166 + 39.28P(\text{kbar})}{13.25 + 15.35\text{Ti} + 4.5\text{Fe} - 1.55\text{Al} + \text{Cr} - \text{NaK} + \left(\ln a^{\text{Cpx}}_{\text{CaCrTs}}\right)^2}, \tag{5.2}$$

respectively. The activity of the CaCr-tchermakitic compenent of clinopyroxene, $a^{\text{Cpx}}_{\text{CaCrTs}}$, is given by $\text{Cr} - 0.81\text{Cr}\#(\text{Na} + \text{K})$ and the chromium number, Cr#, by $\text{Cr}/(\text{Cr} + \text{Al})$. Since temperature appears in the pressure equation and *vice versa*, these equations are solved by iteration.

Application of the Nimis & Taylor (2000) thermobarometer to clinopyroxene data from Mbuji-Mayi and Catoca yielded equilibration pressure and temperature estimates shown in Figure 5.8. Note that estimated equilibration temperatures $\lesssim$ 800 °C lie outwith the calibrated range of the Nimis & Taylor (2000) thermobarometer and as such may not be reliable (relevent samples are shown as triangles in Figure 5.8). Distributions from both clusters define broad arrays of increasing temperature with depth, with gradients steeper than that of the mantle isentrope, consistent with their sampling conductive lithospheric geotherms.

To relate these distributions to the thickness and thermal state of the lithosphere, I followed the approach of M$^{\text{c}}$Kenzie *et al.* (2005) and Mather *et al.* (2011) by fitting modelled steady-state geotherms to the data using the FITPLOT algorithm. The procedure used for calculating continental lithospheric geotherms was outlined in Section 3.1.1 and includes the effects of radiogenic heat production in the crust and temperature-dependent conductivity in the mantle (Hofmeister, 1999). In this case, for completeness, the structure of the thermal boundary layer is included. In the absence of local constraints, total crustal thicknesses for each location were set to 45 km, the average value for the Congo-Kasai Craton (see Section 5.2.1). The FITPLOT algorithm varies thicknesses of the upper/lower crust and mechanical boundary layer and selects the best-fitting model. Results are presented in Table 5.1 and shown in Figure 5.8. Calculated equilibration pressure and temperature distributions from both clusters can be adequately re-

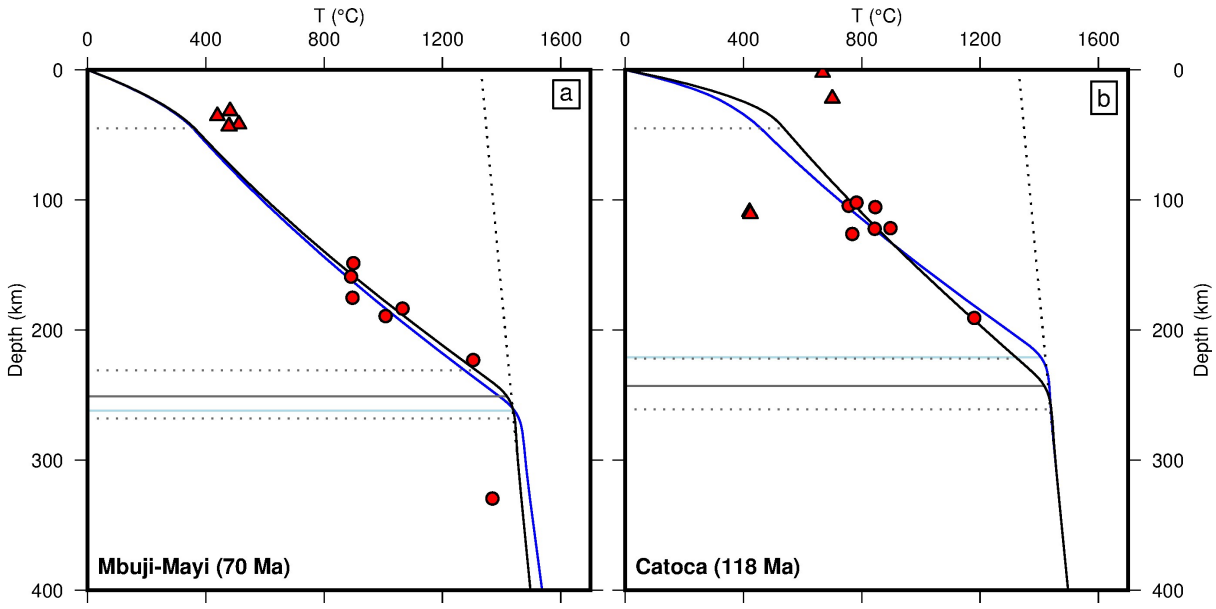

Figure 5.8: Clinopyroxene xenocrysts and lithospheric structure of the Congo-Kasai Craton. (a) Results for Mbuji-Mayi. Red circles = reliable estimates of xenocryst equilibration pressure and temperature used for geotherm fitting; red triangles = estimates of xenocryst equilibration pressure and temperature not used for geotherm fitting (see text for discussion); black line = best-fitting geotherm calculated using FITPLOT algorithm (McKenzie & Bickle, 1988; McKenzie *et al.*, 2005; Mather *et al.*, 2011); blue line = best-fitting geotherm where upper crust thickness is set to 25 km and lower crust thickness to 20 km (i.e. structure obtained from receiver function analysis (Tokam *et al.*, 2010)); black dotted line = isentropic temperature profile for T_p = 1330 °C; solid grey line = best-fitting LAB; solid light blue line = best-fitting LAB where upper crust thickness is set 25 km and lower crust thickness to 20 km; dotted grey lines, from top to bottom = base of crust, best-fitting base of mechanical boundary layer, best-fitting base of thermal boundary layer. (b) As (a), for Catoca.

produced by steady-state geotherms. Best-fitting lithospheric thicknesses are > 250 km for both clusters, consistent with the presence of a thick lithospheric root beneath the Congo-Kasai Craton. Best-fitting thicknesses of upper/lower crust are rather different for the two clusters despite there relative proximity. Therefore, best-fitting geotherms where the crustal structure is fixed to that estimated by Tokam *et al.* (2010) for the Congo-Kasai craton are also presented (Figure 5.8, Table 5.1). In this case, the best-fitting lithospheric thickness increases to 260 km for the Mbuji-Mayi cluster and is reduced to 221 km for the Catoca cluster.

The surface heat flow, q_s, associated with calculated geotherms is given by

$$q_s = \frac{t_{uc}H_{uc} + \left(t_c - t_{uc}\right)H_{lc} + F_{moho}}{k_{cc}} \tag{5.3}$$

where t_{uc} and t_c are the upper crust and total crust thickness, respectively; H_{uc} and H_{lc} the

Table 5.1: Best-fitting steady-state geotherms for the Congo-Kasai Craton.

Location	Samples	t_{uc} (km)	t_{lc} (km)	t_{MBL} (km)	t_{TBL} (km)	t_{LAB} (km)	Calc. q_s (mW m^{-2})	Obs. q_s (mW m^{-2})
Mbuji-Mayi	7	0[a]	45[a]	231	37	251	29	44 ± 20
		25[b]	20[b]	240	38	260	45	
Catoca	7	38[a]	7[a]	222	39	243	55	–
		25[b]	20[b]	201	37	221	47	

[a]Best-fitting crustal structure.
[b]Crustal structure fixed to that determined by Tokam *et al.* (2010) for the Congo-Kasai craton.

heat production rate in the upper and lower crust, respectively; k_{cc} the conductivity of the crust (assumed to be constant); and F_{moho} the heat flux supplied to the base of the crust. Predicted surface heat flow for Mbuji-Mayi and Catoca ranges between 29–54 mW m^{-2} (Table 5.1). Sebagenzi *et al.* (1993) measured surface heat flow at various locations in the southern Congo-Kasai Craton. Their estimate of 44 ± 20 mW m^{-2} at Mbuji-Mayi is consistent with the values obtained here from fitting geotherms to xenocryst pressure-temperature data.

5.2.3 Constraints from tomographic models

An additional way to investigate the thermal and, to a lesser extent, compositional structure of the lithosphere is earthquake tomography, since the speed at which seismic waves propagate through the Earth is dependent on temperature and composition (Faul & Jackson, 2005). Several studies have successfully employed surface-wave tomography in this capacity, since surface-wave velocities are stongly dependent on the depth-distribution of shear-wave velocities, V_s, which are themselves strongly temperature dependent (e.g. Priestley & McKenzie, 2006, 2013; Czarnota *et al.*, 2019; Priestley *et al.*, 2019). Another advantage of surface-wave tomography is that, in regions with limited station coverage such as the Congo basin, good path coverage can still be obtained due to the crossing great-circle paths of horizontally propagating waves (e.g. Crosby *et al.*, 2010). Here, two recent global surface-wave tomographic models are compared: SL2013sv and CAM2016Vsv_200 (Figures 5.9 and 5.10; Schaeffer & Lebedev, 2013; Ho *et al.*, 2016).

Vertical slices through the SL2013sv and CAM2016Vsv_200 models along transects A–A' and B–B' are shown in Figures 5.9d, 5.9e, 5.10d and 5.10e. In both cases, the Congo basin and its surroundings, particularly to the south, are underlain by strongly negative shear-wave velocity anomalies to depths > 200 km. Negative shear-wave anomalies are consistent with the presence of a thick, cold lithospheric root in these regions. At greater depths, shear-wave velocity anomalies

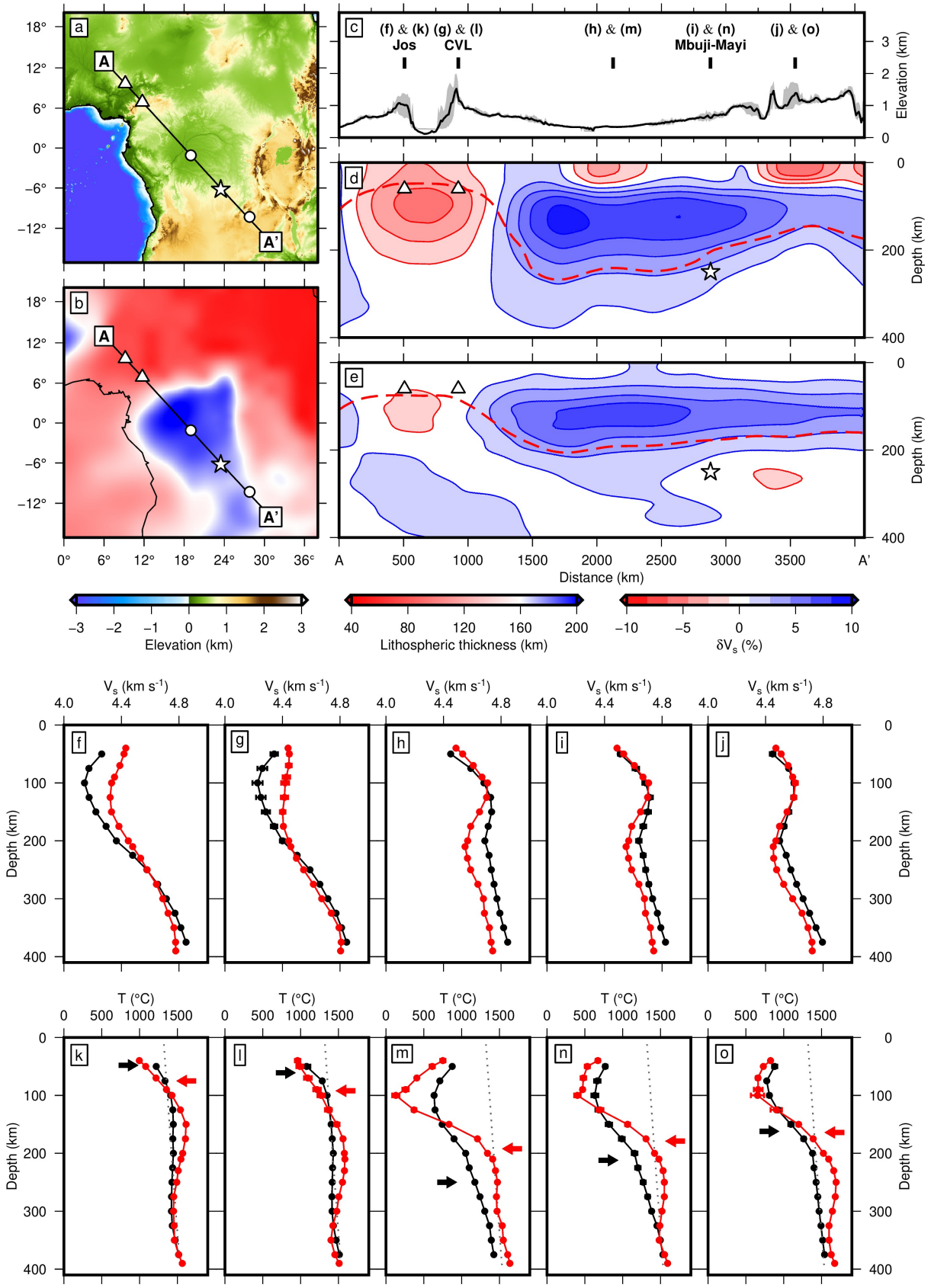

Figure 5.9: *Caption overleaf.*

are weakly negative or neutral.

It is desirable to relate these velocity models to lithospheric structure in a more quantitative way. Priestley & M^{c}Kenzie (2006) proposed a method for doing so which has subsequently been developed by Priestley & M^{c}Kenzie (2013), Czarnota *et al.* (2019) and Priestley *et al.* (2019). This method is used by Czarnota *et al.* (2019) to estimate lithospheric thicknesses from the SL2013sv model, while it was used by Priestley *et al.* (2019) to estimate lithospheric thicknesses from the CAM2016Vsv_200 model. First, shear-wave velocities are converted into temperature using the calibrated parameterisation described in Section 3.3. Within the oceans, where geotherms are disequilibrated, lithospheric thickness is defined using the 1175 °C isotherm, which corresponds to the base of the thickening oceanic plate (Richards *et al.*, 2018). Czarnota *et al.* (2019) also use the 1175 °C isotherm to define the lithospheric thickness within the continents. In contrast, Priestley & M^{c}Kenzie (2006, 2013) and Priestley *et al.* (2019) fit steady-state geotherms to their estimates of temperature as a function of depth using the approach applied to xenolith equilibrium pressures and temperatures in Section 5.2.2 (M^{c}Kenzie *et al.*, 2005; Mather *et al.*, 2011).

Example profiles of V_s as a function of depth for several locations along transects A–A' and B–B' are shown in Figures 5.9f–5.9j and 5.10f–5.10j. Corresponding estimates of temperature as a function of depth are shown in Figures 5.9k–5.9o and 5.10k–5.10o, with associated estimates of lithospheric thickness labelled. Lithospheric thickness estimates are also shown as dashed lines

Figure 5.9: ***Previous page.*** **Surface-wave tomographic models: transect A–A'.** (a) ETOPO1 topographic and bathymetric map of the region surrounding the Congo basin (Amante & Eakins, 2009). Location of transect A–A' with locations of vertical profiles (f–j) and (k–o) shown. Triangles = locations where lithospheric thickness is constrained by geochemistry of mafic volcanic rocks; stars = locations where lithospheric thickness is constrained by geochemistry of peridotite xenoliths; circles = other locations of vertical profiles in (f–j) and (k–o). (b) As (a) with lithospheric thickness map from Priestley *et al.* (2019). (c) Topographic swath A–A' with locations of vertical profiles (f–j) and (k–o) shown. (d) Vertical slice through surface-wave tomographic model of (Schaeffer & Lebedev, 2013) along transect A–A'. Triangles = lithospheric thickness estimates from geochemistry of mafic rocks (Ball, 2019); stars = lithospheric thickness estimates from geochemistry of peridotite xenoliths (Section 5.2.2); red dashed line = lithospheric thickness from Czarnota *et al.* (2019). (e) As (d) with surface-wave tomographic model of Ho *et al.* (2016) and lithospheric thickness from Priestley *et al.* (2019). (f–j) V_s as function of depth at locations shown in (a, b, c). Black lines = model of (Schaeffer & Lebedev, 2013); red lines = model of Ho *et al.* (2016). (k–o) Temperature as function of depth. Black arrows = lithospheric thickness estimate from Czarnota *et al.* (2019); red arrow = lithospheric thickness estimate from Priestley *et al.* (2019); black dotted line = isentropic temperature as function of depth (M^{c}Kenzie & Bickle, 1988).

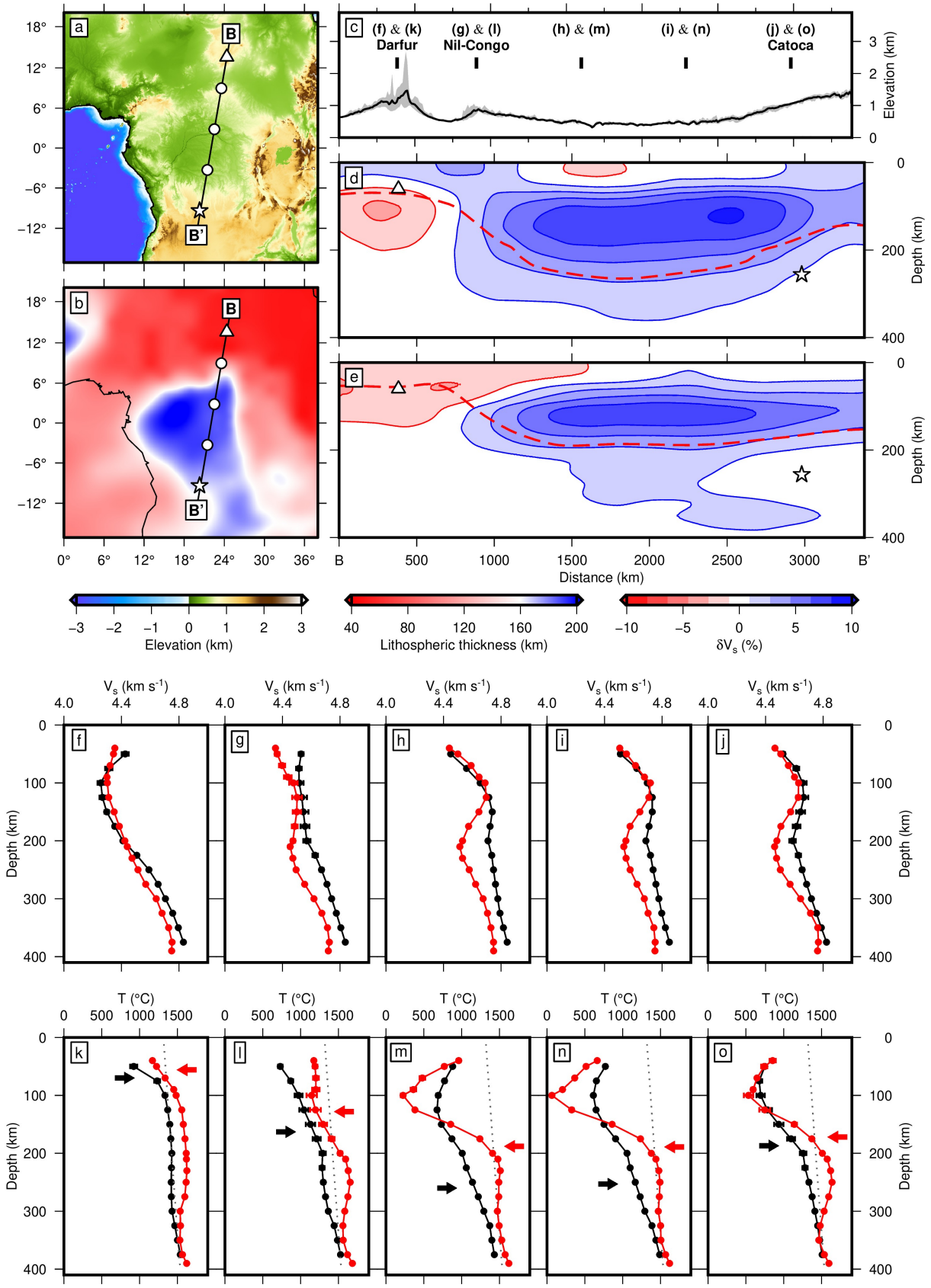

Figure 5.10: Surface-wave tomographic models: transect B–B'. As Figure 5.9.

on the vertical slices in Figures 5.9d, 5.9e, 5.10d and 5.10e, where they are also compared with independent estimates from the geochemistry of mafic volcanic rocks and peridotite xenoliths. The former constraints are from the global study of Ball (2019) and based on rare-earth element modelling, while the latter are from this study (Section 5.2.2). In general, tomographic estimates of lithospheric thickness agree well with independent constraints. Neogene volcanic centres north of the Congo basin (e.g. Jos, Cameroon Volcanic Line, Darfur) are underlain by thin lithosphere (i.e. $\sim$ 60 km). Lithospheric thicknesses beneath the Congo basin are $\sim$ 200–250 km, broadly consistent with but slightly lower than estimates from peridotite xenoliths (Section 5.2.2, Figure 5.8).

A noticeable feature of the tomographically estimated geotherms for the Congo basin discussed here is unusually low temperatures at lithospheric depths (see e.g Figures 5.9m, 5.9n, 5.10m and 5.10n). These low temperature estimates are manifest in slightly different ways in the two models discussed. In the SL2013sv model (black circles and lines in Figures 5.9 and 5.10), temperature increases slowly with depth from $\sim$ 500 °C at depths of $\sim$ 100 km to isentropic temperatures at depths of $>$ 300 km. This cool geotherm results in an estimated transition between conductive lithosphere and convective asthenosphere (taken to be the 1175 °C isotherm) at temperatures several hundred degrees below the isentrope for ambient convecting mantle. In the CAM2016Vsv_200 model (red circles and lines in Figures 5.9 and 5.10), temperatures as low as $\sim$ 0 °C are found at depths of $\sim$ 100 km. These improbably low temperature esimates are unlikely to be the result of crustal bleeding artefacts which usually act to decrease estimated V_s and hence increase estimated temperatures. One possible explanation is depletion of the cratonic lithospheric mantle, which is observed in xenocrysts from the Mbuji-Mayi and Catoca kimberlite clusters (Section 5.2.2). The compositional differences between fertile and depleted mantle are thought to result in a change in V_s of $\sim$ 1%, or $\sim$ 0.05 ms^{-1} at the depths and temperatures of interest here (e.g. Lee, 2003; Priestley & M^{c}Kenzie, 2006). This change corresponds to a change in estimated temperature of $\sim$ 100–200 °C in the parameterisations used by Priestley *et al.* (2019) and Czarnota *et al.* (2019). Thus, depletion of the lithospheric mantle could account for some of the anomolously low temperatures estimated beneath the Congo basin.

5.2.4 Gravity and isostatic modelling

The Congo basin is associated with a prominent negative free-air gravity anomaly of up to -50 mGal (Figure 5.1). This negative anomaly has been invoked as evidence that the basin is

convectively drawn down, which has in turn been invoked to explain the basin's long subsidence history (Hartley & Allen, 1994; Downey & Gurnis, 2009; Crosby *et al.*, 2010). However, it has also been suggested that the anomaly could be explained by the density of structure of the crust and lithospheric mantle (Buiter *et al.*, 2012). Here, I use the crustal and lithospheric template developed in the previous sections to test hypotheses regarding the isostatic state and origin of gravity anomalies of the Congo-Kasai Craton and Congo basin.

On the Congo-Kasai Craton, receiver function, xenolith and tomographic data are consistent with crustal thicknesses of $\sim$ 45 km, roughly half of which forms a mafic lower crustal layer, and lithospheric thicknesses of $\sim$ 200–260 km. The lithospheric mantle appears to be depleted by $\sim$ 35 kg m^{-3} with repsect to ambient convecting mantle. Seismic reflection profiles suggest that the Congo basin underwent some degree of crustal thinning during Neoproterozoic and Cambrian times (Figures 5.4, 5.5 and 5.6). The basin is filled with, on average, 5 $\pm$ 1 km of sediment, with thicknesses reaching up to 9 km in the centre of the basin (Kadima Kabongo *et al.*, 2011). Here, this crustal and lithospheric template is compared with two reference columns: a mid-ocean ridge (MOR) and the adjacent South African Plateau. In each case, relative elevations are calculated by isostatic balance. Densities of the lithospheric and asthenospheric mantle are calculated using steady-state conductive and isentropic geotherms, respectively, as in Section 3.1.1. Crustal density is set to 2,890 kg m^{-3} and sediment density is estimated using an averaged compaction relationship for sandstone and shale (Sclater & Christie, 1980). Gravity anomalies, Δg, are then calculated from the density difference between the basin and reference columns as a function of depth, $\Delta\rho(z)$, using an expression for the gravitational attraction of a cylinder from Turcotte & Schubert (2014), where

$$\Delta g = 2\pi G \int_0^h \Delta\rho(z) \left(1 - \frac{z}{\sqrt{R^2 + z^2}}\right) \mathrm{d}z. \tag{5.4}$$

This expression accounts for the fact that deeper compensating masses contribute less to the gravity field than shallower masses. The gravitational constant, $G = 6.67408 \times 10^{-11}$ m^3 kg^{-1} s^{-2} and the radius of the cylinder, $R = 800$ km. This approach has previously been used by Crosby *et al.* (2010) and Buiter *et al.* (2012) to model gravity anomalies of the Congo basin, using different reference columns and simplified methods for calculating densities. Note that, for simplicity, in the following calculations the basin column is assumed to be air loaded throughout, despite its predicted elevation being below sea level for some combinations of parameters.

In Figures 5.11a–5.11c, the density structure Congo basin is compared to that of a mid-ocean ridge. Key variables are the sediment thickness and the amount of crustal thinning, β, relative to the value of $\sim$ 45 km observed in cratonic regions at the basin's margins (Sandvol *et al.*, 1998; Kosarian, 2006; Hansen *et al.*, 2009; Tokam *et al.*, 2010). Predicted elevation as a function of sediment thickness and crustal thinning is shown in Figure 5.11b. The basin currently lies at mean elevations of 0.45 $\pm$ 0.1 km (e.g. Amante & Eakins, 2009). These elevations can be reproduced with sediment thicknesses of 5 $\pm$ 1 km if crust beneath the Congo basin is thinner by a factor of 1.25–1.37 than that of surrounding cratonic regions (red box in Figure 5.11b). Predicted gravity anomaly as a function of sediment thickness and crustal thinning is shown in Figure 5.11c. At wavelengths of the basin itself and above, mean gravity anomalies are -30 ± 9 mGal (e.g. Tapley *et al.*, 2007). To reproduce anomalies of this magnitude with sediment thicknesses of 5 $\pm$ 1 km, crustal thicknesses beneath the Congo basin must be a factor of 1.24–1.49 thinner than surrounding cratonic regions.

In Figures 5.11d–5.11f, the density structure Congo basin is compared to that of surrounding cratonic regions, which form part of the South African Plateau. Reference crustal and lithospheric thicknesses are set to 45 km and 250 km, respectively. The cratonic regions surrounding the Congo basin lie at elevations of $\sim$ 1 km while free-air gravity anomalies are close to 0 mGal. Again, sediment thickness and amount of crustal thinning are varied and relative elevations and gravity anomalies calculated. For sediment thicknesses of 5 $\pm$ 1 km, observed elevation and gravity differences of 0.55 $\pm$ 0.1 km and -30 ± 9 mGal between the basin and surrounding cratonic regions can be reproduced if crust beneath the Congo basin is thinned by factors of 1.22–1.35 and 1.19–1.47, respectively (red boxes in Figures 5.11e and 5.11f).

Results from comparing the density structure of the Congo basin with two different reference columns are therefore relatively consistent. Elevations and gravity anomalies of the Congo basin and the surrounding craton (South African Plateau) can be reconciled if crustal thicknesses within the basin are a factor of $\sim$ 1.2–1.5 thinner than its surroundings. These values are within the range of existing estimates of stretching based on subsidence modelling (Crosby *et al.*, 2010; Kadima Kabongo *et al.*, 2011; Lucazeau *et al.*, 2015). The modelling performed here, although clearly a significant simplification, suggests that the general topographic and gravity features of the Congo basin can be explained without invoking significant convective draw down. The conclusion that significant gravity anomalies can be generated while isostatic equilibrium is maintained is essentially a result of the fact that, in the Congo basin, low elevations and a low

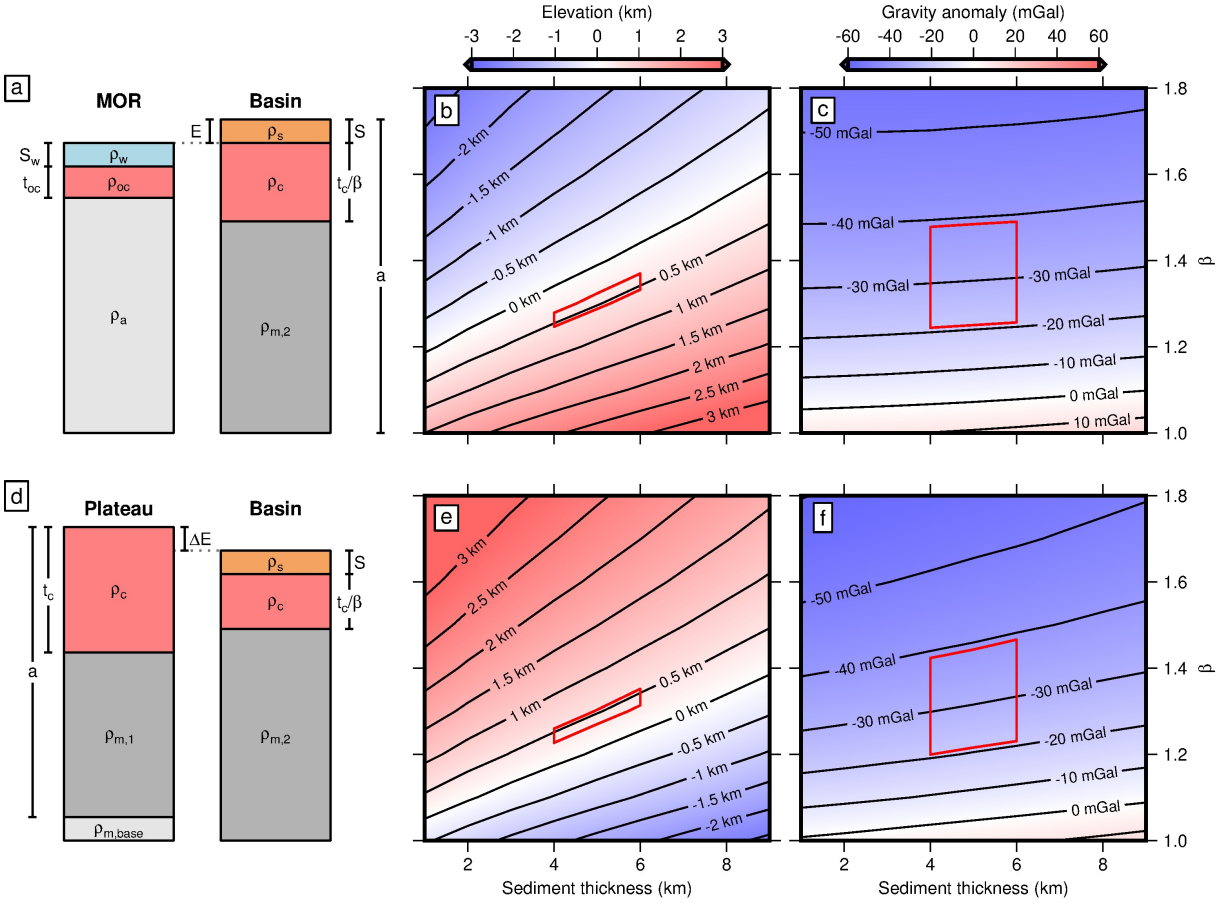

Figure 5.11: Isostatic and gravity modelling. (a) Cartoon outlining idealised lithospheric columns used for mid-oceanic ridge (MOR) and Congo basin. Not to scale. (b) Calculated elevation, E, of Congo basin above sea level as function of sediment thickness and crustal thinning factor. (c) Calculated gravity anomaly. (d-f) As (a-c) for comparison between Congo basin and South African Plateau. Elevation is now relative elevation, ΔE, between the two columns. Red boxes = range of values of $E/\Delta E$ and Δg for Congo basin.

density sediment pile are compensated at the base of relatively thick crust and thick cratonic mantle.

5.3 Subsidence analysis

5.3.1 Subsidence history of the Congo basin

The stratigraphic information summarised in Section 5.1 was used to calculate water-loaded subsidence histories using the backstripping method of Sclater & Christie (1980). Subsidence curves for each of the wells drilled in the Congo basin are shown in Figure 5.12. Similar to subsidence histories calculated for the Grand Canyon region (Section 4.3), subsidence in the

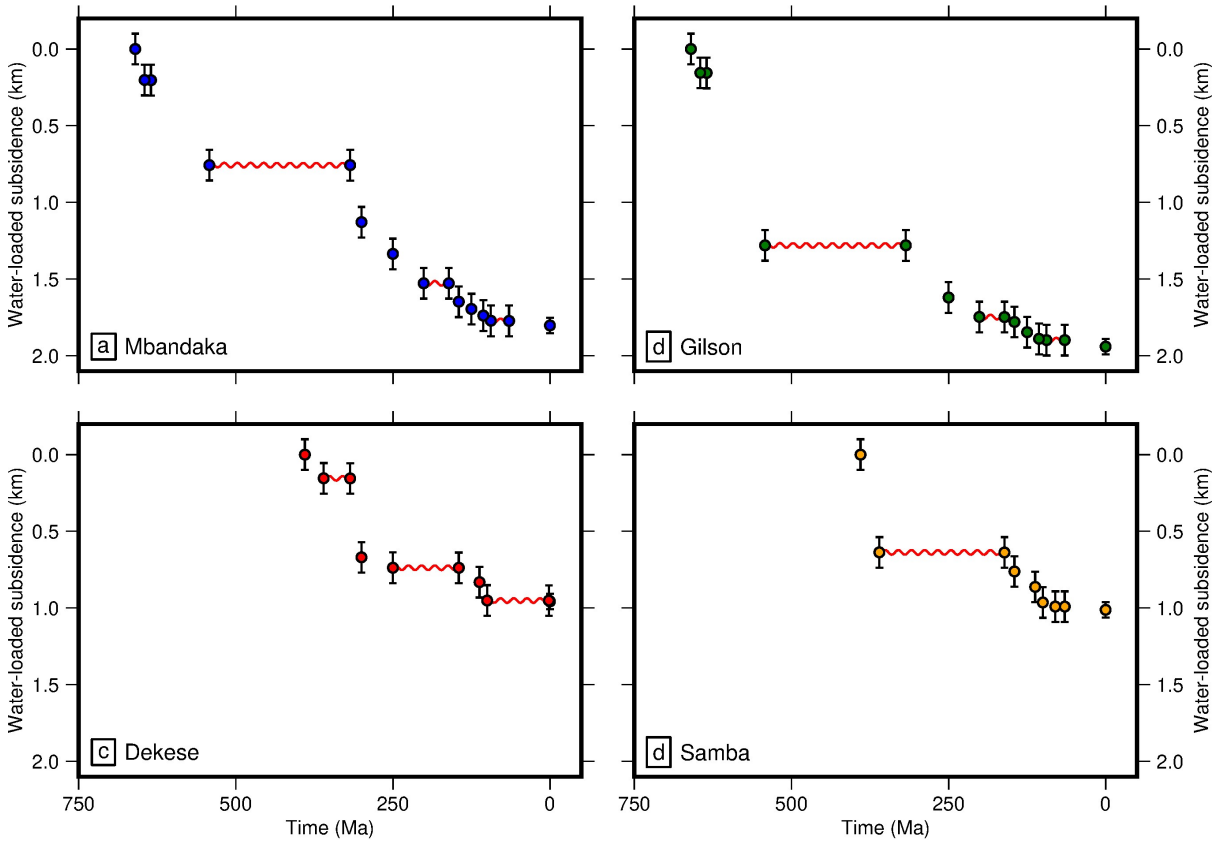

Figure 5.12: Water-loaded subsidence histories of the Congo basin. (a) Water-loaded subsidence for the Mbandaka well. Circles = observed water-loaded subsidence, where error bars reflect uncertainty in water depth; red sinusoids = major unconformities. (b), (c) and (d) As (a), for Gilson, Dekese and Samba wells, respectively.

Congo basin has been strongly episodic. Phases of subsidence corresponding to the major sedimentary packages identified in Section 5.1 occur during Neoproterozoic, Devonian–Triassic and Jurassic–Quaternary times, seperated by major unconformities. Subsidence during Neoproterozoic times appears to correspond to a period of active rifting, evidenced by syn-sedimentary normal faulting. However, the origins of major erosional events and subsequent erosion in Carboniferous–Triassic and Jurassic–Quaternary times are unclear. These unconformities are followed by pulses of subsidence with concave-upward shapes in calculated subsidence curves (Figure 5.12). In the following sections, I will compare observed patterns of water-loaded subsidence with the predictions of a suite of lithospheric stretching and other thermal models.

5.3.2 Lithospheric stretching models

Lithospheric stretching has been recognised as an important basin-forming mechanism for several decades. McKenzie (1978b) proposed a two-stage mechanism for the development of rifted

sedimentary basins. First, the lithosphere is stretched and thinned, accompanied by passive upwelling of asthenospheric material. This syn-rift phase is associated with normal faulting and rapid subsidence. Secondly, during the post-rift phase, stretching ceases and the lithospheric mantle rethickens by conductive cooling. As hot asthenospheric material cools and is encorporated into the lithosphere, thermal contraction results in further subsidence. McKenzie (1978b) derived expressions for syn-rift and post-rift subsidence for the simple case in which rifting is instantaneous. However, if rifting occurs over time periods comparable to the lithospheric time scale of thermal decay, significant cooling will occur during stretching and the approximation of rifting as instantaneous will not be appropriate. As such, Jarvis & McKenzie (1980) developed an advective-diffusive scheme which accounts for lithospheric cooling during stretching. Subsequently, White (1994) used this finite-duration rifting model as the basis for an inverse scheme, allowing strain rate histories to be determined from water-loaded subsidence data.

Here, I develop a modified version of White's (1994) inverse scheme which accounts for heat production in the crust and variable conductivity, heat capacity and expansivity with depth, consistent with thermal models of the continental lithosphere used in previous sections (McKenzie *et al.*, 2005). The appropriate advective-diffusive equation is

$$\rho c_p \frac{\partial T}{\partial t} = \frac{\partial}{\partial z}\left(k\frac{\partial T}{\partial z}\right) + Gz\rho c_p \frac{\partial T}{\partial z} + H, \tag{5.5}$$

where the strain rate, G, is related to the cumulative stretching factor, β, by the expression

$$\beta = \exp\left(\int_0^t G(t)\ \mathrm{d}t\right). \tag{5.6}$$

The first term on the right-hand side of Equation (5.5) describes conductive cooling, while the second term on the right-hand side of Equation (5.5) describes the advection of heat associated with lithospheric stretching. Equation (5.5) is solved numerically using an equivalent Crank-Nicholson scheme to that developed and benchmarked in Chapter 4. At each time step, values of k, c_p, ρ and H as a functon of depth are updated to account for crustal thinning and the evolving thermal structure of the lithospheric mantle. A steady-state geotherm calculated using the procedure outlined in Section 3.1.1 is used as the starting condition, $T_\circ$ (McKenzie *et al.*, 2005). Water-loaded subsidence, S, can then be calculated using the expression

$$S(t) = \frac{t_c(\rho_m - \rho_c)}{(\rho_a - \rho_w)}\Big(1 - \frac{1}{\beta(t)}\Big) - \frac{\rho_0}{(\rho_a - \rho_w)}\int_{t_c}^{a} \exp\Big(\alpha_\circ\big(T(t) - T_\circ\big) + \frac{\alpha_1}{2}\big(T(t)^2 - T_\circ^2\big)\Big)\ \mathrm{d}z. \tag{5.7}$$

$\alpha_\circ$ and α_1 are coefficients which describe the variation in thermal expansivity as a function of temperature (Bouhifd *et al.*, 1996). Equations (5.5)–(5.7) allow water-loaded subsidence as a function of time to be calculated from given strain-rate histories.

To illustrate the affects of including heat production and depth-dependent material properties, synthetic subsidence curves calculated using this scheme are shown in Figure 5.13. In each case, lithosphere with a steady-state thickness of 200 km is stretched by a factor of 1.2 over a period of 50 Myr. First, heat production in the crust is set to zero and, apart from different densities for the crust and mantle, material properties are constant with depth (Figures 5.13a–5.13c). $\sim$ 1 km of water-loaded subsidence occurs rapidly during the syn-rift phase, before slower post-rift subsidence of $\sim$ 0.7 km occurs as the lithosphere gradually re-equilibrates. Radiogenic heat production in the crust is included in Figures 5.13d–5.13f. Since the crust produces less heat after thinning, the lithospheric column becomes cooler and denser, and predicted subsidence slightly increases. In Figures 5.13g–5.13i, the temperature dependence of material properties in the mantle is included. Conductivity as a function of temperature is taken from Hofmeister (1999), heat capacity as a function of temperature from Berman & Aranovich (1996), and expansivity as a function of temperature from Bouhifd *et al.* (1996). Overall, this parameterisation acts to decrease the thermal diffusivity of the lithosphere, so that less subsidence occurs in the syn-rift phase and more during the post-rift phase. Finally, in Figures 5.13j–5.13l, the lithospheric mantle is depleted with respect to ambient convecting mantle. During stretching, upwelling asthenospheric material that replaces lithospheric material is assumed to be undepleted. Including depletion of the lithospheric mantle increases predicted subsidence.

Equations (5.5)–(5.7) can be used in an inverse sense to determine best-fitting strain-rate distributions for observed histories of water-loaded subsidence (White, 1994). The misfit function

$$H = \sqrt{\frac{1}{N}\sum_{i=1}^{N}\left(\frac{S_i^o - S_i^c}{\sigma_i}\right)^2} + W_1\sqrt{\frac{1}{M-1}\sum_{j=2}^{M}\left(G_j - G_{j-1}\right)^2} - \frac{W_2}{M}\sum_{j=1}^{M}\min(G_j, 0), \qquad (5.8)$$

is minimised using Powell's algorithm (Press *et al.*, 1992). The first term on the right-hand side of Equation (5.8) represents the χ^2 misfit between observed, S^o, and calculated, S^c, subsidence, where N is the number of subsidence observations and σ is the uncertainty in observed subsidence. The remaining terms are included to regularise the model. The second term on the right-hand side of Equation (5.8) penalises roughness in the strain-rate distribution and thus encourages the result to be smooth, where M is the number of discrete values of G used.

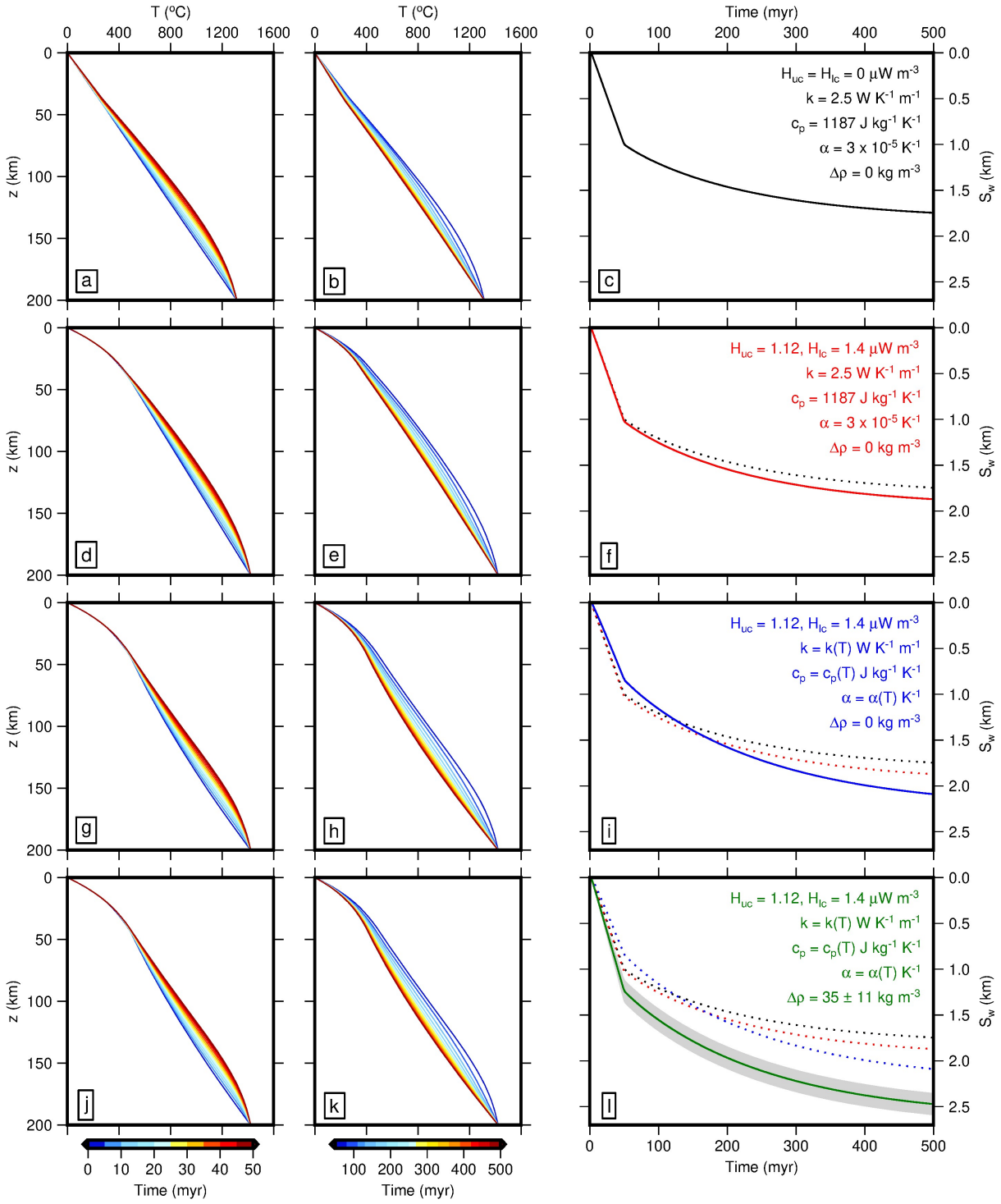

Figure 5.13: Synthetic subsidence curves for stretched lithosphere. In each case, lithosphere is stretched by a factor $\beta = 1.2$ over a period of 50 Ma. (a) Temperature as function of depth and time during syn-rift phase. Material properties are constant within the mantle and there is no crustal heat production or mantle depletion. (b) Post-rift phase. (c) Subsidence history. (d-f) As (a-c) including crustal heat production. (g-i) As before including temperature-dependent material properties in the mantle. (j-l) As before including depletion of lithospheric mantle. Dotted lines in (f), (i) and (l) are subsidence curves from preceding models.

Finally, the third term on the right-hand side of Equation (5.8) penalises negative strain rates. W_1 and W_2 are weighting factors which were set to 100 and 1,000, respectively, for each of the calculations presented here.

The inverse scheme outlined above is applied to the Mbandaka and Gilson wells and the results shown in Figure 5.14. Initially, no restrictions are placed on the timing of lithospheric stretching. Due to the episodic nature of subsidence histories in the Congo basin, best-fitting models involve multiple phases of stretching. For both Mbandaka and Gilson, cumulative stretching by a factor $\beta \sim 1.2$ is required, including Neoproterozoic ($\sim$ 660–542 Ma) and Carboniferous–Triassic ($\sim$ 320–200 Ma) phases, with strain rates of up to ~ 3 Gyr^{-1}. In the case of Mbandaka, the two phases of rifting are of a similar magnitude, whereas for the Gilson well the earlier Neoproterozoic–Cambrian phase is more prominent, due to larger observed subsidence during that period.

Analysis of seismic reflection profiles discussed in Section 5.1.2 highlighted evidence for rifting during Neoproterozoic and Cambrian times, but there appears to have been limited syn-sedimentary deformation associated with subsidence in Carboniferous to Triassic times. Thus, results of inverse modelling in which lithospheric stretching is confined to Neoproterozoic and Cambrian times are also shown in Figure 5.14. For the Mbandaka well, this phase of subsidence is reproduced by strain rates of up to ~ 5 Gyr^{-1}, corresponding to a stretching factor, $\beta \sim 1.12$–1.15. Larger amounts of observed subsidence during Neoproterozoic–Cambrian times at the Gilson well require strain rates of up to ~ 5 Gyr^{-1} over an longer period and $\beta \sim 1.2$–1.3. This large amount of lithospheric stretching overpredicts subsidence during the post-rift phase between Cambrian times and the present day (Figure 5.14d).

These inverse models confirm that the general magnitudes and time scales of subsidence in the Congo basin (i.e. ~ 2 km water-loaded subsidence over a ~ 650 Myr period) can be explained by lithospheric stretching. In these models, long subsidence histories are a result of the thick lithospheric template used, which results in a thermal time constant a factor of 4 greater than that of 'normal' lithosphere (Crosby *et al.*, 2010). However, lithospheric stretching alone appears unable to reproduce the precise shape of observed subsidence curves. When the timing of stretching is unconstrained, significant stretching is inserted in Carboniferous–Triassic times, for which there is no evidence in the basin's stratigraphic architecture. Even so, the occurence of post-rift subsidence means that best-fitting models under- and over-predict subsidence before and after major unconformities, respectively. When stretching is restricted to Neoproterozoic–

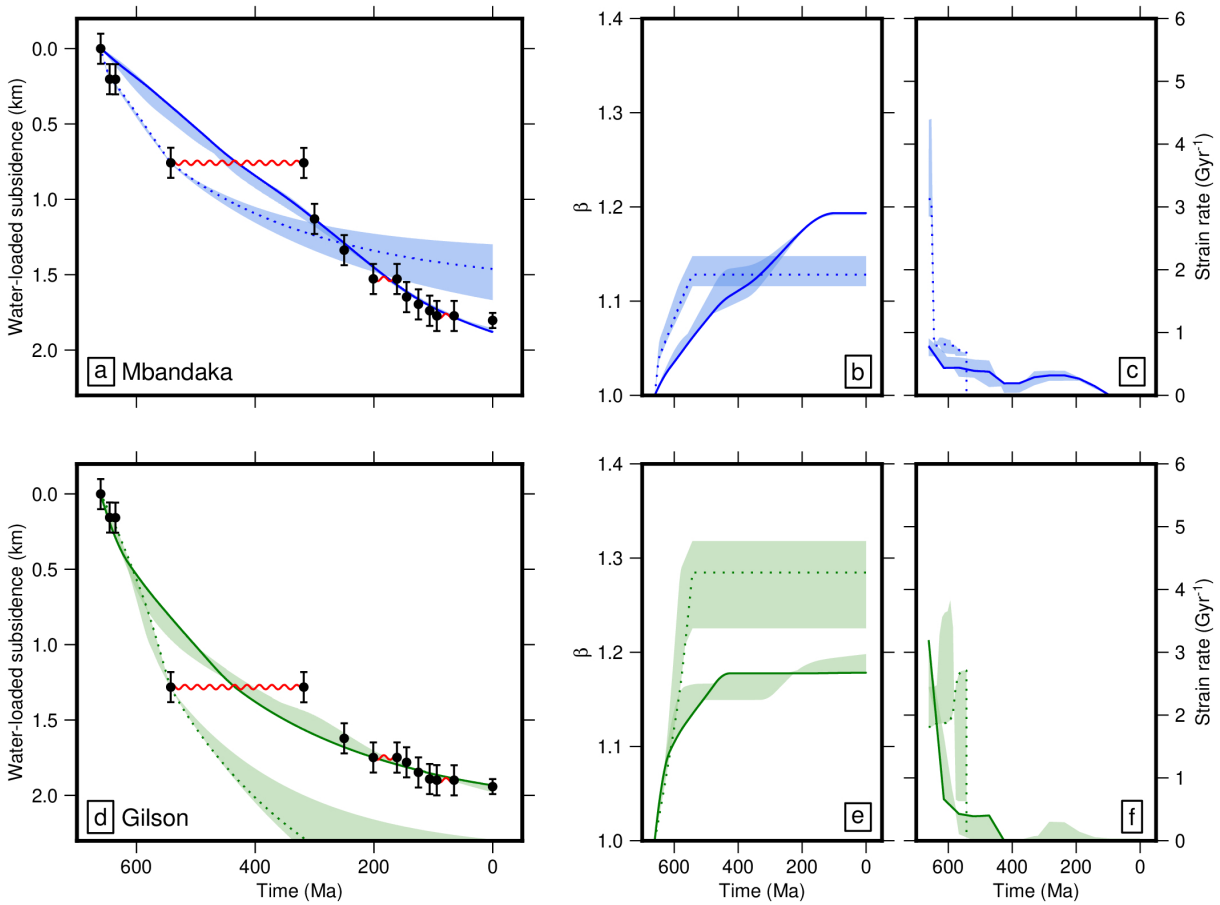

Figure 5.14: Lithospheric stretching models for the Congo basin. (a) Observed and calculated subsidence for the Mbandaka well. Black circles = observed water-loaded subsidence; red sinusoids = major unconformities; blue solid line = best-fitting subsidence history for a = 230 km, where blue band represents range obtained for a = 200–260 km; blue dotted line = best-fitting subsidence history when stretching is confined to Neoproterozoic–Cambrian times. (b) Cumulative stretching factor, β, as function of time. (c) Strain rate as function of time. (d–f) As (a–c) for Gilson well.

Cambrian times, pulses of subsidence in Carboniferous–Triassic and Jurassic–Quaternary times clearly cannot be captured. It therefore seems that, in order to honour contraints from both the basin's stratigraphic architecture and its subsidence history, an alternative mechanism for generating these latter phases of subsidence is required.

5.3.3 Lithospheric and asthenospheric thermal anomalies

Although a Neoproterozoic phase of rifting is able to reproduce the approximate magnitudes and time scales of subsidence in the Congo basin, rifting alone cannot explain its episodic nature. In particular, Carboniferous to Triassic and Jurassic to Quaternary phases of subsidence

follow prominent unconformities and do not appear to be associated with significant faulting, extensional or otherwise. These phases of subsidence may therefore have a deeper lithospheric and/or asthenospheric origin. I now apply the method outlined in Chapter 4 for modelling instantaneous lithospheric thinning and emplacement of asthenospheric material to the subsidence history of the Congo basin.

In this case, lithospheric stretching and the emplacement of putative thermal anomalies are modelled in a coherent framework. First, the scheme described in Section 5.3.2 is used to fit a lithospheric stretching model to the Neoproterozoic–Cambrian phase of syn-rift subsidence. The best-fitting stretching model is then used to project associated post-rift subsidence through early Paleozoic times until the next phase of recorded subsidence in Carboniferous times. At the onset of Carboniferous subsidence, instantaneous lithospheric thinning, emplacement of asthenospheric material and denudation are inserted. The disequilibrated lithospheric geotherm is truncated at a depth $a - \Delta a$ and replaced by an isentropic profile. Water-loaded denudation is set to the amount of post-rift subsidence predicted to occur during the period now spanned by the Cambrian–Carboniferous unconformity. A grid search is used to obtain best-fitting values of Δa and ΔT_p, the excess temperature of emplaced asthenospheric material. Lithospheric cooling and associated subsidence is then projected until the onset of the next phase of subsidence in Jurassic times, and the procedure is repeated.

Results of this combined subsidence modelling are shown in Figure 5.15 for the Mbandaka well. a is set to 228 km, the initial density of the lithospheric mantle to 3,329 kg m^{-3} and the density of asthenospheric mantle replacing stretched lithosphere to 3,364 kg m^{-3}. Also shown is the range of subsidence histories calculated for steady-state lithospheric thicknesses between 200 and 260 km. An adequate fit to observations can be obtained by invoking instances of lithospheric thinning, emplacement of asthenospheric material and denudation in Carboniferous and Jurassic times following a Neoproterozoic phase of stretching. A lithospheric stretching factor of ~ 1.2 is required to reproduce the initial syn-rift subsidence phase. The best-fitting model for the Carboniferous–Triassic phase of subsidence involves removal of 48 km of lithospheric mantle and replacement with asthenospheric material at a potenital temperature of 1505 °C ($\Delta T_p = 175$ °C). More modest values of $\Delta a = 20$ km and replacement with asthenospheric material at a potenital temperature of 1405 °C ($\Delta T_p = 75$ °C) are required by the best-fitting model for the Jurassic–Quaternary phase of subsidence. Predicted denudation associated with each event is 0.47 km for the former and 0.08 km for the latter. In both cases, there are significant trade offs between

best-fitting values of Δa and ΔT_p and a wide range of combinations can reproduce the major features of observed subsidence histories. Best-fitting models generally overpredict subsidence through Cenozoic times. This overprediction may reflect removal of rock in Late Cretaceous times, recorded by a brief unconformity between the Kwango Group and the overlying Cenozoic cover (Figure 5.3). Further removal of rock may have occurred in Cenozoic times, evidenced by the basin's uplifted and exposed margins at the present day (Linol *et al.*, 2015b).

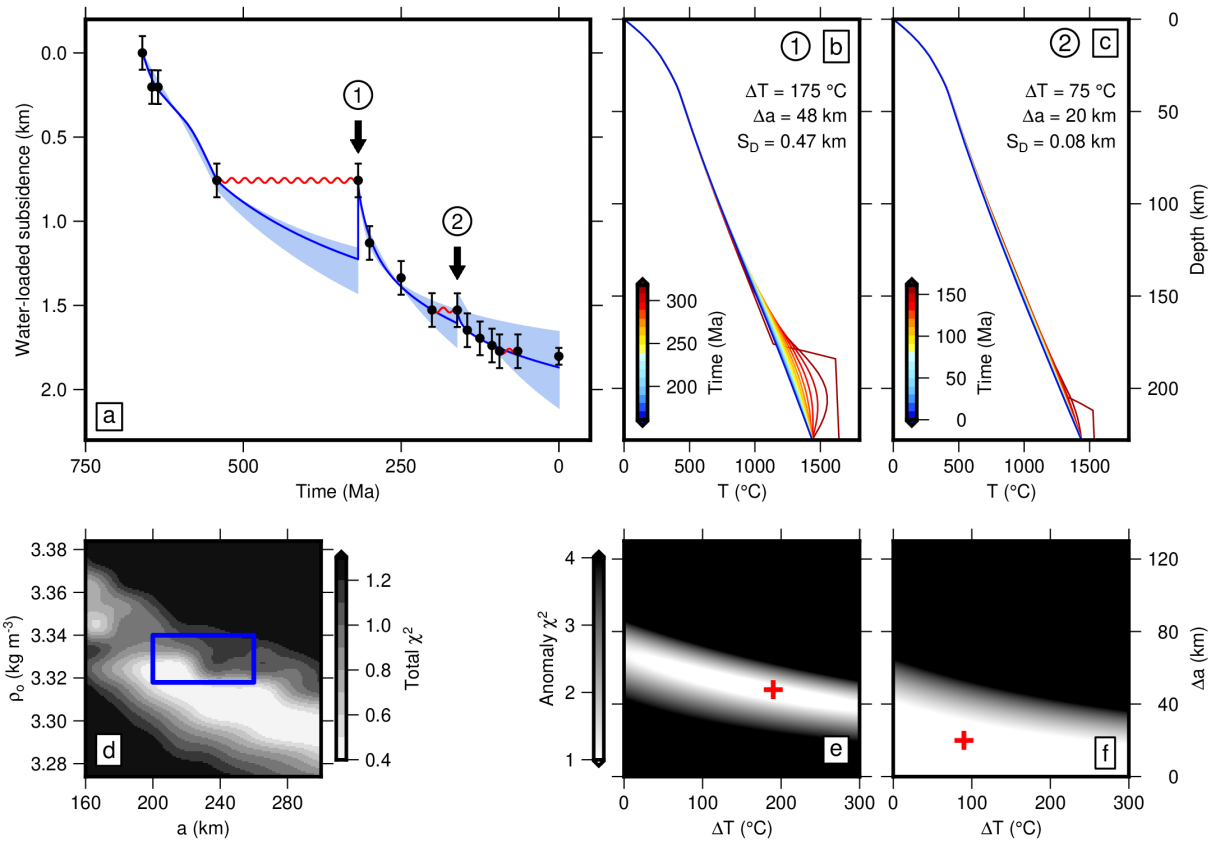

Figure 5.15: Combined modelling of lithospheric stretching and thermal anomalies. (a) Observed and calculated subsidence for the Mbandaka well. Black circles = observed water-loaded subsidence; red sinusoids = major unconformities; blue solid line = best-fitting subsidence history for $a = 230$ km, where blue band represents range obtained for $a = 200$–260 km. Thermal anomalies emplaced at times (1) and (2). (b) Best-fitting temperature as function of depth and time for thermal anomaly (1). (c) Best-fitting temperature as function of depth and time for thermal anomaly (2). (d) Total model misfit as function of steady-state lithospheric thickness, a, and lithospheric depeltion, $\rho_\circ$. Blue box = estimated range for Congo-Kasai Craton. (e) Misfit as function of amount of lithospheric thinning, Δa, and potential temperature anomaly, ΔT_p, for thermal anomaly (1). Red cross = best-fitting model. (f) As (e) for thermal anomaly (2).

Chosen values of steady-state lithospheric thickness and lithospheric depletion exert a significant influence on resulting subsidence models. Although some bounds can be placed on their

values from surface-wave tomographic models and the chemical composition of mantle xenoliths, considerable uncertainties remain. For this reason, I performed a two-parameter sweep through a–$\rho_\circ$ space to examine their influence. Model misfit as a function of a and $\rho_\circ$ is shown in Figure 5.15d. A broad misfit well occurs at values of $a \gtrsim 200$ km and $\rho_\circ \sim 2,280$–$3,340$ kg m^{-3}. There is a gentle trade off with lower values of a requiring higher values of $\rho_\circ$. Values of a and $\rho_\circ$ estimated for the Congo-Kasai Craton from surface-wave tomographic models and the chemical composition of mantle xenoliths lie within and on the edge of this broad misfit well (blue box in Figure 5.15d). This result indicates that independently estimated values of a and $\rho_\circ$ are close to the best-fitting values of these parameters and that the models presented here are a reasonable reflection of the scheme's ability to fit observed subsidence patterns.

Attempts to model subsidence at the Gilson well in this way were unsuccessful, since lithospheric stretching models fit to observed Neoproterozoic subsidence significantly overpredict subsequent subsidence at this well (Figure 5.14d). I note that this scheme is rather sensitive to small errors in syn-rift subsidence histories, which control estimates of lithospheric stretching and post-rift subsidence. Such errors are most likely to arise due to uncertainties in the ages of syn-rift sedimentary rocks, which are considerable in Congo basin. For this reason, specific estimates of lithospheric thinning, asthenospheric temperature and denudation from the Mbandaka well must also be treated with care. Nevertheless, succesful modelling of subsidence at the Mbandaka well does imply that the general magnitudes and time scales of transient uplift, denudation and subsidence can be recreated by reasonable amounts of lithospheric thinning, emplacement of warm asthenospheric material, and subsequent cooling.

5.4 Comparisons with Taoudeni and Parnaíba basins

In this chapter I have investigated the origin and evolution of the Congo basin using a variety of approaches. The stratigraphy consists of four major sequences bounded by regional unconformities. There is evidence for an initial phase of rifting in Neoproterozoic times. Subsequently, the basin appears to have experienced phases of minor shortening and extension. There is limited evidence, however, for major phases of deformation that could explain the formation of basin-wide unconformities. Stretching of thick, depleted lithosphere followed by repeated emplacement of hot asthenospheric material at the base of the lithosphere can explain the magnitudes, time scales and episodic nature of the basin's subsidence history. Are these general results typical of

intracratonic basins? I will now briefly compare the Congo with two other intracratonic basins: Taoudeni of West Africa and Parnaíba of Brazil. For much of the Phanerozoic eon, these basins were located near to the Congo in central Gondwana (Figure 5.16).

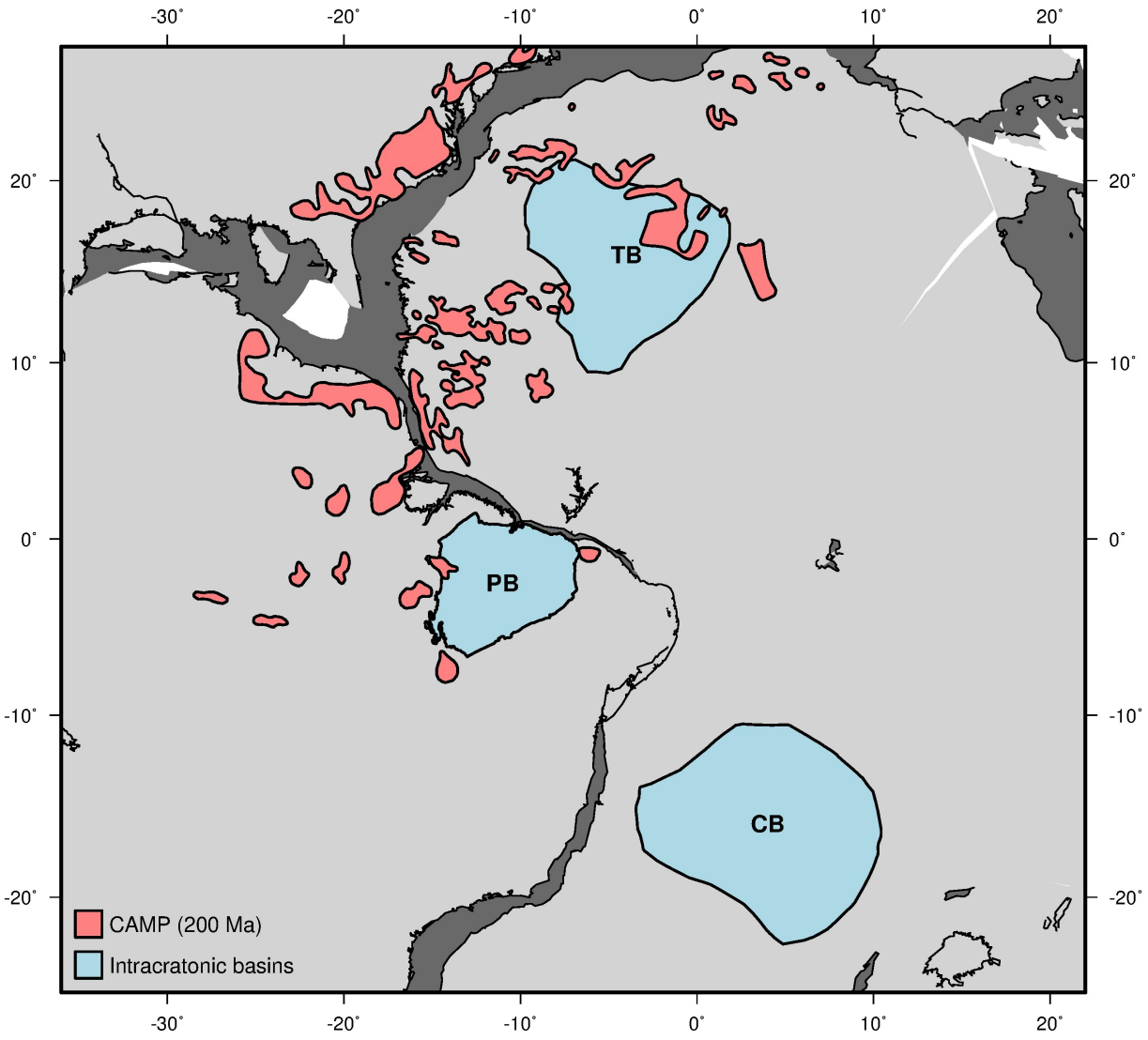

Figure 5.16: Position of Africa, North and South America at 200 Ma. Calculated using GPlates software package and plate reconstruction of Matthews *et al.* (2016a). Light grey polygons = areas enclosed by modern coastlines; dark grey polygons = areas enclosed by continent-ocean boundary; blue polygons = positions of Congo basin (CB), Parnaíba basin (PB) and Taoudeni basin (TB); red polygons = outcropping Central Atlantic Magmatic Province rocks.

5.4.1 Stratigraphy and basin architecture

Parnaíba basin is located in northeast Brazil on the edge of the Amazon and São Francisco Cratons (Figure 5.16). Like the Congo, its stratigraphy consists largely of shallow marine and continental rocks which are divided into several major sequences, bounded by basin-wide unconformities (Figure 5.17; Góes & Feijó, 1994; Vaz *et al.*, 2007). The oldest rocks in the basin are sandstones and shales of the Richão and Jaibaras, or Mirador, Groups, thought to be have been deposited in late Neoproterozoic to Cambrian times (Góes & Feijó, 1994; de Sousa, 1996; Vaz *et al.*, 2007). These rocks were deposited in fault-bounded graben and are thought to represent an early phase of rifting (Góes *et al.*, 1990; de Sousa, 1996; de Castro *et al.*, 2014, 2016). Localised normal faults bounding these graben also displace the overlying Silurian-Devonian Serra Grande group (Rodríguez Tribaldos, 2017). Overlying Devonian–Cretaceous sequences are relatively uniform and undeformed (Góes *et al.*, 1990; Rodríguez Tribaldos, 2017). In Early Jurassic times, basalt flows of the Mosquito Formation were emplaced (Góes & Feijó, 1994; Merle *et al.*, 2011). These basalts are associated with the widespread Central Atlantic Magmatic Province (CAMP; Figure 5.16). A subsequent phase of magmatic activity occured in Cretaceous times, coincident with eruption of the Paraná-Etendeka flood basalts and the opening of the South Atlantic Ocean, resulting in dykes and sills of the Sardinha Formation (Fodor *et al.*, 1990; Merle *et al.*, 2011).

Taoudeni basin is located on the West African Craton (Figure 5.16). Sediments of thickness $\sim$ 2–3 km cover a vast area, similar to that of the Congo. Its stratigraphy is also divided into several major sequences, separated by regional unconformities (Figure 5.17; e.g. Villeneuve, 2005). Borehole, seismic reflection and, particularly from the basin's northern margin, outcrop data reveal a largely uniform succession with some faulting at its base (e.g. Moussine-Pouchkine & Bertrand-Sarfait, 1997; Villeneuve, 2005; Martín-Monge *et al.*, 2016). The sequence begins with the Char and Atar groups, thought to have been deposited in Meso- to Neo-proterozoic times ($\sim$ 1,200–775 Ma, Figure 5.17; Clauer, 1981; Rooney *et al.*, 2010). Where these rocks outcrop along the northern margin of the Taoudeni basin, they occupy fault-bounded half graben and so are thought to have been deposited in a rift setting (Moussine-Pouchkine & Bertrand-Sarfait, 1997). Subsidence then contiued episodically through Late Neoproterozoic and Paleozoic times (Figure 5.17). The cause of this subsidence is unclear, with some authors arguing for additional phases of rifting in Cambrian–Silurian times (e.g. Albert-Villanueva *et al.*, 2016), while others prefer a flexural mechanism associated with loading by Pan-African orogenic belts towards the

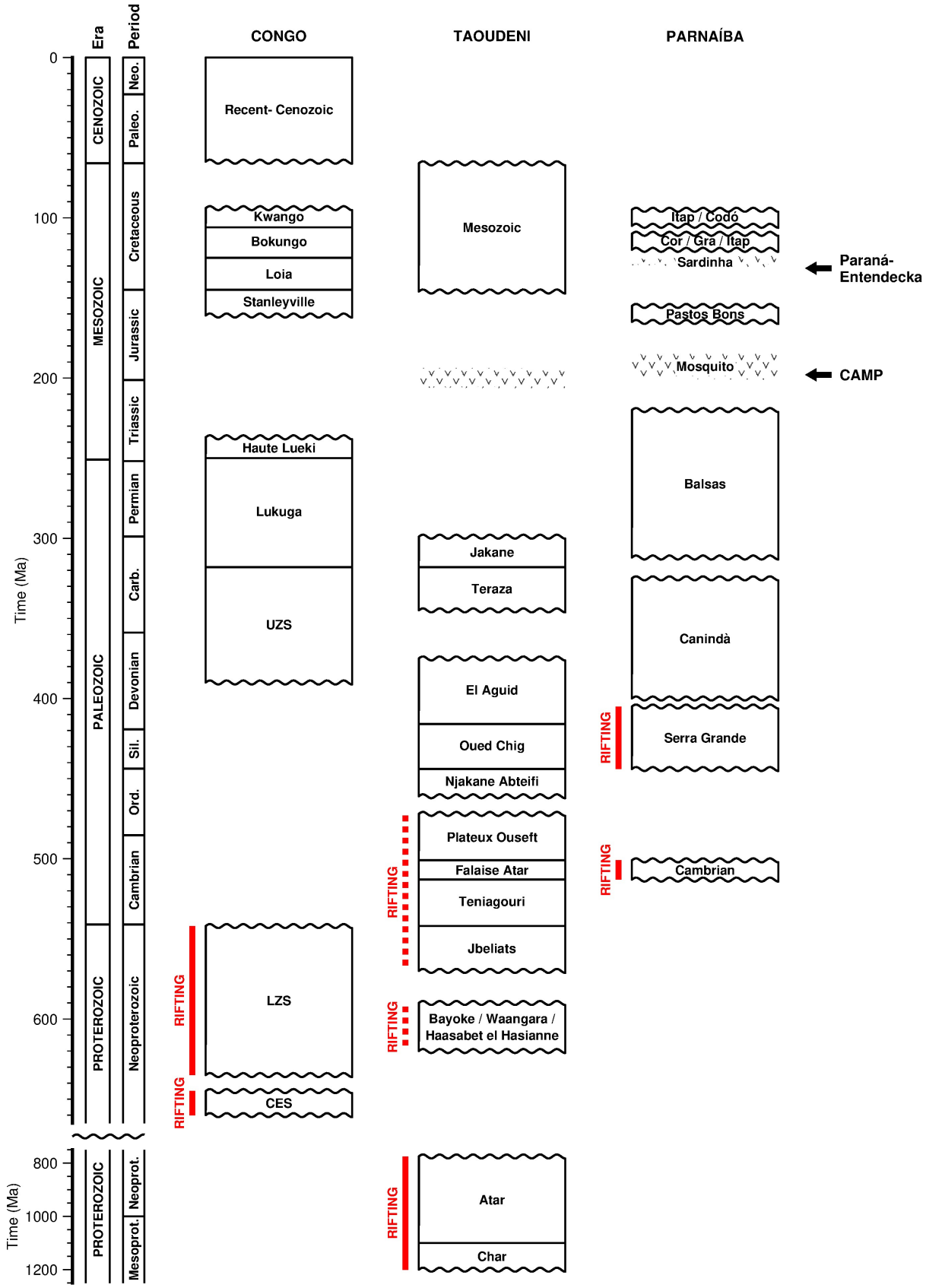

Figure 5.17: *Caption overleaf.*

west (e.g. Moussine-Pouchkine & Bertrand-Sarfait, 1997; Martín-Monge *et al.*, 2016). Around the Triassic-Jurassic boundary, sediments of the Taoudeni basin were intruded by dolerite dykes and sills dated to $\sim$ 205–195 Ma and also associated with the CAMP (Figure 5.16; Sebai *et al.*, 1991; Verati *et al.*, 2005). A thin covering of Cretaceous continental deposits completes the succession (Villeneuve, 2005).

Important stratigraphic and architectural similarities therefore exist between Congo, Parnaíba and Taoudeni intracratonic basins. In each basin, a long stratigraphic record spannning part of the Proterozoic eon and the entire Phanerozoic eon is divided into several 'super-' or 'mega-sequences' separated by regional unconformities. In this sense, the basins are typical of intracratonic basins (e.g. Sloss, 1963). There is also evidence for localised rifting at the base of each basin, while younger rocks are relatively undeformed and define a uniform 'layer-cake' architecture. Structures associated with an early rifting phase have not been identified beneath all intracratonic basins, although this fact may reflect a lack of high-qualtiy seismic imaging elsewhere (e.g. Allen & Armitage, 2012).

5.4.2 Lithospheric template

Vertical slices through the SL2013sv and CAM2016Vsv_200 surface-wave tomographic models along transects crossing Parnaíba and Taoudeni basins are shown in Figures 5.18 and 5.19 (Schaeffer & Lebedev, 2013; Ho *et al.*, 2016). Like the Congo, both basins are underlain by strongly negative V_s anomalies to depths of $\sim$ 200 km (Figures 5.18d, 5.18e, 5.19d and 5.19e). Calculated temperature profiles and lithospheric thickness models of Czarnota *et al.* (2019) and Priestley *et al.* (2019) are also shown. Each model suggests that lithosphere beneath these basins is thick (i.e. $\sim$ 150–200 km). Beneath parts of the West African Craton and Taoudeni basin, the model of Czarnota *et al.* (2019) predicts lithospheric thicknesses greater than 250 km (Figures

Figure 5.17: ***Previous page.*** **Stratigraphy of Congo, Taoudeni and Parnaíba basins.** Stratigraphy of Congo basin based on information from ECL (1988), Daly *et al.* (1991, 1992) and Kadima *et al.* (2011). CES = Carbonate-Evaporite Sequence; LZS = Lower Zaire Sequence. Stratigraphy of Taoudeni basin based on information from Villeneuve (2005), Albert-Villanueva *et al.* (2016) and Martín-Monge *et al.* (2016). Stratigraphy of Parnaíba basin based on information from Góes & Feijó (1994) and Vaz *et al.* (2007). Cor-Gra-Itap = Corda-Grajaú-Itapecuru and Itap-Codó = Itapecuru-Codó Groups. Red solid lines = periods of rifting; red dottted lines = possible periods of rifting; 'v' stippling indicates igneous unit; timing of Central Antlantic (CAMP) and Paraná-Entendecaka Magmatic Pronvinces shown (e.g. Peate, 1997; Marzoli *et al.*, 1999).

5.19d and 5.19k–5.19o).

Lithospheric temperatures calculated by Czarnota *et al.* (2019) and Priestley *et al.* (2019) are unexpectedly low beneath the West African Craton and, to a lesser extent beneath the Amazon Craton at the western end of transect C–C' (Figures 5.18k–5.18o and 5.19k–5.19o). Similar patterns were observed beneath the Congo basin and tentatively attributed to the effects of lithospheric depletion (Section 5.2.3). It is therefore possible that the large lithospheric thicknesses of > 250 km estimated by Czarnota *et al.* (2019) beneath the West African Craton are artificially thick, particularly since they rely on a specific isotherm (1175 °C) as a proxy for the lithosphere-asthenosphere boundary.

Overall, the surface-wave tomographic models of Schaeffer & Lebedev (2013) and Ho *et al.* (2016) are consistent with Parnaíba and Taoudeni basins, like the Congo, residing on thick (i.e. > 150 km) and possibly depleted cratonic lithosphere. Again, these features are typical of many intracratonic basins (e.g. McKenzie & Priestley, 2016).

5.4.3 Subsidence histories

Finally, I compare subsidence histories of Parnaíba and Taoudeni with that of the Congo basin. For Parnaíba, I exploit a published water-loaded subsidence curve calculated for well 2-CP-001-MA, located near the centre of the basin (Rodríguez Tribaldos & White, 2018). For Taoudeni, I backstripped stratigraphic information compiled by Villeneuve (2005) using the procedure described previously (Sclater & Christie, 1980). Water-loaded subsidence histories for each basin are shown in Figures 5.20a and 5.20j. Similar to histories calculated for Congo wells, both curves contain initial phases of rapid subsidence followed by latter phases of more gradual, discontinuous subsidence. Rodríguez Tribaldos & White (2018) showed that the general features of the Parnaíba curve could be adequately modelled using an exponential function, consistent with it being generated by a thermal process. They also proposed that pulses of subsidence separated by unconformities could explained by changing patterns of convective support superimposed on this background thermal process. Here, I test these hypotheses using the modelling strategy developed in Section 5.3.

The results of combined subsidence modelling for Parnaíba and Taoudeni are shown in Figure 5.20. This modelling includes an initial phase of lithospheric stretching and subsequent emplacement of thermal anomalies at the base of the plate. For Parnaíba, initial crustal thickness was

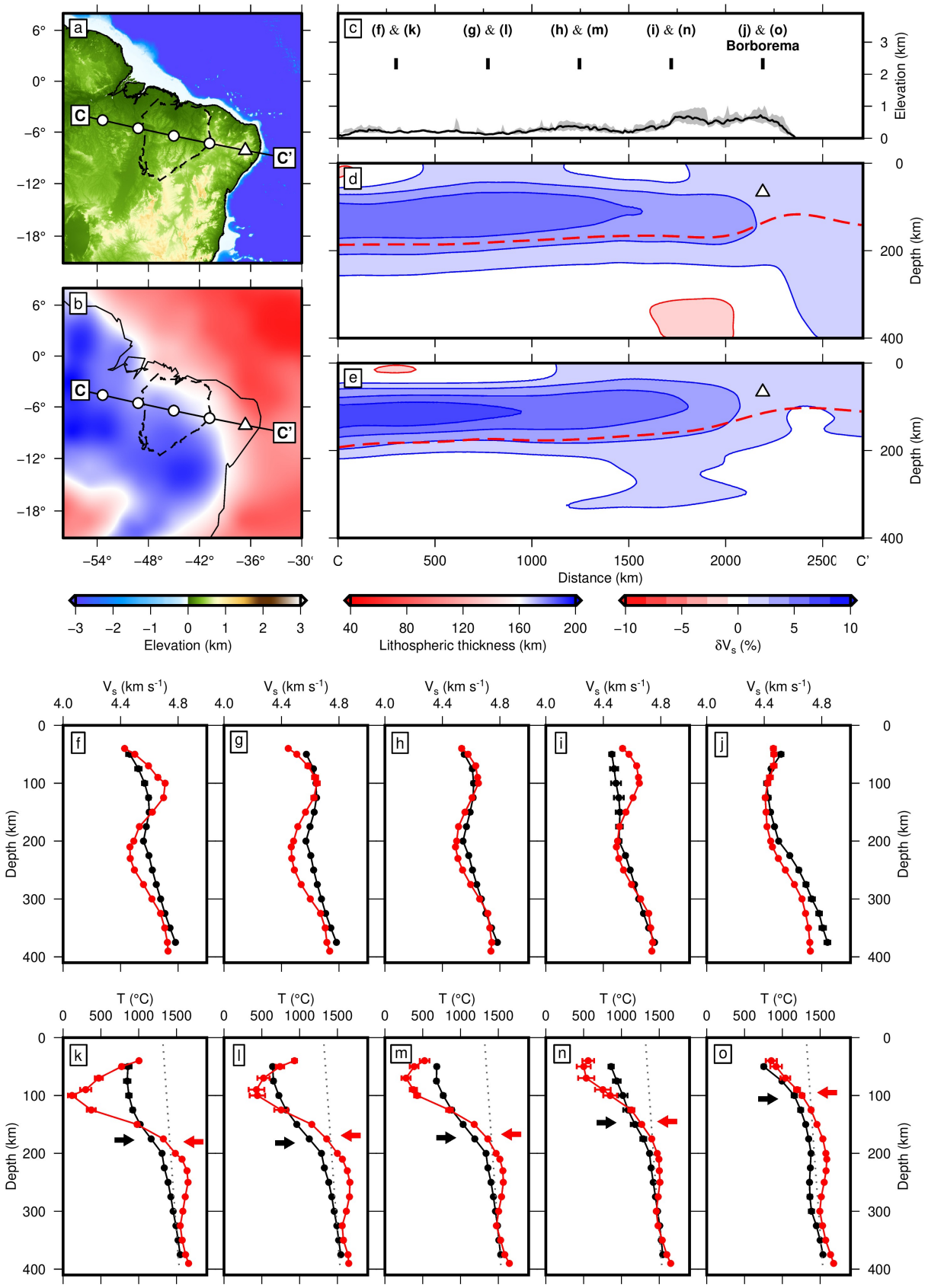

Figure 5.18: Surface-wave tomographic models: transect C–C'. As Figure 5.9.

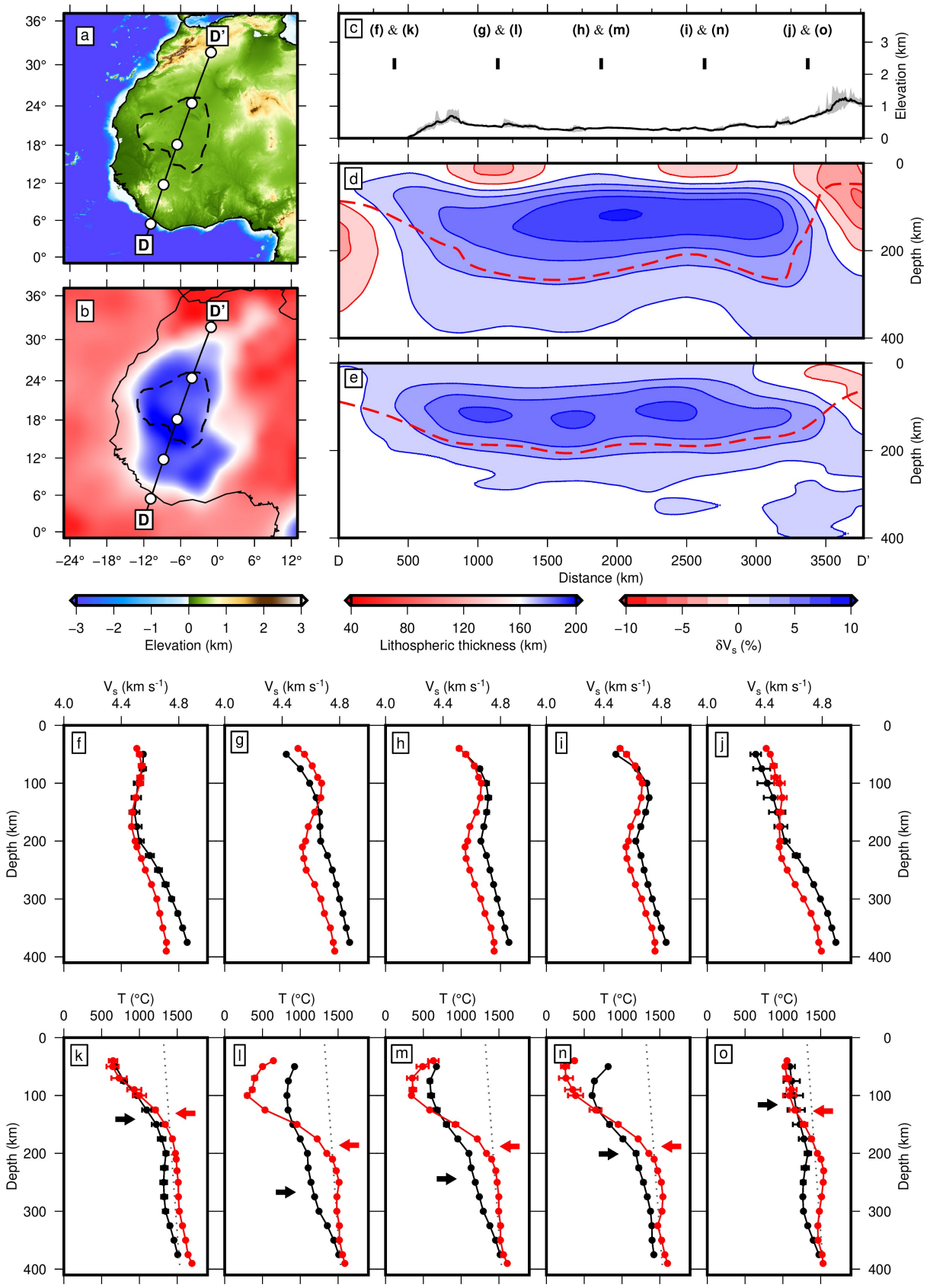

Figure 5.19: Surface-wave tomographic models: transect D–D'. As Figure 5.9.

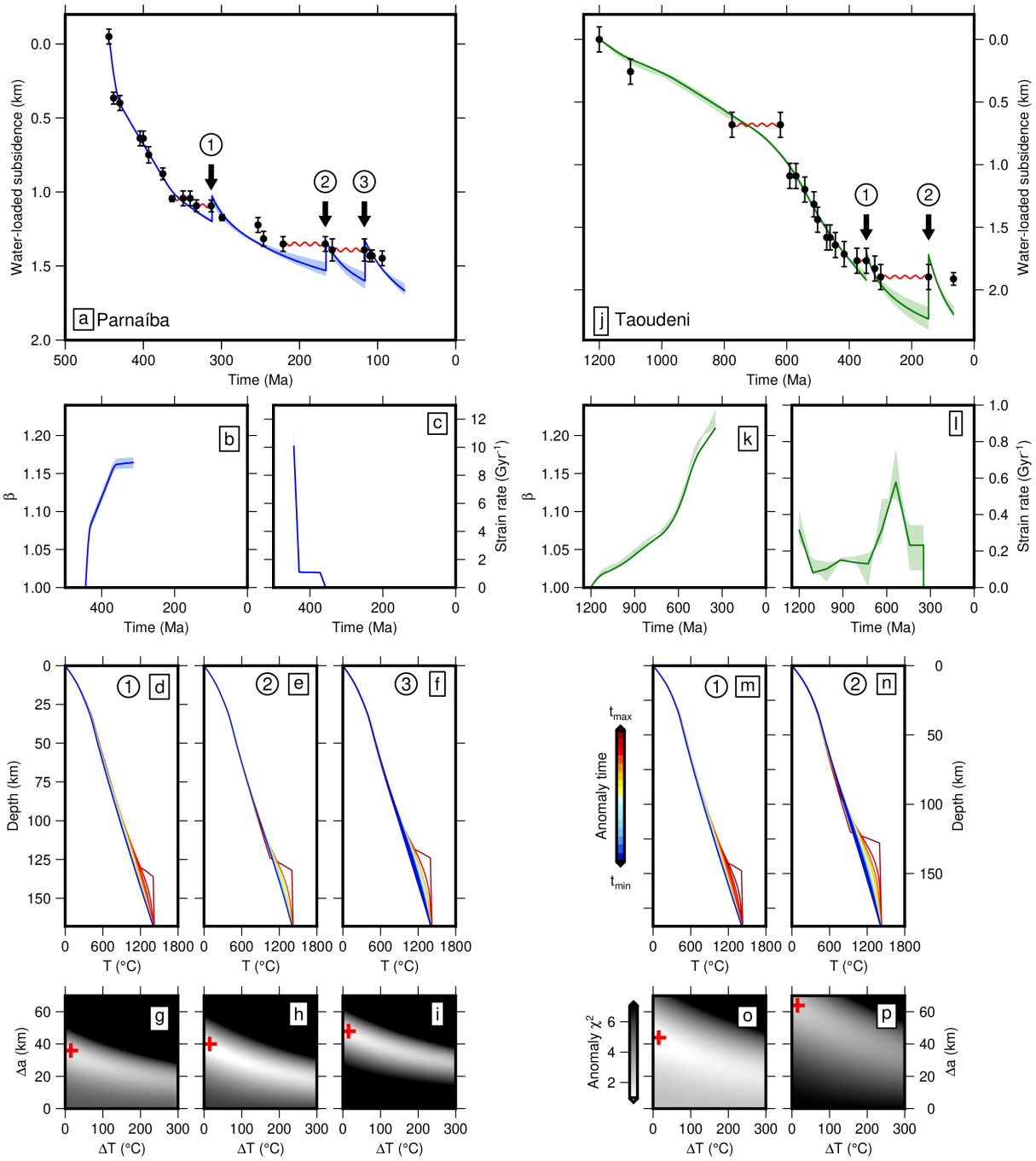

Figure 5.20: Subsidence histories and modelling of Parnaíba and Taoudeni basins. (a) Observed and calculated subsidence for Parnaíba basin. Black circles = observed water-loaded subsidence; red sinusoids = major unconformities; blue solid line = best-fitting subsidence history for $a = 168$ km, where blue band represents range obtained for $a = 156$–180 km. Thermal anomalies emplaced at times (1), (2) and (3). (b) Best-fitting stretching factor, β as function of time. (c) Best-fitting strain rate as function of time. (d–f) Best-fitting temperature as function of depth and time for thermal anomalies (1), (2) and (3). (g–i) Misfit as function of amount of lithospheric thinning, Δa, and potential temperature anomaly, ΔT_p, for thermal anomalies (1), (2) and (3). Red cross = best-fitting model. (j–p) As (a–i) for Taoudeni basin. $a = 188$ km, with band represents range for $a = 184$–192 km.

set to 36 km on the basis of receiver function analyses and a deep seismic reflection profile from the basin's margins (Daly *et al.*, 2014; Luz *et al.*, 2015; Rodríguez Tribaldos, 2017). Steady-state lithospheric thickness was set to 168 ± 12 km (Priestley *et al.*, 2019). Similarly, initial crustal thickness and lithospheric thickness for Taoudeni were set to 44 km and 188 ± 4 km, respectively (Kosarian, 2006; Globig *et al.*, 2016; Priestley *et al.*, 2019).

In both cases, initial phases of subsidence are best fit by cumulative stretching factors of $\sim$ 1.2 (Figures 5.20b and 5.20k). For Parnaíba, an initial phase of stretching at strain rates of $\sim$ 10 Gyr^{-1} is required (Figure 5.20c). This phase corresponds to the Silurian and Devonian Serra Grande Group, which is offset by normal faults in seismic reflection images (Rodríguez Tribaldos, 2017). Subsequently, a second phase of stretching at much lower strain rates of $\sim$ 1 Gyr^{-1} corresponds to the Canindé Group (Devonian and Carboniferous periods; Figure 5.20c). In fact, the lower part of the Canindé Group is offset by normal faults in places, but is generally not linked to active rifting (Rodríguez Tribaldos, 2017). It may therefore be that some other mechanism contributed to subsidence during this period (e.g. convective downwelling, flexure; de Castro *et al.*, 2016; Tozer *et al.*, 2017). It is also worth noting that well 2-CP-001-MA does not penetrate rocks of the pre-Silurian Richão or Jaibaras Groups which occupy graben at the base of Parnaíba basin (Góes *et al.*, 1990; de Sousa, 1996; de Castro *et al.*, 2014, 2016). Any continued post-rift subsidence associated with Neoproterozoic and Cambrian rifting is therefore not included in the models presented here. In either case, the amount of stretching required during Devonian and Carboniferous times would be reduced.

For Taoudeni, best-fitting models require prolonged stretching at strain rates less than 1 Gyr^{-1} (Figure 5.20l). An initial phase of slow stretching corresponds to the Char and Atar Groups. It should be noted that, due to large discrepancies between radiometric ages obtained by different methods for these rocks, the history of subsidence and stretching for this period is poorly constrained (compare, e.g. Clauer, 1981; Rooney *et al.*, 2010). A second phase of more rapid subsidence is required spanning Late Neoproterozoic and Early Paleozoic times. While some authors have associated deposition of these sediments with phases of rifting (e.g. Albert-Villanueva *et al.*, 2016), others have invoked flexural processes linked to the 'Pan-African' orogeny (e.g. Moussine-Pouchkine & Bertrand-Sarfait, 1997; Martín-Monge *et al.*, 2016). It is unlikely that flexural loading at the basin's margins could generate uniform subsidence over such a large area, since to do so would require unreasonably large elastic thicknesses (Gunn, 1943; Watts, 2001). These rocks are also cut by normal faults in some of the cross sections presented by Villeneuve

(2005). Thus, lithospheric stretching would appear to be a plausible mechanism for generating subsidence during this period. Nevertheless, some contribution from flexural loading cannot be ruled out; in this case, reduced stretching would be required.

Following these initial phases of lithospheric stretching, several instances of lithospheric thinning, asthenospheric emplacement and surface denudation are inserted at times corresponding to the end of regional unconformities. In each case, observed subsidence is best fit by thinning of the lithosphere by a few tens of kilometres, emplacement by asthenospheric material at or a few tens of degrees above ambient temperatures and water-loaded denudation of a few hundred metres. These results are similar to those obtained for unconformities and subsidence pulses in the Congo basin (Section 5.3). Again, trade offs between Δa and ΔT mean that the exact values of these parameters are not well constrained (Figures 5.20g–5.20i, 5.20o and 5.20p). Both models predict significant continued subsidence through Cenozoic times which is not represented in the stratigraphy of either basin. Similar to the Congo, the margins of both basins are uplifted and eroded, so this discrepancy may reflect recent or ongoing phases of uplift and denudation (Villeneuve, 2005; Rodríguez Tribaldos & White, 2018). Another explanation may be that, if alternative mechanisms contributed to subsidence during basin initiation (e.g. flexure), lithospheric stretching and subsequent thermal relaxation is overpredicted. This latter explanation would also account for some overprediction of subsidence following the emplacement of thermal anomaly (1) in Parnaíba (Figure 5.20a).

Finally, I note that Congo, Parnaíba and Taoudeni basins each contain prominent unconformities spanning parts of Triassic and Jurassic times (Figure 5.17). During this period, basalts flows of the Mosquito Formation erupted across Parnaíba, while sediments of Taoudeni were intruded by dolerite dykes and sills (Figure 5.16; Sebai *et al.*, 1991; Verati *et al.*, 2005; Merle *et al.*, 2011). These magmatic rocks are associated with the Central Atlantic Magmatic Province (CAMP), which was emplaced across western Africa, northern South America and eastern North America between $\sim$ 205–195 Ma (e.g. Marzoli *et al.*, 1999). Klöcking *et al.* (2018a) modelled rare-earth element concentrations of the Mosquito basalts and concluded that they represented asthenospheric melts generated at shallow depths (i.e. $\sim$ 50 km) and warm temperatures. Development of the CAMP is generally attributed to the affects of an upwelling mantle plume, but insulation of the asthenospheric mantle by aggregated continents has also been invoked (e.g. Coltice *et al.*, 2007). In either case, it would appear that lithospheric thinning and emplacement of warm asthenosphere associated with the CAMP is a plausible mechanism for generating

uplift and denudation associated with Triassic-Jurassic unconformities in Parnaíba and Taoudeni basins, as modelled here. Since the region is underlain by thick cratonic lithosphere, it is conceivable that lithospheric thinning and asthenospheric upwelling affected a wider area without causing the geotherm to cross the solidus and generating melt. Thus, the Triassic-Jurassic unconformity in the Congo basin may also be associated with this event (Figure 5.17).

5.5 Summary

This chapter has focussed on attempting to improve understanding of the origin and evolution of the Congo basin, and intracratonic basins more generally. First, I reviewed information from well and outcrop data, and re-interpreted seismic reflection profiles to characterise stratigraphy and architecture of then basin. There is evidence for Neoproterozoic phases of rifting, interspersed with phases of minor shortening and basin inversion. In constrast, overlying Paleozoic sequences are relatively undisturbed, defining a 'layer-cake' geometry typical of intracratonic basins. These sequences are bounded by basin-wide unconformities. Secondly, I developed a regional crustal and lithospheric framework based on published receiver function analyses, geochemical analyses of peridotite xenoliths, and surface-wave tomographic models. The Congo-Congo-Kasai Craton appears to be underlain by thick crust ($\sim$ 45 km) and thick depleted lithosphere ($\sim$ 200–260 km). Negative free-air gravity anomalies and the basin's elevation are consistent with this framework, if crustal thicknesses beneath the basin are thinner than the surrounding cratonic regions by a factor of about 1.3. Thirdly, I calculated and modelled water-loaded subsidence histories. I showed that the subsidence record can be explained by an initial phase of lithospheric stretching at strain rates < 10 Gyr^{-1} with a cumulative stretching factor of ~ 1.2. Pulses of subsidence separated by unconformities are modelled by the emplacement of thermal anomalies at the base of the lithosphere and their subsequent cooling. Lithospheric thinning of a few tens of kilometres, replacement with asthenospheric material a few tens of degrees above ambient temperatures, and surface denudation of a few hundred metres can adequately reproduce observed subsidence patterns. Fourthly, I compared the Congo with two other intracratonic basins: Parnaíba and Taoudeni. These basins were located close to the Congo for much of Paleozoic times in central Gondwana and share many of its characteristics. There is evidence for rifting at the base of each basin, at least in a localised way, and they are also located on thick, possibly depleted, cratonic lithosphere. Subsidence histories can also be reproduced by initial phases of lithospheric stretching and subsequent phases of uplift and denudation driven by the emplacement of thermal

anomalies at the base of the plate. Convectively driven uplift and denudation, superimposed on some background subsidence process such as post-rift thermal relaxation, appears to be a plausible mechanism for generating the classic 'layer-cake' architecture of intracratonic basins. These basins may represent important records of asthenospheric and lithospheric processes ongoing throughout their long lifetimes.

Chapter 6

Conclusions and Further Work

6.1 Summary

The focus of this dissertation has been to explore ways by which convective processes within the Earth's mantle are expressed in landscapes and sedimentary basins. In turn, I have assessed ways in which analysis of landscape evolution and the stratigraphic record can constrain spatial and temporal patterns of these convective processes, particularly beneath the continents. Three regional case studies were carried out, which concerned: Neogene-Quaternary uplift and magmatism of Anatolia; development of a Carboniferous buried transient landscape from the Grand Canyon region; and evolution of the intracratonic Congo Basin.

Scattered outcrops of emergent marine sedimentary rocks attest to growth of the Anatolian Plateaux in Neogene and Quaternary times (Schildgen *et al.*, 2014). In Chapter 2, I extracted an inventory containing 1,844 longitudinal river profiles from a satellite-derived topographic model. This inventory was modelled using the inverse scheme of Rudge *et al.* (2015) to determine regional uplift histories. The inverse model was calibrated using localised independent observations of uplift and incision rates. In the resulting uplift histories, regional uplift initiated around 20 Ma in Eastern Anatolia and propagated westward. Uplift reached the Central Anatolian Plateau at

10–15 Ma, with additional focussed uplift at its northern and southern margins initiating since 10 Ma. Regional long-term uplift rates reached ~ 0.5 mm yr^{-1}.

In Chapter 3, I compared this regional uplift history with constraints on the evolution of the Anatolian lithospheric and asthenospheric mantle obtained in various ways. Analysis of the relationship between gravity and topography (i.e. admittance) in the spectral domain confirmed that prominent postive long wavelength free-air gravity anomalies over Anatolia are not a result of flexural isostasy alone and that, rather, could be a result of sub-plate topographic support. A comprehensive database comprising geochemical analyses of Neogene and Quaternary mafic magmatic rocks was assembled. Elemental and isotopic compositions were analysed to discern the relative importance subduction-zone and intraplate magmatic processes. There is compelling evidence for a Miocene transition from subduction-related to intraplate-style magmatism in Western Anatolia. Elsewhere, slightly enriched intraplate-style melts erupted throughout Neogene and Quaternary times, with the most recent phase of magmatism migrating from east to west since ~ 12 Ma. Major and rare earth element concentrations of the least evolved samples were modelled to estimate pressures and temperatures of melting (M^{c}Kenzie & O'Nions, 1991; Plank & Forsyth, 2016). In most cases, melt compositions can be explained by adiabatic decompression melting of asthenospheric material beneath thin lithosphere (i.e. ~ 60 km) at a range of temperatures. The highest temperatures of ~ 1400 °C were obtained for samples from eastern Anatolia. Temperature estimates gradually decreased westwards to approximately that of ambient mantle beneath western Anatolia.

Various geodynamic explanations have been proposed for the Neogene-Quaternary growth of the Anatolian Plateaux and contemporaneous magmatism. Popular mechanisms include: fragmentation and/or detachment of subducting African lithosphere (e.g. Keskin, 2003; Schildgen *et al.*, 2014); thinning of the lithospheric mantle (e.g. Şengör *et al.*, 2003; Göğüş & Psyklywec, 2008; Bartol & Govers, 2014); and upwelling warm asthenosphere (e.g. Faccenna *et al.*, 2013). Numerical models suggest that each of these mechanisms could generate observed regional uplift of 1–2 km at rates of up to ~ 0.5 mm yr^{-1} (Göğüş & Psyklywec, 2008; Duretz *et al.*, 2011; van Hunen & Allen, 2011; Bartol & Govers, 2014).

The results presented in Chapters 2 and 3 provide useful observational constraints with which to test these competing conceptual models. In particular, consistent patterns link the timing and extent of uplift and magmatism with the magnitude of asthenospheric thermal anomalies. Simple isostatic calculations suggest that the combined affects of warm, westward-propagating

asthenosphere along with thinning of lithospheric mantle can explain the majority of observed uplift. Thermal erosion of the lithospheric mantle by warm asthenosphere could explain the apparent coincidence of these two phenomena (e.g. Yuen & Fleitout, 1985; Olson *et al.*, 1988; Davies, 1994). The Afar plume is proposed as a source of anomalously hot asthenospheric mantle, linking the growth of the Anatolian Plateaux to Cenozoic uplift of western Arabia (Faccenna *et al.*, 2013; Wilson *et al.*, 2014). Additionally, the striking transition from subduction-zone to intraplate style magmatism around 10 Ma is consistent with the opening of a slab tear beneath Western Anatolia at that time (Innocenti *et al.*, 2005; Agostini *et al.*, 2007; Klaver *et al.*, 2016). No such evidence is observed in the compositions of Neogene and Quaternary magmatic rocks from Central or Eastern Anatolia (*contra* Wilson *et al.*, 1997; Keskin, 2003). Nevertheless, body-wave tomographic models suggest that slab tearing is ongoing beneath southern Central Anatolia, which could be contributing to additional rapid uplift observed there (Biryol *et al.*, 2011; Schildgen *et al.*, 2014). Accumulation of slab material at transition-zone depths beneath Eastern Anatolia implies that slab detachment has occurred, most likely in Paleogene times (Biryol *et al.*, 2011). This detachment could have influenced the initition of uplift in Eastern Anatolia and controlled the propagation of sub-plate thermal anomalies.

More extensive temporal records of convective processes may be provided by the stratigraphy of sedimentary basins (e.g. Jones *et al.*, 2001; Peterson *et al.*, 2010). In particular, prominent Paleogene unconformities in the Faroe-Shetland Basin and North Sea have recently been shown to be ancient fluvial landscapes, thought to record transient uplift associated with the Icelandic plume (Shaw Champion *et al.*, 2008; Hartley *et al.*, 2011; Stucky de Quay *et al.*, 2017). The Carboniferous Surprise Canyon Formation, which outcrops throughout the Grand Canyon, North America, records another example of such an ancient landscape now exposed at the Earth's surface.

In Chapter 4, I investigated potential causes and consequences of this transient landscape. Reviews of stratigraphic and chronologic information confirmed that channels of the Surprise Canyon Formation represent a $\sim$ 10 Myr period of base-level fall, landscape development and subsequent resubmergence. Taking into account sediment compaction, a conservative estimate of required base-level fall is 280 ± 90 m. This magnitude, along with inconsistencies between the timing of events and current reconstructions of Carboniferous glaciation, suggests that glacio-eustatic fluctuations cannot explain observed base-level fall, and that surface uplift is required. A compilation of water-loaded subsidence histories suggests that transient uplift was followed by a

period of regional subsidence which cannot be fully explained by the effects of flexural loading by nearby mountain ranges. It is shown that magnitudes and timescales of uplift and subsidence can reproduced by the arrival of warm asthenospheric material, thinning of the lithospheric mantle by a few tens of kilometres, and subsequent conductive cooling. Transient uplift appears to have affected a $\sim$ 1,500 km stretch of the western North American margin, possibly migrating from north to south, and may have caused re-organisation of regional drainage networks.

Regional unconformities are also prominent features of the intracratonic basins (Sloss, 1963). It has been suggested that these unconformities, and the pulses of sedimentation that follow them, may record convective transient uplift events (Rodríguez Tribaldos & White, 2018). The formation of intracratonic basins themselves also remains unclear, but has been linked to convective draw down and ancient lithospheric stretching (Hartley & Allen, 1994; Armitage & Allen, 2010; Allen & Armitage, 2012).

In Chapter 5, the origins and evolution of the Congo Basin were discussed. I reviewed stratigraphic information and re-interpreted seismic reflection profiles in order to characterise the basin's architecture. The basin's stratigraphy comprises four major sequences bounded by regional unconformities. There is evidence for a Neoproterozoic phase of rifting, which provides a plausible mechanism for the basin's formation. Localised deformation suggests that the basin subsequently underwent phases of minor shortening and extension, but does not provide a clear explanation for the formation of basin-wide unconformities. Published receiver function analyses, geochemical analyses of peridotite xenoliths and seismic tomographic models were used to constrain the composition and thickness of the crust and lithospheric mantle. It appears that a prominent negative free-air gravity anomaly overlying the basin can be accounted for by presence of low density sediment and thinned crust. I then calculated and modelled water-loaded subsidence histories. Observed subsidence patterns can be recreated by an initial phase of lithospheric stretching followed by phases of uplift, denudation and resubmergence driven by the emplacement of warm asthenosphere at the base of the lithosphere. Similar characteristics were identified in Parnaíba and Taoudeni basins.

6.2 Further Work

Understanding of interactions between Neogene and Quaternary uplift and landscape evolution on the Anatolian Plateaux could be improved in a number of ways. The accuracy of regional

uplift histories obtained by inverse modelling of longitudinal river profiles is dependent on the abundance and quality of available independent constraints. Thus, refined age estimates for emergent marine sedimentary rocks and an expanded database of long-term incision rate estimates would increase confidence in and allow more detailed interpretation of calculated uplift histories. Comparison of predicted incision rates with estimates of sediment flux to offshore basins could provide valuable additional constraints on rates of uplift and erosion (e.g. Cilicia and Adana basins, eastern Mediterranean; Walsh-Kennedy *et al.*, 2014). The inverse modelling scheme applied here is also a significant simplification in several respects. First, the drainage planform is assumed to be fixed with respect to time, and, secondly, evolution of river channels is considered in isolation. The impacts of these two assumptions could be investigated using full landscape evolution models, which include channel migration processes and erosion on hill slopes (e.g. Badlands, Landlab; Salles, 2016; Hobley *et al.*, 2017).

Constraints on melting processes and conditions beneath Anatolia could also be improved. As the number of published whole-rock geochemical analyses increases, the regional analysis performed here could be refined and differences and similarities between individual provinces could be discerned. It may be possible to investigate the temporal evolution of individual provinces. Estimates of the temperatures and depths of melting from major and rare earth element modelling are strongly sensitive to chosen values of source water content and oxidation state. The values of these parameters are not known Anatolia, which represents the greatest source of uncertainty in the calculations performed here. Thus, constraining these values, for example by analysis of melt inclusions in olivine phenocrysts, would improve the reliability of estimated melting depths and temperatures (Plank & Forsyth, 2016). Another potential source of new information may be geochemical compositions of peridotite xenoliths, which are common products of intraplate magmatism. Such analyses have not been obtained for Anatolia, but could provide important constraints on the composition and thermal structure of the lithospheric mantle. These constraints would inform isostatic calculations, helping to determine the extent to which Anatolian topography is isostatically compensated. Thermobarometric estimates of xenolith equilibration temperatures and pressures may also help to elucidate timings, amounts and mechanisms of lithospheric thinning. Finally, several recent studies have provided estimates of surface heat flow across Anatolia (e.g. Ilkışık, 1995; Dolmaz *et al.*, 2005; Balkan-Pazvantoglu & Erkan, 2019). Surface heat flow is controlled by the geothermal gradient and so these measurements could provide additional independent constraints on lithospheric thicknesses and asthenospheric temperatures.

Further analysis would also improve understanding of the Carboniferous transient landscape recorded by the Surprise Canyon Formation. Careful mapping of Surprise Canyon Formation outcrops along with under- and over-lying units, including accurate measurement of their elevations, may allow structural corrections to be applied and longitudinal profiles to be reconstructed. Given the inaccessibility of many outcrops, a repeat of the extensive surveying completed by G. H. Billingsley, S. S. Beus and colleagues during the 1970s and 1980s is probably unrealistic, but a targeted study may be feasible. The biggest source of uncertainty in modelling of water-loaded subsidence histories is the lack of constraint on any background subsidence that may have been ongoing. Modelling of subsidence histories calculated from more complete Paleozoic successions in nearby southern Utah may allow background subsidence associated with, for example, Neoproterozoic and Cambrian rifting to be characterised. Expansion of subsidence analysis to other shelves which contain evidence for transient uplift, such as the Leadville and Madison shelves, may provide further insights into spatial and temporal patterns of convective support beneath western North America in Carboniferous times.

Studies of the Congo basin have generally been hampered by a lack of observational constraints. The arguments presented here could be developed by analysis of additional seismic reflection profiles. Modern reprocessing of these profiles may provide better imaging of the basin's deep structure. However, significant advances will probably require acquisition of new datasets. For example, additional well data, modern seismic reflection and refraction data, and receiver function analyses would each provide important insights into the region's stratigraphic and crustal architecture. Comparisons with Parnaíba and Taoudeni would be improved by more detailed evaluation of their crustal and lithospheric structure, for example by compiling receiver function estimates of crustal thickness and velocity structure and by calculating and modelling xenolith equilibration pressures and temperatures.

In modelling subsidence following ancient transient uplift events in both the Grand Canyon region and intracratonic basins, I used a simplified scheme in which lithospheric thinning and emplacement of warm asthenosphere at the base of the lithosphere were considered instantaneous and subsequent cooling was treated as purely diffusive. In reality, some physical process must control the arrival of warm asthenosphere and its subsequent cooling is likely to be at least partly advective. It has been proposed that dissipation of warm plume-head material at the base of the plate can be modelled using gravity current theory (e.g. Bercovici & Lin, 1996; Vasilyev *et al.*, 2001). Schemes in which warm asthenosphere actively erodes the lithospheric mantle have also

been proposed (e.g. Yuen & Fleitout, 1985; Olson *et al.*, 1988; Davies, 1994). It is likely that development and application of more physical models of the lithosphere-asthenosphere system will provide further insights into the generation of transient uplift and subsidence in sedimentary basins.

References

Abgarmi, B., Delph, J. R., Ozacar, A. A., Beck, S. L., Zandt, G., Sandvol, E., Turkelli, N., & Biryol, C. B., 2017. Structure of the crust and African slab beneath the central Anatolian Plateau from receiver functions: New insights on isostatic compensation and slab dynamics, *Geosphere*, **13**(6), 1,774–1,787.

Adiyaman, O., Chorowicz, J., Arnaud, O. N., Gündogdu, M. N., & Gourgaud, A., 2001. Late Cenozoic tectonics and volcanism along the North Anatolian Fault: new structural and geochemical data, *Tectonophysics*, **338**, 135–165.

Agostini, S., Doglioni, C., Innocenti, F., Manetti, P., Tonarini, S., & Savasçin, M., 2007. The transition from subduction-related to intraplate Neogene magmatism in the Western Anatolia and Aegean area, in *Cenzozoic volcanism in the Mediterranean Area*, edited by L. Beccaluva, G. Bianchini, & M. Wilson, pp. 1–15, The Geological Society of America, Boulder, Colorado, Geological Society of America Special Paper 418.

Airy, G. B., 1855. On the Computation of the Effect of the Attraction of Mountain Masses as disturbing the Apparent Astronomical Latitude of Stations in Geodetic Surveys, *Monthly Notices of the Royal Astronomical Society*, **16**(2), 42–43.

Akbaş, B., Akdeniz, N., Aksay, A., Altun, İ. E., Balcı, V., Bilginer, E., Bilgiç, T., Duru, M., Ercan, T., Gedik, İ., Günay, Y., Güven, İ. H., Hakyemez, H. Y., Konak, N., Papak, İ., Pehlivan, Ş., Sevin, M., Şenel, M., Tarhan, N., Türkecan, A., Ulu, Ü., Uğuz, M. F., & Yurtsever, A., 2011. *Geological map of Turkey*, General Directorate of Mineral Research and Exploration, Ankara, Turkey.

Akbayram, K., Sorlien, C. C., & Okay, A. I., 2016. Evidence for a minimum 52 ± 1 km of total offset along the northern branch of the North Anatolian Fault in northwest Turkey, *Tectonophysics*, **668–669**, 35–41.

Aktağ, A., Önal, A. Ö., & Sayit, K., 2019. Geochemistry of the post-collisional Miocene mafic Tunceli Volcanics, Eastern Turkey: Implications for the nature of the mantle source and melting systematics, *Geochemistry*, **79**, 113–129.

Aktuğ, B., Parmaksiz, E., Kurt, M., Lenk, O., Kiliçoğlu, A., Ali Gürdal, M., & Özdemir, S., 2013. Deformation of Central Anatolia: GPS implications, *Journal of Geodynamics*, **67**, 78–96.

Aktuğ, B., Nocquet, J. M., Cingöz, A., Parsons, B., Erkan, Y., England, P., Lenk, O., Gürdal, M. A., Kilicoglu, A., Akdeniz, H., & Tekgül, A., 2009. Deformation of western Turkey from a combination of permanent and campaign GPS data: Limits to block-like behavior, *Journal of Geophysical Research: Solid Earth*, **114**(10), 1–22.

Al-Hajri, Y., White, N., & Fishwick, S., 2009. Scales of transient convective support beneath Africa, *Geology*, **37**(10), 883–886.

Albert-Villanueva, E., Permanyer, A., Tritlla, J., Levresse, G., & Salas, R., 2016. Solid hydrocarbons in Proterozoic dolomites, Taoudeni Basin, Mauritania, *Journal of Petroleum Geology*, **39**(1), 5–28.

Aldanmaz, E., Pearce, J. A., Thirwall, M. F., & Mitchell, J. G., 2000. Petrogenetic evolution of late Cenozoic, post-collision volcanism in western Anatolia, Turkey, *Journal of Volcanology and Geothermal Research*, **102**, 67–95.

Aldanmaz, E., Köprübaşı, Gürer, O. F., Kaymakçı, N., & Gourgaud, A., 2006. Geochemical constraints on the Cenozoic, OIB-type alkaline volcanic rocks of NW Turkey: Implications for mantle sources and melting processes, *Lithos*, **86**, 50–76.

Aldanmaz, E., Pickard, M., Meisel, T., Altunkaynak, c., Sayıt, K., Şen, P., Hanan, B. B., & Furman, T., 2015. Source components and magmatic processes in the genesis of Miocene to Quaternary lavas in western Turkey: constraints from HSE distribution and Hf-Pb-Os isotopes, *Contributions to Mineral Petrology*, **170**, 23.

Alıcı, P., Temel, A., Gourgaud, A., Vidal, P., & Gündogdu, M. N., 2001. Quaternary tholeiitic to alkaline volcanism in the Karasu Valley, Dead Sea Rift Zone, Southeast Turkey: Sr-Nd-Pb-O isotopic and trace-element approached to crust-mantle interaction, *International Geology Review*, **43**, 120–138.

Alıcı, P., Temel, A., & Gourgaud, A., 2002. Pb-Nd-Sr isotope and trace element geochemistry of Quaternary extension-related alkaline volcanism: a case study of Kula region (western Anatolia, Turkey), *Journal of Volcanology and Geothermal Research*, **115**, 487–510.

Alıcı Şen, P., Temel, A., & Gourgaud, A., 2004. Petrogenetic modelling of Quaternary post-collisional volcanism: a case study of central and eastern Anatolia, *Geological Magazine*, **141**(1), 81–98.

Allen, P. A., 2011. Surface impact of mantle processes, *Nature Geoscience*, **4**, 498–499.

Allen, P. A. & Allen, J. R., 1990. *Basin Analysis*, Blackwell, Oxford, UK.

Allen, P. A. & Armitage, J. J., 2012. Cratonic basins, in *Tectonics of Sedimentary Basins: Recent Advances*, edited by C. Busby & A. Azor, pp. 602–620, Blackwell Publishing.

Alpaslan, M., 2007. Early to middle Miocene intra-continental basaltic volcanism in the northern part of the Arabian plate, SE Anatolia, Turkey: geochemistry and petrogenesis, *Geological Magazine*, **144**(5), 867–882.

Alpaslan, M., Yilmaz, H., & Temel, A., 2004. Geochemistry of post-collision Pliocene-Quaternary Karasar basalt (Divriği-Sivas, Eastern Turkey): Evidence for partial melting processes, *Geologica Carpathica*, **55**(6), 487–50.

Altunkaynak, c. & Genç, c. C., 2008. Petrogenesis and time-progressive evolution of the Cenozoic continental volcanism in the Biga Peninsual, NW Anatolia (Turkey), *Lithos*, **102**, 316–340.

Amante, C. & Eakins, B. W., 2009. ETOPO1 1 arc minute global relief model: Procedures, data sources and analysis, NOAA Technical Memorandum NESDIS NGDC-24, National Geophysical Data Center, NOAA.

Anderson, J. L. & Morrison, J., 1992. The role of anorogenic granites in the Proterozoic crustal development of North America, in *Proterozoic Crustal Evolution*, edited by K. C. Condie, pp. 263–299, Elsevier, New York, U.S.A.

Angus, D. A., Wilson, D. C., Sandvol, E., & Ni, J. F., 2006. Lithospheric structure of the Arabian and Eurasian collision zone in eastern Turkey from *S*-wave receiver functions, *Geophysical Journal International*, **166**, 1335–1346.

Archer, A. W. & Greb, S, F., 1995. An Amazon-scale drainage system in the early Pennsylvanian of central North America, *The Journal of Geology*, **103**(6), 611–627.

Arger, J., Mitchell, J., & Westaway, R. W. C., 2000. Neogene and Quaternary volcanism of southeastern Turkey, in *Tectonics and Magmatism in Turkey and the Surrounding Area*, edited by E. Bozkurt, W. J. A., & J. D. A. Piper, pp. 459–487, The Geological Society of London, London, Special Publications 173.

Armitage, J. J. & Allen, P. A., 2010. Cratonic basins and the long-term subsidence history of continental interiors, *Journal of the Geological Society*, **167**, 61–70.

Asan, K. & Ertürk, M. A., 2013. First evidence of lamprophyric magmatism from the Konya region, Turkey: A genetic link to high-K volcanism, *Acta Geologica Sinica*, **87**(6), 1617–1629.

Asan, K. & Kurt, H., 2011. Petrology and geochemistry of post-collisional Early Miocene volcanism in the Karacadağ area (Central Anatolia, Turkey), *Acta Geologica Sinica*, **85**(5), 1100–1117.

Ashchepkov, I. V., Rotman, A. Y., Somov, S. V., Afanasiev, V. P., Downes, H., Logvinova, A. M., Nossyko, S., Shimupi, J., Palessky, S. V., Khmelnikova, O. S., & Vladykin, N. V., 2012. Composition and thermal structure of the lithospheric mantle beneath kimberlite pipes from the Catoca cluster, Angola, *Tectonophysics*, **530–531**, 128–151.

Audet, P., 2014. Toward mapping the effective elastic thickness of planetary lithospheres from a spherical wavelet analysis of gravity and topography, *Physics of the Earth and Planetary Interiors*, **226**, 48–82.

Aydar, E. & Gourgaud, A., 2002. Garnet-bearing basalts: an example from Mt. Hasan, Central Anatolia, Turkey, *Mineralogy and Petrology*, **75**, 185–201.

Aydin, F., 2008. Contrasting complexities in the evolution of calc-alkaline and alkaline melts of the Nigde volcanic rocks, Turkey: textural, mineral chemical and geochemical evidence, *European Journal of Mineralogy*, **20**, 101–118.

Aydin, F., Karsli, O., & Chen, B., 2008. Petrogenesis of the Neogene alkaline volcanics with implications for post-collisional lithospheric thinning of the Eastern Pontides, NE Turkey, *Lithos*, **104**, 249–266.

Aydin, F., Schmitt, A. K., Siebel, W., Sönmez, M., Ersoy, Y., Lermi, A., Dirik, K., & Duncan, R., 2014. Quaternary bimodal volcanism in the Niğde Volcanic Complex (Cappadocia, central Anatolia, Turkey): age, petrogenesis and geodynamic implications, *Conrtibutions to Mineralogy and Petrology*, **168**(1078).

Ayele, A., 2002. Active compressional tectonics in central Africa and implications for plate tectonic models: evidence from fault mechanism studies of the 1998 earthquakes in the Congo Basin, *Journal of African Earth Sciences*, **35**, 45–50.

Bağcı, U., Alpaslan, M., Frei, R., Kurt, M. A., & Temel, A., 2011. Different degrees of partial melting of the enriched mantle source for PlioQuaternary basic volcanism, Toprakkale (Osmaniye) Region, Southern Turkey, *Turkish Journal of Earth Sciences*, **20**, 115–135.

Bakırcı, T., Yoshizawa, K., & Özer, M. F., 2012. Three-dimensional *S*-wave structure of the upper mantle beneath Turkey from surface wave tomography, *Geophysical Journal International*, **190**, 1058–1076.

Balkan-Pazvantoglu, E. & Erkan, K., 2019. Temperature-depth curves and heat flow in central part of Anatolia, Turkey, *Tectonophysics*, **757**, 24–34.

Ball, P. W., 2019. Global Relationships Between Intraplate Magmatism and Dynamic Topography, Ph. D. Dissertation, University of Cambridge.

Ball, P. W., White, N. J., Masoud, A., Nixon, S., Hoggard, M. J., Maclennan, J., Stuart, F. M., Oppenheimer, C., & Kröpelin, 2019. Quantifying Asthenospheric and Lithospheric Controls on Mafic Magmatism Across North Africa, *Geochemistry, Geophysics, Geosystems*, **20**(7), 3,520–3,555.

Ballato, P., Uba, C. E., Landgraf, A., Strecker, M. R., Sudo, M., Stockli, D. F., Friedrich, A., & Tabatabaei, S. H., 2011. Arabia-Eurasia continental collision: Insights from late Tertiary foreland-basin evolution in the Alborz Mountains, Northern Iran, *Bulletin of the Geological Society of America*, **123**(1-2), 106–131.

Barbeau, D. L., 2003. A flexural model for the Paradox Basin: implications for the tectonics of the Ancestral Rocky Mountains, *Basin Research*, **15**, 97–115.

Bartol, J. & Govers, R., 2014. A single cause for uplift of the Central and Eastern Anatolian plateau?, *Tectonophysics*, **637**, 116–136.

Bebout, G. E., 2007. Metamorphic chemical geodynamics of subduction zones, *Earth and Planetary Science Letters*, **260**, 373–393.

Becker, J., Sandwell, D., Smith, W., Braud, J., Binder, B., Depner, J., D., F., Factor, J., Ingalls, S., Kim, S.-H., Ladner, R., Marks, K., Nelson, S., Pharoah, A., Trimmer, R., von Rosenberg, J., Wallace, G., & Weatherall, P., 2009. Global bathymetry and elevation data at 30 arc second resolution: SRTM30_plus, *Marine Geology*, **32**(4), 355–371.

Bercovici, D. & Lin, J., 1996. A gravity current model of cooling mantle plume heads with temperature-dependent buoyancy and viscosity, *Journal of Geophysical Research*, **101**(B2), 3,291–3,309.

Berman, R. G. & Aranovich, L. Y., 1996. Optimized standard state and solution properties of minerals 1. Model calibration for olivine, orthopyroxene, cordierite, garnet, and ilmenite in the system FeO-MgO-CaO-Al_2O_3-TiO_2-SiO_2, *Contributions to Mineral Petrology*, **126**, 1–24.

Beus, S. S., 1999. Megafossil paleontology of the Surprise Canyon Formation, in *Geology of the Surprise Canyon Formation of the Grand Canyon, Arizona*, edited by G. H. Billingsley & S. S. Beus, pp. 69–96, Museum of Northern Arizona Bulletin 61, Flagstaff, AZ, USA.

Beus, S. S. & Martin, H., 1999. Age and correlation, in *Geology of the Surprise Canyon Formation of the Grand Canyon, Arizona*, edited by G. H. Billingsley & S. S. Beus, pp. 117–120, Museum of Northern Arizona Bulletin 61, Flagstaff, AZ, USA.

Beus, S. S. & Morales, M., 2003. *Grand Canyon Geology*, Oxford University Press, New York, USA, 2nd edn.

Beuthin, J. D., 1994. A sub-Pennsylvanian paleovalley system in the Central Appalachian Basin and its implications for tectonic and eustatic controls on the origin of the regional Mississippian-Pennsylvanian unconformity, in *Tectonic and eustatic controls of sedimentary cycles*, edited by J. M. Dennison & F. R. Ettensohn, pp. 107–120, Society for Sedimentary Geology.

Bezinski, D. K., 2017. Trilobites from the Redwall Limestone (Mississippian) of Arizona, *Annals of Carnegie Museum*, **84**(2), 165–171.

Billingsley, G. H., 1999. Paleovalleys of the Surprise Canyon Formation in Grand Canyon, in *Geology of the Surprise Canyon Formation of the Grand Canyon, Arizona*, edited by G. H. Billingsley & S. S. Beus, pp. 17–52, Museum of Northern Arizona Bulletin 61, Flagstaff, AZ, USA.

Billingsley, G. H., 2000. Geological map of the Grand Canyon 30' × 60' quadrangle, Mohave and Coconino Counties, northwestern Arizona, U.S. Geological Survey Geologic Investigations Series I-2688.

Billingsley, G. H. & Beus, S. S., 1984. The Surprise Canyon Formation – an upper Mississippian and lower Pennsylvanian(?) rock unit in the Grand Canyon, Arizona, *United States Geological Survey Bulletin*, **1605-A**, A27–A33.

Billingsley, G. H. & Beus, S. S., 1999. *Geology of the Surprise Canyon Formation of the Grand Canyon, Arizona*, Museum of Northern Arizona Bulletin 61, Flagstaff, AZ, USA.

Billingsley, G. H. & McKee, E. D., 1982. Pre-Supai buried valleys, in *The Supai Group of the Grand Canyon*, vol. Professional Paper 1173, pp. 137–154, United States Geological Survey, Washington D.C.

Billingsley, G. H. & Wellmeyer, J. L., 2003. Geological map of the Mount Trumbull 30' × 60' quadrangle, Mohave and Coconino Counties, northwestern Arizona, U.S. Geological Survey Geologic Investigations Series I-2766.

Billingsley, G. H., Beus, S. S., & Grover, P., 1999. Stratigraphy of the Surprise Canyon Formation, in *Geology of the Surprise Canyon Formation of the Grand Canyon, Arizona*, edited by G. H. Billingsley & S. S. Beus, pp. 9–16, Museum of Northern Arizona Bulletin 61, Flagstaff, AZ, USA.

Billingsley, G. H., Block, D. L., & Dyer, H. C., 2006. Geologic map of the Peach Springs 30' × 60' quadrangle, Coconino County, northernwestern Arizona, U.S. Geological Survey Geologic Investigations Series I-2895.

Billingsley, G. H., Felger, T. J., & Priest, S. S., 2006. Geologic map of the Valle 30' × 60' quadrangle, Coconino County, northern Arizona, U.S. Geological Survey Geologic Investigations Series I-2895.

Billingsley, T. J., Priest, S. S., G. H., & Felger, 2007. Geologic map of the Cameron 30' × 60' quadrangle, Coconino County, northern Arizona, U.S. Geological Survey Geologic Investigations Series I-2977.

Billingsley, T. J., Stoffer, P. W., & Priest, S. S., 2012. Geologic map of the Tuba City 30' × 60' quadrangle, Coconino County, northern Arizona, U.S. Geological Survey Scientific Investigations Map 3227.

Bird, P., 1979. Continental delamination and the Colorado Plateau, *Journal of Geophysical Research*, **84**(B13), 7,561–7,571.

Biryol, C. B., Beck, S. L., Zandt, G., & Özacar, A. A., 2011. Segmented African lithosphere beneath the Anatolian region inferred from teleseismic P-wave tomography, *Geophysical Journal International*, **184**(3), 1037–1057.

Bishop, J. W., Montañ, I. P., Gulbranson, E. L., & Brenckle, P. L., 2009. The onset of mid-Carboniferous glacio-eustasy: Sedimentologic and diagenetic constraints, Arrow Canyon, Nevada, *Palaeogeography, Palaeoclimatology, Palaeoecology*, **276**, 217–243.

Bishop, J. W., Montañ, I. P., & Osleger, D. A., 2010. Dynamic Carboniferous climate change, Arrow Canyon, Nevada, *Geosphere*, **6**(1), 1–34.

Blake, Jr., B. M. & Beuthin, J. D., 2008. Deciphering the mid-Carboniferous eustatic event in the central Appalachian foreland basin, southern West Virginia, USA, in *Resolving the Late Paleozoic ice age in space and time, Geological Society of America Special Paper 441*, edited by C. R. Fielding, T. D. Frank, & J. L. Isbell, pp. 249–260, Geological Society of America.

Blundy, J. & Wood, B., 2003. Partitioning of trace elements between crystals and melts, *Earth and Planetary Science Letters*, **210**, 383–397.

Bohn, R. T., 1977. A subsurface correlation of Permian-Triassic strata in Lisbon Valley, Utah, *Brigham Young University Geology Studies*, **24**(2), 103–116.

Boschi, L., Faccenna, C., & Becker, T. W., 2010. Mantle structure and dynamic topography in the Mediterranean Basin, *Geophysical Research Letters*, **37**, L20303.

Bose, M. N. & Kar, R. K., 1976. Palaeozoic sporae dispersae from Zaïre (Congo): Assises glaciaires et periglaciaire from the Lukuga Valley, *Annals du Musée de Congo Belge, Tervuren (Belgique), Serie in-8° – Sciences Geologiques*, **77**, 1–19.

Bose, M. N. & Kar, R. K., 1978. Biostratigraphy of the Lukuga Group in Zaïre, *Annals du Musée de Congo Belge, Tervuren (Belgique), Serie in-8° – Sciences Geologiques*, **82**, 97–113.

Bouhifd, M. A., Andrault, D., Fiquet, G., & Richet, P., 1996. Thermal expansion of forsterite up to melting point, *Geophysical Research Letters*, **23**(10), 1,143–1,146.

Bozkurt, E., Winchester, J. A., Ruffet, G., & Rojay, B., 2008. Age and chemistry of Miocene volcanic rocks from the Kiraz Basin of the Küçük Menderes Graben: Its significance for the extensionsional tectonics of Southwestern Anatolia, Turkey, *Geodinamica Acta*, **21**(5–6), 239–257.

Braun, J., 2010. The many surface expressions of mantle dynamics, *Nature*, **3**, 825–833.

Bristol, H. M. & Howard, R. H., 1971. Paleogeographic map of the sub-Pennsylvanian Chesterian (upper Mississippian) surface in the Illinois Basin, Illinois State Geological Survey Circular 458.

Brocher, T. M., 2005. Empirical relations between elastic wavespeeds and density in the Earths crust, *Bulletin of the Seismological Society of America*, **95**(6), 2,081–2,092.

Brounce, M. N., Kelley, K. A., & Cottrell, E., 2014. Variations in $Fe^{3+}/\Sigma Fe$ of Mariana Arc basalts and mantle wedge fO_2, *Journal of Petrology*, **55**(12), 2513–2536.

Bruckschen, P., Oesmann, S., & Veizer, J., 1999. Isotope stratigraphy of the European Carboniferous: Proxy signals for ocena chemistry, climate and tectonics, *Chemical Geology*, **161**, 127–163.

Buiter, S. J. H., Steinberger, B., Medvedev, S., & Tetreault, J. L., 2012. Could the mantle have caused subsidence of the Congo Basin?, *Tectonophysics*, **514–517**, 62–80.

Buket, E. & Temel, A., 1998. Major-element, trace-element, and SrNd isotopic geochemistry and genesis of Varto (Muş) volcanic rocks, Eastern Turkey, *Journal of Volcanology and Geothermal Research*, **85**, 405–422.

Burke, K., 1996. The african plate, *South African Journal of Geology*, **99**(4), 341–409.

Cahen, L., Ferrand, J. J., Haarsma, M. J. F., Lepersonne, J., & Verbeek, T., 1959. Description du Sondage de Samba, *Annals du Musée de Congo Belge, Tervuren (Belgique), Serie in-8° – Sciences Geologiques*, **29**, 210.

Cahen, L., Ferrand, J. J., Haarsma, M. J. F., Lepersonne, J., & Verbeek, T., 1960. Description du Sondage de Dekese, *Annals du Musée de Congo Belge, Tervuren (Belgique), Serie in-8° – Sciences Geologiques*, **34**, 115.

Caillaud, A., Blanpied, C., & D, D., 2017. The Upper Jurassic Stanleyville Group of the eastern Congo Basin: An example of perennial lacustrine system, *Journal of African Earth Sciences*, **132**, 80–98.

Campion, A., Maloof, A., Schoene, B., Oleynik, S., Sanz-López, J., Blanco-Ferrera, S., Merino-Tomé, O., Ramón Bahamonde, J., & Pedro Fernández, L., 2018. Constraining the timing and amplitude of early Serpukhovian glacioeustasy with a continuous carbonate record in northern Spain, *Geochemistry, Geophysics, Geosystems*, **19**, 2,647–2,660.

Carslow, H. S. & Jaeger, J. C., 1959. *Conduction of heat in solids*, Oxford University Press, Oxford, U.K., 2nd edn.

Cazenave, A., Dominh, K., Allegre, C. J., & Marsh, J. G., 1986. Global relationship between oceanic geoid and topography, *Journal of Geophysical Research*, **91**(B11), 11,439–11,450.

Cazenave, A., Dominh, K., Rabinowicz, M., & Ceuleneer, G., 1988. Geoid and depth anomalies over ocean swells and troughs: Evidence of an increasing trend of the geoid to depth ratio with age of plate, *Journal of Geophysical Research*, **93**(B7), 8,064–8,077.

Çakır, O. & Erduran, M., 2004. Constraining crustal and uppermost mantle structure beneath station TBZ (Trabzon, Turkey) by receiver function and dispersion analyses, *Geophysical Journal International*, **158**, 955–971.

Çakır, O. & Erduran, M., 2011. On the P and S receiver functions used for inverting the one-dimensional upper mantle shear-wave velocities, *Surveys in Geophysics*, **32**, 71–98.

Çiner, A., Kosun, E., & Deynoux, M., 2002. Fluvial, evaporitic and shallow-marine facies architecture, depositional evolution and cyclicity in the Sivas Basin (Lower to Middle Miocene), Central Turkey, *Journal of Asian Earth Sciences*, **21**, 147–165.

Chakrabarti, R., Basu, A. R., & Ghatak, A., 2012. Chemical geodynamics of Western Anatolia, *International Geology Review*, **54**(2), 227–248.

Chamorro, C. R., Garcia-Cuesta, J. L., Mondéjar, M. E., & Pérez-Madrazo, A., 2014. Enhanced geothermal systems in Europe: An estimation and comparison of the technical and sustainable potentials, *Energy*, **65**, 250–263.

Cipollari, P., Cosentino, D., Radeff, G., Schildgen, T. F., Faranda, C., Grossi, F., Gliozzi, E., Smedile, A., Gennari, R., Darbaş, G., Dudas, F. Ö., Gürbüz, K., Nazik, A., & Echtler, H., 2012. Easternmost Mediterranean evidence of the Zanclean flooding event and subsequent surface uplift: Adana Basin, southern Turkey, *Geological Society, London, Special Publications*, **372**(1), 473–494.

Cipollari, P., Halásová, E., Gürbüz, K., & Cosentino, D., 2013. Middle-Upper Miocene paleogeography of southern Turkey: Insights from stratigraphy and calcareous nannofossil biochronology of the Olukpınar and Başyayla sections (Mut-Ermenek Basin), *Turkish Journal of Earth Sciences*, **22**(5), 820–838.

Clauer, N., 1981. Rb-Sr and K-Ar dating of Precambrian clays and glauconies, *Precambrian Research*, **15**(15), 331–352.

Çoban, H., 2007. Basalt magma genesis and fractionation in collision- and extension-related provinces: A comparison between eastern, central and western Anatolia, *Earth-Science Reviews*, **80**(3-4), 219–238.

Çoban, H. & Flower, M. F. J., 2007. Late Pliocene lamproites from Bucak, Isparta (southwestern Turkey): Implications for mantle 'wedge' evolution during Africa-Anatolian plate convergence, *Journal of Asian Earth Sciences*, **29**, 160–176.

Çoban, H., Karacık, Z., & Işık Ece, Ö., 2012. Source contamination and tectonomagmatic signals of overlapping Early to Middle Miocene orogenic magmas associated with shallow continental subduction and asthenospheric mantle flows in Western Anatolia: A record from Simav (Kütahya) region, *Lithos*, **140–141**, 119–141.

Cochran, J. R. & Talwani, M., 1977. Free-air gravity anomalies in the world's oceans and their relationship to residual elevation, *Geophysical Journal International*, **50**(3), 495–552.

Colli, L., Ghelichkhan, S., & Bunge, H.-P., 2016. On the ratio of dynamic topography and gravity anomalies in a dynamic Earth, *Geophysical Research Letters*, **43**(6), 2510–2516.

Colpron, M. & Nelson, J. L., 2009. A Paleozoic northwest passage: Incursion of Caledonian, Baltican and Siberian terranes into eastern Panthalassa, and the early evolution of the North American Cordillera, in *Earth Accretionary Systems in Space and Time*, edited by P. A. Cawood & A. Kröner, pp. 273–307, The Geological Society, London, U.K., Special Publkication 318.

Coltice, N., P. B. R., Bertrand, H., Ricard, Y., & Rey, P., 2007. Global warming of the mantle at the origin of flood basalts over supercontinents, *Geology*, **35**(2), 391–394.

Condon, D., Zhu, M., Bowring, S., Wang, W., Yang, A., & Jin, Y., 2005. U-Pb ages from the Neoproterozoic Doushantuo Formation, China, *Science*, **308**(5718), 95–98.

Conrad, C. P. & Husson, L., 2009. Infl uence of dynamic topography on sea level and its rate of change, *Lithosphere*, **1**(2), 110–120.

Cosentino, D., Schildgen, T. F., Cipollari, P., Faranda, C., Gliozzi, E., Hudákovčá, N., Lucifora, S., & Strecker, M. R., 2012. Late Miocene surface uplift of the southern margin of the Central Anatolian plateau, Central Taurides, Turkey, *Bulletin of the Geological Society of America*, **124**(1-2), 133–145.

Cottrell, E. & Kelley, K. A., 2011. The oxidation state of Fe in MORB glasses and the oxygen fugacity of the upper mantle, *Earth and Planetary Science Letters*, **305**, 270–282.

Craig, T. J., Jackson, J. A., Priestley, K., & McKenzie, D., 2011. Earthquake distribution patterns in Africa: their relationship to variations in lithospheric and geological structure, and their rheological implications, *Geophysical Journal International*, **185**, 403–434.

Crosby, A. G., Fishwick, S., & White, N., 2010. Structure and evolution of the intracratonic Congo Basin, *Geochemistry, Geophysics, Geosystems*, **11**(6), Q06010.

Czarnota, K., Roberts, G., White, N., & Fishwick, S., 2014. Spatial and temporal patterns of Australian dynamic topography from river profile modeling, *Journal of Geophysical Research: Solid Earth*, **119**, 1384–1424.

Czarnota, K., Hoggard, M. J., Richards, F. D., Huston, D. L., & Jacques, L., 2019. Gigayear stability of cratonic edges controls global distribution of sediment-hosted metals, Preprint.

Dalton, C. A., Langmuir, C. H., & Gale, A., 2014. Geophysical and geochemical evidence for deep temperature variations beneath mid-ocean ridges, *Science*, **344**(6179), 80–83.

Daly, M. C., Lawrence, S. R., Kimun'a, D., & Binga, M., 1991. Late Paleozoic deformation in central Africa: a result of distant collision?, *Nature*, **350**, 605–607.

Daly, M. C., Lawrence, S. R., Diemu-Tshiband, K., & Matouana, B., 1992. Tectonic evolution of the Cuvette Centrale, Zaire, *Journal of the Geological Society*, **149**, 539–546.

Daly, M. C., Andrade, V., Barousse, C. A., Costa, R., McDowell, K., Piggott, N., & Poole, A. J., 2014. Brasiliano crustal structure and the tectonic setting of the Parnaíba basin of NE Brazil: Results of a deep seismic reflection profile, *Tectonics*, **33**, 2,102–2,120.

Davies, G. F., 1994. Thermochemical erosion of the lithosphere by mantle plumes, *Journal of Geophysical Research*, **99**(B8), 15,709–15,722.

Davydov, V. I., Korn, D., & Schmitz, M. D., 2012. The Carboniferous Period, in *The Geologic Time Scale 2012*, edited by F. M. Gradstein, J. G. Ogg, M. Schmitz, & G. Ogg, pp. 603–651, Elsevier.

de Castro, D. L., Fuck, R. A., Phillips, J. D., Vidotti, R. M., Bezerra, F. H. R., & Dantas, E. L., 2014. Crustal structure beneath the Paleozoic Parnaíba Basin revealed by airborne gravity and magnetic data, Brazil, *Tectonophysics*, **614**, 128–145.

de Castro, D. L., Bezerra, F. H. R., Fuck, R. A., Phillips, J. D., & Vidotti, R. M., 2016. Geophysical evidence of pre-sag rifing and post-rifting fault reactivation in the Parnaíba basin, Brazil, *Solid Earth*, **7**, 529–548.

de Sousa, M. A., 1996. Regional gravity modelling and geohistory of the Parnaíba Basin (NE Brazil), Ph. D. Dissertation, University of Newcastle upon Tyne.

De Voto, R. H., 1988. Late Mississippian paleokarst and related mineral deposits, Leadville Formation, Central Colorado, in *Paleokarst*, edited by N. P. James & P. W. Choquette, pp. 278–305, Springer-Verlag, New York.

Dehler, C., Gehrels, G., Porter, S., Heizler, M., Karlstrom, K., Cox, G., Crossey, L., & Timmons, M., 2017. Synthesis of the 780–740 Ma Chuar, Uinta Mountain and Pahrum (ChUMP) groups, western USA: Implications for Laurentia-wide cratonic marine basins, *Geological Society of America Bulletin*, **129**(5/6), 607–624.

Demir, T., Westaway, R., Bridgland, D., Pringle, M., Yurtmen, S., Beck, A., & Rowbotham, G., 2007. Ar-Ar dating of late Cenozoic basaltic volcanism in northern Syria: Implications for the history of incision by the River Euphrates and uplift of the northern Arabian Platform, *Tectonics*, **26**, TC3012.

Demir, T., Seyrek, A., Westaway, R., Guillou, H., Scaillet, S., Beck, A., & Bridgland, D. R., 2012. Late Cenozoic regional uplift and localised crustal deformation within the northern Arabian Platform in southeast Turkey: Investigation of the Euphrates terrace staircase using multidisciplinary techniques, *Geomorphology*, **165–166**, 7–24.

Deniel, C., Aydar, E., & Gourgaud, A., 1998. The Hasan Dagi stratovolcano (Central Anatolia, Turkey): evolution from calc-alkaline to alkaline magmatism in a collision zone, *Journal of Volcanology and Geothermal Research*, **87**, 275–302.

DePaulo, D. J., 1981. Trace element and isotopic effects of combined wallrock assimilation and fractional crystallization, *Earth and Planetary Science Letters*, **53**, 189–202.

Di Giuseppe, P., Agostini, S., Lustrino, M., Karaoğlu, Ö., Yilmaz Savaşçın, M., Manetti, P., & Ersoy, Y., 2017. Transition from compression to strike-slip tectonics revealed by MiocenePleistocene volcanism west of the Karlıova Triple Junction (East Anatolia), *Journal of Petrology*, **58**(10), 2,055–2,087.

di Giuseppe, P., Agostini, S., Manetti, P., Yilmaz Savaşçın, M., & Conticelli, S., 2018. Sublithospheric origin of Na-alkaline and calc-alkaline magmas in a post-collisional tectonic regime: Sr-Nd-Pb isotopes in recent monogenetic volcanism of Cappadocia, Central Turkey, *Lithos*, **316–317**, 304–322.

Dickinson, W. R. & Lawton, T. F., 2003. Sequential inetrcontinental suturing as the ultimate control for Pennsylvanian Ancestral Rocky Mountain deformation, *Geology*, **31**(7), 609–612.

Dilek, T. & Altunkaynak, S., 2010. Geochemistry of Neogene Quaternary alkaline volcanism in western Anatolia, Turkey, and implications for the Aegean mantle, *International Geology Review*, **52**(4–6), 631–655.

Dixon, J. E., Leist, L., Langmuir, C., & Schilling, J.-G., 2002. Recycled dehydrated lithosphere observed in plume-influenced mid-ocean-ridge basalt, *Nature*, **420**, 385–389.

Dolmaz, M. N., Hisarli, Z. M., Ustaömer, T., & Orbay, N., 2005. Curie point depths based on spectrum analysis of aeromagnetic data, West Anatolian Extensional Province, Turkey, *Pure and Applied Geophysics*, **162**, 571–590.

Downey, N. J. & Gurnis, M., 2009. Instantaneous dynamics of the cratonic Congo basin, *Journal of Geophysical Research*, **114**(B06401).

Droste, J. B. & Keller, S. J., 1989. Development of the Mississippian-Pennsylvanian unconformity in Indiana, Indiana Geological Survey Occasional Paper 55.

Dumitru, T. A., Duddy, I. R., & Green, P. F., 1994. Mesozoic-Cenzoic burial, uplift, and erosion history of the west-central Colorado Plateau, *Geology*, **22**, 499–502.

Duretz, T., Gerya, T. V., & May, D. A., 2011. Numerical modelling of spontaneous slab breakoff and subsequent topographic response, *Tectonophysics*, **502**, 244–246.

Dyer, B., Maloof, A. C., & Higgins, J. A., 2015. Glacioeustasy, meteoric diagenesis, and the carbon cycle during the Middle Carboniferous, *Geochemistry, Geophysics, Geosystems*, **16**, 3383–3399.

Dziewonski, A. M., Chou, T. A., & Woodhouse, J. H., 1981. Determination of earthquake source parameters from waveform data for studies of global and regional seismicity, *Journal of Geophysical Research*, **86**(B4), 2825–2852.

ECL, 1988. Hydrocarbon potential of Cuvette Centrale, Republic of Zaire, Tech. rep., Exploration Consultants Limited.

Ekici, T., 2016. Collision-related slab break-off volcanism in the Eastern Anatolia, Kepez volcanic complex (Turkey), *Geodinamica Acta*, **28**(3), 223–239.

Ekici, T., 2016. Petrology and Ar/Ar chronology of Erdembaba and Kuyucak Volcanics Eexposed along the North Anatolian Fault Zone (Eastern Pontides, NE Turkey): Implications for the Late Cenozoic geodynamic evolution of Eastern Mediterranean Region, *Journal of the Geological Society of India*, **87**, 411–423.

Ekici, T., Alpaslan, M., Parlak, O., & Temel, A., 2007. Geochemistry of the Pliocene basalts erupted along the Malatya-Ovacik fault zone (MOFZ), eastern Anatolia, Turkey: Implications for source characteristics and partial melting processes, *Chemie der Erde*, **67**, 201–212.

Ekici, T., Alpaslan, M., Parlak, O., & Uçurum, A., 2009. Geochemistry of the middle Miocene collision-related Yamadağı (Eastern Anatolia) calc-alkaline volcanics, Turkey, *Turkish Journal of Earth Science*, **18**, 511–528.

Ekici, T., Macpherson, C. G., & Otlu, N., 2012. Polybaric melting of a single mantle source during the Neogene Siverek phase of the Karacadağ Volcanic Complex, SE Turkey, *Lithos*, **146–147**, 152–163.

Ekici, T., Macpherson, C. G., Otlu, N., & Fontignie, D., 2014. Foreland Magmatism during the Arabia-Eurasia Collision: Pliocene-Quaternary Activity of the Karacadağ Volcanic Complex, SW Turkey, *Journal of Petrology*, **55**(9), 1,753–1,777.

Ekström, G., Nettles, M., & Dziewonski, A. M., 2012. The global CMT project 2004–2010: centroid moment tensors for 13,017 earthquakes, *Physics of the Earth and Planetary Interiors*, **200–201**, 1–9.

Elliott, T., 2003. Tracers in the Slab, in *Inside the Subduction Factory*, edited by J. Eiler, pp. 23–45, American Geophysical Union, Washington D.C., Gephysical Monograph 138.

Emre, Ö., Duman, T. Y., Özalp, S., Elmacı, H., Olgun, Ş., & Şaroğlu, F., 2013. *Active fault map of Turkey*, General Directorate of Mineral Research and Exploration, Ankara, Turkey.

England, P., Houseman, G., & Nocquet, J. M., 2016. Constraints from GPS measurements on the dynamics of deformation in Anatolia and the Aegean, *Journal of Geophysical Research: Solid Earth*, **121**(12), 8888–8916.

Ercan, T., Tokel, S., Matsuda, J., Ui, T., Notsu, K., & Fujitani, T., 1992. New geochemical, isotopic and radiometric data of the Quaternary volcanism of Hasandağı-Karacadağ (central Anatolia), *TJK Bülteni*, **7**, 8–21.

Erduran, M., 2009. Teleseismic inversion of crustal *S*-wave velocities beneath Isparta station, *Journal of Geodynamics*, **47**, 225–236.

Erkül, F., Helvacı, C., & Sözbilir, H., 2005. Evidence for two episodes of volcanism in the Bigadiç borate basin and tectonic implications for western Turkey, *Geological Journal*, **40**, 545–570.

Erkül, F., Çolak, C., Erkül, S. T., & Varol, E., 2019. Geology and geochemistry of the Middle Miocene Yağcıköy volcanic complex, western Turkey: Wide-rift alkaline volcanism associated with incipient stages of slab tearing, *Journal of Asian Earth Sciences*, **179**, 112–126.

Ersoy, E. Y. & Helvacı, C., 2016. Geochemistry and petrology of the lower Miocene bimodal volcanic units in the TunçbilekDomaniç basin, western Anatolia, *International Geology Review*, **58**(10), 1,234–1,252.

Ersoy, E. Y., Helvacı, C., & Palmer, M. R., 2010. Mantle source characteristics and melting models for the early-middle Miocene mafic volcanism in Western Anatolia: Implications for enrichment processes of mantle lithosphere and origin of K-rich volcanism in post-collisional settings, *Journal of Volcanology and Geothermal Research*, **198**, 112–128.

Ersoy, Y., Helvacı, C., Sözbilir, H., Erkül, F., & Bozkurt, E., 2008. A geochemical approach to Neogen-Quaternary volcanic activity of western Anatolia: An example of episodic bimodal volcanism within the Selendi Basin, Turkey, *Chemical Geology*, **255**, 265–282.

Ersoy, Y. E., Helvacı, C., & Palmer, M. R., 2012. Petrogenesis of the Neogene volcanic units in the NE–SW-trending basins in western Anatolia, Turkey, *Contributions to Mineral Petrology*, **163**, 379–401.

Ersoy, Y. E., Palmer, M. R., Uysal, I., & Gündoğan, I., 2014. Geochemistry and petrology of the Early Miocene lamproites and related volcanic rocks in the Thrace Basin, NW Anatolia, *Journal of Volcanology and Geothermal Research*, **283**, 143–158.

Ettensohn, F. R., 1994. Tectonic control on formation and cyclicity of major Appalachian unconformities and associated stratigraphic sequences, in *Tectonic and eustatic controls of sedimentary cycles*, edited by J. M. Dennison & F. R. Ettensohn, pp. 217–241, Society for Sedimentary Geology.

Faccenna, C., Becker, T. W., Jolivet, L., & Keskin, M., 2013. Mantle convection in the Middle East: Reconciling Afar upwelling, Arabia indentation and Aegean trench rollback, *Earth and Planetary Science Letters*, **375**, 254–269.

Faccenna, C., Becker, T. W., Auer, L., Billi, A., Boschi, L., Brun, J. P., Capitanio, F. A., Funiciello, F., Horvàth, F., Jolivet, L., Piromallo, C., Royden, L., Rossetti, F., & Serpelloni, E., 2014. Mantle dynamics in the Mediterranean, *Reviews of Geophysics*, **52**, 283–332.

Faul, U. H. & Jackson, I., 2005. The seismological signature of temperature and grain size variations in the upper mantle, *Earth and Planetary Science Letters*, **234**, 119–134.

Fielding, C. R., Frank, T. D., & Isbell, J. L., 2008. The late Paleozoic ice age — A review of current understanding and synthesis of global climate patterns, in *Resolving the late Paleozoic ice age in time and space, Geological Society of America Special Paper 441*, edited by C. R. Fielding, T. D. Frank, & J. L. Isbell, pp. 343–354, Geological Society of America.

Fitton, J. G., James, D., & Leeman, W. P., 1991. Basic magmatism associated with Late Cenozoic extension in the Western United States: compositional variations in space and time, *Journal of Geophysical Research*, **96**(B8), 13,693–17,711.

Flament, N., Gurnis, M., & Múller, R. D., 2013. A review of observations and models of dynamic topography, *Lithosphere*, **5**(2), 189–210.

Fodor, R. V., Sial, A. N., Mukusa, S. B., & McKee, E. H., 1990. Petrology, isotope characteristics, and K-Ar ages of the Maranhão, northern Brazil, Mesozoic basalt province, *Contributions to Mineral Petrology*, **104**, 555–567.

Förste, C., Bruinsma, S. L., Flechtner, F., Marty, J.-C., Lemoine, J.-M., Dahle, C., Abrikosov, O., Neumayer, K. H., Biancale, R., Barthelmes, F., & Balmino, G., 2012. A preliminary update of the Direct approach GOCE Processing and a new release of EIGEN-6C, in *AGU Fall Meeting*, San Francisco, USA.

Forte, A. M., Quéré, S., Moucha, R., Simmons, N. A., Grand, S. P., Mitrovica, J. X., & Rowley, D. B., 2010. Joint seismicgeodynamic-mineral physical modelling of African geodynamics: A reconciliation of deep-mantle convection with surface geophysical constraints, *Earth and Planetary Science Letters*, **295**, 329–341.

Foster, A. N. & Jackson, J. A., 1998. Source parameters of large African earthquakes: implications for crustal rheology and regional kinematics, *Geophysical Journal International*, **143**, 422–448.

Fowler, C. M. R. & Nisbet, E. G., 1995. The subsidence of the Williston Basin, *Canadian Journal of Earth Sciences*, **22**(3), 408–415.

Fox, M., Goren, L., May, D. A., & Willett, S. D., 2014. Inversion of fluvial channels for paleorock uplift rates in Taiwan, *Journal of Geophysical Research: Earth Surface*, **119**, 1853–1875.

Frahme, C. W. & Vaughn, E. B., 1983. Paleozoic geology and seismic stratigraphy of the northern Uncompahgre Front, Grand County, Utah, in *Rocky Mountain foreland basins and uplifts*, edited by J. D. Lowell & R. Gries, pp. 201–212, Rocky Mountain Association of Geologists, Denver, Colorado, USA.

Francalanci, L., Innocenti, F., Manetti, P., & Savasçin, M. Y., 2000. Neogene alkaline volcanism of the Afyon-Isparta area, Turkey: petrogenesis and geodynamic implications, *Mineralogy and Petrology*, **70**, 285–312.

Frimmel, H. E., Tack, L., Basei, M. S., Nutman, A. P., & Boven, A., 2006. Provenance and chemostratigraphy of the Neoproterozoic West Congolian Group in the Democratic Republic of Congo, *Journal of African Earth Sciences*, **46**, 221–239.

Gehrels, G. E., Blakey, R., Karlstrom, K. E., Timmons, J. M., Dickinson, B., & Pecha, M., 2011. Detrital zircon u-pb geochronology of paleozoic strata in the grand canyon, arizona, *Lithosphere*, **3**(3), 183–200.

Gencalioglu-Kuscu, G., 2011. Geochemical characterization of a Quaternary monogenetic volcano in Erciyes Volcanic Complex: Cora Maar (Central Anatolian Volcanic Province, Turkey), *International Journal of Earth Sciences*, **100**, 1967–1985.

Gencalioglu-Kuscu, G. & Geneli, F., 2010. Review of post-collisional volcanism in the Central Anatolian Volcanic Province (Turkey), with special reference to the Tepekoy Volcanic Complex, *International Journal of Earth Sciences*, **99**, 593–621.

Gençoğlu Korkmaz, G., Asan, K., Kurt, H., & Morgan, G., 2017. $^{40}Ar/^{39}Ar$ geochronology, elemental and Sr-Nd-Pb isotope geochemistry of the Neogene bimodal volcanism in the Ykselen area, NW Konya (Central Anatolia, Turkey), *Journal of African Earth Sciences*, **129**, 427–444.

Ghiorso, M. S., Hirschmann, M. M., Reiners, P. W., & Kress, V. C. I., 2002. The pMELTS: A revision of MELTS for improved calculation of phase relations and major element partitioning related to partial melting of the mantle to 3 GPa, *Geochemistry, Geophysics, Geosystems*, **3**(5), 1–35.

Gibson, S. A. & Geist, D., 2010. Geochemical and geophysical estimates of lithospheric thickness variation beneath Galápagos, *Earth and Planetary Science Letters*, **300**(3–4), 275–286.

Giresse, P., 2005. Mesozoic–Cenozoic history of the Congo Basin, *Journal of African Earth Sciences*, **43**, 301–315.

Globig, J., Fernàndez, M., Torne, M., Vergés, J., Robert, A., & Faccenna, C., 2016. New insights into the crust and lithospheric mantle structure of Africa from elevation, geoid, and thermal analysis, *Journal of Geophysical Research: Solid Earth*, **121**, 5,389–5,424.

Góes, A. M. O. & Feijó, F., 1994. Bacia do Parnaíba, *Boletim de Geociências da Petrobrás*, **8**(1), 57–68.

Góes, A. M. O., Souza, J., & Teixeira, L., 1990. Estágio exploraório e perspectivas petrolíferas da Bacia do Parnaíba, *Boletim de Geociências da Petrobrás*, **4**(1), 55–64.

Göğüş, O. H. & Psyklywec, R. N., 2008. Mantle lithosphere delamination driving plateau uplift and synconvergent extension in eastern Anatolia, *Geology*, **36**(9), 723–726.

Göğüş, O. H. & Ueda, K., 2018. Peeling back the lithosphere: Controlling parameters, surface expressions and the future directions in delamination modeling, *Journal of Geodynamics*, **117**, 21–40.

Göğüş, O. H., Psyklywec, R. N., Şengör, A. M. C., & Gün, E., 2017. Drip tectonics and the enigmatic uplift of the Central Anatolian Plateau, *Nature Communications*, **8**(1538).

Gök, R., Mahdi, H., Al-Shukri, H., & Rodgers, A. J., 2008. Crustal structure of Iraq from receiver functions and surface wave dispersion: implications for understanding the deformation history of the Arabian-Eurasian collision, *Geophysical Journal International*, **172**, 1179–1187.

Goren, L., Fox, M., & Willett, S. D., 2014. Tectonics from fluvial topography using formal linear inverion: Theory and applications to the Inyo Mountains, California, *Journal of Geophysical Research: Earth Surface*, **119**, 1615–1681.

Govers, R. & Fichtner, A., 2016. Signature of slab fragmentation beneath Anatolia from full-waveform tomography, *Earth and Planetary Science Letters*, **450**, 10–19.

Grossman, E. L., Yancey, T. E., Bruckschen, P., Chuvashov, B., Mazzullo, S. J., & Mii, H.-s., 2008. Glaciation, aridification, and carbon sequestration in the permo-carboniferous: The isotopic record from low latitudes.

Grover, P. W., 1989. Stratigraphy and depositional environment of the Surprise Canyon Formation, and upper Mississippian carbonate-clastic estuarine deposit, Grand Canyon, Arizona, MSc. Dissertation, Northern Arizona University.

Grutter, H. S., 2009. Pyroxene xenocryst geotherms: Techniques and application, *Lithos*, **112S**, 1,167–1,178.

Grützner, T., Prelević, D., & Akal, C., 2013. Geochemistry and origin of ultramafic enclaves and their basanitic hostrock from Kula Volcano, Turkey, *Lithos*, **180–181**, 58–73.

Güçtekin, A. & Köprübaşı, N., 2009. Geochemical characteristics of mafic and intermediate volcanic rocks from the Hasandağ and Erciyes volcanoes (Central Anatolia, Turkey), **18**, 1–27.

Gunn, R., 1943. A quantitative evaluation of the influence of the lithosphere on the anomalies of gravity, *Journal of the Franklin Institute*, **236**, 47–65.

Gürsoy, O., Kaya, Ş., Çakir, Z., Tatar, O., & Canbaz, O., 2017. Determining lateral offsets of rocks along the eastern part of the North Anatolian Fault Zone (Turkey) using spectral classification of satellite images and field measurements, *Geomatics, Natural Hazards and Risk*.

Gürsu, S., 2016. A new petrogenetic model for meta-granitic rocks in the central and southern Menderes Massif – W Turkey: Implications for Cadomian crustal evolution within the Pan-African mega-cycle, *Precambrian Research*, **275**, 450–470.

Gutschick, R. C. & Sandberg, C. A., 1983. Mississippian continental margins of the conterminous United States, *Society of Economic Paleontologists and Mineralogists Special Publication No. 33*, pp. 79–96.

Hager, B. H., Clayton, R. W., Richards, M. A., Comer, R. P., & Dziewonski, A. M., 1985. Lower mantle heterogeneity, dynamic topography and the geoid, *Nature*, **33**, 541–545.

Hamdani, Y., Mareschal, J.-C., & Arkani-Hamed, J., 1991. Phase changes and thermal subsidence in intracontinental sedimentary basins, *Geophysical Journal International*, **106**, 657–665.

Hanne, D., White, N., Butler, A., & Jones, S., 2004. Phanerozoic vertical motions of Hudson Bay, *Canadian Journal of Earth Sciences*, **41**, 1,181–1,200.

Hansen, S. E., Nyblade, A. A., & Julià, J., 2009. Estimates of crustal and lithospheric thickness in sub-Saharan Africa from *S*-wave receiver functions, *South African Journal of Geology*, **112**, 229–240.

Hart, S. R., Hauri, E. H., Oschmann, L. A., & Whitehead, J. A., 1992. Mantle Plumes and Entrainment: Isotopic Evidence, *Science*, **256**(5056), 517–520.

Hartley, R. A., Roberts, G. G., White, N., & Richardson, C., 2011. Transient convective uplift of an ancient buried landscape, *Nature Geoscience*, **4**(8), 562–565.

Hartley, R. W. & Allen, P. A., 1994. Interior cratonic basins of Africa: relation to continental break-up and role of mantle convection, *Basin Research*, **6**, 95–113.

Heine, C., Müller, R. D., Steinberger, B., & Torskiv, T. H., 2008. Subsidence in intracontinental basins due to dynamic topography, *Physics of the Earth and Planetary Interiors*, **171**, 252–264.

Helvacı, C., Ersoy, E. Y., Sözbilir, H., Erkül, F., Sümer, O., & Uzel, B., 2009. Geochemistry and $^{40}Ar/^{39}Ar$ geochronology of Miocene volcanic rocks from the Karabarun Peninsula: Implications ofr amphibole-bearing lithospheric mantle source, Western Anatolia, *Journal of Volcanology and Geothermal Research*, **185**, 181–202.

Herzberg, C., Asimow, P. D., Arndt, N., Niu, Y., Lesher, C. M., Fitton, J. G., Cheadle, M. J., & Saunders, A. D., 2007. Temperatures in ambient mantle and plumes: constraints from basalts, picrites and komatiites, *Geochemistry, Geophysics, Geosystems*, **8**(2).

Hintze, L. F., 1988. *Geologic History of Utah*, Department of Geology, Brigham Young University, Provo, UT, USA.

Hirschmann, M. M., 2010. Partial melt in the oceanic low velocity zone, *Physics of the Earth and Planetary Interiors*, **179**, 60–71.

Hirschmann, M. M. & Stolper, E. M., 1996. A possible role for garnet pyroxenite in the origin of the "garnet signature" in MORB, *Contributions to Mineralogy and Petrology*, **124**, 185–208.

Ho, T., Priestley, K., & Debayle, 2016. A global horizontal shear velocity model of the upper mantle from multimode Love wave measurements, *Geophysical Journal International*, **207**, 542–561.

Hobley, D. E. J., Adams, J. M., Nudurupati, S. S., Hutton, E. W. H., Gasparini, N. M., Istanbulluoglu, E., & Tucker, G. E., 2017. Creative computing with landlab: an open-source toolkit for building, coupling, and exploring two-dimensional numerical models of earth-surface dynamics, *Earth Surface Dynamics*, **5**, 21–46.

Hoffman, K.-H., Condon, D. J., Bowring, S. A., & Crowley, J. L., 2004. U-Pb zircon date from the Neoproterozoic Ghaub Formation, Namibia: Constraints on Marinoan glaciation, *Geology*, **32**(9).

Hofmeister, A. M., 1999. Mantle values of thermal conductivity and the geotherm from phonon lifetimes, *Science*, **283**(5,408), 1,699–1706.

Hoggard, M. J., White, N., & Al-Attar, D., 2016. Global dynamic topography observations reveal limited influence of large-scale mantle flow, *Nature Geoscience*, **9**, 456–463.

Hoggard, M. J., Winterbourne, J., Czarnota, K., & White, N., 2017. Oceanic residual depth measurements, the plate cooling model and global dynamic topography, *Journal of Geophysical Research: Solid Earth*, **122**(3), 2328–2372.

Horton, D. E., Poulsen, C. J., & Pollard, D., 2010. Influence of high-latitude vegetation feedbacks on late Paleozoic glacial cycles, *Nature Geoscience*, **3**, 572–577.

Horton, D. E., Poulsen, C. J., Montañnez, & DiMichele, W. A., 2012. Eccentricity-paces lare Paleozoic climate change, *Palaeogeography, Palaeoclimatology, Palaeoecology*, **331–331**, 150–161.

Houseman, G. A., M^{c}Kenzie, D. P., & Molnar, P., 1981. Convective instability of a thickened boundary layer and its relevance for the thermal evolution of continental convergent belts, *Journal of Geophysical Research*, **86**(B7), 6,115–6,132.

Howard, A. D. & Kerby, G., 1983. Channel changes in badlands, *Geological Society of America Bulletin*, **94**, 739–752.

Howard, R. H. & Whitaker, S. T., 1988. Hydrocarbon accumulation in a paleovalley at Mississippian-Pennsylvanian unconformity near Hardinville, Crawford County, Illinois: A model paleogeomorphic trap, Illinois Petroleum 129.

Hubert-Ferrari, A., Armijo, R., King, G., Meyer, B., & Aykut, B., 2002. Morphology, displacement, and slip-rates along the North Anatolian Fault, Turkey, *Journal of Geophysical Research*, **107**(B10), 2235.

Huffman, Jr., A. C. H. & Condon, S. M., 1993. Stratigraphy, structure, and paleogeography of Pennsylvanian and Permian Rocks, San Juan Basin and Adjacent Areas, Utah, Colorado, Arizona, and New Mexico, *United States Geological Survey Bulletin*, **1808-O**, O1–O44.

Hüsing, S. K., Zachariasse, W.-J., van Hinsbergen, D. J. J., Krijgsman, W., Inceoz, M., Harzhauser, M., Mandic, O., & Kroh, A., 2009. Oligocene-Miocene basin evolution in SE Anatolia, Turkey: constraints on the closure of the eastern Tethys gateway, *Geological Society, London, Special Publications*, **311**(1), 107–132.

Ilkışık, O. M., 1995. Regional heat flow in western Anatolia using silica temperature estimates from thermal springs, *Tectonophysics*, **244**, 175–184.

Innocenti, F., Agostini, S., Di Vincenzo, G., Doglioni, C., Manetti, P., Savaşçin, M. Y., & Tonarini, S., 2005. Neogene and Quaternary volcanism in Western Anatolia: Magma sources and geodynamic evolution, *Marine Geology*, **221**(1-4), 397–421.

Isik, V., Uysal, I. T., Caglayan, A., & Seyitoglu, G., 2014. The evolution of intraplate fault systems in central Turkey: Structural evidence and Ar-Ar and Rb-Sr age constraints for the Savcili Fault Zone, *Tectonics*, **33**(10), 1875–1899.

Italiano, F., Yuce, G., Di Bella, M., Rojay, B., Sabatino, G., Tripodo, A., Martelli, M., Rizzo, A. L., & Misseri, M., 2017. Noble gases and rock geochemistry of alkaline intraplate volcanics from the Amik and Ceyhan-Osmaniye areas, SE Turkey, *Chemical Geology*, **469**, 34–46.

Jackson, J. & M^{c}Kenzie, D., 1988. The relationship between plate motions and seismic moment tensor, and the rates of active deformation in the Mediterranean and Middle East, *Geophysical Journal*, **93**, 45–73.

Jarvis, G. T. & M^{c}Kenzie, D. P., 1980. Sedimentary basin formation with finite extension rates, *Earth and Planetary Science Letters*, **48**, 42–52.

Jennings, E. S. & Holland, T. J. B., 2015. A simple thermodynamic model for melting of peridotite in the system NCFMASOCr, *Journal of Petrology*, **56**(5), 869–892.

Jolivet, L. & Brun, J. P., 2010. Cenozoic geodynamic evolution of the Aegean, *International Journal of Earth Sciences*, **99**(1), 109–138.

Jones, S. M., White, N., & Lovell, B., 2001. Cenozoic and Cretaceous transient uplift in the Porcupine Basin and its relationship to a mantle plume, pp. 345–360, Geological Society of London.

Jordan, T. H., 1978. Composition and development of the continental tectosphere, *Nature*, **274**, 544–548.

Kaban, M. K., Schwintzer, P., Artemieva, I. M., & Mooney, W. D., 2003. Density of the continental roots: Compositional and thermal contributions, *Earth and Planetary Science Letters*, **209**, 53–69.

Kadima, E., Delvaux, D., Sebagenzi, S. N., Tack, L., & Kabeya, S. M., 2011. Structure and geological history of the Congo Basin: an integrated interpretation of gravity, magnetic and reflection seismic data, *Basin Research*, **23**, 499–527.

Kadima Kabongo, E., Ntabwoba, S. S. M., & Lucazeau, F., 2011. A proterozoic-rift origin for the structure and the evolution of the cratonic congo basin.

Karaoğlu, O., Helvacı, C., & Ersoy, Y., 2010. Petrogenesis and $^{40}Ar/^{39}Ar$ geochronology of the volcanic rocks of the Uşak-Güre basin, western Türkiye, *Lithos*, **119**, 193–210.

Karato, S.-i., 2011. Water distribution across the mantle transition zone and its implications for global material circulation, *Earth and Planetary Science Letters*, **301**, 413–423.

Karlstrom, K. E. & Bowring, S. A., 1993. Proterozoic orogenic history of Arizona, in *Transcontinental Proterozoic provinces, Precambrian: Conterminous U.S.*, edited by W. R. Van Schmus & M. E. Bickford, vol. C-2, pp. 188–228, Geological Society of America, Boulder, Colorado, U.S.A.

Karlstrom, K. E., Bowring, S. A., Dehler, C. M., Knoll, A. H., Porter, S. M., Des Marais, D. J., Weil, A. B., Sharp, Z. D., Geissman, J. W., Elrick, M. B., Timmons, J. M., Crossey, L. J., & Davidek, K. L., 2000. Chuar Group of the Grand Canyon: Record of breakup of Rodinia, associated change in the global carbon cycle, and ecosystem expansion by 740 Ma, *Geology*, **28**(7), 619–622.

Karlstrom, K. E., Hagadorn, J., Gehrels, G., Matthews, W., Schmitz, M., Madronich, L., Mulder, J., Pecha, M., Giesler, D., & Crossey, L., 2018. Cambrian Sauk transgression in the Grand Canyon region redefined by detrital zircons, *Nature Geoscience*, **11**, 438–443.

Katsura, T., Yamada, H., Nishikawa, O., Song, M., Kubo, A., Shinmei, T., Yokoshi, S., Aizawa, Y., Yoshino, T., Walter, M. J., Ito, E., & Funakoshi, K.-i., 2004. Olivine-wadsleyite transition in the system $(Mg, Fe)_2SiO_2$, *Journal of Geophysical Research: Solid Earth*, **109**(B02209).

Katz, R. F., Spiegelmann, M., & Langmuir, C. H., 2003. A new parameterization of hydrous mantle melting, *Geochemistry, Geophysics, Geosystems*, **4**(9).

Kelley, K. A., Plank, T., Newman, S., Stolper, E. M., Grove, T. L., Parman, S., & Hauri, E. H., 2010. Mantle melting as a function of water content beneath the Mariana Arc, *Journal of Petrology*, **51**(8), 1711–1738.

Kempton, P. D., Fitton, J. G., Hawkesworth, C. J., & Ormerod, D. S., 1991. Isotopic and trace element constraints on the composition and evolution of the lithosphere beneath the southwestern United States, *Journal of Geophysical Research*, **96**(B8), 13,713–13,735.

Kent, W. N. & Rawson, R. R., 1980. Depositional environments of the Mississippian Redwall Limestone in northeastern Arizona, in *Paleozoic Paleogeography of the West-Central United States: Rocky Mountain Symposium 1*, edited by T. D. Fouch & E. R. Magathan, pp. 101–109, Society of Economic Paleontologists and Mineralogists, Los Angeles, California, USA.

Keskin, M., 2003. Magma generation by slab steepening and breakoff beneath a subduction-accretion complex: An alternative model for collision-related volcanism in Eastern Anatolia, Turkey, *Geophysical Research Letters*, **30**(24), 7–10.

Keskin, M., 2007. Eastern Anatolia: A hotspot in a collision zone without a mantle plume, in *Plates, plumes and planetary processes*, edited by G. R. Foulger & D. M. Jurdy, pp. 693–722,

The Geological Society of America, Boulder, Colorado, Geological Society of America Special Paper 430.

Keskin, M., Pearce, J. A., & Mitchell, J. G., 1998. Volcano-stratigraphy and geochemistry of collision-related volcanism on the Erzurum-Kars Plateua, northeastern Turkey, *Journal of Volcanology and Geothermal Research*, **85**, 355–404.

Kheirkhah, M., Allen, M. B., & Emami, M., 2009. Quaternary syn-collision magmatism from the Iran/Turkey borderlands, *Journal of Volcanology and Geothermal Research*, **182**, 1–12.

Kind, R., Eken, T., Tilmann, F., Sodoudi, F., Taymaz, T., Bulut, F., Yuan, X., Can, B., & Schneider, F., 2015. Thickness of the lithosphere beneath Turkey and surroundings from S-receiver functions, *Solid Earth*, **6**, 971–984.

Klaver, M., Djuly, T., de Graaf, S., Sakes, A., Wijbrans, J., Davies, G., & Vroon, P., 2015. Temporal and spatial variations in provenance of Eastern Mediterranean Sea: Implications for Aegean and Aeolian arc volcanism, *Geochemica et Cosmochimica Acta*, **153**, 149–168.

Klaver, M., Davies, G. R., & Vroon, P. Z., 2016. Subslab mantle of African provenance infiltrating the Aegean mantle wedge, *Geology*, **44**(5), 367–370.

Klein, G. d., 1991. Origin and evolution of North American cratonic basins, *South African Journal of Geology*, **94**(1), 3–18.

Klein, G. d. & Hsui, A. T., 1987. Origin of cratonic basins, *Geology*, **15**, 1,094–1,098.

Klöcking, M., White, N. J., & Maclennan, J., 2018. Role of basaltic magmatism within the Parnaíba cratonic basin, NE Brazil, in *Cratonic Basin Formation: A Case Study of the Parnaíba Basin of Brazil, Geological Society Special Publication 472*, edited by M. C. Daly, R. A. Fuck, J. Julià, D. I. M. Macdonald, & A. B. Watts, pp. 309–319, Geological Society, London.

Klöcking, M., White, N. J., Maclennan, J., M^{c}Kenzie, D., & Fitton, J. G., 2018. Quantitative Relationships Between Basalt Geochemistry, Shear Wave Velocity, and Asthenospheric Temperature Beneath Western North America, *Geochemistry, Geophysics, Geosystems*, **19**(9), 3,376–3,404.

Kluth, C. F. & Coney, P. J., 1981. Plate tectonics of the Ancestral Rocky Mountains, *Geology*, **9**, 10–15.

Kocaarslan, A. & Ersoy, E. Y., 2018. Petrologic evolution of Miocene-Pliocene mafic volcanism in the Kangal and Gürün basins (Sivas-Malatya), central east Anatolia: Evidence for Miocene anorogenic magmas contaminated by continental crust, *Lithos*, **310–311**, 392–408.

Komut, T., 2014. High surface topography related to upper mantle flow beneath Eastern Anatolia, *Geophysical Journal International*, **203**, 1,263–1,273.

Komut, T., Gray, R., Pysklywec, R., & Göğüş, O. H., 2012. Mantle flow uplift of western Anatolia and the Aegean: Interpretations from geophysical analyses and geodynamic modeling, *Journal of Geophysical Research*, **117**(B11412).

Korn, D., 2006. Ammonoideen, in *Stratigraphie von Deutschland VI. Unterkarbon (Mississippium). — Schriftenreihe der Deutschen Gesselschaft für Geowissenschaften 41*, edited by Deustche Stratigraphie Kommission, pp. 147–170, Deutschen Gesselschaft für Geowissenschaften, Hannover, Germany.

Kosarian, M., 2006. Lithospheric structure of North Africa and western Eurasia, PhD. Dissertation, The Pennsylvania State University.

Kosman, C. W., Kopylova, M. G., Stern, R. A., Hagadorn, J. W., & Hurlbut, J. F., 2016. Cretaceous mantle of the Congo craton: Evidence from mineral and fluid inclusions in Kasai alluvial diamonds, *Lithos*, **265**, 42–56.

Kürkçüoğlu, B., Pickard, M., Şen, P., Hanan, B. B., Sayit, K., Plummer, C., Sen, E., Yurur, T., & Furman, T., 2015. Geochemistry of mafic lavas from Sivas, Turkey and th eevolution of Anatolian lithosphere, *Lithos*, **232**, 229–241.

Kürkcüglu, B., 2010. Geochemistry and petrogenesis of basaltic rocks from the Develidağ volcanic complex, Central Anatolia, Turkey, *Journal of Asian Earth Sciences*, **37**.

Kürkcüglu, B., Sen, E., Aydar, E., Gourgaud, A., & Gündogdu, N., 1998. Geochemical approach to magmatic evolution of Mt. Erciyes stratovolcano Central Anatolia, Turkey, *Journal of Volcanology and Geothermal Research*, **85**.

Kürüm, S. & Tanyıldızı, Ö., 2017. Geochemical and Sr-Nd isotopic characteristics of Upper Cretaceous (calc-alkaline) and Miocene (alkaline) volcanic rocks: Elazığ, Eastern Taurides, Turkey, *Journal of Asian Earth Science*, **134**, 332–344.

Kürüm, S., Önal, A., Boztuğ, D., Spell, T., & Arslan, M., 2008. $^{40}Ar/^{39}Ar$ age and geochemistry of the post-collisional Miocene Yamadağ volcanics in the Arapkir area (Malatya Province), eastern Anatolia, Turkey, *Journal of Asian Earth Science*, **33**, 229–251.

Lane, H. R. & Brenckle, P. L., 2005. Type Mississippian subdivisions and biostratigraphic succession, in *Stratigraphy and biostratigraphy of the Mississippian subsystem (Carboniferous System) in its type region, the Mississippi River Valley of Illinois, Missouri and Iowa*, edited by P. H. Heckel, pp. 76–105, Illinois State Geological Survey, Champaign, IL, USA.

Lane, H. R., Brenckle, P. L., Basemann, J. F., & Richards, B., 1999. The IUGS boundary in the middle of the Carboniferous: Arrow Canyon, Nevada, USA, *Episodes*, **22**(4), 272–283.

Langmuir, C. H., Bezoós, A., Escrig, S., & Parman, S. W., 2006. Chemical Systematics and Hydrous Melting of the Mantle in Back-Arc Basins, in *Back-Arc Spreading Systems: Geological, Biological, Chemical, and Physical Interactions*, edited by D. M. Christie, C. R. Fisher, S.-M. Lee, & S. Givens, pp. 87–146, American Geophysical Union, Geophysical Monograph Series 166.

Laske, G. & Masters, G., 1997. A global digital map of sediment thickness, *Eos, Transactions American Geophysical Union*, **78**(F483).

Lawrence, S. R. & Makazu, M. M., 1988. Zaire's Central basin: Prospectivity outlook, *Oil and Gas Journal*, **19**, 105–108.

Lawton, T. F., Cashman, P. H., Trexler, Jr., J. H., & Taylor, W. J., 2017. The late Paleozoic Southwestern Laurentian Borderland, *Geology*, **45**(8), 675–678.

Le Pichon, X. & Kreemer, C., 2010. The Miocene-to-present kinematic evolution of the Eastern Mediterranean and Middle East and its implications for dynamics, *Annual Reviews of Earth and Planetary Sciences*, **38**, 323–351.

Leary, R. J., Umhoefer, P., Smith, M. E., & Riggs, N., 2017. A three-sided orgoen: A new tectonic model for Ancestral Rocky Mountain uplift and basin development, *Geology*, **45**(8), 735–738.

Lebedev, V. A., Bubnov, S. N., Chugaev, A. V., Dudauri, O. Z., & Vashakidze, G. T., 2007. Geochronology and Genesis of Subalkaline Basaltic Lava Rivers at the Dzhavakheti Highland, Lesser Caucasus: KAr and SrNd Isotopic Data, *Geochemistry International*, **45**(3), 211–225.

Lebedev, V. A., Bubnov, S. N., Dudauri, O. Z., & Vashakidze, G. T., 2008. Geochronology of Pliocene volcanism in the Dzhavakheti Highland (the Lesser Caucasus). Part 1: Western part of the Dzhavakheti Highland, *Stratigraphy and Geological Correlation*, **16**(2), 204–224.

Lebedev, V. A., Bubnov, S. N., Dudauri, O. Z., & Vashakidze, G. T., 2008. Geochronology of Pliocene volcanism in the Dzhavakheti Highland (the Lesser Caucasus). Part 1: Eastern part of the Dzhavakheti Highland. Regional geological correlation, *Stratigraphy and Geological Correlation*, **16**(5), 553–574.

Lebedev, V. A., Sharkov, E. V., Ünal, E., & Keskin, M., 2016. Late Pleistocene Tendürek Volcano (Eastern Anatolia, Turkey): 1. Geochronology and petrographic characteristics of igneous rocks, *Petrology*, **24**(2), 127–152.

Lebedev, V. A., Sharkov, E. V., Ünal, E., & Keskin, M., 2016. Late Pleistocene Tendürek Volcano (Eastern Anatolia, Turkey): 2. Geochemistry and petrogenesis of the rocks, *Petrology*, **24**(2), 234–270.

Lee, C. A., 2003. Compositional variation of density and seismic velocities in natural peridotites at STP conditions: Implications for seismic imaging of compositional heterogeneities in the upper mantle, *Journal of Geophysical Research*, **108**(B9).

Lee, C. T. A., Luffi, P., Plank, T., Dalton, H., & Leeman, W. P., 2009. Constraints on the depths and temperatures of basaltic magma generation on Earth and other terrestrial planets using new thermobarometers for mafic magmas, *Earth and Planetary Science Letters*, **279**(1-2), 20–33.

Lighthill, M. J. & Whitham, G. B., 1955. On kinematic waves I. Flood movement in long rivers, *Proceedings of the Royal Society A: Mathematical, Physical and Engineering Sciences*, **229**(1,178), 281–316.

Linol, B., de Wit, M. J., Barton, E., Guillocheau, F., de Wit, M. C., & Colin, J.-P., 2015. Paleogeography and tectono-stratigraphhy of Carboniferous–Permian and Triassic 'Karoo-like' sequences of the Congo Basin, in *Geology and Resource Potential of the Congo Basin*, edited by M. J. de Wit, F. Guillocheau, & M. C. J. de Wit, pp. 111–134, Springer, Heidelberg.

Linol, B., de Wit, M. J., Guillocheau, F., de Wit, M. C., Anka, Z., & Colin, J.-P., 2015. Formation and Collapse of the Kalahari Duricrust ['African Surface'] Across the Congo Basin, with Implications for Changes in Rates of Cenozoic Off-Shore Sedimentation, in *Geology and Resource Potential of the Congo Basin*, edited by M. J. de Wit, F. Guillocheau, & M. C. J. de Wit, pp. 193–211, Springer, Heidelberg.

Lucas, S. G. & Heckert, A. B., 2005. Mesozoic stratigraphy at Durango, in *56th Field Conference Guidebook, Geology of the Chama Basin*, edited by S. G. Lucas, K. E. Zeigler, V. W. Lueth, & D. E. Owen, pp. 160–169, New Mexico Geological Society, Socorro, New Mexico, USA.

Lucazeau, F., Armitage, J., & Kadima Kabongo, É., 2015. Thermal regime and evolution of the Congo Basin as an intracratonic basin, in *Geology and Resource Potential of the Congo Basin*, edited by M. J. de Wit, F. Guillocheau, & M. C. J. de Wit, pp. 229–244, Springer, Heidelberg.

Lüdecke, T., Mikes, T., Rojay, F. B., Cosca, M. A., & Mulch, A., 2013. Stable isotope-based reconstruction of Oligo-Miocene paleoenvironment and paleohydrology of Central Anatolian lake basins (Turkey), *Turkish Journal of Earth Sciences*, **22**(5), 793–819.

Lustrino, M. & Wilson, M., 2007. The circum-Mediterranean anorogenic Cenozoic igneous province, *Earth-Science Reviews*, **81**, 1–65.

Lustrino, M., Keskin, M., Mattioli, M., Lebedev, V. A., Chugaev, A., Sharkov, E., & Kavak, O., 2010. Early activity of the largest Cenozoic shield volcano in the circum-Mediterranean area: Mt. Karacadağ, SE Turkey, *European Journal of Mineralogy*, **22**, 343–362.

Lustrino, M., Keskin, M., Mattioli, M., & Kavak, O., 2012. Heterogenous mantle sources feeding the volcanic activity of Mt. Karacadağ (SE Turkey), *Journal of Asian Earth Sciences*, **46**, 120–139.

Luz, R. M. N., Julià, J., & do Nascimento, A. F., 2015. Bulk crustal properties of the Borborema Province, NE Brazil, from P-wave receiver functions: Implications for models of intraplate Cenozoic uplift, *Tectonophysics*, **644–645**, 81–91.

Mahatsente, R., Önal, G., & Çemen, I., 2018. Lithospheric structure and the isostatic state of Eastern Anatolia: Insights from gravity data modelling, *Lithosphere*, **10**(2), 279–290.

Mamet, B. & Skipp, B., 1970. Lower Carboniferous calcareous foraminifera: Prelimenary zonation and stratigraphic implications for the Mississippian of North America, in *Sixième Congrès International de Stratigraphie et de Géologie du Carbonifière, Sheffield 11th to 16th September 1967: Compte Rendu*, vol. 3, pp. 1129–1146.

Martin, H., 1992. Conodont biostratigraphy and paleoenvironment of the Surprise Canyon Formation (late Mississippian), Grand Canyon, Arizona, MSc. Dissertation, Northern Arizona University.

Martin, H. & Barrick, J. E., 1999. Conodont Biostratigraphy, in *Geology of the Surprise Canyon Formation of the Grand Canyon, Arizona*, edited by G. H. Billingsley & S. S. Beus, pp. 97–116, Museum of Northern Arizona Bulletin 61, Flagstaff, AZ, USA.

Martín-Monge, A., Baudino, R., Gairifo-Ferreira, L. M., Tocco, R., Badalì, M., Ochoa, M., Haryono, S., Soriano, S., El Hafiz, N., Hernán-Gómez, J., Chacón, B., Brisson, I., Grammatico, G., Varadé, R., & Abdallah, H., 2016. An unusual Protetozoic petroleum play in Western Africa: the Atar Group carbonates (Taoudeni Basin, Mauritania), pp. 119–157, Geological Society, London.

Marzoli, A., Renne, P. R., Piccirillo, E. M., Ernesto, M., Bellieni, G., & De Min, A., 1999. Extensive 200-million-year-old continental flood basalts of the Central Atlantic Magmatic Province, *Science*, **284**, 616–618.

Maslyn, R. M., 1977. Fossil tower karst near Molas Lake, Colorado, *The Mountain Geologist*, **14**(1), 17–25.

Mather, K. A., Pearson, D. G., McKenzie, D., Kjarsgaard, B. A., & Priestley, K., 2011. Constraints on the depth and thermal history of cratonic lithosphere from peridotite xenoliths, xenocrysts and seismology, *Lithos*, **125**, 729–742.

Matthews, K. J., Maloney, K. T., Zahirovic, S., Williams, S. E., Seton, M., & Müller, 2016. Global plate boundary evolution and kinematics since the late Paleozoic, *Global and Planetary Change*, **146**, 226–250.

Matthews, S., Shorttle, O., & Maclennan, J., 2016. The temperature of the Icelandic mantle from olivine-spinel aluminum exchange thermometry, *Geochemistry, Geophysics, Geosystems*, **17**, 4725–4752.

McBride, E. F., 2016. Stratigraphy, petrography, and depositional history of the Ignacio Quartzite and McCracken Sandstone Member of the Elbert Formation, southwestern Colorado, U.S.A., *Rocky Mountain Geology*, **51**(2), 23–68.

McKee, E. D., 1963. Nomenclature for lithologic subdivisions of the Mississippian Redwall Limestone, Arizona, *United States Geological Survey Professional Paper*, **475-C**(65), C21–C22.

McKee, E. D., 1975. The Supai Group—Subdivision and nomenclature, *United States Geological Survey Bulletin*, **1395-J**, J1–J11.

McKee, E. D., 1982. Erosion Surfaces, in *The Supai Group of the Grand Canyon*, vol. Professional Paper 1173, pp. 155–176, United States Geological Survey, Washington D.C.

McKee, E. D. & Gutschick, R. C., 1969. *History of the Redwall Limestone of Northern Arizona*, vol. Memoir 114, The Geological Society of America, Boulder, Colorado.

McPhee, P. J. & van Hinsbergen, D. J. J., 2019. Tectonic reconstruction of Cyprus reveals Late Miocene continental collision of Africa and Anatolia, *Gondwana Research*, **68**, 158–173.

McPhee, P. J., Altıner, D., & van Hinsbergen, D. J. J., 2018. First balanced cross section across the Taurides fold-thrust belt: Geological constraints on the subduction history of the Antalya slab in southern Anatolia, *Tectonics*, **37**, 3,738–3,759.

McQuarrie, N. & van Hinsbergen, D. J. J., 2013. Retrodeforming the Arabia-Eurasia collision zone: Age of collision versus magnitude of continental subduction, *Geology*, **41**(3), 315–318.

Meijers, M. J. M., Brocard, G. Y., Cosca, M. A., Lüdecke, T., Teyssier, C., Whitney, D. L., & Mulch, A., 2018. Rapid late Miocene surface uplift of the Central Anatolian Plateau margin, *Earth and Planetary Science Letters*, **497**, 29–41.

Menard, H. W., 1973. Depth anomalies and the bobbing motion of drifting islands, *Journal of Geophysical Research*, **78**(23), 5,128–5,137.

Merle, R., Marzoli, A., Bertrand, H., Reisberg, L., Verati, C., Zimmermann, C., Chiaradia, M., Bellieni, G., & Ernesto, M., 2011. $^{40}Ar/^{39}Ar$ ages and Sr-Nd-Pb-Os geochemistry of CAMP tholeiites from Western Maranhão basin (NE Brazil), *Lithos*, **122**, 137–151.

Meyers, William, J., 1988. Pelokarstic features in Mississippian limestones, Wyoming, in *Paleokarst*, edited by N. P. James & P. W. Choquette, pp. 307–328, Springer-Verlag, New York.

Miall, A., 1997. *The Geology of Stratigraphic Sequences*, Springer, Berlin.

Michael, P., 1995. Regionally distinctive sources of depleted MORB: Evidence from trace elements and H_2O, *Earth and Planetary Science Letters*, **131**(3–4), 301–320.

Middleton, M. F., 1989. A model for the formation of intracratonic sag basins, *Geophysical Journal International*, **99**, 665–676.

Mii, H.-S., Grossman, E. L., & Yancey, T. E., 1999. Carboniferous isotope stratigraphies of North America: Implications for Carboniferous paleoceonagraphy and Mississippian glaciation, *Geological Society of America Bulletin*, **111**(7), 960–973.

Mii, H.-s., Grossman, E. L., Yancey, T. E., Chuvashov, B., & Egorov, A., 2001. Isotopic records of brachiopod shells from the Russian Platform — evidence for the onset of mid-Carboniferous glaciation, *Chemical Geology*, **175**, 133–147.

Miller, E. L., Miller, M. M., Stevens, C. H., Wright, J. E., & Madrid, R., 1992. Late Paleozoic paleogeographic and tectonic evolution of the western U.S. Cordillera, in *The Cordilleran Orogen: Conterminous U.S., The Geology of North America v. G-3*, edited by B. C. Burchfiel, P. W. Lipman, & M. L. Zoback, pp. 57–106, Geological Society of America, Boulder, CO, USA.

Miller, K. G., Kominz, M. A., Browning, J. V., Wright, J. D., Mountain, G. S., Katz, M. E., Sugarman, P. J., Cramer, B. S., Christie-Blick, N., & Pekar, S. F., 2005. The Phanerozoic record of global sea-level change, *Science*, **310**(5,752), 1,293–1298.

Molinari, I. & Morelli, A., 2011. EPcurst: a reference model for the European Plate, *Geophysical Journal International*, **185**(1), 352–364.

Montañez, I. P. & Poulsen, C. J., 2013. The Late Paleozoic Ice Age: An evolving paradigm, *Annual Reviews of Earth and Planetary Sciences*, **41**, 629–656.

Morgan, W. J., 1965. Gravity anomalies and convection currents: 1. a sphere and cylinder sinking beneath the surface of a viscous fluid, *Journal of Geophysical Rsearch*, **70**(24), 6,175–6,187.

Moussine-Pouchkine, A. & Bertrand-Sarfait, J., 1997. Tectonosedimentary subdivisions in the Neoproterozoic to Early Cambrian cover of the Taoudenni Basin (Algeria-Mauritania-Mali), *Journal of African Earth Sciences*, **24**(4), 425–443.

McKenzie, D., 1977. Surface deformation, gravity anomalies and convection, *Geophysical Journal of the Royal Astranomical Society*, **48**, 211–238.

McKenzie, D., 1978. Active tectonics of the Alpine-Himalayan belt: the Aegean Sea and surrounding regions, *Geophysical Journal of the Royal Astronomical Society*, **55**, 217–254.

McKenzie, D., 1978. Some remarks on the development of sedimentary basins, *Earth and Planetary Science Letters*, **40**, 25–32.

McKenzie, D., 2003. Estimating T_e in the presence of internal loads, *Journal of Geophysical Research*, **108**(B9), 2438.

McKenzie, D., 2010. The influence of dynamically supported topography on estimates of T_e, *Earth and Planetary Science Letters*, **295**(1–2), 127–138.

McKenzie, D. & Bickle, M. J., 1988. The volume and composition of melt generated by extension of the lithosphere, *Journal of Petrology*, **29**(3), 625–679.

McKenzie, D. & Fairhead, D., 1997. Estimates of the effective elastic thickness of the continental lithosphere from Bouger and free air gravity anomalies, *Journal of Geophysical Research*, **102**(B12), 27,523–27,552.

McKenzie, D. & O'Nions, R. K., 1991. Partial melt distributions from inversion of rare earth element concentrations, *Journal of Petrology*, **32**(5), 1021–1091.

McKenzie, D. & Priestley, K., 2016. Speculations on the formation of cratons and cratonic basins, *Earth and Planetary Science Letters*, **435**, 94–104.

McKenzie, D. & Rodríguez Tribaldos, V., 2018. Lithospheric heating by crustal thickening: a possible origin of the Parnaíba Basin, in *Cratonic Basin Formation: A Case Study of the Parnaíba Basin of Brazil, Geological Society Special Publication 472*, edited by M. C. Daly, R. A. Fuck, J. Julià, D. I. M. Macdonald, & A. B. Watts, pp. 37–44, Geological Society, London.

McKenzie, D., Jackson, J., & Priestley, K., 2005. Thermal structure of oceanic and continental lithosphere, *Earth and Planetary Science Letters*, **233**, 337–349.

Mulder, J. A., Karlstrom, K. E., Fletcher, K., Heizler, M. T., Timmons, J. M., Crossey, L. J., Gehrels, G. E., & Pecha, M., 2017. The syn-orogenic sedimentary record of the Grenville Orogeny in southwest Laurentia, *Precambrian Research*, **294**, 33–52.

Neill, I., Meliksetian, K., Allen, M. B., Navasardyan, G., & Karapetyan, S., 2013. PlioceneQuaternary volcanic rocks of NW Armenia: Magmatism and lithospheric dynamics within an active orogenic plateau, *Lithos*, **180–181**, 24–41.

Neill, I., Meliksetian, K., Allen, M. B., Navasardyan, G., & Kuiper, K., 2015. Petrogenesis of mafic collision zone magmatism: The Armenian sector of the Turkish-Iranian Plateau, *Chemical Geology*, **403**, 24–41.

Nilsen, T. H. & Stewart, J. H., 1980. The Antler orogeny — Mid-Paleozoic tectonism in western North America, *Geology*, **8**, 298–302.

Nimis, P. & Grütter, H., 2010. Internally consistent geothermometers for garnet peridotites and pyroxenites, *Contributions to Mineralogy and Petrology*, **159**(3), 411–427.

Nimis, P. & Taylor, W. R., 2000. Single clinopyroxene thermobarometry for garnet peridotites. Part I. Calibration and testing of a Cr-in-Cpx barometer and an enstatite-in-Cpx thermometer, *Contributions to Mineralogy and Petrology*, **139**, 541–554.

Noble, L. F., 1922. A section of the Paleozoic formations of the Grand Canyon at the Bass Trail, *United States Geological Survey Professional Paper*, **131-B**, B23–B73.

Nocquet, J.-M., 2012. Present-day kinematics of the Mediterranean: A comprehensive overview of GPS results, *Tectonophysics*, **579**, 220–242.

Notsu, K., Fujitani, T., Ui, T., Matsuda, J., & Ercan, T., 1995. Geochemical features of collision-related volcanic rocks in central and eastern Anatolia, Turkey, *Journal of Volcanology and Geothermal Research*, **64**, 171–192.

Öğretmen, N., Cipollari, P., Frezza, V., Faranda, C., Karanika, K., Gliozzi, E., Radeff, G., & Cosentino, D., 2018. Evidence for 1.5 km of uplift of the Central Anatolian Plateaus southern margin in the last 450 kyr and implications for its multiphased uplift history, *Tectonics*, **37**, 359–390.

Olson, P., Schubert, G., Anderson, C., & Goldman, P., 1988. Plume formation and lithosphere erosion: a comparison of laboratory and numerical experiments, *Journal of Geophysical Research*, **93**(B12), 15,065–15,084.

O'Malley, C. P., 2019. Quantitative Analysis of River Profiles and Fluvial Landscapes, Ph. D. Dissertation, University of Cambridge.

Oyan, P., 2018. Petrogenesis of the quaternary mafic alkaline volcanism along the African-Anatolian plates boundary in Turunçlu-Delihalil (Osmaniye) region in southern Turkey, *Lithos*, **314–315**, 630–645.

Oyan, P., 2018. Geochemistry and Petrology of Tutak (Ağrı) Volcanic Rocks: Partial Melting of Amphibole Bearing Garnet Peridotite, *Çukurova University Journal of the Faculty of Engineering and Architecture*, **33**(3), 41–56.

Oyan, P., 2018. Geochemical and petrologic evolution of Otlakbaşı basaltic volcanism to the east of Lave Van, *Bulletin of the Mineral Research and Exploration*, **157**, 1–2.

Oyan, V., Keskin, M., Lebedev, V. A., Chugaev, A. V., & Sharkov, E. V., 2016. Magmatic evolution of the Early Pliocene Etrüsk stratovolcano, Eastern Anatolia Collision Zone, Turkey, *Lithos*, **256–257**, 88–108.

Oyan, V., Keskin, M., Lebedev, V. A., Chugaev, A. V., & Sharkov, E. V., 2016. Petrology and Geochemistry of the Quaternary Mafic Volcanism to the NE of Lake Van, Eastern Anatolian Collision Zone, Turkey, *Journal of Petrology*, **58**(9), 1,701–1,728.

Özdemir, Y. & Güleç, N., 2014. Geological and geochemical evolution of the quaternary Süphan Stratovolcano, Eastern Anatolia, Turkey: Evidence for the lithosphere-asthenosphere interaction in post-collisional volcanism, *Journal of Petrology*, **55**(1), 37–62.

Özdemir, Y., Karaoğlu, O., Tolluoğlu, A. U., & Güleç, N., 2006. Volcanostratigraphy and petrogenesis of the Nemrut stratovolcano (East Anatolian High Plateau): The most recent post-collisional volcanism in Turkey, *Chemical Geology*, **226**, 189–211.

Özdemir, Y., , Blundy, J., & Güleç, N., 2011. The importance of fractional crystallization and magma mixing in controlling chemical differentiation at Sphan stratovolcano, eastern Anatolia, Turkey, *Contributions to Mineralogy and Petrology*, **162**, 573–597.

Özdemir, Y., Mercan, Ç., Oyan, V., & Özdemir, A. A., 2019. Composition, pressure, and temperature of the mantle source region of quaternary nepheline-basanitic lavas in Bitlis Massif, Eastern Anatolia, Turkey: A consequence of melts from Arabian lithospheric mantle, *Lithos*, **328–329**, 115–129.

Palmer, A. N. & Palmer, M. V., 1995. The Kaskaskia paleokarst of the northwestern Rocky Mountains and Black Hills, northwestern USA, *Carbonates and Evaporites*, **10**(2), 148–160.

Parlak, O., Kop, A., Ünlügenç, U. C., & Demirkol, C., 1998. Geochronology and geochemistry of basaltic rocks in the Karasu Graben around Kırıkhan (Hatay), S. Turkey, *Turkish Journal of Earth Sciences*, **7**, 53–61.

Parlak, O., Delaloye, M., Kozlu, H., & Fontignie, D., 2000. Trace element and Sr-Nd isotope geochemistry of the alkali basalts observed along the Yumurtalık Fault (Adana) in southern Turkey, *Yerbilimleri*, **2000**, 137–148.

Parsons, B. & McKenize, D., 1978. Mantle convection and the thermal structure of the plates, *Journal of Geophysical Research*, **83**(B9), 4,485–4,496.

Parsons, B. & Sclater, J. G., 1977. An analysis of the variation of ocean floor bathymetry and heat flow with age, *Journal of Geophysical Research*, **82**(5), 803–827.

Paton, S. M., 1992. *The relationship between extension and volcanism in Western Turkey, the Aegean Sea and Central Greece*, Ph.D. thesis, University of Cambridge.

Paul, J. D., Roberts, G. G., & White, N., 2014. The African landscape through space and time, *Tectonics*, **33**(6), 898–935.

Pawlewicz, M. J., Steinshouer, D. W., & Gautier, D. L., 2000. Map showing geology, oil and gas fields and geologic provinces of Europe including Turkey, Open-File Report 97-470I, United States Geological Survey.

Pearce, J., Bender, J., De Long, S., Kidd, W., Low, P., Güner, Y., Saroglu, F., Yilmaz, Y., Moorbath, S., & Mitchell, J., 1990. Genesis of collision volcanism in Eastern Anatolia, Turkey, *Journal of Volcanology and Geothermal Research*, **44**, 189–229.

Peate, D. W., 1997. The Paraná-Etendeka Province, in *Large Igneous Provinces: Continental, Oceanic, and Planetary Flood Volcanism, Geophysical Monograph 239*, edited by J. J. Mahoney & M. F. Coffin, pp. 217–245, American Geophysical Union, Washington, D.C., U.S.A.

Peirce, H. W., 1981. The Mississippian and Pennsylvanian (Carboniferous) systems in the United States—Arizona, *United States Geological Survey Professional Paper*, **1110-Z**.

Pekeris, C. L., 1935. Thermal convection in the interior of the Earth, *Geophysical Supplements to the Monthly Notices of the Royal Astronomical Society*, **3**(8), 343–367.

Peltier, W. R., Forte, A. M., Mitrovica, J. X., & Dziewonski, A. M., 1992. Earth's gravitational field: seismic tomography resolves the enigma of the Laurentian anomaly, *Geophysical Research Letters*, **19**(5), 1,555–1,558.

Persits, F., Ahlbrandt, T., Tuttle, M., Charpentier, R., Brownfield, M., & Takahashi, K., 2002. Map showing geology, oil and gas fields and geologic provinces of Africa, version 2.0, Open-File Report 97-470A, United States Geological Survey.

Peterson, K. D., Nielsen, S. B., Clausen, O. R., Stephenson, R., & Gerya, T., 2010. Small-scale mantle convection produces stratigraphic sequences in sedimentary basins, *Science*, **329**, 827–830.

Philpotts, A. R. & Ague, J. J., 2009. *Principles of Igneous and Metamorphic Petrology*, Cambridge University Press, Cambridge, U.K., 2nd edn.

Phipps Morgan, J., Morgan, W. J., Zhang, Y.-S., & Smith, W. H. F., 1995. Observational hints for a plume-fed, suboceanic asthenosphere and its role in mantle convection, *Journal of Geophysical Research*, **100**(B7), 12,753–12,767.

Pivin, M., Féménias, O., & Demaiffe, D., 2009. Metasomatic mantle origin for Mbuji-Mayi and Kundelungu garnet and clinopyroxene megacrysts (Democratic Republic of Congo), *Lithos*, **112S**, 951–960.

Pivin, M., Berger, J., & Demaiffe, D., 2011. Nature and origin of an exceptional Cr-rich kyanite-bearing clinopyroxenite xenolith from Mbuji-Mayi kimberlite (DRC), *European Journal of Mineralogy*, **23**, 257–268.

Plank, T. & Forsyth, D., 2016. Thermal structure and melting conditions in the mantle beneath the Basin and Range province from seismology and petrology, *Geochemistry, Geophysics, Geosystems*, **17**, 1312–1338.

Plank, T. & Langmuir, C. H., 1998. The chemical composition of subducting sediment and its consequences for the crust and mantle, *Chemical Geology*, **145**, 325–394.

Platevoet, B., Elitok, Ö., Guillou, H., Bardintzeff, J.-M., Yagmurlu, F., Nomade, S., Poisson, A., Deniel, C., & Özgür, N., 2014. Petrology of Quaternary volcanic rocks and related plutonic xenoliths from Gölcük volcano, Isparta Angle, Turkey: Origin and evolution of the high-K alkaline series, *Journal of Asian Earth Sciences*, **92**, 53–76.

Poidevin, J.-L., 2007. Stratigraphie isotipique du strontium et datation des formations carbonatées et glaciogéniques néoprotéroziques du Nord et de l'Ouest du craton Congo, *Comptes Rendus Géoscience*, **339**(3–4), 259–723.

Poisson, A., Guezou, J. C., Ozturk, A., Inan, S., Temiz, H., Gürsöy, H., Kavak, K. S., & Özden, S., 1996. Tectonic setting and evolution of the Sivas Basin, central Anatolia, Turkey, *International Geology Review*, **38**(9), 838–853.

Poisson, A., Orszag-Sperber, F., Kosun, E., Bassetti, M.-A., Müller, C., Wernlu, R., & Rouchy, J.-M., 2011. The late Cenozoic evolution of the Aksu basin (Isparta Angle; SW Turkey). New Insights, *Bulletin de la Société Géologique de France*, **182**(2), 133–148.

Polat, A., Kerrich, R., & Casey, J. F., 1997. Geochemistry of Quaternary basalts erupted along the East Anatolian and Dead Sea fault zones of southern Turkey: implications for mantle sources, *Lithos*, **40**, 55–68.

Pollastro, R. M., Karshbaum, A. S., & Viger, R. J., 2000. Map showing geology, oil and gas fields and geologic provinces of Arabian Peninsula, Open-File Report 97-470B, United States Geological Survey.

Poole, F. G. & Sandberg, C. A., 1977. Mississippian paleogeography and tectonics of the western United States, in *Paleozoic paleogeography of the Western United States, Pacific Coast Paleogeography Symposium 1*, edited by J. H. Stewart, C. H. Stevens, & A. E. Fritsche, pp. 67–85, Society of Economic Paleontologists and Mineralogists, Los Angeles, CA, U.S.A.

Pratt, J. H., 1855. On the attraction of the Himalaya Mountains, and of the elevated regions beyond them, upon the plumb-line in India, *Philisophical Transactions of the Royal Society*, **145**, 53–100.

Prave, A. R., Condon, D. J., Hoffman, K. H., Tapster, S., & Fallick, A. E., 2016. Duration and nature of the end-Cryogenian (Marinoan) glaciation, *Geology*, **44**(8), 631–634.

Prelević, D., Akal, C., Foley, S. F., Romer, R. L., Stracke, A., & van den Bogaard, P., 2012. Ultrapotassic mafic rocks as geochemical proxies for post-collisional dynamics of orogenic lithospheric mantle: the case of southwestern Anatolia, Turkey, *Journal of Petrology*, **53**(5), 1019–1005.

Prelević, D., Akal, C., Romer, R. L., Mertz-Kraus, R., & Helvacı, C., 2015. Magmatic response to slab tearing: Constraints from the Afyon Alkaline Volcanic Complex, Western Turkey, *Journal of Petrology*, **56**(3), 527–562.

Press, W. H., Teukolsky, S. A., Vetterling, W. T., & Flannery, B. P., 1992. *Numerical recipes in Fortran: the art of scientific computing*, Cambridge University Press, Cambridge, UK.

Priestley, K. & McKenzie, D., 2006. The thermal structure of the lithosphere from shear wave velocities, *Earth and Planetary Science Letters*, **244**, 285–301.

Priestley, K. & McKenzie, D., 2013. The relationship between shear wave velocity, temperature, attenuation and viscosity in the shallow part of the mantle, *Earth and Planetary Science Letters*, **381**, 78–91.

Priestley, K., McKenzie, D., & Ho, T., 2019. A Lithosphere-Asthenosphere Boundary—a global model derived from multimode surface-wave tomography and petrology, in *Lithospheric Discontinuities, Geophysical Monograph 239*, edited by H. Yuan & B. Romanowicz, pp. 111–123, American Geophysical Union, Washington, D.C., U.S.A.

Pritchard, D., Roberts, G. G., White, N. J., & Richardson, C. N., 2009. Uplift histories from river profiles, *Geophysical Research Letters*, **36**(24), 1–5.

Putirka, K. D., Perfit, M., Ryerson, F. J., & Jackson, M. G., 2007. Ambient and excess mantle temperatures, olivine thermometry, and active vs. passive upwelling, *Chemical Geology*, **241**, 177–206.

Ramsbottom, W. H. C. & Saunders, W. B., 1985. Evolution and evolutionary biostratigraphy of Carboniferous ammonoids, *Journal of Paleontology*, **59**(1), 123–139.

Reid, M. R., Schleiffarth, W. K., Cosca, M. A., Delph, J. R., Blichert-Toft, J., & Cooper, K. M., 2017. Shallow melting of MORB-like mantle under hot continental lithosphere, Central Anatolia, *Geochemistry, Geophysics, Geosystems*, **18**, 1866–1888.

Reilinger, R., McClusky, S., Vernant, P., Lawrence, S., Ergintav, S., Cakmak, R., Ozener, H., Kadirov, F., Guliev, I., Stepanyan, R., Nadariya, M., Hahubia, G., Mahmoud, S., Sakr, K., ArRajehi, A., Paradissis, D., Al-Aydrus, A., Prilepin, M., Guseva, T., Evren, E., Dmitrotsa, A., Filikov, S. V., Gomez, F., Al-Ghazzi, R., & Karam, G., 2006. GPS constraints on continental deformation in the Africa-Arabia-Eurasia continental collision zone and implications for the dynamics of plate interactions, *Journal of Geophysical Research: Solid Earth*, **111**(5), 1–26.

Ricard, Y., Richards, M., Lithgow-Bertelloni, C., & Le Stunff, Y., 1993. A geodynamic model of mantle density heterogeneity, *Journal of Geophysical Research*, **98**(B12), 21,895–21,909.

Rice, C. L., 1984. Sandstone units of the Lee Formation and related strata in Eastern Kentucky, *United States Geological Survey Professional Paper*, **1151-G**(65).

Rice, C. L., 1985. Terrestrial vs. marine depositional model—A new assessment of subsurface lower Pennsylvanian rocks of southwestern Virginia, *Geology*, **13**, 786–789.

Richards, F. D., 2018. Global analysis of predicted and observed dynamic topography, Ph. D. Dissertation, University of Cambridge.

Richards, F. D., Hoggard, M. J., & White, N. J., 2016. Cenozoic epeirogeny of the Indian peninsula, *Geochemistry, Geophysics, Geosystems*, **17**, 4920–4954.

Richards, F. D., Hoggard, M. J., Cowton, L. R., & White, N. J., 2018. Reassessing the thermal structure of oceanic lithosphere with revised global inventories of basement depths and heat flow measurements, *Journal of Geophysical Research: Solid Earth*, **123**, 9,136–9,161.

Richardson-Bunbury, J. M., 1992. *Basalts of Kula and their relation to extension in western Turkey*, Ph.D. thesis, University of Cambridge.

Ritsema, J. & van Heijst, H., 2000. New seismic model of the upper mantle beneath Africa, *Geology*, **28**(1), 63–66.

Ritter, S. M., 1991. Conodont-based revision of Upper Devonian-Lower Pennsylvanian stratigraphy in the Lake Mead region of northwestern Arizona and southeastern Nevada, *Brigham Young University Geology Studies*, **37**, 125–138.

Robert, U., Foden, J., & Varne, R., 1992. The Dodecanese Province, SE Aegean: A model for tectonic control on potassic magmafism, *Lithos*, **28**, 241–260.

Roberts, G. G. & White, N., 2010. Estimating uplift rate histories from river profiles using African examples, *Journal of Geophysical Research: Solid Earth*, **115**(2), 1–24.

Roberts, G. G., White, N. J., Martin-Brandis, G. L., & Crosby, A. G., 2012. An uplift history of the Colorado Plateau and its surroundings from inverse modeling of longitudinal river profiles, *Tectonics*, **31**(TC4022).

Rodríguez Tribaldos, V., 2017. Epeirogeny of South America and evolution of Parnaíba Basin, northeast Brazil, Ph. D. Dissertation, University of Cambridge.

Rodríguez Tribaldos, V. & White, N., 2018. Implications of preliminary subsidence analyses for the Parnaíba cratonic basin, in *Cratonic Basin Formation: A Case Study of the Parnaíba Basin of Brazil, Geological Society Special Publication 472*, edited by M. C. Daly, R. A. Fuck, J. Julià, D. I. M. Macdonald, & A. B. Watts, pp. 147–156, Geological Society, London.

Ronchi, P., Ortenzi, A., Borromeo, O., Claps, M., & Zempolich, W. G., 2010. Depositional setting and diagenetic processes and their impact on the reservoir quality in the late Visean-Bashkirian Kashagan carbonate platform (Pre-Caspian Basin, Kazakhstan, *American Association of Petroleum Geologists Bulletin*, **94**(9), 1,313–1,348.

Rooney, A. D., Selby, D., Houzay, J.-P., & Renne, P. R., 2010. ReOs geochronology of a Mesoproterozoic sedimentary succession, Taoudeni basin, Mauritania: Implications for basin-wide correlations and ReOs organic-rich sediments systematics, *Earth and Planetary Science Letters*, **289**, 486–496.

Rooney, A. D., Strauss, J. V., Brandon, A. D., & Macdonald, F. A., 2015. A Cryogenian chronology: Two long-lasting synchronous Neoproterozoic glaciations, *Geology*, **43**(5), 459–462.

Rooney, A. D., Austermann, J., Smith, E. F., Li, Y., Selby, D., Dehler, C. M., Schmitz, M. D., Karlstrom, K. E., & Macdonald, F. A., 2017. Coupled Re-Os and U-Pb geochronology of the Tonian Chuar Group, Grand Canyon, *Geological Society of America Bulletin*, **130**(7/8), 1,085–1,098.

Rose, E., 2006. Nonmarine aspects of the Cambrian Tonto Group of the Grand Canyon, USA, and broader implications, *Paleoworld*, **15**, 223–241.

Rose, P. R., 1976. Mississipian carbonate shelf margins, western United States, *Journal of Research of the United States Geological Survey*, **4**(4), 449–466.

Ross, C. A. & Ross, J. P., 1985. Late Paleozoic depositional sequences are synchronous and worldwide, *Geology*, **13**, 194–197.

Ross, C. A. & Ross, J. R. P., 1988. Late Paleozoic transgressive-regressive deposition, in *Sea-level changes – An integrated approach, SEPM Special Publications no. 42*, edited by C. K. Wilgus, B. S. Hastings, C. A. Ross, H. Posamentier, J. van Wagoner, & C. G. St. C. Kendall, pp. 227–247, The Society of Economic Paleontologists and Mineralogists, Tulsa, OK, USA.

Rudge, J. F., Shaw Champion, M. E., White, N., McKenzie, D., & Lovell, B., 2008. A plume model of transient diachronous uplift at the Earth's surface, *Earth and Planetary Science Letters*, **267**, 146–160.

Rudge, J. F., Roberts, G. G., White, N. J., & Richardson, C. N., 2015. Uplift histories of Africa and Australia from linear inverse modeling of drainage inventories, *Journal of Geophysical Research F: Earth Surface*, **120**(5), 894–914.

Rygel, M. C., Fielding, C. R., Frank, T. D., & Birgenheier, L. P., 2008. The magnitude of late Paleozoic glacioeustatic fluctuations: a synthesis, *Journal of Sedimentary Research*, **78**, 500–511.

Salaün, G., Pedersen, H. A., Paul, A., Farra, V., Karabulut, H., Hatzfeld, D., Papazachos, C., Childs, D. M., & Pequegnat, C., 2012. High-resolution surface wave tomography beneath the Aegean-Anatolia region: Constraints on upper-mantle structure, *Geophysical Journal International*, **190**(1), 406–420.

Salles, T., 2016. Badlands: A parallel basin and landscape dynamics model, *SoftwareX*, **5**, 195–202.

Saltzman, M. R., 2003. Late Paleozoic ice age: Oceanic gateway or $p\mathrm{CO}_2$?, *Geology*, **31**(2), 151–154.

Sando, W. J., 1974. Ancient solution phenomena in the Madison Limestone (Mississippian) of north-central Wyoming, *Journal of Research of the United States Geological Survey*, **2**(2), 133–141.

Sando, W. J., 1985. Revised Mississippian time scale, western interior range, conterminous United States, *United States Geological Survey Bulletin*, **1605-A**, A15–A26.

Sando, W. J., 1988. Madison Limestone (Mississippian) paleokarst: a geologic synthesis, in *Paleokarst*, edited by N. P. James & P. W. Choquette, pp. 256–277, Springer-Verlag, New York.

Sando, W. J., Gordon, Jr., M., & Dutro, Jr., T., 1975. Stratigraphy and geologic history of the Amsden Formation (Mississippian and Pennsylvanian) of Wyoming, *United States Geological Survey Professional Paper*, **848-A**.

Sando, W. J., Bamber, E. W., & Richards, B. C., 1990. The rugose coral *Ankhelasma*—Index to Viséan (Lower Carboniferous) shelf margin in the Western Interior of North America, *United States Geological Survey Bulletin*, **1895**, B1–B29.

Sandvol, E., Seber, D., Calvret, A., & Barazangi, M., 1998. Grid search modeling of receiver functions: Implications for crustal structure in the Middle East and North Africa, *Journal of Geophysical Research*, **103**(B11), 26,899–26,917.

Saunders, P., Priestley, K., & Taymaz, T., 1998. Variations in the crustal structure beneath western Turkey, *Geophysical Journal International*, **134**, 373–389.

Saunders, W. B. & Ramsbottom, W. H. C., 1986. The mid-Carboniferous eustatic event, *Geology*, **14**, 208–212.

Schaeffer, A. J. & Lebedev, S., 2013. Global shear speed structure of the upper mantle and transition zone, *Geophysical Journal International*, **194**(1), 417–449.

Schildgen, T. F., Cosentino, D., Bookhagen, B., Niedermann, S., Yıldırım, C., Echtler, H., Wittmann, H., & Strecker, M. R., 2012. Multi-phased uplift of the southern margin of the Central Anatolian plateau, Turkey: A record of tectonic and upper mantle processes, *Earth and Planetary Science Letters*, **317-318**, 85–95.

Schildgen, T. F., Cosentino, D., Caruso, A., Buchwaldt, R., Yıldırım, C., Bowring, S. A., Rojay, B., Echtler, H., & Strecker, M. R., 2012. Surface expression of eastern Mediterranean slab dynamics: Neogene topographic and structural evolution of the southwest margin of the Central Anatolian Plateau, Turkey, *Tectonics*, **31**(2).

Schildgen, T. F., Yıldırım, C., Cosentino, D., & Strecker, M. R., 2014. Linking slab break-off, Hellenic trench retreat, and uplift of the Central and Eastern Anatolian plateaus, *Earth-Science Reviews*, **128**, 147–168.

Sclater, J. G. & Christie, P. A. F., 1980. Continental stretching: an explanation of the post-mid-Cretaceous subsidence of the central North Sea basin, *Journal of Geophysical Research*, **85**(B7), 3711–3739.

Sebagenzi, M. N., Vasseur, G., & Louis, P., 1993. First heat flow and density determinations from Southeastern Zaïre (Central Africa), *Journal of African Earth Sciences*, **16**(4), 413–423.

Sebai, A., Feraud, G., Bertrand, H., & Hanes, J., 1991. $^{40}Ar/^{39}Ar$ dating and geochemistry of tholeiitic magmatism related to the early opening of the Central Atlantic, *Earth and Planetary Science Letters*, **104**, 455–472.

Semiz, B., Ersoy, E. Y., Özpınar, Y., Helvacı, C., Palmer, M. R., & Billor, M. Z., 2015. $^{40}Ar/^{39}Ar$ geochronology, geochemistry and petrology of volcanic rocks from the Simav Graben, western Turkey, *Contributions to Mineral Petrology*, **170**, 24.

Şengör, A. M. C. & Yilmaz, Y., 1981. Tethyan evolution of Turkey: A plate tectonic approach, *Tectonophysics*, **75**(3-4).

Şengör, A. M. C., Görür, N., & Şaroğlu, 1985. Strike-slip faulting and related basin formation in zones of tectonic escape: Turkey as a case study, in *Strike-slip deformation, baisn formation, and sedimentation*, edited by K. T. Biddle & N. Christie-Black, vol. 37, pp. 227–264, Society for Economical Paleontology and Mineralogy Special Publication, Tulsa, USA.

Şengör, A. M. C., Özeren, S., Genç, T., & Zor, E., 2003. East Anatolian high plateau as a mantle-supported, north-south shortened domal structure, *Geophysical Research Letters*, **30**(24), 2–5.

Şengör, A. M. C., Tüysüz, O., İmren, C., Sakınç, M., Eyidoğan, H., Görür, N., Le Pichon, X., & Rangin, C., 2005. The North Anatolian Fault: A new look, *Annual Reviews of Earth and Planetary Sciences*, **33**, 37–112.

Şengör, A. M. C., Özeren, M. S., Keskin, M., Sakinç, M., Özbakir, A. D., & Kayan, I., 2008. Eastern Turkish high plateau as a small Turkic-type orogen: Implications for post-collisional crust-forming processes in Turkic-type orogens, *Earth-Science Reviews*, **90**(1-2), 1–48.

Seyitoğlu, G., Anderson, D., Nowell, G., & Scott, B., 1997. The evolution from Miocene potassic to Quaternary sodic magmatism in western Turkey: implications for enrichment processes in the lithospheric mantle, *Journal of Volcanology and Geothermal Research*, **76**, 127–147.

Shaw, D. M., 1970. Trace element fractionation during anatexis, *Geochemica et Cosmochemica Acta*, **34**, 237–243.

Shaw Champion, M. E., White, N. J., Jones, S. M., & Lovell, J. P. B., 2008. Quantifying transient mantle convective uplift: An example from the Faroe-Shetland basin, *Tectonics*, **27**(TC1002).

Shirley, D. H., 1989. Geochemical facies analysis of the Surprise Canyon Formation in Fern Glen Channelway, Central Grand Canyon, Arizona, MSc. Dissertation, Northern Arizona University.

Shorttle, O., Maclennan, J., & Lambart, S., 2014. Quantifying lithological variability in the mantle, *Earth and Planetary Science Letters*, **395**, 24–40.

Siever, R., 1951. The Mississippian-Pennsylvanian unconformity in southern Illinois, *The Bulletin of the American Association of Petroleum Geologists*, **35**(3), 542–581.

Skipp, B., 1969. Foraminifera, in *History of the Redwall Limestone of Northern Arizona, Geological Society of America Memoir 114*, edited by E. D. McKee & R. C. Gutschick, pp. 173–256, The Geological Society of America, Boulder, Colorado, U.S.A.

Sklar, L. & Dietrich, W. E., 1998. River longitudinal profiles and bedrock incision models: Stream power and the influence of sediment supply, in *Rivers Over Rock: Fluvial Processes in Bedrock Channels, Geophysical Monograph 107*, edited by K. J. Tinkler & E. E. Wohl, pp. 237–260, American Geophysical Union, San Francisco, USA.

Skolbeltsyn, G., Mellors, R., Gök, R., Türkelli, N., Yetirmishli, G., & Sandvol, E., 2014. Upper mantle S wave velocity structure of the East Anatolian-Caucasus region, *Tectonics*, **33**(3), 207–221.

Sloss, L. L., 1963. Sequences in the cratonic interior of North America, *Geological Society of America Bulletin*, **74**, 93–114.

Smith, W. H. F. & Sandwell, D. T., 1997. Global sea floor topography from satellite altimetry and ship depth soundings, *Science*, **277**, 1,956–1,962.

Steinberger, B., 2007. Effects of latent heat release at phase boundaries on flow in the Earths mantle, phase boundary topography and dynamic topography at the Earths surface, *Physics of the Earth and Planetary Interiors*, **164**, 2–20.

Stracke, A., Hofmann, A. W., & Hart, S. R., 2005. FOZO, HIMU, and the rest of the mantle zoo, *Geochemistry, Geophysics, Geosystems*, **6**(5).

Stucky de Quay, G., Roberts, G. G., Watson, J. S., & Jackson, C. A.-L., 2017. Incipient mantle plume evolution: Constraints from landscapes buried beneath the North Sea, *Geochemistry, Geophysics, Geosystems*, **18**(3), 973–993.

Sturmer, D. M., Trexler, Jr., J. H., & Cashman, P. H., 2018. Tectonic analysis of the Pennsylvanian Ely-Bird Spring Basin: Late Paleozoic tectonism on the southwestern Laurentia Margin and the distal limit of the Ancestral Rocky Mountains, *Tectonics*, **37**, 604–620.

Sugden, P. J., Savov, I. P., Wilson, M., Meliksetian, K., Navasardyan, G., & Halama, R., 2019. The thickness of the mantle lithosphere and collision-related volcanism in the Lesser Caucasus, *Journal of Petrology*, **60**(2), 199–230.

Tack, L., Delvaux, D., Kadima, E., Delpomdor, F., Tahon, A., Dumont, P., Hanon, M., Fernandez-Alonso, M., Baudet, D., Dewaele, D., Cibambula, E., Kanda Nkula, V., & Mpiana,

C., 2008. The 1.000 m thick Redbeds sequence of the Congo River Basin (CRB): a generally overlooked testimony in Central Africa of post-Gondwana amalgamation (550 My) and pre-Karoo break-up (320 My), in *22nd Colloquium of African Geology, Hammamet, Tunisia, November 4-6 2008, Abstract Book*, pp. 86–88.

Taghizadeh-Farahmand, F., Sodoudi, F., Afsari, N., & Ghassemi, M. R., 2010. Lithospheric structure of NW Iran from *P* and *S* receiver functions, *Journal of Seismology*, **14**, 823–836.

Tait, J., Delpomdor, F., Préat, A., Tack, L., Straathof, G., & Nkula, V. K., 2011. Neoproterozoic sequences of the West Congo and Lindi/Ubangi Supergroups in the Congo Craton, Central Africa, in *The Geological Record of Neoproterozoic Glaciations, Geological Society, London, Memoirs 36*, edited by E. Arnaud, G. P. Halverson, & G. Shields-Zhou, pp. 185–194, The Geological Society of London.

Takei, Y., 2017. Effects of partial melting on seismic velocity and attenuation: A new insight from experiments, *Annual Review of Earth and Planetary Sciences*, **45**, 447–470.

Tankut, A., Güleç, N., Wilson, M., Toprak, V., Savaşçin, Y., & Akiman, O., 1998. Alkali Basalts From the Galatia Volcanic Complex, NW Central Anatolia, Turkey, *Turkish Journal of Earth Sciences*, **7**, 269–274.

Tapley, B. D., Ries, J., Bettadpur, S., Chambers, D., Cheng, M., Condi, F., & Poole, S., 2007. The GGM03C Mean Earth Gravity Model from GRACE, in *Eos Transactions*, vol. 88, Abstract G42A-03 presented at AGU Fall Meeting 2017, San Francisco, USA.

Tarboton, D. G., 1997. A new method for the determination of flow directions and upslope areas in grid elevation models, *Water Resources Research*, **33**(2), 309–319.

Taylor, W. R., 1998. An experimental test of some geothermometer and geobarometer formulations for upper mantle peridotites with application to the thermobarometry of fertile lherzolite and garnet websterite, *Neues Jahrbuch für Mineralogie*, **172**(2/3), 381–408.

Temel, A., Gündoğdu, M. N., & Gourgaud, A., 1998. Petrological and geochemical characteristics of Cenozoic high-K calc-alkaline volcanism in Konya, Central Anatolia, Turkey, *Journal of Volcanology and Geothermal Research*.

Temel, A., Yüruür, T., Alıcı, P., Varol, E., Gourgaud, A., Bellon, H., & Demirbağ, H., 2010. Alkaline series related to Early-Middle Miocene intra-continental rifting in a collision zone: An example from Polatlı, Central Anatolia, Turkey, *Journal of Asain Earth Science*, **38**, 298–306.

Tezel, T., Shibutani, T., & Kaypak, B., 2010. Crustal variation in western Turkey inferred from the receiver function analysis, *Tectonophysics*, **492**, 240–252.

Tezel, T., Shibutani, T., & Kaypak, B., 2013. Crustal thickness of turkey determined by receiver function, *Journal of Asian Earth Sciences*, **75**, 36–45.

Thompson, R. N., Ottley, C. J., Smith, P. M., Pearson, D., G., Pickin, A. P., Morrison, M. A., Leat, P. T., & Gibson, S. A., 2005. Source of Quaternary alkalic basalts, picrites and basanites of the Potrillo Volcanic Field, New Mexico, USA: lithosphere or convecting mantle?, *Journal of Petrology*, **46**(8), 1603–1643.

Tidwell, W. D., Jennings, J. R., & Beus, S. S., 1992. A Carboniferous flora from the Surprise Canyon Formation in the Grand Canyon, Arizona, *Journal of Paleontology*, **66**(6), 1013–1021.

Timmons, J. M., Karlstrom, K. E., Dehler, C. M., Geissman, J. W., & Heizler, M. T., 2001. Proterozoic multistage (ca. 1.1 and 0.8 Ga) extension recorded in the Grand Canyon Supergroup and establishment of northwest- and north-trending grains in the southwestern United States, *Geological Society of America Bulletin*, **113**(2), 163–181.

Timmons, J. M., Karlstrom, K. E., Heizler, M. T., Bowring, S. A., Gehrels, G. E., & Crossey, L. J., 2005. Tectonic inferences from the ca. 1255–1100 Ma Unkar Group and Nankoweap Formation, Grand Canyon: Intracratonic deformation and basin formation during protracted Grenville orogenesis, *Geological Society of America Bulletin*, **117**(11/12), 1573–1595.

Timmons, J. M., Bloch, J., Fletcher, K., Karlstrom, K. E., Heizler, M., & Crossey, L. J., 2012. The Grand Canyon Unkar Group: Mesoproterozoic basin formation in the continental interior during supercontinent assembly, in *Grand Canyon geology: Two billion years of Earth's History, Geological Society of America Special Paper 489*, edited by J. Timmons & K. Karlstrom, pp. 25–48, Geological Society of America, Boulder, Colorado, U.S.A.

Tohver, E., D'Agrella-Filho, M. S., & Trindade, R. I. F., 2006. Paleomagnetic record of Africa and South America for the 1200500 Ma interval, and evaluation of Rodinia and Gondwana assemblies, *Precambrian Research*, **147**, 193–222.

Tokam, A.-P. K., Tabod, C. T., Nyblade, A. A., Julià, J., Wiens, D. A., & Pasyanos, M. E., 2010. Structure of the crust beneath Cameroon, West Africa, from the joint inversion of Rayleigh wave group velocities and receiver functions, *Geophysical Journal International*, **183**, 1,061–1,076.

Tomkin, J. H., Brandon, M. T., Pazzaglia, F. J., Barbour, J. R., & Willett, S. D., 2003. Quantitative testing of bedrock incision models for Clearwater River, NW Washington State, *Journal of Geophysical Research*, **108**(B8), 2308.

Tozer, B., Watts, A. B., & Daly, M. C., 2017. Crustal structure, gravity anomalies, and subsidence history of the Parnaíba cratonic basin, Northeast Brazil, *Journal of Geophysical Research: Solid Earth*, **122**, 5,591–5,621.

Tunoğlu, C., 1991. Orta Pontidler'de Devrekani Havzası'nın (Kastamonu kuzeyi) lithostratigrafi birimleri, in *Suat Erk Jeoloji Sempozyumu, Bildiriler Kitabı*, pp. 183–191, Ankara Üniversitesi, Fen Fakültesi, Ankara.

Tunoğlu, C., 1994. Microfacies analysis of the upper Paleocene–middle Eocene carbonate sequence Devrekani Basin (Northern Kastamonu), *Geological Bulletin of Turkey*, **37**(2), 43–51.

Turcotte, D. L. & Schubert, G., 2014. *Geodynamics*, Cambridge University Press, Cambridge, U.K., 3rd edn.

Uluocak, E. Ş., Pysklywec, R., & Göğüş, O. H., 2016. Present-day dynamic and residual topography in Central Anatolia, *Geophysical Journal International*, **206**(3), 1515–1525.

Uslular, G. & Gençalioğlu-Kuşcu, G., 2019. Mantle source heterogeneity in monogenetic basaltic systems: A case study of Eğrikuyu monogenetic field (Central Anatolia, Turkey), *Geosphere*, **15**(2).

van der Meijde, M., van der Lee, S., & Giardini, D., 2003. Crustal structure beneath broadband seismic stations in the Mediterranean region, *Geophysical Journal International*, **152**, 729–739.

van Hinsbergen, D. J. J., Kaymakci, N., Spakman, W., & Torsvik, T. H., 2010. Reconciling the geological history of western Turkey with plate circuits and mantle tomography, *Earth and Planetary Science Letters*, **297**(3-4), 674–686.

van Hunen, J. & Allen, M. B., 2011. Continental collision and slab break-off: A comparison of 3-D numerical models with observations, *Earth and Planetary Science Letters*, **302**, 27–37.

van Wijk, J., Koning, D., Axen, G., Coblentz, D., Gragg, E., & Sion, B., 2018. Tectonic subsidence, geoid analysis, and the Miocene-Pliocene unconformity in the Rio Grande rift, southwestern United States: Implications for mantle upwelling as a driving force for rift opening, *Geosphere*, **14**(2), 684–709.

Vanacore, E. A., Taymaz, T., & Saygin, E., 2013. Moho structure of the Anatolian Plate from receiver function analysis, *Geophysical Journal International*, **193**, 329–337.

Varol, E. & Alpaslan, M., 2012. Quaternary Basaltic Volcanism Reflecting Heterogeneous Mixture of Two Mafic Melts: Gölova Basaltic Rocks, Southern Anatolia, Turkey, *Geochemistry International*, **50**(1), 63–73.

Vasilyev, O. V., Ten, A. A., & Yuen, D. A., 2001. Temperature-dependent viscous gravity currents with shear heating, *Physics of Fluids*, **13**(12), 3,364–3,674.

Vaz, P. T., Andrade, G. D., Ribeiro, J., Filho, W., Antônio, W., & Travassos, S., 2007. Bacia do Parnaíba, *Boletim de Geociências da Petrobrás*, **15**(2), 253–263.

Veevers, J. J. & Powell, C. M., 1987. Late Paleozoic glacial episodes in Gondwanaland reflected in transgressive-regressive depositional sequences in Euramerica, *Geological Society of America Bulletin*, **98**, 475–487.

Verati, C., Bertrand, H., & Féraud, G., 2005. The farthest record of the Central Atlantic Magmatic Province into West Africa craton: Precise $^{40}Ar/^{39}Ar$ dating and geochemistry of Taoudenni basin intrusives (northern Mali), *Earth and Planetary Science Letters*, **235**, 391—407.

Verbeek, T., 1970. Géologie et lithologie du Lindien (Précambrien Supérieur du nord de la République Démocratique du Congo), *Annals du Musée de Congo Belge, Tervuren (Belgique), Serie in-8° – Sciences Geologiques*, **66**, 311.

Villeneuve, M., 2005. Paleozoic basins in West Africa and the Mauritanide thrust belt, *Journal of African Earth Sciences*, **43**, 166–195.

Vinnik, L. P., Erduran, M., Oreshin, S. I., Kosarev, G. L., Kutlu, Y. A., Çakir, Ö., & Kiselev, S. G., 2014. Joint inversion of *P*- and *S*-receiver functions and dispersion curves of rayleigh waves: the results for the Central Anatolian Plateau, *Physics of the Solid Earth*, **50**(5), 622–631.

Walsh-Kennedy, S., Aksu, A., Hall, J., Hiscott, R., Yaltırak, C., & Çifçi, C., 2014. Source ot sink: The development of the latest Messinian to Pliocene-Quaternary Cilicia and Adana Basins and their linkages with the onland Mut Basin, eastern Mediterranean, *Tectonophysics*, **622**, 1–21.

Watts, A. B., 2001. *Isostasy and flexure of the lithosphere*, Cambridge University Press, Cambridge, U.K.

Webb, G. E., 1994. Paleokarst, paleosol, and rochy-shore deposits at the Mississippian-Pennsylvanian unconformity, northwestern Arkansas, *Geological Society of America Bulletin*, **106**, 634–648.

Weil, A. B., Geissman, J. W., Heizler, M., & van der Voo, R., 2003. Paleomagnetism of middle Proterozoic mafic intrusions and upper Proterozoic (Nankoweap) red beds from the lower Grand Canyon supergroup, Arizona, *Tectonophysics*, **375**, 199–220.

Weissel, J. K. & Seidl, M. A., 1998. Inland propagation of erosional escarpments and river profile evolution across the southeast Australian passive continental margin, in *Rivers Over Rock: Fluvial Processes in Bedrock Channels*, edited by K. J. Tinkler & E. E. Whol, pp. 189–206, American Geophysical Union, Geophysical Monograph Series 107.

Whipple, K. X., 2009. The influence of climate on the tectonic evolution of mountain belts, *Nature Geoscience*, **2**, 97–104.

Whipple, K. X. & Tucker, G. E., 1999. Dynamics of the stream-power river incision model: implications for height limits of mountain ranges, landscape response times, and research needs, *Journal of Geophysical Research*, **104**(B8), 17,661–17,644.

Whipple, K. X. & Tucker, G. E., 2002. Implications of sediment-flux dependent river incision models for landscape evolution, *Journal of Geophysical Research*, **107**(B2).

White, N., 1994. An inverse method for determining lithospheric strain rate variation on geological timescales, *Earth and Planetary Science Letters*, **122**, 351–371.

White, N. & Lovell, B., 1997. Measuring the pulse of a plume with the sedimentary record, *Nature*, **387**, 888–891.

White, R. S., McKenzie, D., & O'Nions, R. K., 1992. Oceanic crustal thickness from seismic measurements and rare earth element, *Journal of Geophysical Research*, **97**(B13), 19,683–19,715.

Willett, S. D., McCoy, S. W., Perron, J. T., & Chen, C.-Y., 2014. Dynamic reorganization of river basins, *Science*, **343**, 1248765.

Wilson, J. W. P., Roberts, G. G., Hoggard, M. J., & White, N. J., 2014. Cenozoic epeirogeny of the Arabian Peninsula from drainage modeling, *Geochemistry, Geophysics, Geosystems*, **15**, 3723–3761.

Wilson, M., Tankut, A., & Guleç, N., 1997. Tertiary volcanism of the Galatia province, northwest Central Anatolia, Turkey, *Lithos*, **42**(1–2), 105–121.

Winterbourne, J., White, N., & Crosby, A., 2014. Accurate measurements of residual topography from the oceanic realm, *Tectonics*, **33**, 982–1,015.

Xie, X. & Heller, P. L., 2009. Plate tectonics and basin subsidence history, *Geological Society of America Bulletin*, **121**, 55–64.

Yamauchi, H. & Takei, Y., 2016. Polycrystal anelasticity at near-solidus temperatures, *Journal of Geophysical Research: Solid Earth*, **121**, 7790–7820.

Yıldırım, C., Schildgen, T. F., Echtler, H., Melnick, D., & Strecker, M. R., 2011. Late Neogene and active orogenic uplift in the Central Pontides associated with the North Anatolian Fault: Implications for the northern margin of the Central Anatolian Plateau, Turkey, *Tectonics*, **30**(TC5005).

Yıldırım, C., Melnick, D., Ballato, P., Schildgen, T. F., Echtler, H., Erginal, A. E., Kıyak, N. G., & Strecker, M. F., 2013. Differential uplift along the northern margin of the Central Anatolian Plateau: inferences from marine terraces, *Quaternary Science Reviews*, **81**, 12–28.

Yıldırım, C., Sarikaya, M. A., & Çiner, A., 2016. Late Pleistocene intraplate extension of the Central Anatolian Plateau, Turkey: Inferences from cosmogenic exposure dating of alluvial fan, landslide, and moraine surfaces along the Ecemiş Fault Zone, *Tectonics*, **35**(6), 1446–1464.

Yıldız, A., Toker, V., Demircan, H., & Sevim, S., 2003. Paleoenvironmental interpretation and findings of Pliocene-Pleistocene nannoplankton, planktic foraminifera, trace fossil in the Mut Basin, *Yerbilimleri*, **28**, 123–144.

Yılmaz, K., 2010. Origin of anorogenic lamproite-like potassic lavas from the Denizli region in Western Anatolia Extensional Province, Turkey, *Mineralogy and Petrology*, **99**, 219–239.

Yuen, D. A. & Fleitout, L., 1985. Thinning of the lithosphere by small-scale convective destabilization, *Nature*, **313**, 125–128.

Yurtmen, S., Rowbotham, G., Işler, F., & Floyd, P., 2000. Petrogenesis of Basalts from Southern Turkey: the Plio-Quaternary Volcanism to the North of skenderun Gulf, in *Tectonics and Magmatism in Turkey and the Surrounding Area*, edited by E. Bozkurt, W. J. A., & J. D. A. Piper, pp. 489–512, The Geological Society of London, London, Special Publications 173.

Yurtmen, S., Guillou, H., Westaway, R., Rowbotham, G., & Tatar, O., 2002. Rate of strike-slip motion on the Amanos Fault (Karasu Valley, southern Turkey) constrained by KAr dating and geochemical analysis of Quaternary basalts, *Tectonophysics*, **344**, 207–246.

Zhao, M.-Y. & Zheng, Y.-F., 2014. Marine carbonate records of terrigenous input into Paleotethyan seawater: Geochemical constraints from Carboniferous limestones, *Geochemicia et Cosmochemica Acta*, **141**, 508–531.

Zhu, L., Mitchell, B. J., Akyol, N., Cemen, I., & Kekovali, K., 2006. Crustal thickness variations in the Aegean region and implications for the extension of continental crust, *Journal of Geophysical Research*, **111**.

Zindler, A. & Hart, S., 1986. Chemical Geodynamics, *Annual Reviews of Earth and Planetary Sciences*, **14**, 493–571.

Zor, E., Sandvol, E., Gürbüz, C., Türkelli, N., Seber, D., & Barazangi, M., 2003. The crustal structure of the East Anatolian plateau (Turkey) from receiver functions, *Geophysical Research Letters*, **30**(24), 8044.

Zor, E., Özalaybey, S., & Gürbüz, C., 2006. The crustal structure of the eastern Marmara region, Turkey by teleseismic receiver functions, *Geophysical Journal International*, **167**, 213–222.